FROST DETERIORATION IN CONCRETE DUE TO DEICING SALT EXPOSURE: MECHANISM, MITIGATION AND CONCEPTUAL SURFACE SCALING MODEL

by

Zhichao Liu

A dissertation submitted in partial fulfillment
of the requirements for the degree of
Doctor of Philosophy
(Civil Engineering)
in the University of Michigan
2014

Doctoral Committee:

Professor Will Hansen, Chair
Associate Professor Claus Borgnakke
Associate Professor Eddy A. B. Koenders
Associate Professor Jason P. McCormick

This thesis is dedicated to my beloved wife Jun Chen.

ACKNOWLEDGEMENT

I am deeply indebted to many individuals without whose help I never could have finished this formidable task.

First of all, I wish to express my most sincere gratitude to Professor Will Hansen, my thesis advisor, for his constant guidance, encouragement and patience throughout this whole process. Together, we experienced cyclic frustration and excitement, but ultimately a great sense of fulfillment.

Many thanks go to my committee members Prof. Claus Borgnakke, Prof. Eddy Koenders, and Prof. Jason McCormick for your valuable suggestions and comments that help improve this thesis.

I would like to extent my appreciation to other professors and staff in the Department for offering me help and advice and to my friends for your companion. I wish to give my special thanks to Jan Pantolin, the Technical Services Supervisor, and Bo Meng, the Graduate Student Research Assistant, for providing a lot of laboratory assistance to my testing and measurement.

I also would like to thank Andy Bennett and John Belcher from MDOT for facilitating the test on field samples.

Finally, thank you to my parents and wife for their love, support and sacrifice!

TABLE OF CONTENTS

LIST OF FIGURES

LIST OF TABLES

ABSTRACT

Michigan is located in a wet-freeze climate zone. During winter the deicing-salt application is needed to melt snow on highways. Freezing in the presence of a deicing salt solution is considered a severe concrete exposure condition. Prolonged exposure in pavement joints has been found to erode the concrete binder material (portland cement paste) when coupled with its low internal frost resistance (i.e. insufficient air and poorly drained joints). This creates a weak zone resulting in joint spalling from heavy wheel loading. Many highways have been found to suffer this type of distress within ten years requiring expensive joint repairs. This research investigates the material level mechanisms for frost deterioration under deicing salt exposure by the aid of systematic application of various experimental techniques, such as sub-freezing length change measurement, micro- and macro-characterization of scaling properties and nitrogen sorption test. A new conceptual model is provided for the surface deterioration that occurs within a thin surface layer when exposed to a deicing salt solution. The major stress producing mechanism is ice-growth within the capillary pores exacerbated by cryogenic suction of the liquid brine present on the surface, thus feeding further ice-growth and leading to high tensile stresses in the direction of least internal restraint and "popping" of thin mortar flakes. This process repeats itself for every freeze-thaw cycle. These findings pave the way for the proposal of sorptivity as a performance-based criterion to evaluate scaling resistance in concrete and its theoretical nature is enhanced by a refined model capable of capturing the effect of pore size characteristics (pore volume, its size distribution and connectivity). This further leads to the identification and application of effective mitigation techniques, including reconfiguration of paste pore system towards a more refined and discontinued structure and utilization of a hydrophobic pore liner in the silicate substrate of hydration products as surface treatment.

CHAPTER 1 INTRODUCITON

1.1 Problem Statement

Concrete is the most widely used construction material in the world and its presence is felt in numerous ways in our daily lives: the buildings where we live and work and the infrastructure that connects us. Thus, it is no exaggeration to say that concrete lays the foundation for our modern society. In addition, the enormous application of concrete holds the promise that it can be part of the solution, if aided with breakthroughs in concrete science and engineering, to a sustainable development in society and economy while minimizing the ecological footprint.

However, popularity does not guarantee immunity. Most of the concrete structures are exposed to the environment where deleterious species can penetrate into concrete via a variety of transport mechanisms, leading to a range of durability related problems and undermining its serviceability, among which, frost damage is one of the most severe and also extensively studied topics.

Frost attack on concrete is a distress resulting from the phase transformation associated with the freezing of internal moisture. It essentially manifests itself from two aspects (Figure 1.1): (1) generation of internal cracks and disintegration (internal pure frost attack) and a common laboratory indicator is the decrease in relative dynamic modulus (RDM); (2) progressive swelling and flaking of mortars on the surface exposed to de-icing salts (salt scaling) which is characterized by the normalized mass loss per unit test area. The latter case is caused by the combined action of salt-frost and is generally believed to be more severe in magnitude.

The most immediate relation that can be established to salt frost scaling is probably the spalling of the sidewalk in front of our houses, which is considered nothing more than an aesthetical issue. Nevertheless, this deterioration needs to be seriously addressed if it occurs in concrete structures such as pavements, bridge decks, where surface scaling is normally the precursor to other durability-related issues. This is because the removal of concrete skin renders it vulnerable

to the ingress of moisture and hazardous chemicals. Several case studies are presented below to showcase this.

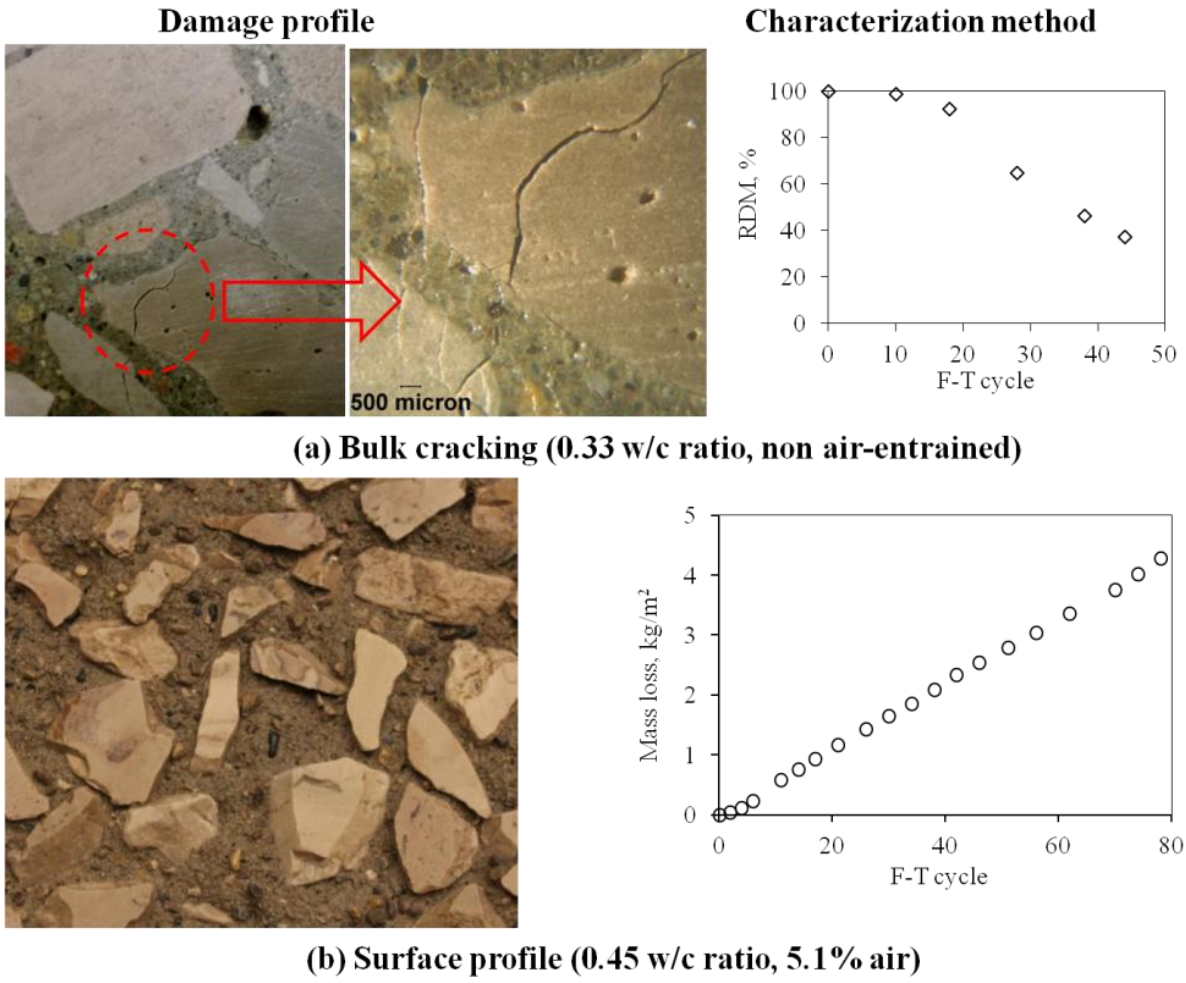

(a) Bulk cracking (0.33 w/c ratio, non air-entrained)

(b) Surface profile (0.45 w/c ratio, 5.1% air)

Figure 1.1 Frost damage in concrete

Joint damage has developed in several highway projects in Michigan, USA, where deicer salts are used extensively for snow melting purposes (Figure 1.2(a)). Typical for these cases are a combination of liquid entrapment in the joint areas associated with poor drainage and low concrete frost resistance due to insufficient air-void system. Dark spots (joint staining) are typically seen in the joints (Figure 1.2(b)), a sign of higher moisture content due to the hygroscopic characteristic of deicer salts entrapped in the joint. Joint cores show that frost deterioration of the portland cement paste develops at the bottom of a saw-cut, which leads to a localized weakening. Eventually, spalling develops from truck-loading and the process continues until a severely spalled joint requires full-depth replacement (Figure 1.3) (Hansen and Kang

2010). Accelerated corrosion of embedded reinforcing bars is a typical consequence of salt frost scaling, which is illustrated in a bridge located in the northern part of China (Harbin). The corroded rebar is exposed in different structural components due to the gradual deterioration of the cover concrete (Figure 1.4).

Severe surface scaling also occurred in a new shipyard located along one of the coastal cities of China (Qingdao), as seen in Figure 1.5. This scenario embodies the two indispensable components simultaneously: freezing weather (the snow) and presence of salt (the sea water). The concrete mix has a high w/c ratio (0.5) and no air entrainment, both of which have been demonstrated to be essential factors in controlling salt frost scaling.

Figure 1.2 (a) Joint distress associated with salt frost deterioration and (b) transverse joint staining (by courtesy of Prof. Will Hansen)

Figure 1.3 Joint spalling at the bottom of a saw-cut joint associated with deicer salt scaling (by courtesy of Prof. Will Hansen)

(a) Bridge column (b) Bottom of the bridge wall

Figure 1.4 Rebar corrosion in bridge due to salt frost scaling (by courtesy of Xin Ge)

(a) Shipyard exposed to freezing and sea water

(b) Concrete spalling

(c) Concrete slab surface scaling

(d) Close-up view of the scaled surface

Figure 1.5 Salt scaling in a newly-build shipyard in Qingdao, China (by courtesy of Xingtao Huang)

The severity of salt-frost deterioration has drawn a lot of attentions to concrete researchers and technologists alike. One essential dimension involves deciphering the mechanism behind it, which will lend support to the existing techniques and more importantly open new windows towards improving the scaling resistance in concrete. Indeed, many theories have been developed with their own merits and drawbacks, but none of them is able to account for the whole spectrum of laboratory and field observations, which serves as the major motivation for this work.

1.2 Scope of investigation

This thesis centers on the continued investigation of a hypothesized scaling theory (Lindmark 1998, Kang 2012) by a multitude of experimental methods and theoretical analyses, which is extended towards the construction of a conceptual model and performance-based prediction criterion. This further serves as the basis for developing effective mitigation methodologies and preparation guidelines of concrete mixes geared towards high durability and sustainability.

The primary objectives of this research are condensed in Figure 1.6 and detailed below, which covers three aspects: mechanism, prediction and mitigation.

- investigate the characteristics of bulk moisture absorption in concrete with air entrainment to different degrees and clarify its relationship to internal cracking and salt frost scaling.
- identify the liquid transport mechanism that governs concrete scaling by monitoring the length-change profiles in small-scale concrete specimens under various exposures and surface treatment conditions.
- substantiate the continuous ice growth as the main reason for pore pressure buildup, which leads to the construction of a conceptual scaling model.
- build the thermodynamic foundation so as to semi-quantitatively account for the effects, such as salt presence, temperature and pore structure of concrete, on ice growth.
- develop and validate an analytical model for concrete sorptivity used as the performance-based criterion for assessing scaling resistance.
- evaluate different mitigation techniques on salt frost scaling, which provides insight towards the field application in preparing durable concrete mixes.

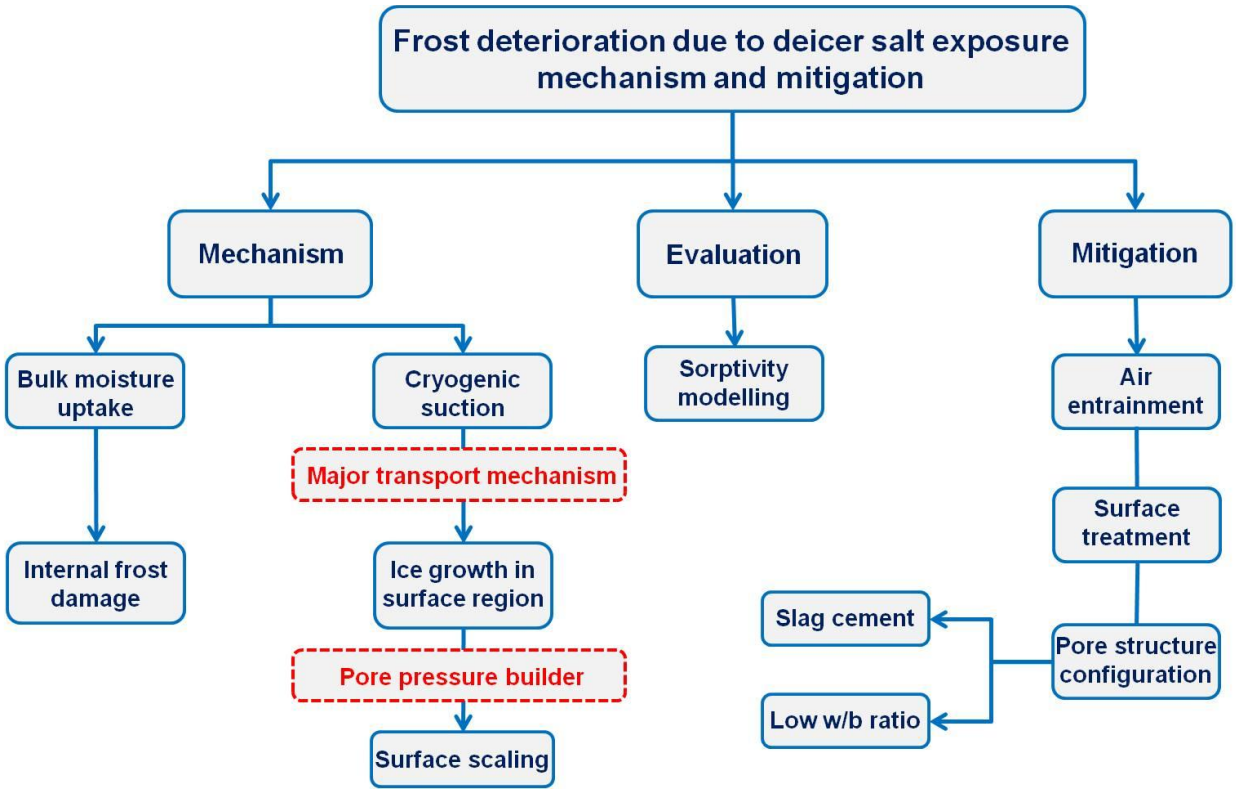

Figure 1.6 Thesis road map

1.3 Thesis Organization

The thesis is organized in the following manner: Chapter 2 gives an introduction to the microstructure of cement paste and the air void characteristics, along with the liquid transport mechanisms in general and the moisture absorption behavior in air entrained concrete. The experimental techniques employed in this research are outlined in Chapter 3. This is followed by Chapter 4 on the investigation of bulk moisture uptake in concrete under repetitive freezing-thawing exposure. Its dominant transport mechanism is explored and its relationship to salt frost scaling is elucidated. In Chapter 5, salt frost scaling properties in air-entrained concrete are thoroughly examined before the validation of the cryogenic suction as the major mechanism for scaling using both experimental and analytical methods, by which several frequently detected phenomena are reasonably interpreted and a conceptual model is introduced. In Chapter 6, a performance-based criterion using sorptivity, an indicator of capillary suction rate, is proposed in evaluating scaling resistance of concrete and its theoretical nature is enhanced by the refined model based on paste pore structure properties. Factors affecting this parameter are discussed. The main purpose of this research points towards the preparation guidelines of concrete mixes

with improved durability and sustainability from the field and laboratory perspectives in Chapter 7. Finally, Chapter 8 summarizes the major findings of the thesis and provides recommendations for possible extensions of this work.

CHAPTER 2 LIQUID TRANSPORT IN CONCRETE-AN OVERVIEW

2.1 General

Concrete is a versatile construction material with its applications extending from bridge piers embedded deep into the ground to offshore platforms. As a result, concrete is exposed to a variety of mechanical loads (compression, flexural, torsion and dynamic, etc.) and environmental loads (fire hazard, penetration of deleterious species, etc.). The transport of liquid into concrete is the culprit of many durability-related issues: water saturation of concrete leading to frost damage; migration of chloride ions causing the corrosion of reinforcements; ingress of sulfate inducing detrimental expansion, not to mention the alkali-aggregate reaction (AAR), carbonation, etc. Furthermore, the porous skeleton of concrete and the presence of cracks substantially facilitate the transport process. Thus, a better comprehension of the mechanisms governing liquid transport into concrete and the physical properties controlling its magnitude forms an essential component in the construction of performance-based evaluation for concrete durability.

This chapter starts with the synopsis of the pore characteristics (including capillary and gel pores and the entrained air voids) in concrete with a focus on the discussion of air void properties. Different liquid transport mechanisms are then reviewed which is followed by a section devoted to the transport features in air-entrained concretes.

2.2 Pore structure of concrete

Cement hydration is a persistent process and starts, upon its contact with water, from a liquid state to a viscoelastic state, followed by further development into a hardened material, which is illustrated in Figure 2.1.

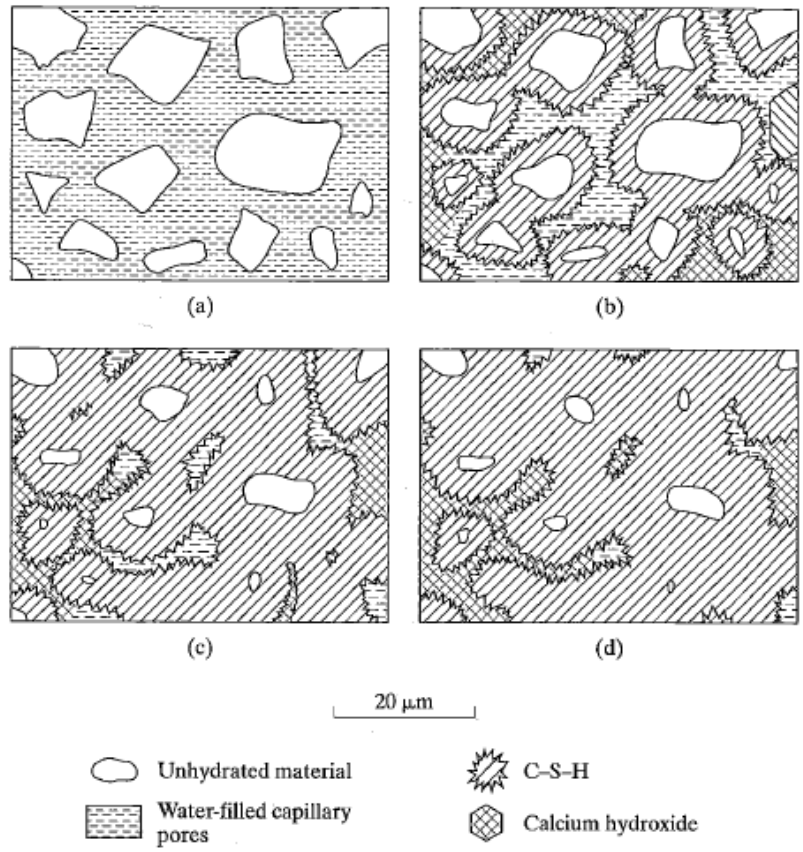

Figure 2.1 Schematic representation of microstructure evolution with time (a: initial mix, b: 7 days, c: 28days, d: 90 days) (Mindess et al. 2003)

At the microscopic level, the structure of hydrated cement paste consists of unhydrated cement grains embedded in a matrix of hydration products which is a semi-continuous system of water-filled or empty capillary pores. Specifically, the hydration products of cement include a variety of compounds, collectively referred to as C-S-H gel and crystals of calcium hydroxide ($Ca(OH)_2$). The C-S-H gel, interwoven with $Ca(OH)_2$ crystals, fills part of the space in between cement grains before hydration and the rest of the unoccupied space forms the capillary pore system, either empty or water filled. At a submicroscopic level, C-S-H gel is a porous matrix with extremely high surface area which is composed of ill-shaped particles and the gel pores. A model on the probable structure of cement paste was proposed and presented in Figure 2.2 (Feldman and Sereda 1968)

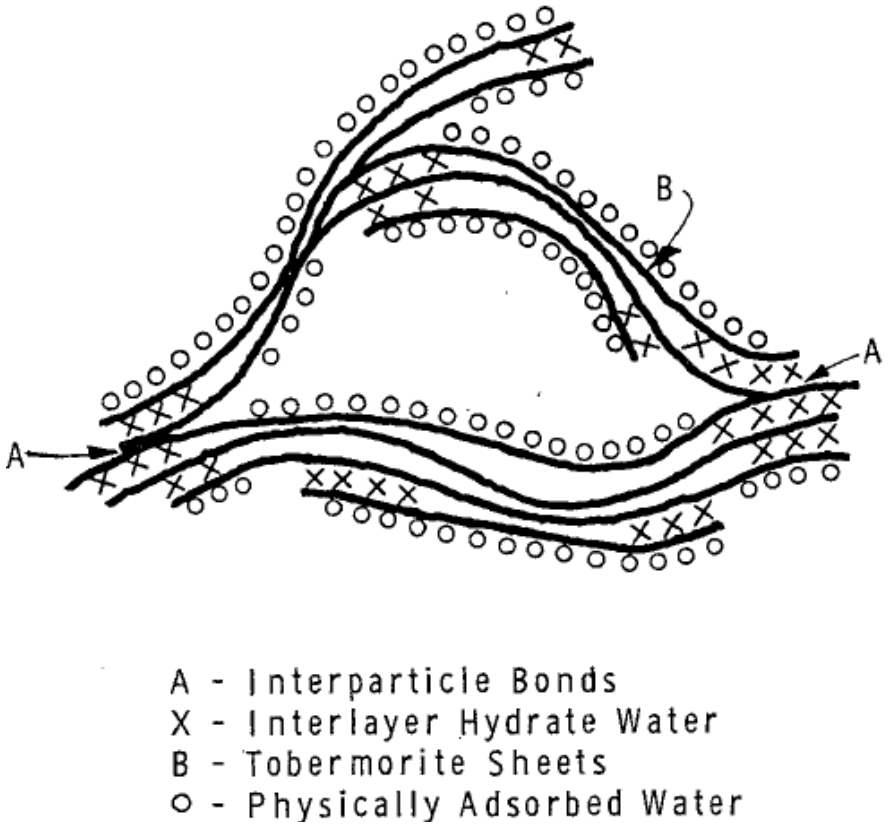

Figure 2.2 A hypothesized structure of cement paste (Feldman and Sereda 1968)

As aforementioned, there are two types of pores present in the structure of cement paste and they are capillary pores and gel pores. Capillary pores are the remnants of water-filled space and its volume is decreased with the progression of cement hydration. The size of capillary pores typically lies in the range of several nanometers up to 10 μm. Gel pores are associated with the formation of C-S-H gel and are the interconnected interstitial space between gel particles. Gel pores are much smaller than capillary pores and are normally below 3 nm in nominal diameter. A break-down of the pore size classification is listed in Table 2.1.

Table 2.1 Classification of pores in cement paste (Mindess et al. 2003)

Pore type	Diameter	Description
capillary pores	10,000-50 nm	large capillaries (macropores)
	50-10 nm	medium capillaries (large mesopores)
	10-2.5 nm	small isolated capillaries (small mesopores)
gel pores	2.5-0.5 nm	micropores
	≤ 0.5 nm	interlayer spaces

Porosity is the volume fraction of pores with respect to the gross volume of cement paste. Powers and Brownyard put forward a series of simplified formula to calculate the porosity based on the information of water cement ratio (w/c) and the degree of hydration α (Powers and Brownyard 1947).

- **Capillary porosity** $P_c = \frac{w/c - 0.36\alpha}{w/c + 0.32}$ (2-1)
- **Gel porosity** $P_g = \frac{w_g}{V_{hp}} = \frac{0.18\alpha}{0.68\alpha}$=0.26 (2-2)

  (assume gel pores are completely filled with gel water w_g. V_{hp} is the volume of hydrated cement)

It can be seen that the volume of gel pores is a constant for normally hydrated cement and accounts for around 1/4 of the cement hydrates and 1/3 of the gel solids.

The microstructure of cement hydrates adjacent to inert inclusions (aggregate, fibers and steel bars, etc.) is found to differ significantly from the bulk paste. This region is known as the interfacial transition zone (ITZ) which is characterized by an increased porosity and a reduced mechanical strength (Ollivier et al. 1995, Scrivener et al. 2004). Thus, ITZ in concrete is believed to be the facilitator of ingress of species exposed to the environment and one of the initiators of microcracks under load.

The origin of ITZ is generally thought to be a result of the "wall" effect: the packing issues of cement grains against aggregate due to the incompatibility in size, as described by (Scrivener et al. 2004) that "A flat solid object placed at random in an assembly of cement grains would cut through grains. As this is impossible the packing of grains is disrupted to give a zone of higher porosity and smaller grains in the zone close to the aggregate" (Figure 2.3).

As indicated by its name, ITZ represents a transitional region between aggregate and the bulk paste with a gradient in physical properties. The typical width of this zone is in the range of 20-40 μm (Mindess et al. 2003).

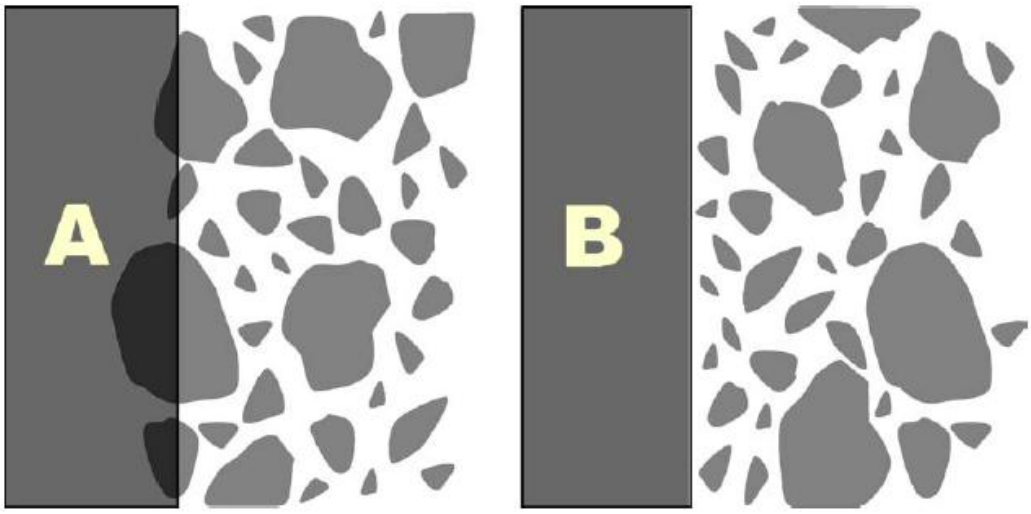

Figure 2.3 Schematic description of the "wall" effect contributing to ITZ (Scrivener et al. 2004)

2.3 Features of air void system in concrete

Concrete subjected to a freezing environment needs an adequate amount of entrained air bubbles to protect its structural integrity by providing internal shelter spots to accommodate the excessive hydraulic pressure build-up. A typical profile of air void distribution in concrete is shown in Figure 2.4. The incorporation of air bubbles into concrete can be realized by adding an air-entraining agent either during concrete mixing or during the manufacturing of cement.

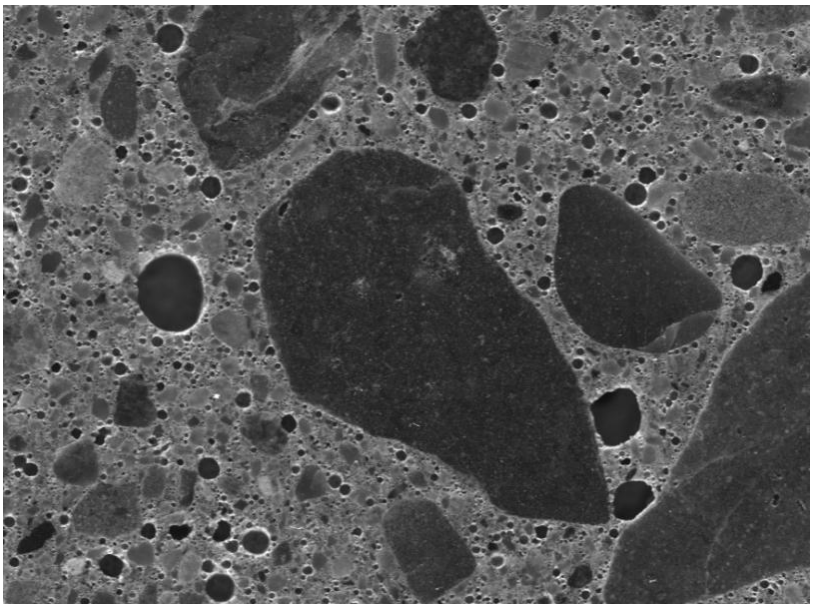

Figure 2.4 Air void profile in hardened concrete

It has been confirmed that the sheer number of air voids in concrete is as important as the spacing between them. This section provides a literature review of the characteristics of air void system, supplemented by the research work of the author, with an aim to better interpreting the results from air void analysis.

2.3.1 Air content *A*

Air content is the most straightforward parameter for the air void system of concrete and it is a direct indicator of the amount of air bubbles contained in the paste matrix. In some Standards or Provisions (ACI 318 2005, ACI 301 1999), a specific air content range is recommended for the protection of concrete against frost damage, depending on the severity of exposure.

- **Visualization of air void profile**

More often than not, air content is nothing but a number (low, medium or high) and limited effort has been made to visualize the air void in concrete partially due to the difficulty of obtaining a satisfactory concrete section with good polishing quality. In this research the author has been rigorously trained and practicing on a large number of concrete specimens, made in the laboratory or received from the field, with a decent collection of microscopic pictures. A selection of these pictures is presented to show concretes with different air contents in the hope to provide more context into the concept of air content (Figure 2.5).

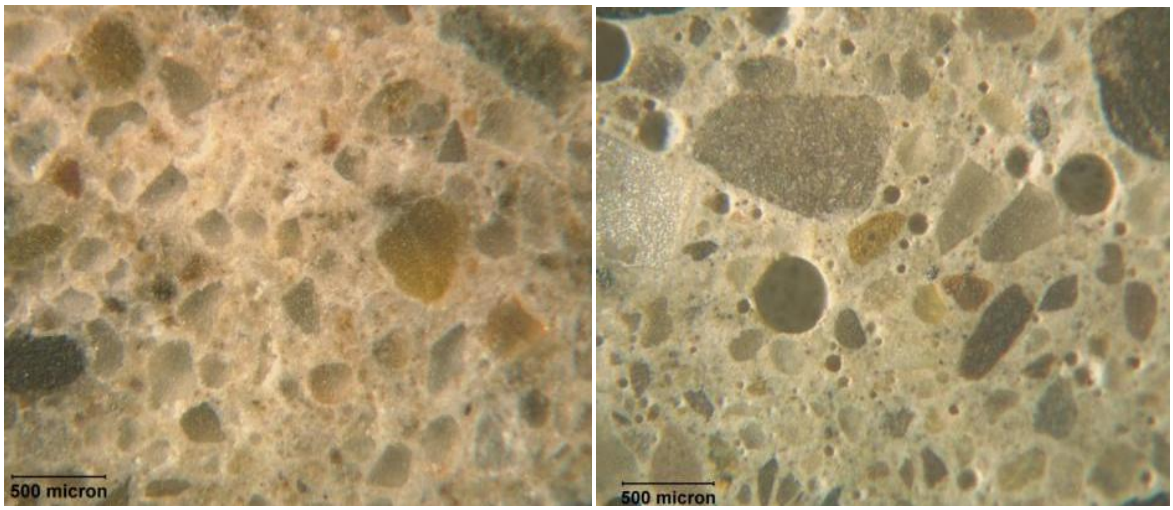

(a) no entrained air (b) low air (3.0%)

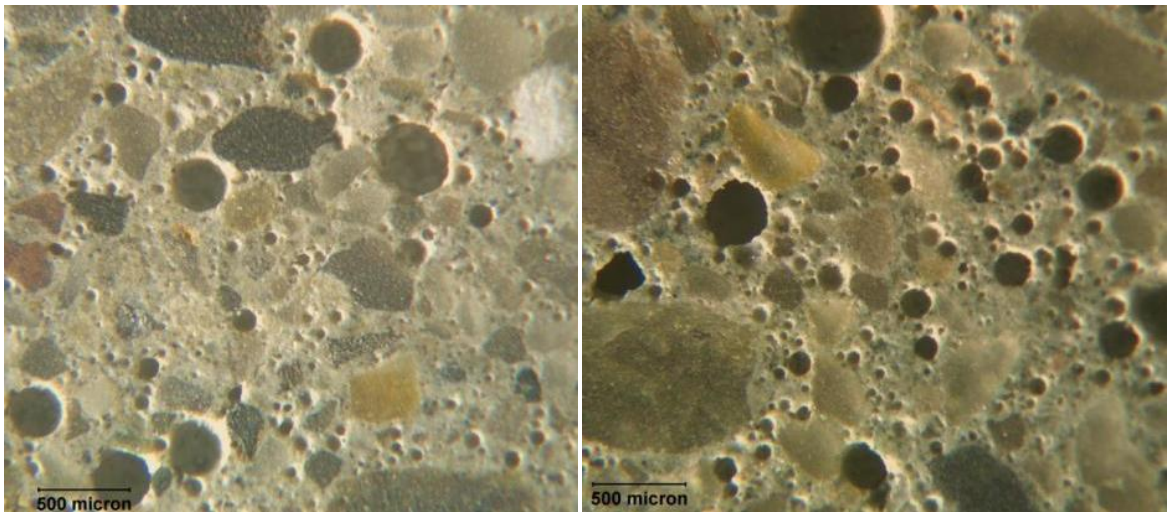

(c) medium air (5.0%) (d) high air (7.5%)

Figure 2.5 Microscopic profile of air voids in concrete

- **Entrained and entrapped air voids**

There is a wide size distribution in the air voids and ASTM C 125 (2000) defines them into two categories on the basis of their size and shape, which is quoted as "an entrapped air void is characteristically 1 mm or more in width and irregular in shape; an entrained air void is typically between 10 and 1000 μm in diameter and spherical or nearly so". The entrapped air voids are shown in Figure 2.6. It has to be borne in mind that this definition is totally empirical and tells nothing about the physical function of these two types of air voids. However, it is usually a good practice to make a distinction between the total air content (sum of entrapped and entrained air voids) and the entrained air content (entrained air voids only), since entrapped air voids are mostly the big cavities generated unintentionally during mixing and placing of concrete whereas entrained air voids are a product of the air entraining agent. Entrapped air voids can notoriously undermine the strength of concrete and more importantly, the Power's spacing factor is reduced with the presence of big air voids, as will be shown later, and the frost-resistant performance of a concrete can be overestimated if only the total air content is used. As a result, entrained air content is more desirable in the evaluation of concrete against frost damage.

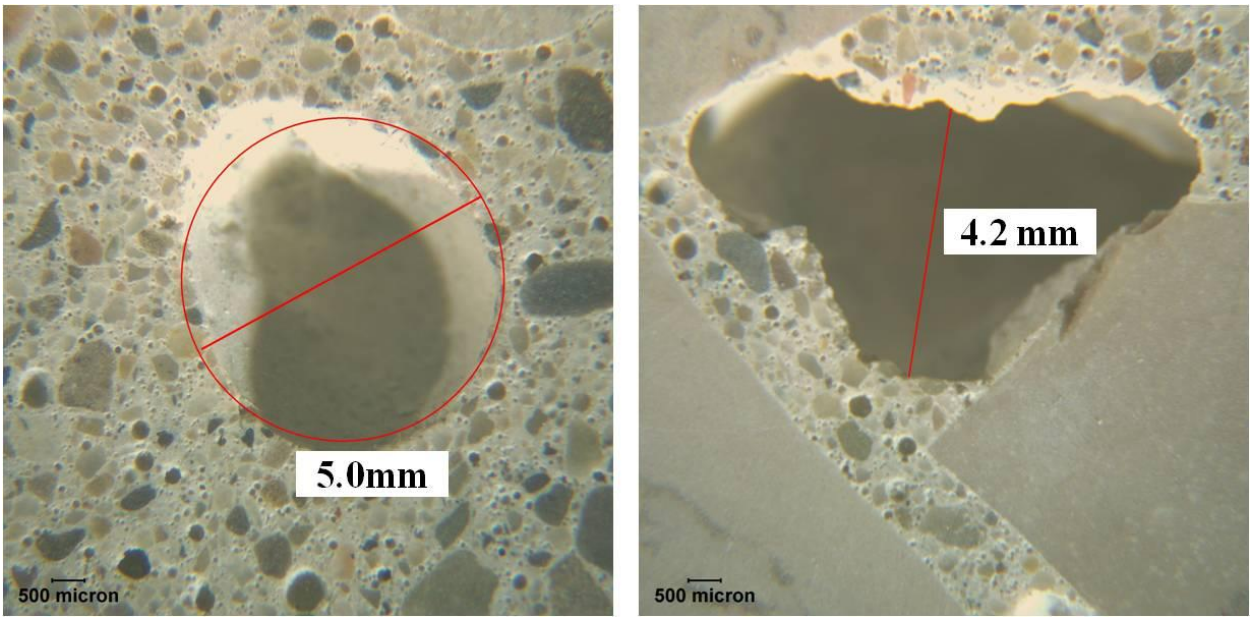

Figure 2.6 Entrapped air voids in concrete

- **Normalization of air content**

Air content is normally expressed as the volume ratio of air voids to concrete and this treatment works fine in concrete that has a relatively narrow range of aggregate content (60-70 vol.%). However, confusion will arise when it comes to mortar mixes with a low aggregate volume, given the fact that frost damage is essentially a phenomenon happening in the pore structure of the cement paste and the protection domain of air voids is actually the paste. Thus, a set of concrete and mortar samples with the same air content can have substantially different densities of air voids in the paste, which can be characterized by the spacing factor or specific surface. For instance, four concrete samples are assumed to have 7% air and 40 mm^{-1} specific surface but varied aggregate volume (20%, 40%, 60% and 80%). It can be seen in Figure 2.7 that the calculated Powers' spacing factors are quite different even with the same air content. This can sometimes give rise to misinterpretation of experimental results, especially in some papers with cement mortar being the investigation subject. However, if we normalize the air content with respect to the paste volume and re-plot it, a logical correlation is obtained: spacing factor is decreased with more air present.

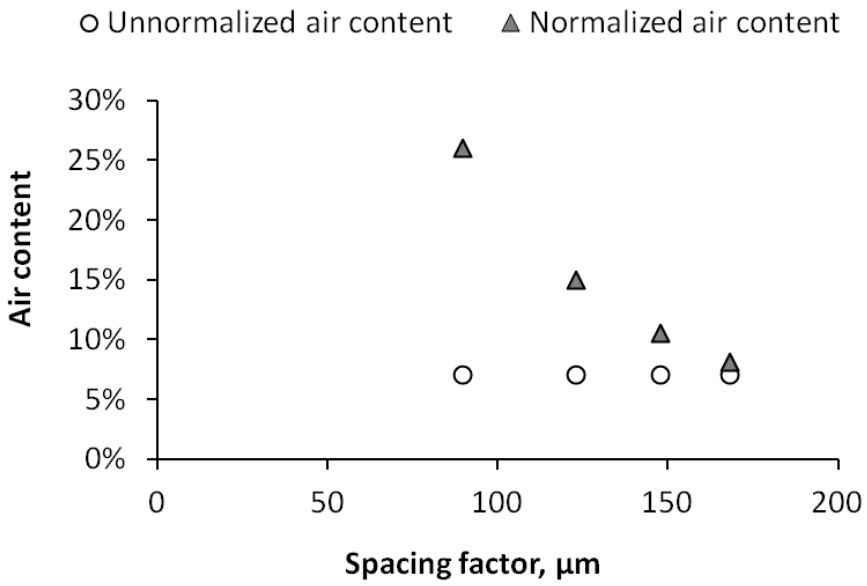

Figure 2.7 Relation between air content and spacing factor

2.3.2 Spacing factor $\bar{L}$

The dispersion quality of air voids in concrete is as important as, if not more than, their accommodation capacity, viz. the air content. Spacing factor is the well accepted indicator of the distance water must travel to reach the nearest air void without creating destructive stresses.

A couple of different spacing equations have been proposed (Attiogbe 1993, Fagerlund 1977, Philleo 1983, Pleau and Pigeon 1996, Powers 1949), and they generally fall into two categories (Snyder et al. 2001):

- **paste-void proximity:** representation of a volume fraction of a shell of paste surrounding an air void (Fagerlund's, Philleo's, Pleau and Pigeon's, Powers' spacing factors).
- **void-void proximity:** representation of surface-to-surface distance between two air voids. It can be the distance from the surface of an air void to the surface of the nearest air void or the average length of paste between two air voids intersected by a random line (Attiogbe's spacing factor)

Powers' spacing factor is the most commonly used and will be the focus of this section. Below is a brief revisit of its derivation.

In his model, Powers transformed the 3-D problem into a 2-D plane problem and used the linear traverse method as the basis to compute the spacing factor. The principle of linear traverse analysis is that a straight probe line travels across a plane section of a polished concrete and the following parameters are recorded: T_a-the total length over air voids, T_t-the total traverse length, N-the total number of air voids intersected. Then,

air content is $A = \frac{T_a}{T_t}$ (2-3)

void frequency $n = \frac{N}{T_t}$ (2-4)

average chord length across the air voids $l = \frac{T_a}{N} = \frac{A}{n}$ (2-5)

specific surface $\alpha = \frac{4}{l} = \frac{4n}{A}$ (2-6)

The spacing factor $\bar{L}$ is geometrically defined as "the difference between the radius of the sphere of influence r_m and the radius of the bubble r_h", that is, $\bar{L} = r_m - r_h$.

Two situations were considered in the computation of the spacing factor $\bar{L}$.

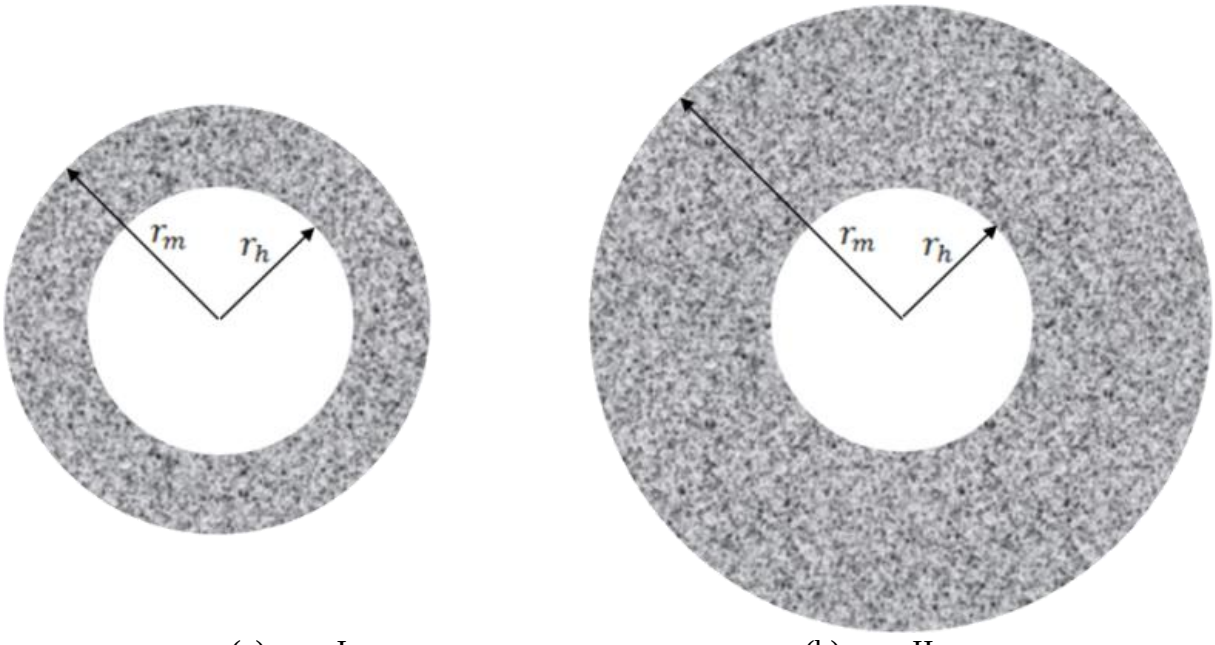

(a) case I (b) case II

Figure 2.8 Sketch of relative volume ratio between paste to air voids

Case I: $\boldsymbol{p/A} < 4.342$

The volume of paste is relatively low (Figure 2.8(a)) and a decent accuracy can be achieved by assuming that the gradient in the cross-sectional area of the paste shell is so small that a constant area can be used as $A_h = 4\pi {r_h}^2 = \alpha A$ and the paste volume is $p = \bar{L} A_h = \bar{L} \alpha A$.

So the spacing factor is $\bar{L} = \frac{p}{\alpha A}$ (2-7)

Case II: $\boldsymbol{p/A} \geq 4.342$

The above-mentioned assumption will no long be valid with the increase of paste content (Figure 2.8(b)). Powers made three further assumptions to simplify the calculation.

(1) All the air voids are monosized spheres with the same specific surface as what is measured in the linear traverse method.

(2) Each of the equal-sized spheres is located at the center of a cube. The volume of an array of such cubes packed together, alone with the inclusive air voids, is equal to the combined volume of air and paste in concrete.

(3) The "sphere of influence" is the radius of the sphere circumscribing the cube.

To obtain r_m, the following parameters need to be calculated first.

The number of the hypothetical cubes (or air voids) $N_h = \frac{A}{4/3\pi r_h^3} = \frac{A\alpha^3}{36\pi}$ (2-8)

The volume of each hypothetical cube $V_c = \frac{P+A}{N_h}$ (2-9)

Thus, $r_m = \frac{\sqrt{3}}{2}(V_c)^{1/3} = \frac{\sqrt{3}}{2}\left(\frac{P+A}{N_h}\right)^{1/3} = \frac{4.19}{\alpha}\left(\frac{P+A}{A}\right)^{1/3}$ (2-10)

By definition, the spacing factor is

$$\bar{L} = r_m - r_h = \frac{4.19}{\alpha}\left(\frac{P+A}{A}\right)^{1/3} - \frac{3}{\alpha} = \frac{3}{\alpha}\left[1.40\left(\frac{P}{A}+1\right)^{1/3} - 1\right] \quad (2\text{-}11)$$

$r_h = \frac{3}{\alpha}$ and α is the specific surface.

There is one drawback associated with Powers' spacing factor, that is, adding more air bubbles into concrete actually makes the spacing factor larger (Attiogbe 1993, Sommer 1979, Walker 1980), which does not make any sense, as indicated in Figure 2.9. The reason for that is because

the number of the hypothetical voids is not the same as the actual number of voids in concrete, but is related to a constant specific surface. The smaller the size class is, the more the hypothetical bubbles are (Figure 2.10) and the smaller the spacing between the air bubbles is, even when the radius of the air bubbles is also increased. This anomaly is illustrated in Figure 2.11 (Pleau et al. 1990).

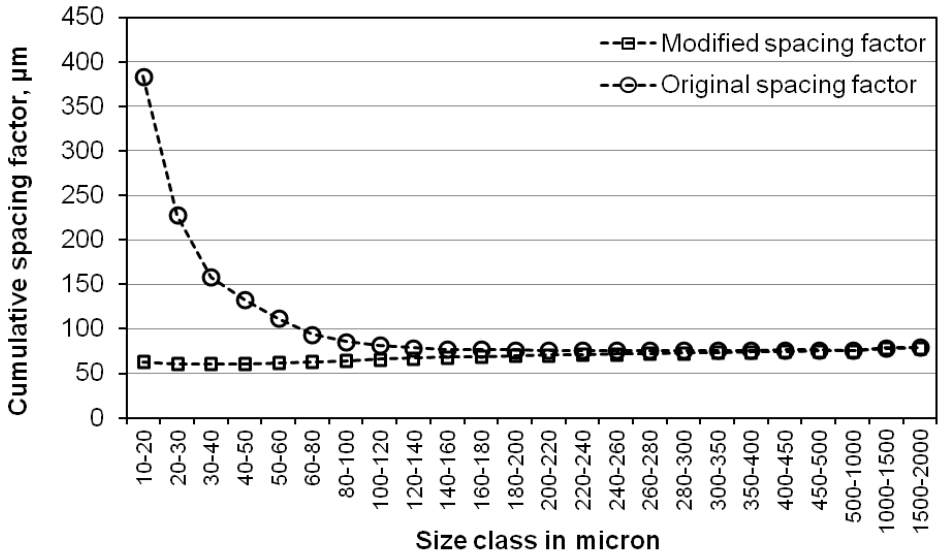

Figure 2.9 Spacing factor variation with more air being counted (air content=7.0%)

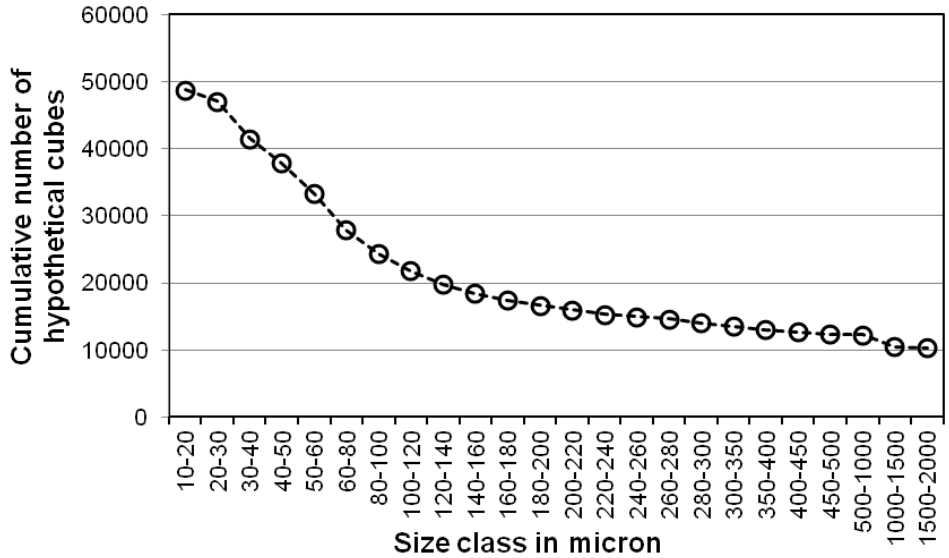

Figure 2.10 Variation in cumulative number of hypothetical cubes with more air being counted (air content=7.0%)

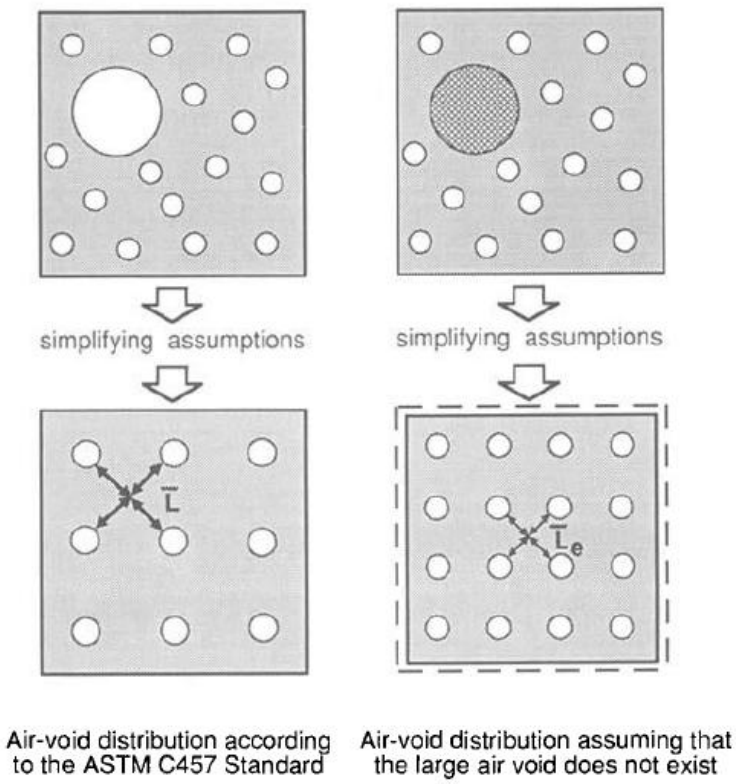

Figure 2.11 Schematic representation of the effect of big voids on the spacing factor (Pleau et al. 1990)

To remedy this defect, Walker proposed a modified equation to calculate the spacing factor for the small entrained voids by incorporating a scaling factor (Walker 1980), that is

$$N_{hm} = \frac{A\alpha^3}{36\pi} \times \frac{N_i}{N_t} \tag{2-12}$$

and the modified spacing factor equation is

$$\bar{L} = r_m - r_h = \frac{3}{\alpha}\left[1.40 \times \frac{N_t}{N_i} \times \left(\frac{P}{A} + 1\right)^{1/3} - 1\right] \tag{2-13}$$

As can be seen from Figure 2.9, the modified spacing factor decreases with more air voids present and the two spacing factors start converging at the size ranging up to 100 microns, which is consistent with the statement that small entrained air is more efficient in frost protection (Powers 1949).

2.3.3 Air void clustering

Air void clustering is the localized agglomeration of air bubbles with exceptionally high concentration. It often occurs in the paste adjacent to coarse aggregate particles, as seen in Figure

2.12(a, b and d). Sometimes it is also observed in the paste or along the edge of a big air void (Figure 2.12(c)). The presence of air void clustering is believed to be the culprit for abnormal strength loss of concrete in the field, since it creates a weak zone to facilitate the propagation of cracks. A comprehensive study by (Kozikowski et al. 2005) on the mechanism leading to the occurrence of air void clustering revealed that factors such as concrete mixing procedure (mixing time, late addition of water and retempering), the type of air entraining agent and aggregate shape/mineralogy can be attributed to this unwanted phenomenon.

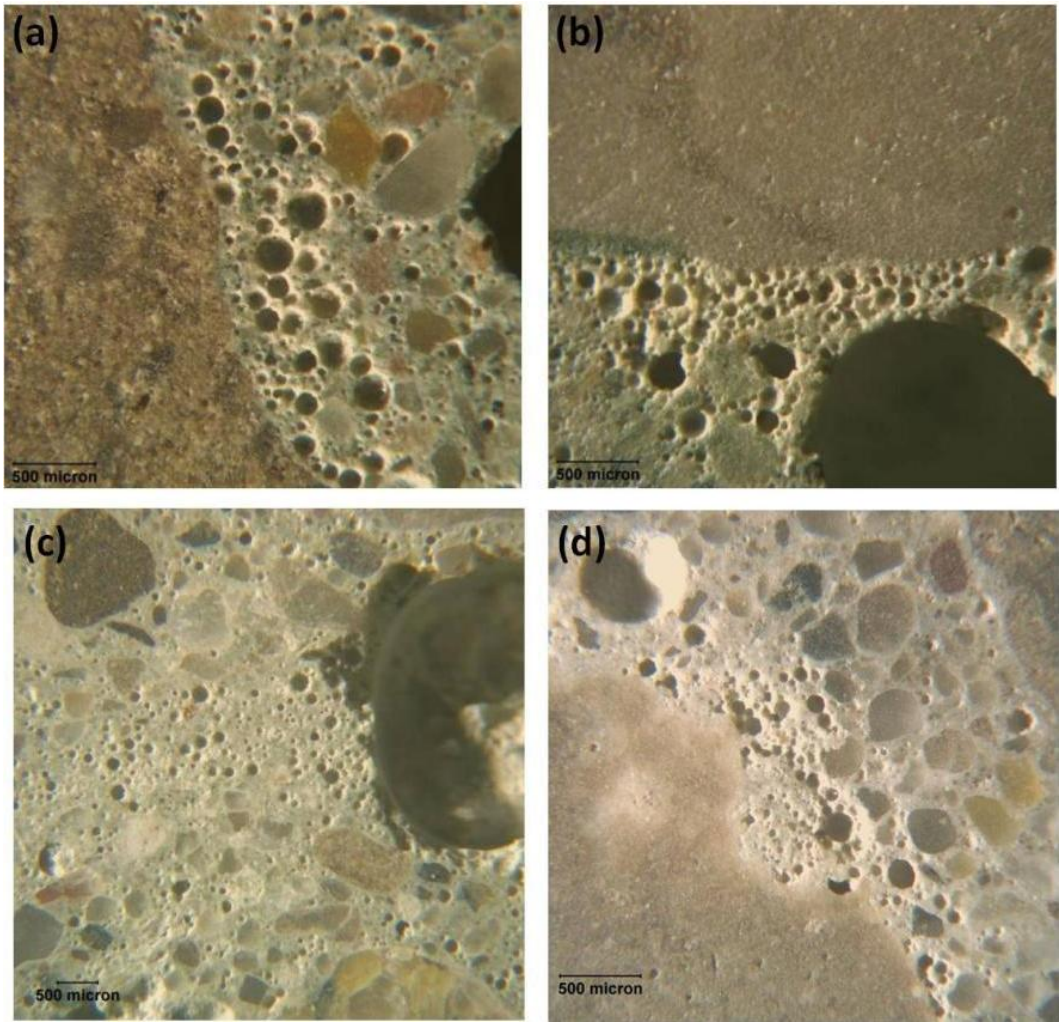

Figure 2.12 Air void clustering in concrete

2.3.4 Infilling in air void

Microscopic examination of concrete pavement exposed to a combined salt and frost attack has revealed the repeated observation of air voids being filled to varied degrees by a solid substance (Hansen and Kang 2010, Schlorholtz and Amenson 1995, Stark 1997), as seen in Figure 2.13. Several studies came to the conclusion that these infillings are ettringite deposits (Rachel et al. 2007, Stark 1997).

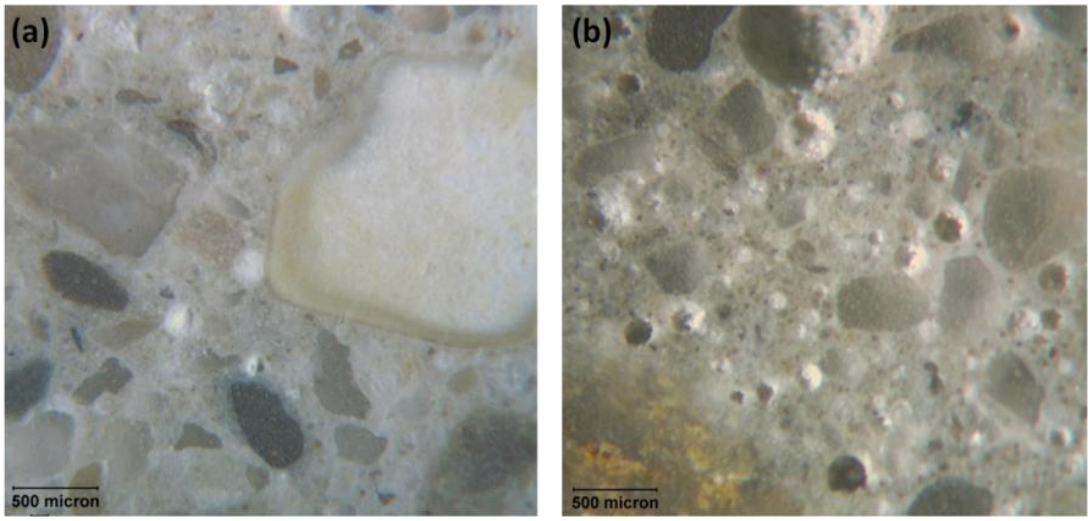

Figure 2.13 Infilling in air void

Ettringite (6 calcium aluminate-trisulfate-32-hydrate) is a calcium sulfoaluminate hydrate, formed in the hydration of tricalcium aluminate (C_3A) with the presence of gypsum. The primary initial reaction of C_3A takes the following form:

$$3CaO \cdot Al_2O_3 + 3CaSO_4 \cdot 2H_2O + 26H_2O \rightarrow 3CaO \cdot Al_2O_3 \cdot 3CaSO_4 \cdot 32H_2O \quad (2\text{-}14)$$

Tricalcium aluminate Gypsum Water Ettringite

Stark proposed a series of chemical reactions of phase transformation, leading to the formation of ettringite in concrete under salt-frost exposure (Stark 1997), as illustrated in Figure 2.14. It states that the presence of chloride ions facilitates the decomposition of monosulphate and the concomitant formation of monochloride (Friedel's salt), which eventually results in the formation of ettringite.

It can be seen that the formation of ettringite requires the availability of pore solution, such as in the pores and cracks of concrete. Then why is ettringite also found in the air voids (Figure 2.15)?

Ouyang and Lane came up with this question and they thought that the air void lost its protection function against freezing pressure due to the crack intersection through the void, then the air void becomes accessible to moisture, which makes possible the formation of ettringite (Ouyang and Lane 1999). As a matter of fact, it has been experimentally demonstrated that the expulsion of air out of the air voids due to the repetitive "pump" effect, resulting in water-filled voids (Kang 2010, Liu et al. 2012).

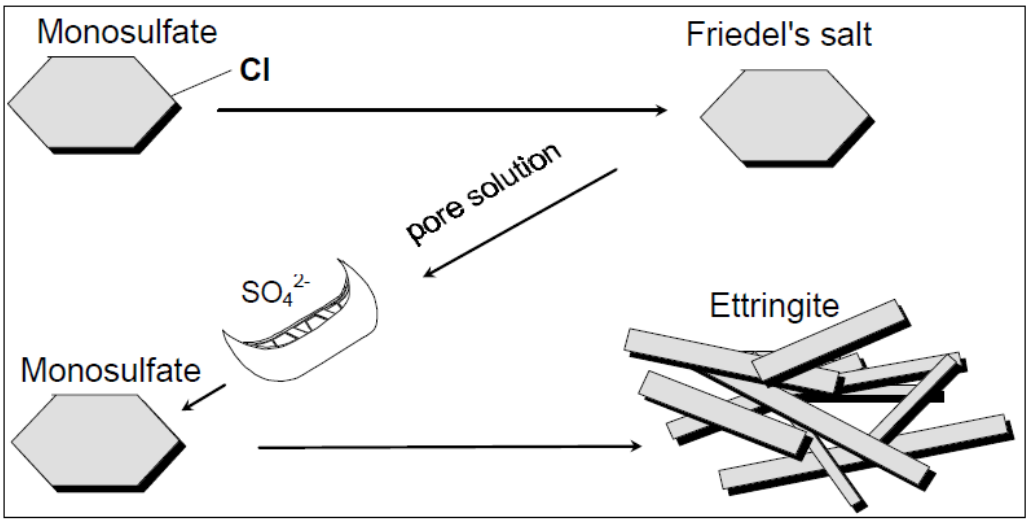

Figure 2.14 Mechanism of ettringite formation under salt exposure (Stark 1997)

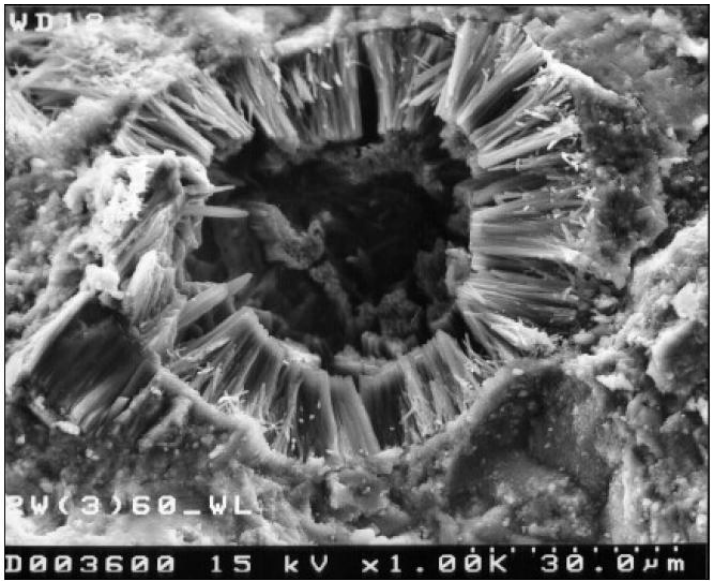

Figure 2.15 Ettringite formation in the air void (Bollmann and Stark 1996)

It should be noted that the formation of ettringite is not the cause of malfunction of air voids as the pressure relieving agent. It is just a process facilitated by the consequential water filling of the air voids under F-T exposure. Caution should be taken in the interpretation of any results correlating the scaling severity to the amount of ettringite formed.

2.4 Transport mechanisms

In this section, mechanisms behind the ingress of liquid into concrete are reviewed, which sets out a theoretical framework for the correct experimental analysis of the transport processes.

2.4.1 Diffusion

Diffusion is a mass transfer process from areas of higher concentration to areas of lower concentrations. Fick's first law states that the rate of diffusion is a function of the concentration gradient and the diffusion coefficient.

$$F = -D\frac{\partial c}{\partial x} \tag{2-15}$$

F is the mass flux (g/m^{2}s), D is the diffusion coefficient (m^2/s), c is concentration (g/m^3) and x is the flowing distance (m).

Deicing salt solution is of special interest in the study of salt frost deterioration. When we analyze the diffusion between a strong salt solution and a weak salt solution, one thing should be brought into attention, that is the diffusion process is not an one-way movement. As a matter of fact, there is the diffusion of salt from the high concentration solution (hypertonic) to the low concentration solution (hypotonic) and simultaneously of water from the low concentration solution (hypotonic) to the high concentration solution (hypertonic), until reaching the same concentration in both salt and water (Figure 2.16).

Another thing that always causes confusion among people is the two concepts of diffusion and osmosis. Actually, osmosis can be taken as a special form of diffusion, where it is a one-way movement, meaning only the solvent (usually water) is allowed to move through a semi-permeable membrane to a highly concentrated solution (which is however low in water concentration), as illustrated on the right side of Figure 2.16. The driving force behind the diffusion process is the vapor pressure difference between the solutes or solvents in two differently concentrated solutions.

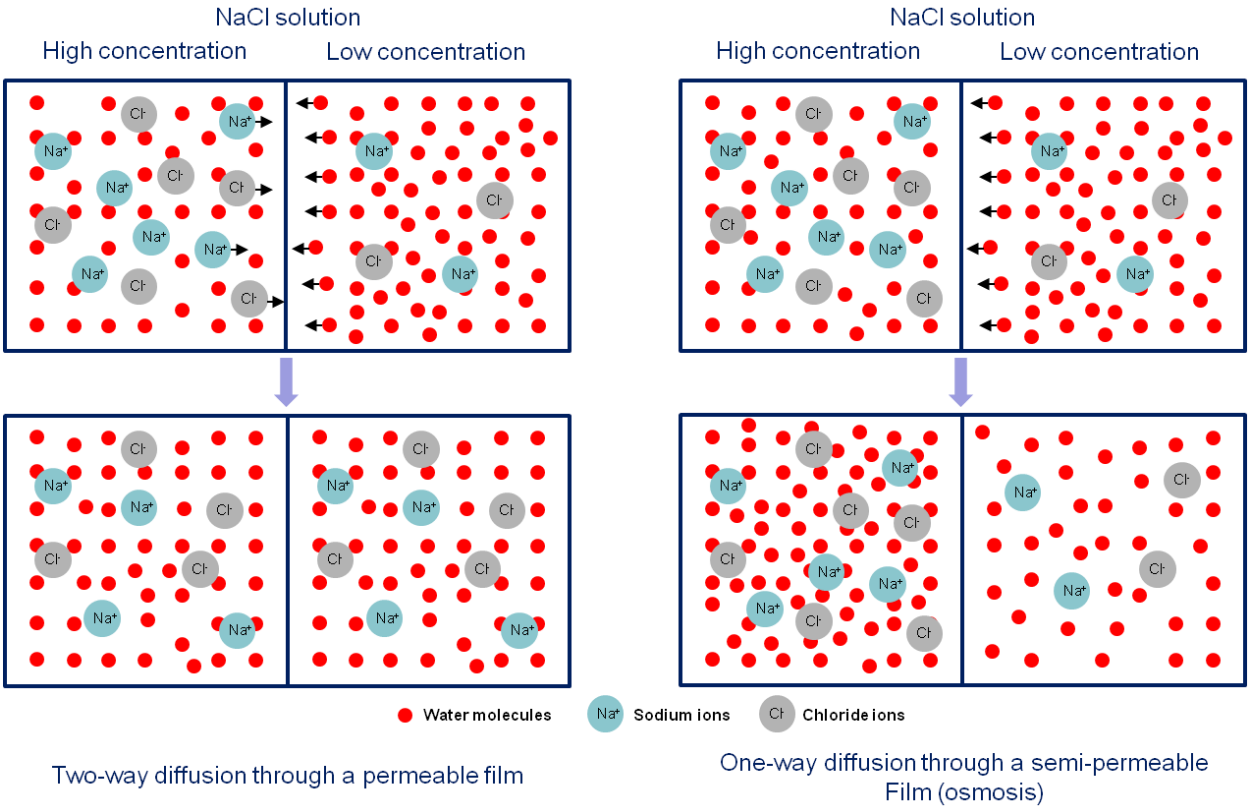

Figure 2.16 Schematic representation of diffusion and osmosis process

2.4.2 Permeation

Permeation is the penetration of a permeate (liquid or gas) into a solid by a pressure head and is related to a material property, the coefficient of permeability.

The flow of an incompressible liquid in concrete can be characterized by Darcy's law for laminar flow through a porous medium.

$$\frac{dq}{dt}\frac{1}{A} = \frac{K'\rho g}{\eta}\frac{\Delta h}{L} \tag{2-16}$$

$\frac{dq}{dt}$ is the flow rate (m^3/s), A is penetrated area (m^2), Δh is the pressure head drop along the flow length (m), L is the flow length (m), η is dynamic viscosity of the liquid (Pa·s), ρ is the density of the liquid (kg/m^3) and g is the acceleration due to gravity (m/s^2). K' is the coefficient of permeability in m^2 and is an intrinsic material property independent of the liquid.

Among the liquid involved, water is the most common medium. Thus, another expression can be obtained regarding the flow of water through concrete.

$$\frac{dq}{dt}\frac{1}{A} = K\frac{\Delta h}{L} \tag{2-17}$$

K is generally termed as the coefficient of water permeability in m/s. As for the conversion of these two coefficients, $K = 9.75 \times 10^6 K'$ at $T = 20$ ℃.

2.4.3 Capillary suction

The permeability of concrete has long been hailed as the most reliable parameter in determining the ease with which, water can penetrate concrete based on the merits of its well established theory (Darcy's law) and experimental methods. However, the associated saturated flow devoids the capillary suction, an important driving force behind moisture transport in concrete, of any role to play in this regard. Moreover, in construction engineering, saturated flow is rarely encountered given the fact that civil engineering materials (concrete, masonry, bricks, etc) is under alternate exposure to moisture and dryness. As a result, unsaturated flow theory can more accurately characterize the transport behavior of moisture into concrete and it can be described by the extended Darcy's Law (Hall and Hoff 2002):

$$q = K(\theta)F_c(\theta) \tag{2-18}$$

q is the vector flow velocity (m/s), $K(\theta)$ is the hydraulic conductivity (m/s) and $F_c(\theta)$ is the capillary force (m/m), which can be expressed in terms of capillary potential Ψ (m),

$$F_c(\theta) = -\nabla\Psi(\theta) \tag{2-19}$$

The capillary potential Ψ bears the physical meaning of the energy needed to move unit weight of liquid from the porous body to an external reservoir of the same liquid at the same temperature and elevation.

In the case of a flow with isotropic conductivity $K(\theta)$, the extended Darcy's Law can be rewritten as:

$$q = -K(\theta)\nabla\Psi \tag{2-20}$$

or

$$q = -D(\theta) \tag{2-21}$$

$D(\theta) = K(\theta)\frac{\mathrm{d}\Psi}{\mathrm{d}\theta}$ is the hydraulic diffusivity.

The unsaturated flow theory has multiple merits in that it provides a unified framework in which the concepts of capillary suction and permeability are embedded simultaneously and their dependence on water content θ is immediately embodied (Hall 1989).

When combining Eq. 2-21 with the continuity equation (Eq. 2-22) below,

$$\frac{\partial \theta}{\partial t} = -\nabla q \tag{2-22}$$

it yields

$$\frac{\partial \theta}{\partial t} = \nabla(K(\theta)\nabla\Psi) \tag{2-23}$$

Since $D(\theta) = K(\theta)\frac{\mathrm{d}\Psi}{\mathrm{d}\theta} = K(\theta)\frac{\mathrm{d}\Psi}{\mathrm{d}x}\frac{\mathrm{d}x}{\mathrm{d}\theta}$, $K(\theta)\nabla\Psi = D(\theta)\nabla\theta$.

Thus,

$$\frac{\partial \theta}{\partial t} = \nabla D(\theta)\nabla\theta = \frac{\partial}{\partial x}(D\frac{\partial \theta}{\partial x}) \text{ (one dimensional horizontal flow)} \tag{2-24}$$

Eq. 2-24 is in the same form of Fick's second law and Boltzmann transformation can be employed to convert it into a solvable ordinary differential equation by introducing a new variable ϕ which is a function of both x and t.

$$\phi = xt^{-1/2} \tag{2-25}$$

After the Boltzmann transformation, Eq. 2-24 can be rewritten as follows in the case of an one-dimensional diffusion process.

$$2\frac{d}{d\phi}(D\frac{d\theta}{d\phi}) + \phi\frac{d\theta}{d\phi} = 0 \tag{2-26}$$

When Eq. 2-26 is restricted by the boundary conditions $\theta = \theta_s$ at $x = 0, t \geq 0$ ($\phi = 0$) and $\theta = \theta_d$ at $> 0, t = 0$ ($\phi \to \infty$) , it can be solved as

$$x(\theta, t) = \phi(\theta)\, t^{1/2} \tag{2-27}$$

What this equation represents forms the key element of the unsaturated flow theory. When we integrate $x(\theta, t)$ with respect to the water θ at a specific time t, the cumulative amount of water absorbed i (m) is given as

$$i = \int_{\theta_d}^{\theta_s} x(\theta, t)d\,\theta = \left(\int_{\theta_d}^{\theta_s} \phi(\theta)d\,\theta\right) t^{1/2} = St^{1/2} \tag{2-28}$$

This is the definition of **sorptivity** S (m/s$^{1/2}$), a physical property of porous materials in evaluating the capillary suction rate. Eq. 2-28 is also the theoretical foundation for the frequently observed $t^{1/2}$ law of water absorption into concrete. Another analytical approach will be proposed in Chapter 6 in the computation of sorptivity from the pore structure of cement paste.

2.5 Liquid transport in air-entrained concrete

Water transport behavior is of great relevance to the frost durability of concrete and the governing mechanisms, as previously discussed, are the diffusion and capillary suction, since field concrete is rarely under a pressure gradient. Liquid transport in air-entrained concrete can be visualized as a continuous paste matrix with dispersed air voids enclosed by a spectrum of capillary pores of different sizes and degrees of connectivity (Figure 2.17). In modern concrete with low w/c ratio or the incorporation of supplementary cementitious materials, its pore structure is complicated and altered in such a way that the continuity is reduced with more constrictions (Pigeon and Pleau 1995). When concrete comes into contact with water, capillary suction is activated to pump water up in those well-connected pores immediately. Water keeps flowing upward and then bifurcates upon encountering the air voids (due to the presence of air pressure) or pores with an abrupt change in shape and size (the sketch is out of scale for the sake of better visualization, since the nominal diameter of an air void is several orders of magnitude larger than the capillary pores). After all the connected pore are filled, the main mechanism switches to the slow diffusion into the air voids and those less-well connected pores.

As a result, the liquid uptake in air-entrained concrete can be characterized by a bi-linear pattern as presented in Figure 2.18, featuring an initially rapid capillary suction process followed by a slow diffusion-controlled transport into air voids or poorly connected pores (Sandström et al. 2012). Rate of transport can be described by the slope, the first segment being sorptivity S or the initial rate of absorption (ASTM C1585) and the secondary one being the secondary rate of absorption C. The inflection point indicates the arrival of capillary saturation in connected pores.

Both the capillary suction and diffusion processes are square-root time dependent, thus moisture uptake in concrete can be described as

$$i = St^{0.5} + Ct^{d} \tag{2-29}$$

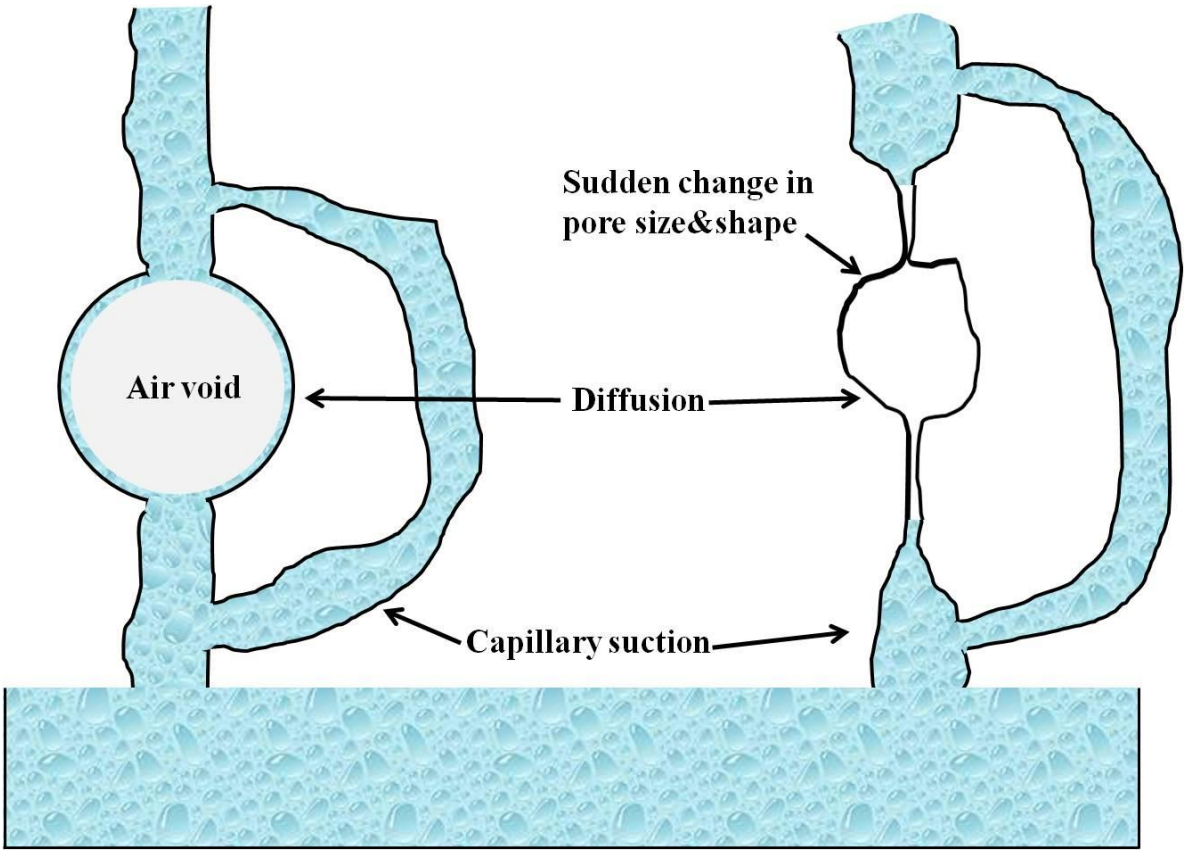

Figure 2.17 Schematic representation of water uptake in concrete with entrained air voids

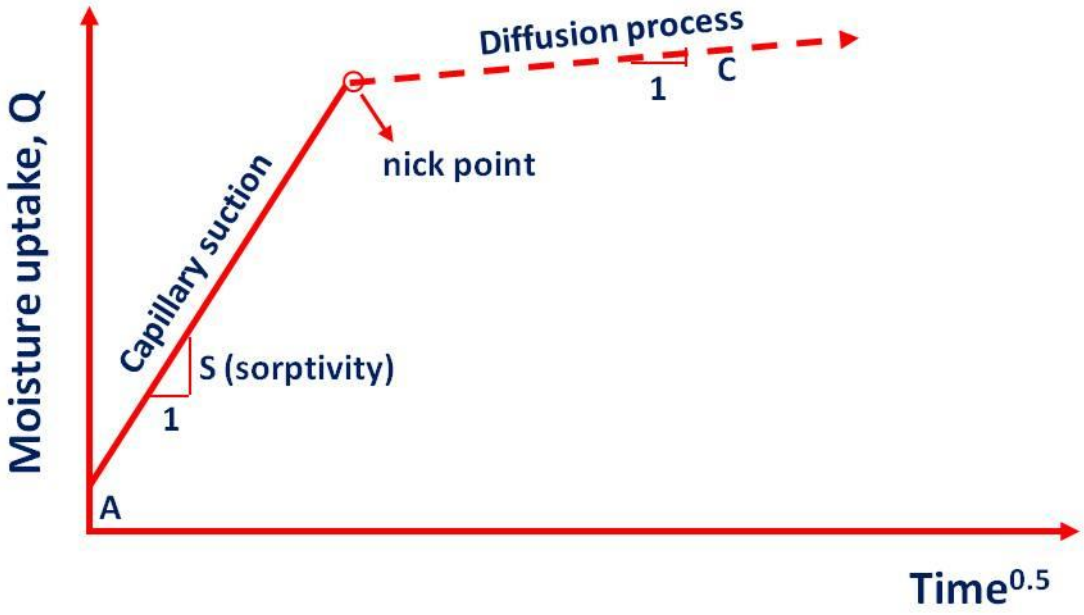

Figure 2.18 Idealized liquid transport in air-entrained concrete

Figure 2.19 shows the measured moisture uptake curves in concretes of different air contents. It can be seen enclosure of air voids initially reduces the absorption rate (Figure 2.19(b)) since they increase the disconnectivity of the pore structure (Figure 2.17). The slow diffusion into air voids are clearly demonstrated in Figure 2.19(c) where concrete with higher air content produces more absorption. The effect of air content on the two absorption processes is also shown in Figure 2.20.

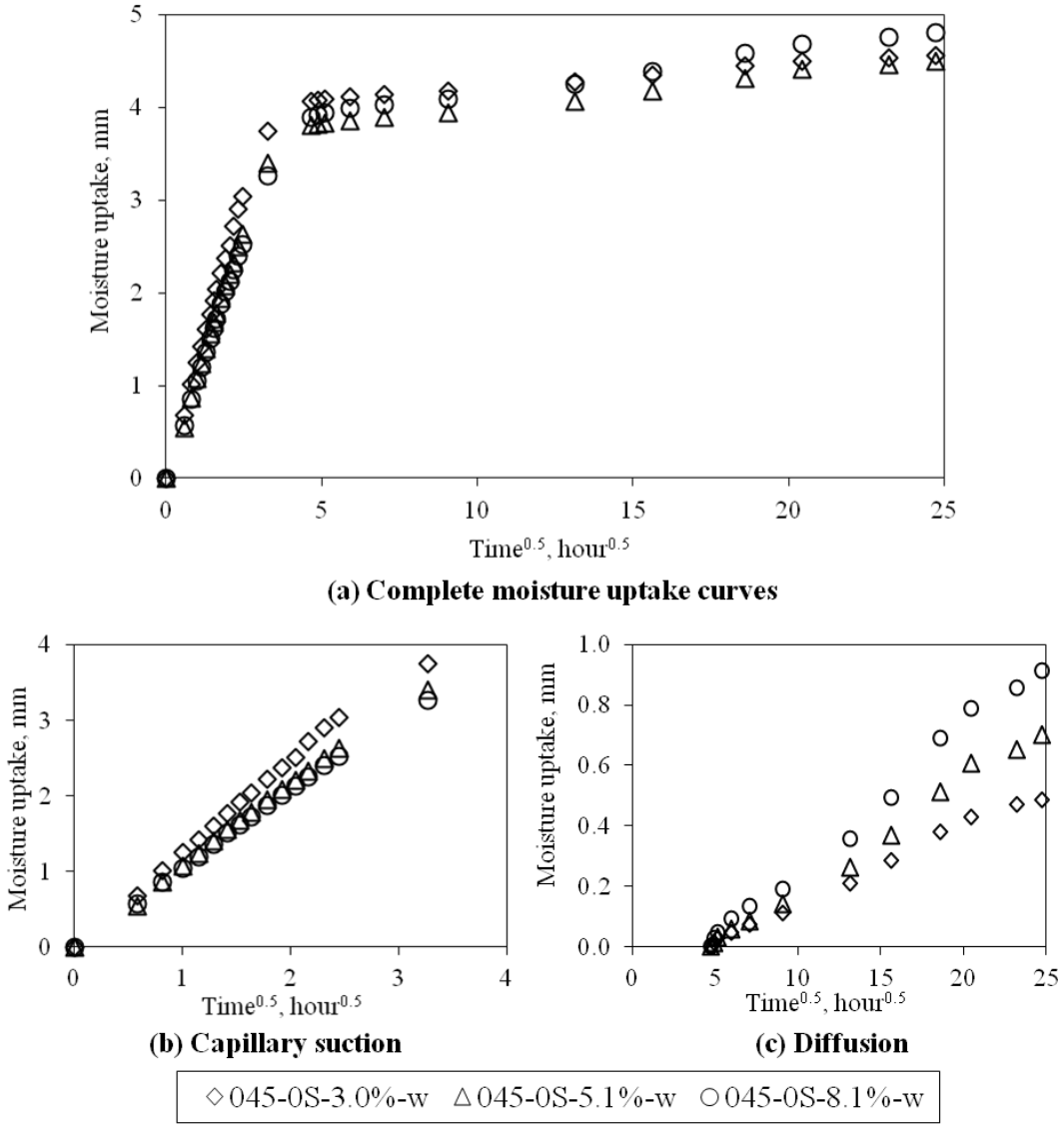

Figure 2.19 Measured moisture uptake in concretes of different air contents

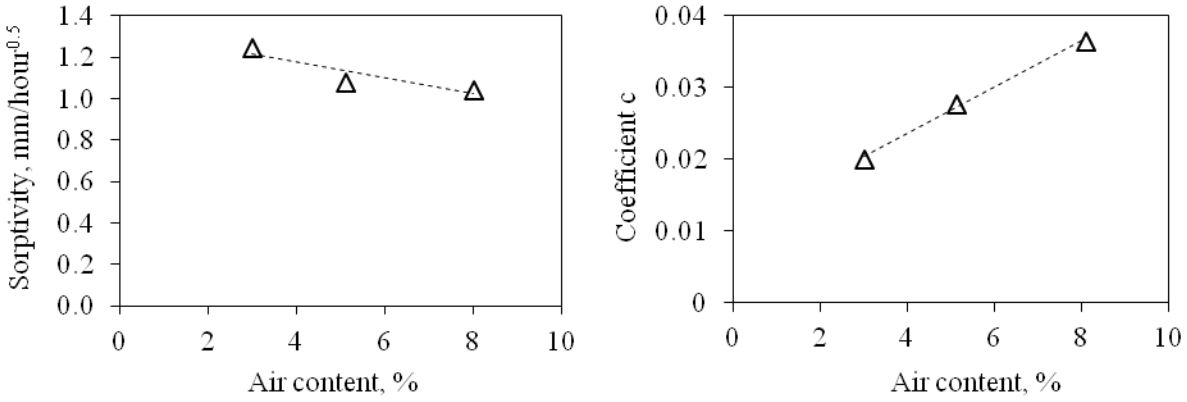

(a) (b)

Figure 2.20 Effect of air content on moisture uptake in concrete

2.6 Summary of findings

This chapter presents an overview on the fundamental characteristics of the liquid transport properties in concrete. There are essentially three different types of transport mechanisms in concrete (diffusion, permeation and capillary suction), of which the capillary suction is the most important one, given the nature of concrete moisture condition in the field. Moisture absorption occurs in concrete through the network of capillary and gel pores in the porous hydration products. The entrainment of air voids interferes with the absorption processes in different ways at the early and later ages. As a result, the pore structure and air void features in cementitious paste are reviewed as well.

CHAPTER 3 EXPERIMENTAL PROGRAM

An extensive experimental program is employed for the thesis work, including salt frost scaling test, air void analysis, pore structure characterization and low temperature dilatometry measurement, etc. In this section, material properties, mix design and test procedures are detailed.

3.1 Materials

Type I portland cement and grade 120 slag cement were used as cementitious materials and their characteristics are shown in Table 3.1. Fine aggregate was silica sand with a fineness modulus of 2.43. Coarse aggregate was limestone with a 25 mm nominal maximum size. A commercially available lightweight aggregate Nesolite was used with a dry rodded unit weight of 800 kg/m^3. The gradation of aggregate is shown in Figure 3.1. A commercially available silane was used for surface treatment.

Table 3.1 Characteristics of portland cement and slag cement

	portland cement	slag cement
CaO, %	62.4	38.0
SiO_2, %	20.4	37.5
Al_2O_3, %	5.04	7.77
Fe_2O_3, %	2.51	0.43
SO_3, %	2.75	3.21
Na_2O, %	0.25	0.28
K_2O, %	0.67	0.46
MgO, %	3.43	10.7
C_3S	53.66	--
C_2S	18.01	--
C_3A	9.11	--
C_4AF	7.64	--
Blaine fineness, cm^2/g	3920	5508

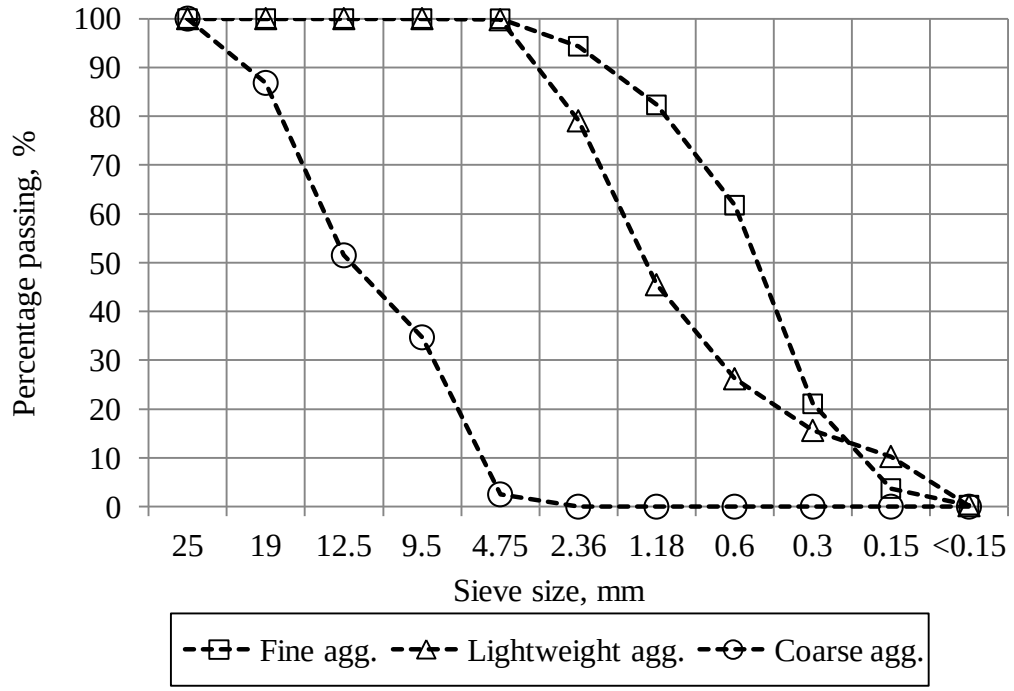

Figure 3.1 Gradation curves for aggregate

3.2 Mix characteristics and concrete specimen preparation

Air-entrained concrete mixes with two w/b ratios (0.33 and 0.45, denoted as 033-0S and 045-0S respectively) and one replacement level with slag cement at 0.45 w/b ratio (50% by weight of total cementitious materials, denoted as 045-50S) were prepared. Cylindrical specimens (150 mm in diameter and 300 mm in height) for 045-0S and 045-50S mixes were cast in the laboratory according to (ASTM C192), while concrete beams (150 mm × 150 mm × 550 mm) for 033-0S mix were made in a ready-mix plant and delivered to the laboratory after one-day curing. For mixes made in the laboratory, coarse aggregate, part of the mixing water along with the liquid superplasticizer were added to the mixer before it started rotation. This was followed by the addition of fine aggregate, cement and the rest of the mixing water with the air entrainer after the mixer started rotation. The mixing procedure consists of 3-minute mixing, 3-minute rest, followed by 2-minute final mixing. A slump of 80-100 mm was achieved with a superplasticizer dosage of 4.0 ml/kg cementitious material. The dosage of air entrainer varied from 0.9-1.5 ml/kg cementitious material to achieve an air content of 3.0-8.1%. All the specimens were removed from the mould after one day and then submerged in tap water at 20 °C for another 27 days. The

basic mix design is listed in Table 3.2 and detailed information will be presented in the following chapters.

Table 3.2 Mix design of concrete

Mix	Mix proportion, kg/m^3				
	portland cement	slag cement	sand	gravel	water
033-0S	390	0	672	1068	129
045-0S	290	0	775	1115	130
045-50S	145	145	775	1115	130

3.3 Test procedures

3.3.1 Air void analysis

The air void analysis of concrete specimens is carried out based on ASTM C457 (2000). Square specimens of 100 mm by 100 mm (4 in. by 4 in.) are cut from the mid-depth portion of 150 mm (6 in.) diameter cores with the testing surface parallel to the pavement surface. Specimens are then carefully polished with silicon carbide abrasives to obtain a smooth surface with undamaged paste and clearly defined air voids. The polished surface is pretreated by filling all the air voids with a white powder and the rest of the surface is darkened by a permanent marker to produce a sharp contrast. The RapidAir 457, an automatic image analysis system, is used to perform the air void analysis on polished sample (Figure 3.2).

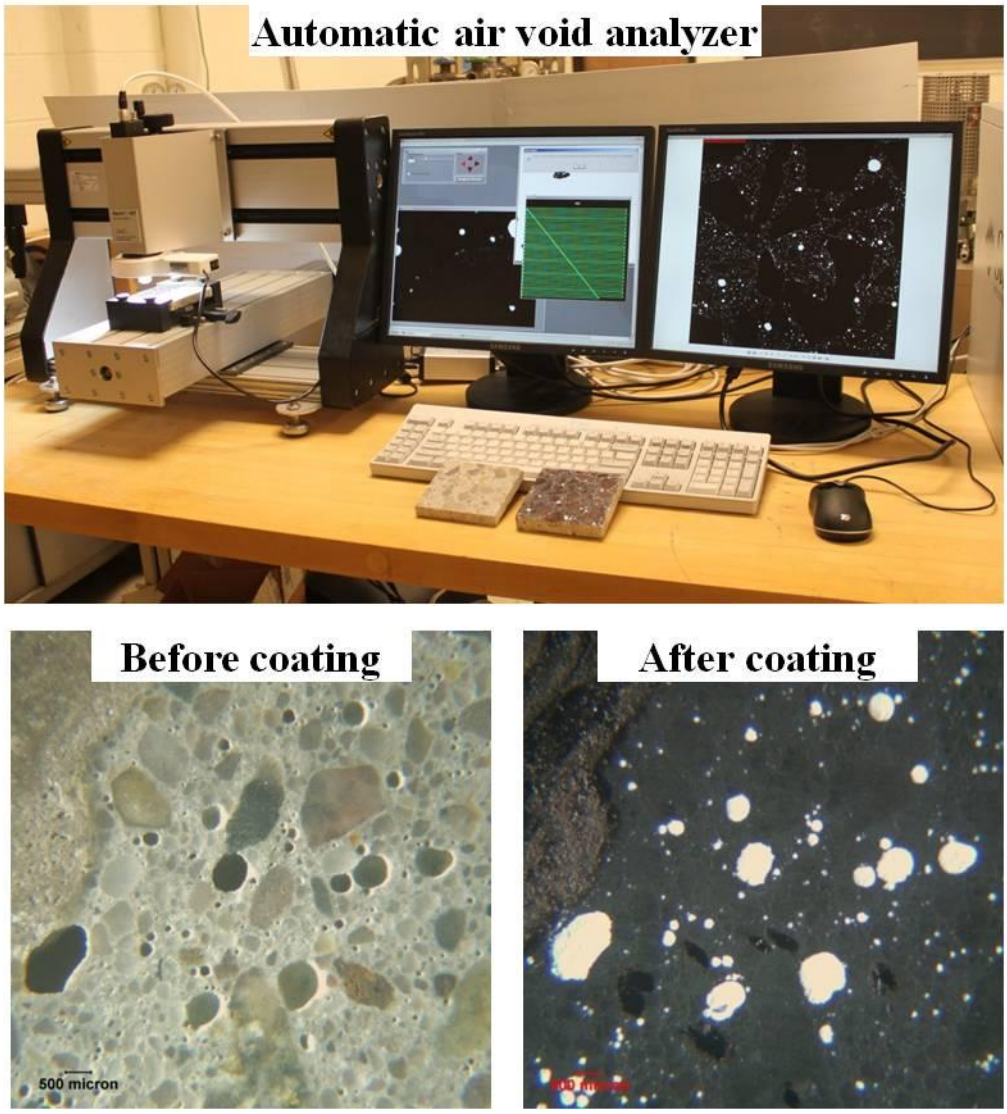

Figure 3.2 Specimens treated for air void analysis

3.3.2 Surface scaling, internal damage, moisture uptake and sorptivity measurements

Laboratory testing procedure on salt frost scaling typically consists of cumulative mass loss measurement, internal cracking detection and weight gain after a certain F-T cycles. A number of test methods have been developed and listed in Table 3.3 in the Appendix.

In this study, frost resistance of air-entrained concrete specimens in the presence of a salt solution was tested according to the RILEM TC 176-IDC CIF-Test: Capillary suction, internal damage and freeze thaw test (Setzer et al. 2004) by a salt frost test machine (Figure 3.3(a)). However, a modification was made to the preconditioning procedure such that the moisture condition in specimens was clearly defined prior to F-T test and continuously monitored during

the test, which is important for evaluating the salt frost scaling results in a laboratory test procedure (Setzer 1993). The test procedure was described as follows.

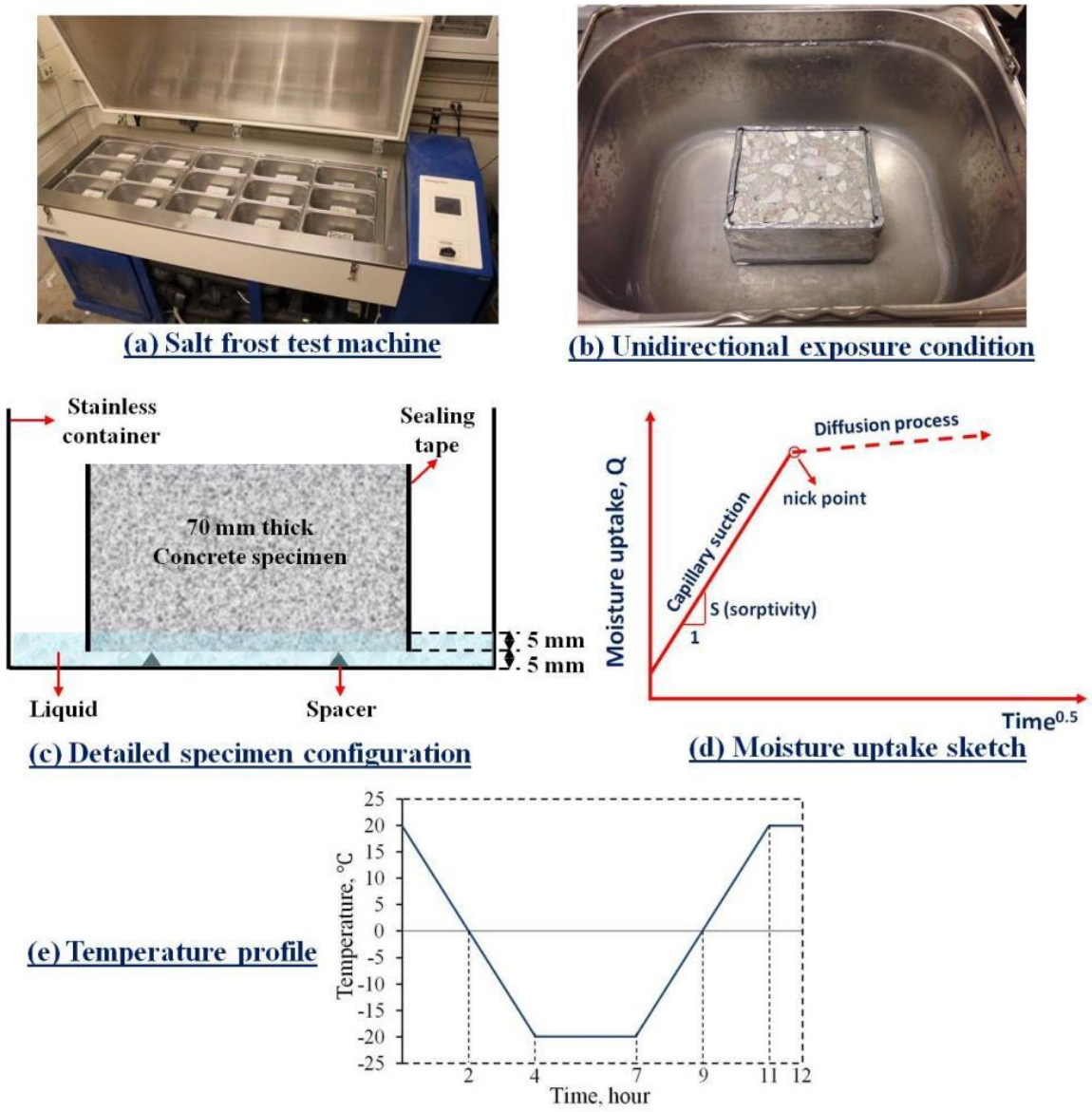

Figure 3.3 RILEM CIF test machine configuration

A standard specimen has a lateral dimension of 120 mm by 110 mm and a thickness of 70±2 mm. All the specimens were cut from the cylinders or beams with the test surface parallel to the two ends. They were dried in the oven at 50 °C for 3-4 weeks until near constant weight was reached.

After drying treatment, lateral surfaces of the specimens were sealed by the aluminum foil with butyl rubber (Figure 3.3(b)). This was followed by one-week moisture uptake in demineralized

water with the test surface immersed in demineralized water by 5 mm (Figure 3.3(c)) and the weight gain was regularly recorded and followed the profile shown in Figure 3.3(d). F-T test typically starts after the nick point. Sorptivity was determined as the slope of the initial linear water absorption curve against the square root of time.

Pre-conditioned specimens were transferred to a climate chamber and exposed to a specific temperature profile fluctuating between 20 ℃ and -20 ℃ in 12 hours for each cycle (Figure 3.3(e)).

During the one-hour isothermal period at 20 °C, scaled-off materials were collected and dried at 105 ℃ to constant weight, from which mass loss per unit surface area ML (g/m^2) was determined.

$$ML\ (\mathrm{g/m^2}) = \frac{\mu_n}{A_c} \times 10^4 \tag{2-1}$$

where μ_n (g) is the cumulative dry weight of the scaled-off materials after the nth F-T cycle, A_c (cm^2) is the area of the concrete test surface.

Permanent moisture uptake I (mm^3/mm^2) in concrete is calculated from the weight measurement of the specimen and the scaled-off materials, including both the total absorption I_t based on the dry specimen weight m_0 and the additional absorption during F-T exposure I_a based on the presaturated specimen weight (m_1).

$$I_t(mm^3/mm^2) = \frac{(m_n+\mu_{n0})-m_0}{\rho A_c} \times 10 \tag{2-2}$$

$$I_a(mm^3/mm^2) = \frac{(m_n+\mu_{n0})-m_1}{\rho A_c} \times 10 \tag{2-3}$$

where m_n(g) is the remaining specimen weight and μ_{n0} is the saturated weight of the scaled-off materials after the nth F-T cycles, ρ is the density of the test liquid (g/m^3).

μ_{n0} in Eqs. 2 and 3 can be computed by assuming the same moisture content in the saturated scaled-off materials as in the remaining bulk concrete, that is

$$\frac{\mu_{n0}-\mu_n}{\mu_n} = \frac{(m_n+\mu_{n0})-m_0}{m_0} \tag{2-4}$$

Thus, $\mu_{n0} = \frac{m_n\mu_n}{m_0-\mu_n}$ (2-5)

Internal damage in concrete after the n^{th} F-T cycle is evaluated by the relative dynamic modulus of elasticity (RDM) calculated from the ultrasonic transit time in the coupling medium (typically water at 20 ℃). The transit time is measured by a Pundit Plus ultrasonic digital indicating tester with 54 kHz transducers.

3.3.3 Low temperature dilatometry test

A 10 mm×10 mm×90 mm prism was cut from the 150 mm×300 mm concrete cylinder. The prism was dried in the oven at 50 ℃ to a near-constant weight and then pre-saturated with a test solution for about 2 hours, until the rapid rise in moisture uptake ended. Several sponge segments were pre-saturated with the exposure liquid and placed on the top surface to retain a liquid reservoir while preventing the formation of continuous ice sheets, then the prism was wrapped by a plastic foil to minimize moisture loss during the test (Figure 3.4).

The specimen was then placed in a high-resolution dilatometer (1.25 nm/digit) equipped with a liquid nitrogen dewar for low temperature control (Figure 3.5), where it was subjected to a similar temperature cycle as the surface scaling test, except that an additional 3-hour isothermal stage at -10 ℃ was added (Figure 3.6). The change in length and temperature of the specimen was simultaneously measured by the pushrod and the thermocouple touching one of the lateral surfaces of specimen, respectively.

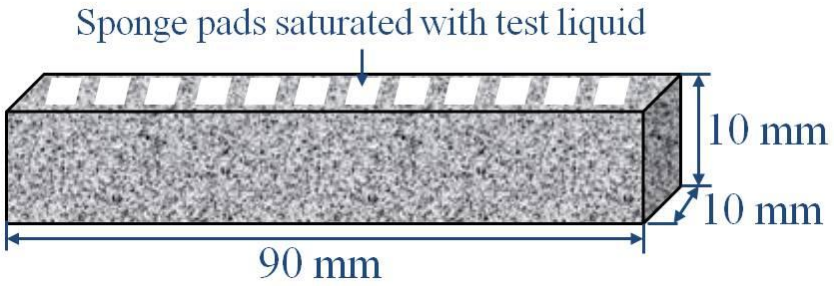

Figure 3.4 Dimension of LTD specimen and the liquid retainment technique on test surfaces

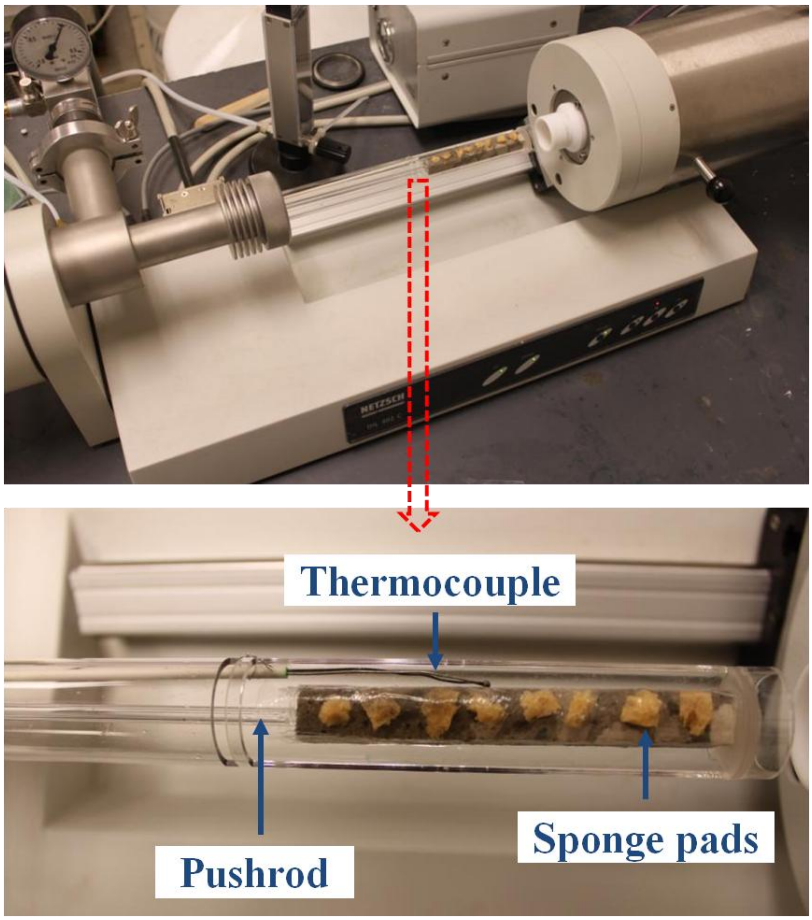

Figure 3.5 Low temperature dilatometer

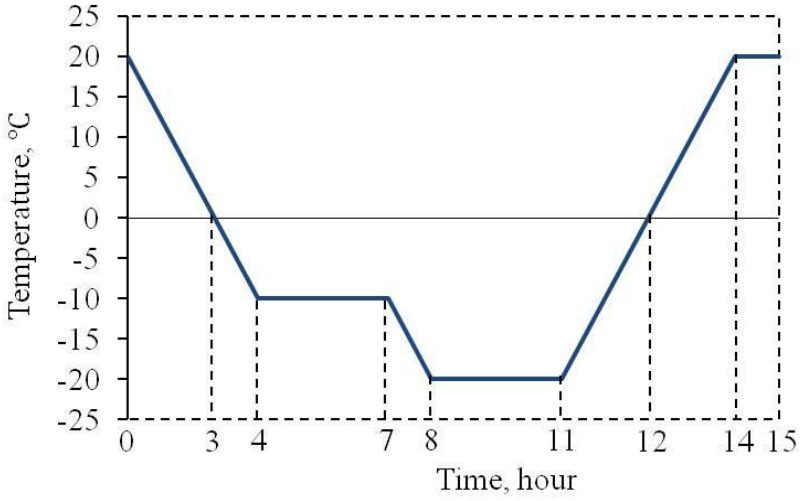

Figure 3.6 Temperature profile of LTD test

3.3.4 Pore structure measurement

Sorption isotherms and cumulative pore size distribution were measured on mortar samples with and without silane impregnation and the scaled-off materials consisting of cement paste and sand particles collected during the F-T test.

Preparation of the mortar samples: a thin concrete slice (~4 mm) was sawed from the same cylinder as the F-T test specimens, followed by 24-hour oven drying at 50 °C. The control mortar samples were obtained by removing the coarse aggregate from half of the slice and then carefully grinding the mortar to small particles. The other half of the slice was treated with silane on the top and bottom sides with a coverage rate of 2.9 m^2/L. After 24-hour curing, the mortar samples with silane treatment were obtained using the same procedure. Both the samples were then vacuum dried for at least 14 days in a vacuum desiccator.

Preparation of the scaled-off materials: they were collected in the first two cycles for the untreated specimens. However, the mass loss was very limited for the silane treated specimens, their collection was extended to more than 50 cycles, but still before the accelerated mass loss occurred so that it was within the penetration depth of silanes. During the thawing stage of each F-T cycle, the test surface of the specimen was carefully examined for any scaling. The scaled-off materials, if there were any, were brushed off the surface and collected in a filter paper. This procedure makes sure that no additional F-T exposure was added to the scaled-off materials once they were generated. Considering their fine particle size, air drying was adopted to scaled-off materials at 20 ℃ and 65±5% RH for 24 hours before vacuum drying for at least 14 days in a vacuum desiccator.

Nitrogen sorption isotherms were measured on duplicate samples by a Quantachrome Autosorb-1 (Figure 3.7). The sample weight was determined by a sensitive balance and it ranged from 0.1-0.2 grams. Prior to the sorption test, the sample was outgassed for ~12 hours until it passed the leak test. The cumulative pore size distribution was calculated by the Barrett, Joyner, Hallenda (BJH) method (Barrett et al. 1951) using data from the adsorption isotherm with a relative pressure range of 0.01-0.995.

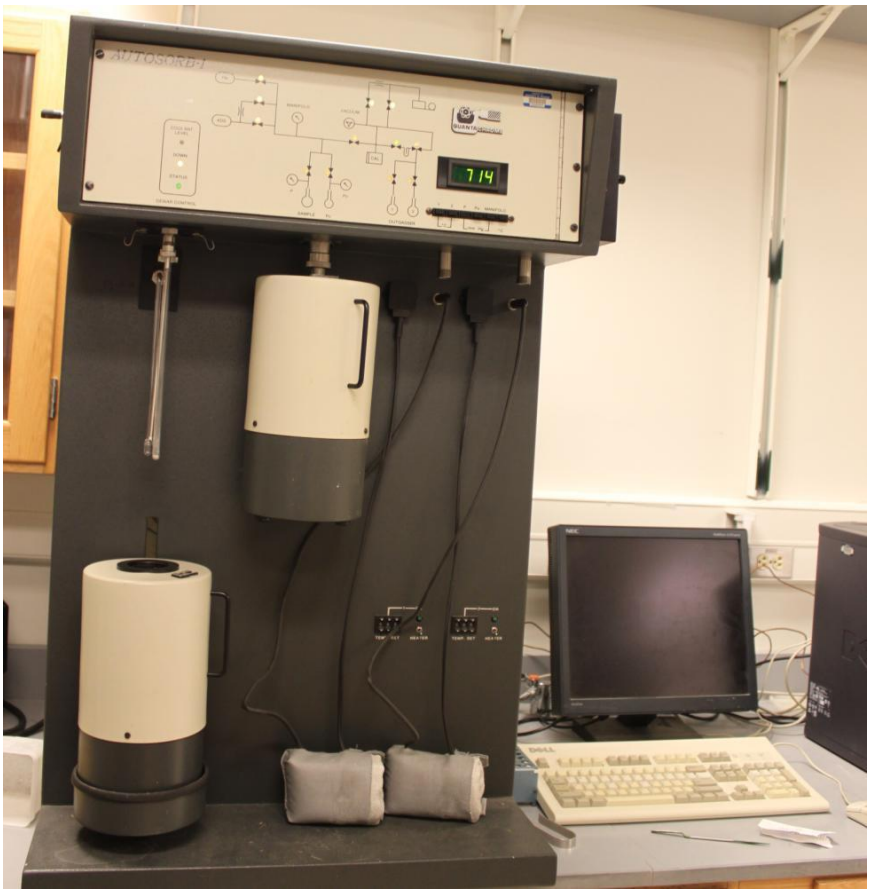

Figure 3.7 Quantachrome Autosorb-1

Appendix

Table 3.3 Test methods for salt frost scaling

	ASTM C672	MTO LS 412	DD CEN/TS 12390-9		
			Slab test	Cube test	CDF/CIF TEST
	USA	ONTARIO CANADA	EUROPE		
Specimen preparation	molded block or cut from a hardened concrete structure	molded block or cut from a hardened concrete structure	Cut from 150mm cube at the age of 21day	Molded cube	Formed from 150mm cube by the PTFE plate
Specimen size	Surface area≥0.045m^2 Height≥70mm	300×300×75 mm	150×150×50 mm	100×100×100 mm	110×150×70 mm
Test surface	Finished	Finished	Sawed	Formed	Formed
Untested surfaces	Exposed to air	Exposed to air	Wrapped by rubber cloth	--	Lateral surfaces wrapped by epoxy sealing or aluminum foil, top surface exposed to air
Curing	1d mold 13d moist 14d air (23±2 ℃, 45%-55%RH)	1d mold 13d moist 14d air (23±2 ℃, 45%-55%RH)	1d mold 6d water 21d in air (20±2 ℃, 65±5%RH)	1d mold 6d water 20d in air (20±2 ℃, 65±5%RH)	1d mold 6d water 21d in air (20 ℃, 65%RH)
Test liquid	4g CaCl/100 ml solution	3% NaCl solution	3% NaCl solution		3% NaCl solution
Presaturation	--	--	3mm thick demineralized water for 3d	submerged in test liquid for 1d	5mm thick demineralized water for 7d
Application of test liquid	one sided, 6mm deep liquid retained by a	one sided, 6mm deep liquid retained	one sided, 3mm deep liquid	all-sided (submerged)	one sided (test surface immersed by

	dike of 25mm wide and 20mm high along the perimeter	by a dike of 25mm wide and 20mm high along the perimeter	retained by the rubber cloth of 20mm high along the perimeter		5mm into test liquid)
Temperature profile	16-18 hours in a freezing environment 6-8 hours in lab air ((23±2 ℃, 45%-55%RH))	16-18 hours in a freezing environment 6-8 hours in lab air ((23±2 ℃, 45%-55%RH))	See Figure 3.8	See Figure 3.9	See Figure 3.3(e)
cooling-thawing rate	lowering to -18±2 ℃ within 16-18 hours	lowering to -18±2 ℃ within 16-18 hours			10 ℃/hour-10 ℃/hour
Duration of one F-T cycle	22-26 hours	22-26 hours	24 hours	24 hours	12 hours
	ASTM C672	MTO LS 412	DD CEN/TS 12390-9		
			Slab test	Cube test	CDF/CIF TEST
	USA	ONTARIO CANADA	EUROPE		
Test duration	Typically 50 cycles	50 cycles	Typically 56 cycles	Typically 56 cycles	Typically 28 cycles
Measurement frequency	every 5 cycles	every 5 cycles	7, 14, 28, 42, 56 (70, 84, 98, 112) cycles		14, 28 cycles (additional 4-6 cycles recommended)
Reported results	1. Visual rating 2. Mass loss (optional)	1. Visual rating 2. Mass loss	1. Dilation 2. Internal damage 3. Mass loss		1. Mass loss 2. Internal damage
Damage criterion	--	--	Dilation>0.1% UPTT>112 (or RDM<80%) Mass loss<1000g/m^2 after 56 cycles	Mass loss<3% by weight after 56 cycles	Mass loss<1500g/m^2 after 28 cycles

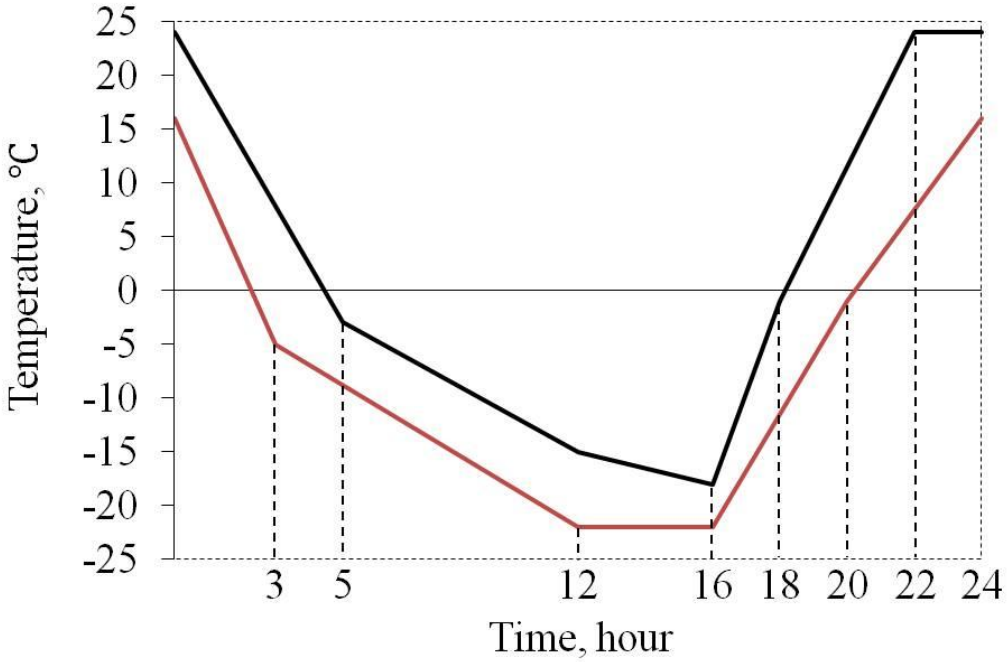

Figure 3.8 Temperature profile for slab test

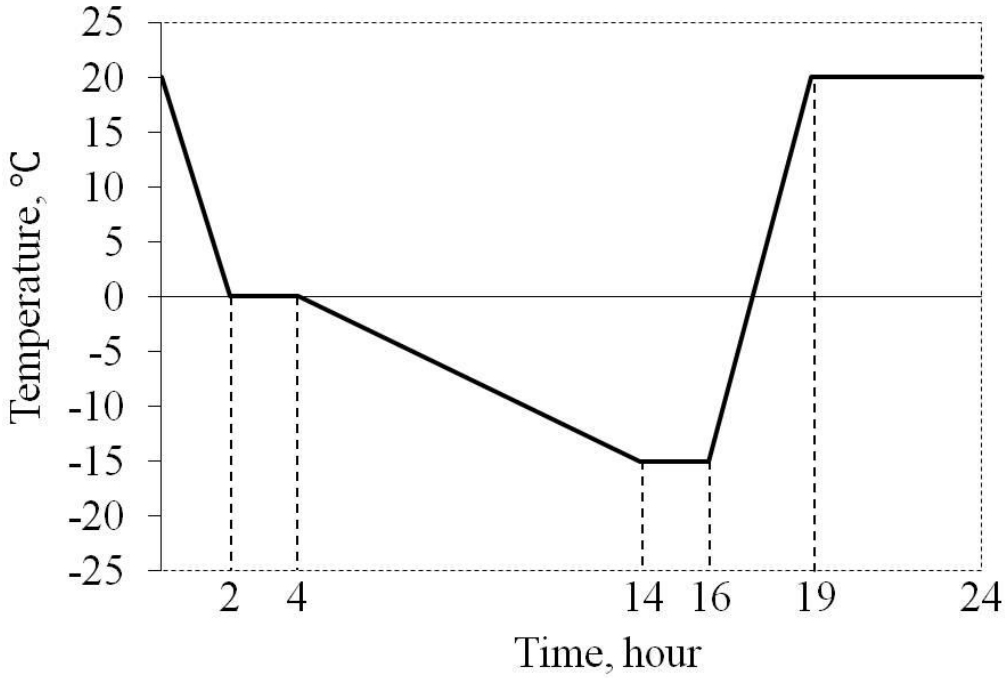

Figure 3.9 Temperature profile for cube test

CHAPTER 4 BULK MOISTURE UPTAKE IN CONCRETE UNDER FREEZING AND THAWING EXPOSURE

4.1 General

Under continuous wet exposure, F-T action yields higher moisture uptake in concrete beyond the isothermal capillary suction (Jacobsen 1995, Auberg and Setzer 1997, Fagerlund 1992, Rønning 2011), where several transport mechanisms have been reviewed (Jacobsen 2002). These moisture transport processes dominate during different stages of freezing-thawing. Hydraulic pressure is a rapid pumping effect due to instant ice formation near concrete surface (Powers 1945). Micro-ice-body growth is a slow process that causes liquid uptake primarily during the sub-freezing period (Powers and Helmuth 1953, Lindmark 1998) where unfrozen liquid is drawn towards the frozen sites spontaneously due to chemical potential difference between water and ice (Powers and Helmuth 1953, Pickett 1953, MacInnis and Whiting 1979). It has also been suggested that concrete upon thawing absorbs external liquid as a result of a volume contraction accompanying pore ice melting that is preceded by the melting of surface ice (Geiker and Thaulow 1996), or it is a combination of micro ice growth and thawing suction (Bager and Jacobsen 1999). A common consequence is the increase in degree of saturation, which ultimately leads to internal damage or surface scaling upon a critical saturation level.

Surface scaling is the progressive removal of cement paste typically embedded with sand particles and is substantially exacerbated when concrete surface is exposed to a moderate salt solution (Verbeck and Klieger 1957). The degree of saturation in the surface region depends on both the initial moisture condition due to curing and pre-treatment and the moisture ingress into concrete by those different mechanisms under freezing-thawing condition. Thus, measurement on the weight gain of concrete specimens has been linked to salt scaling (Jacobsen and Sellevold, 1994, Geiker and Thaulow 1996).

However, mixed results were found on the magnitude of moisture absorption under water and a salt solution and its correlation to salt scaling (Fagerlund 1992, Jacobsen and Sellevold 1994, Rønning 1999). Interpretation is further complicated by the remaining debate over the major mechanism on salt frost scaling.

In this chapter, the moisture absorption property associated with both isothermal room-temperature condition and freeze-thaw action was systematically investigated under different exposure conditions. The relationship between the bulk moisture uptake and scaling resistance is explored.

4.2 Permanent bulk moisture uptake in concrete under freezing-thawing exposure

The permanent moisture uptake in the bulk specimen, as computed from the measurement of weight gain during the presaturation stage and the F-T test, is shown in Figure 4.1 for different concretes mixes. Once F-T exposure commences, the moisture absorption is notably accelerated in the 033-0S and 045-50S mixes (Figure 4.1 (a)-(e)), which has been reported in other studies as well (Jacobsen and Sellevold 1994, Auberg and Setzer 1997, Fagerlund 1992, Rønning 2001). However, such acceleration is not clearly seen in the 045-0S concrete (Figure 4.1(f)-(h)) and only slight additional absorption occurs which may be the slow diffusion of liquid into the entrained air voids (Fagerlund 2004).

The increased absorption is associated with the pore structure characteristics of these concretes: Lowering w/cm ratio or incorporating supplementary cementitious materials (slag cement in this case) has been shown to alter the pore structure in the paste in such a way that its pore discontinuity and tortuosity are increased with refined pore sizes (Garboczi and Bentz 1996, Pigeon and Pleau 1995, Roy and Idorn 1982, Manmohan and Mehta 1981). Thus, there is an increased fraction of poorly-connected capillary pores in the low w/cm or slag cement systems which remain inaccessible during the 7-day isothermal presaturation period, while the F-T action accelerates the filling of those pores (Sandstrom et al. 2012) by the “pumping effect” associated with several transport mechanisms (Jacobsen 2002). In order to investigate which mechanism dominates this rapid moisture uptake, concrete specimens cut from field samples were treated with silane on the test surface, followed by 7-day presaturation and F-T test. It is consistent that moisture absorption is markedly increased when F-T commences and no difference is noted between the two exposure conditions (Figure 4.2). Silane is a pore liner which forms a

hydrophobic layer on the pore walls such that suction due to the capillary force is prevented, thus capillary suction under thawing may not be a factor. This point is further strengthened by the presence of very limited moisture in concrete pores prior to the F-T test. As a result, it is concluded that the transient external ice formation pushing water inwards is the major transport mechanism for the measured bulk moisture uptake, at least in the silane treated specimens. This process is so severe that the hydrophobic effect is overcome. For the specimens already with a decent amount of moisture during the presaturation period, the added suction due to melting of pore ice may be able to open up the pores, leading to the accelerated uptake.

In addition, no internal damage is observed in these mixes, as evidenced by the almost constant RDM with F-T cycles (Figure 4.3). This is also consistent with the moisture uptake measurement on the re-dried specimens that have undergone repetitive F-T cycles. It is found out that the absorption of the tested specimens remains unchanged during the presaturation stage and is slightly higher during the F-T stage (Figure 4.4). This indicates the opening effect on the pore structure is mostly reversible.

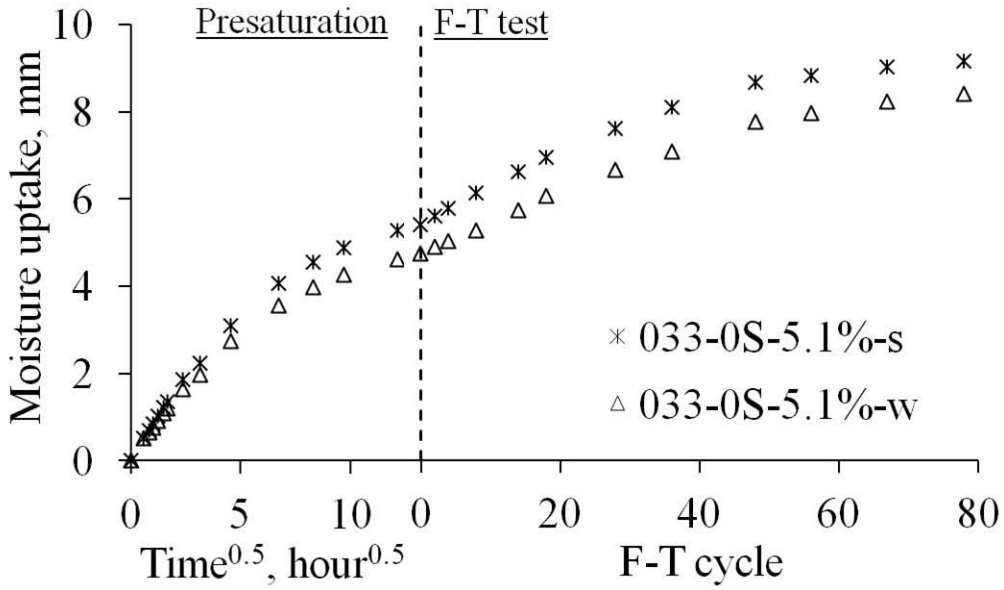

(a) 033-0S-5.1%

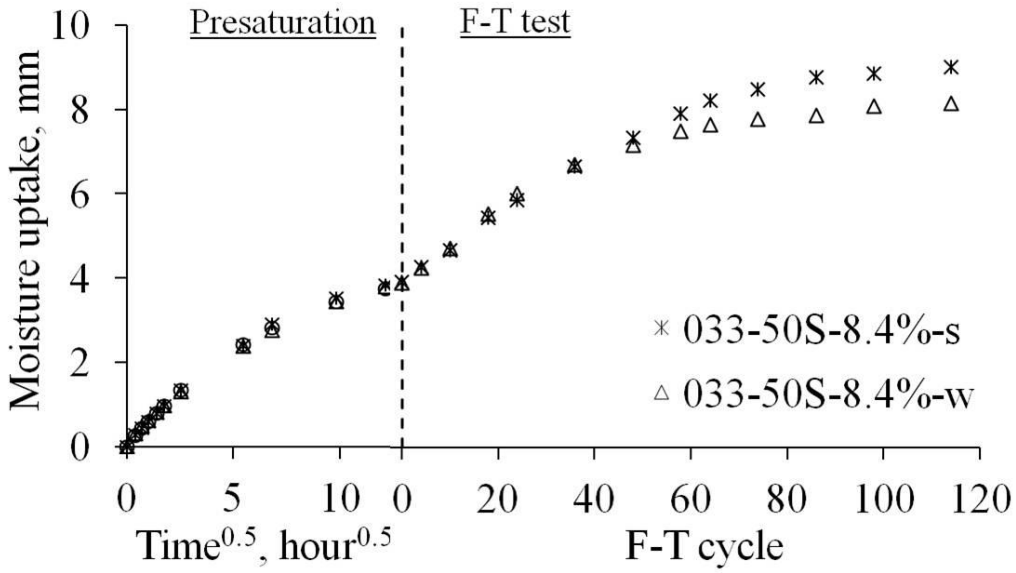

(b) 033-50S-8.4%

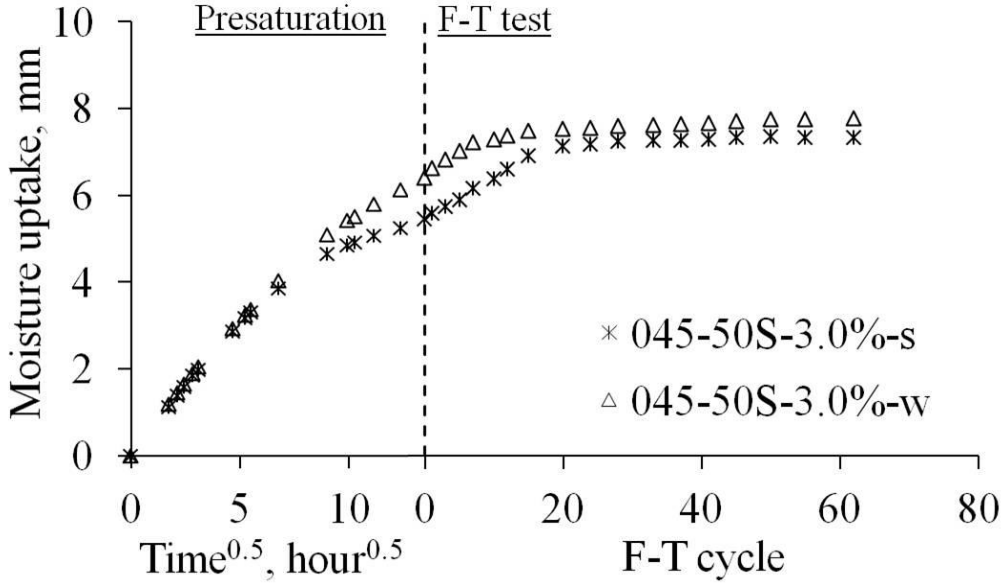

(c) 045-50S-3.0%

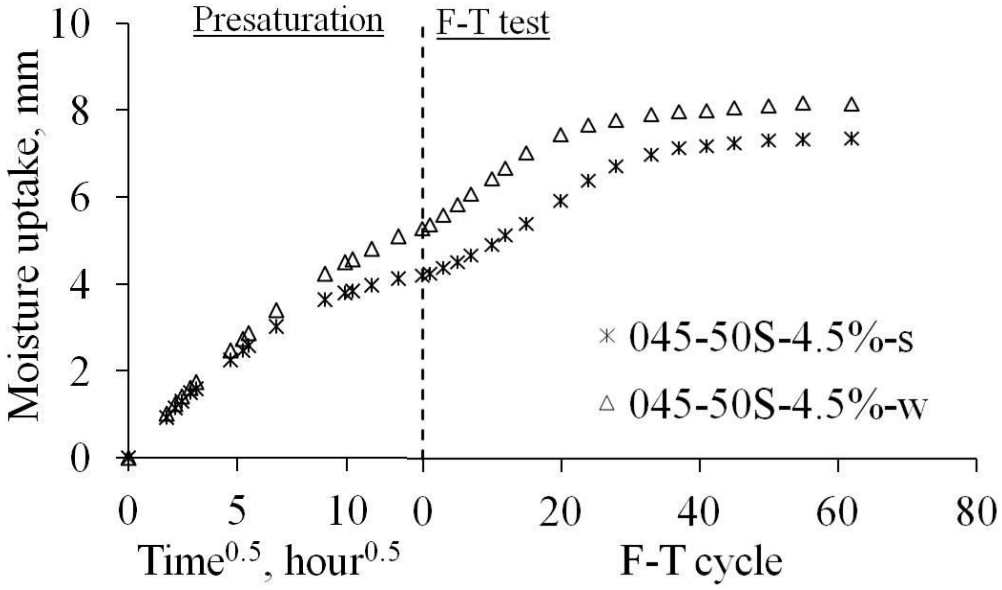

(d) 045-50S-4.5%

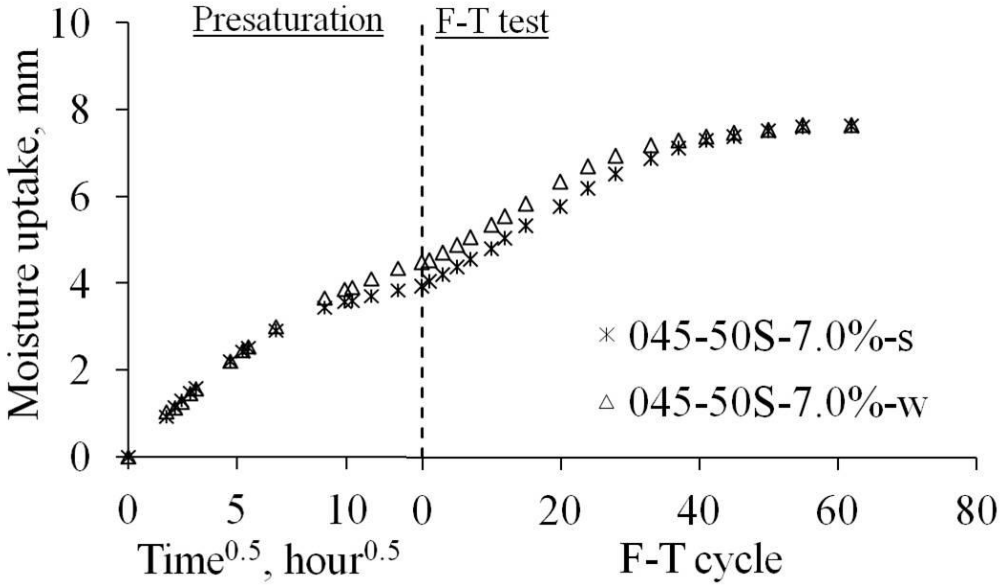

(e) 045-50S-7.5%

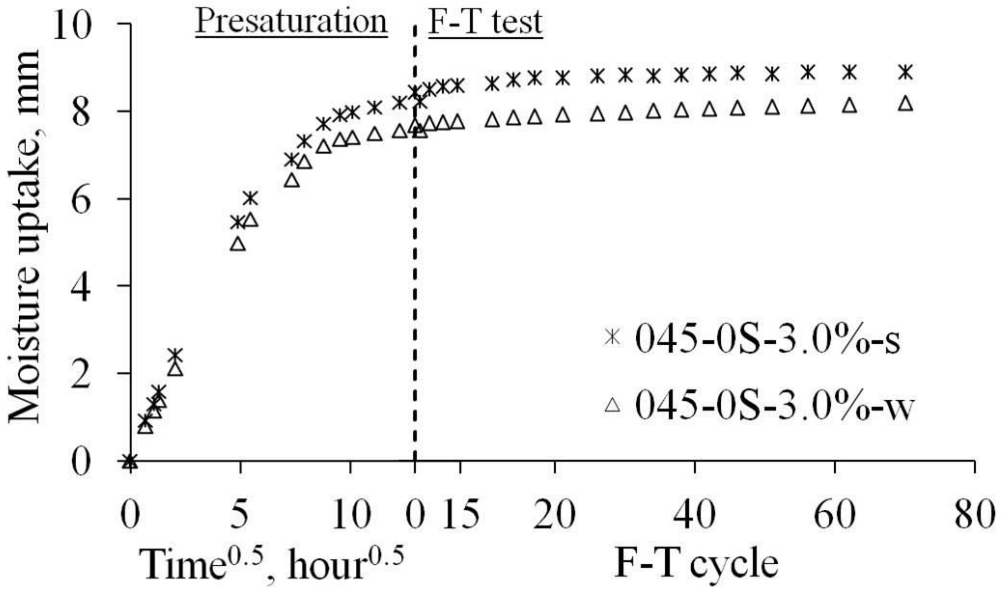

(f) 045-0S-3.0%

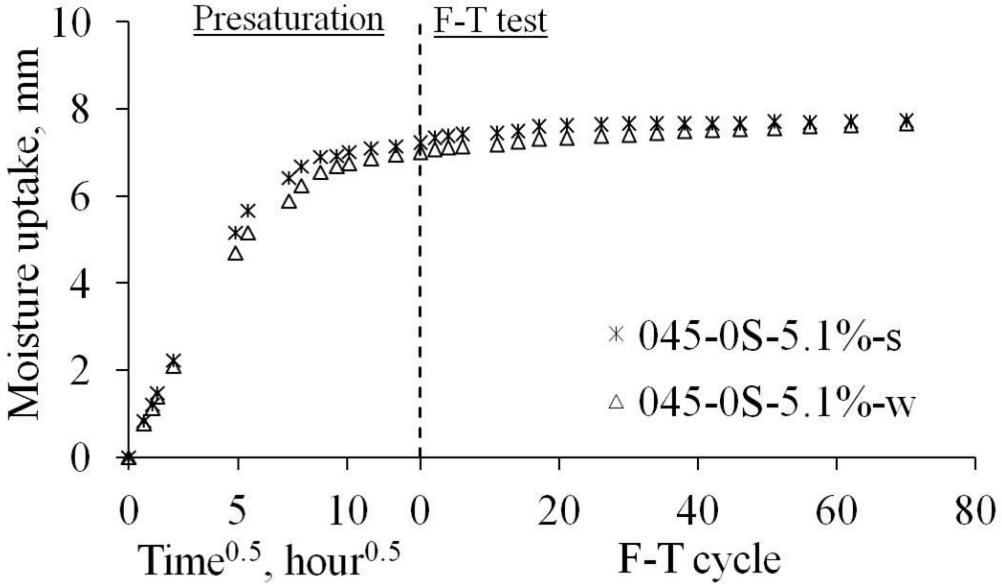

(g) 045-0S-5.1%

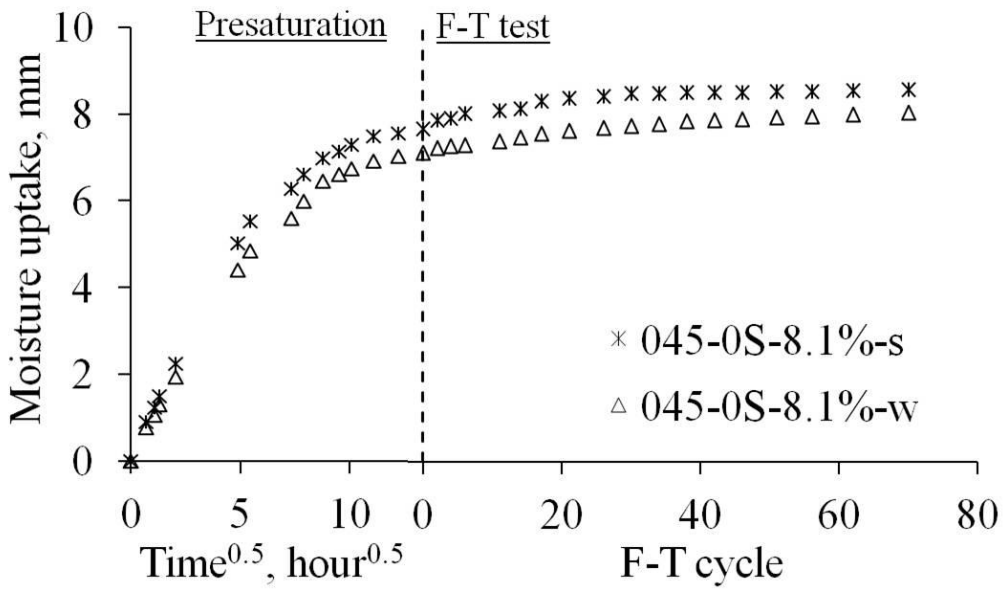

(h) 045-0S-8.1%

Figure 4.1Accelerated moisture uptake in concrete due to F-T action

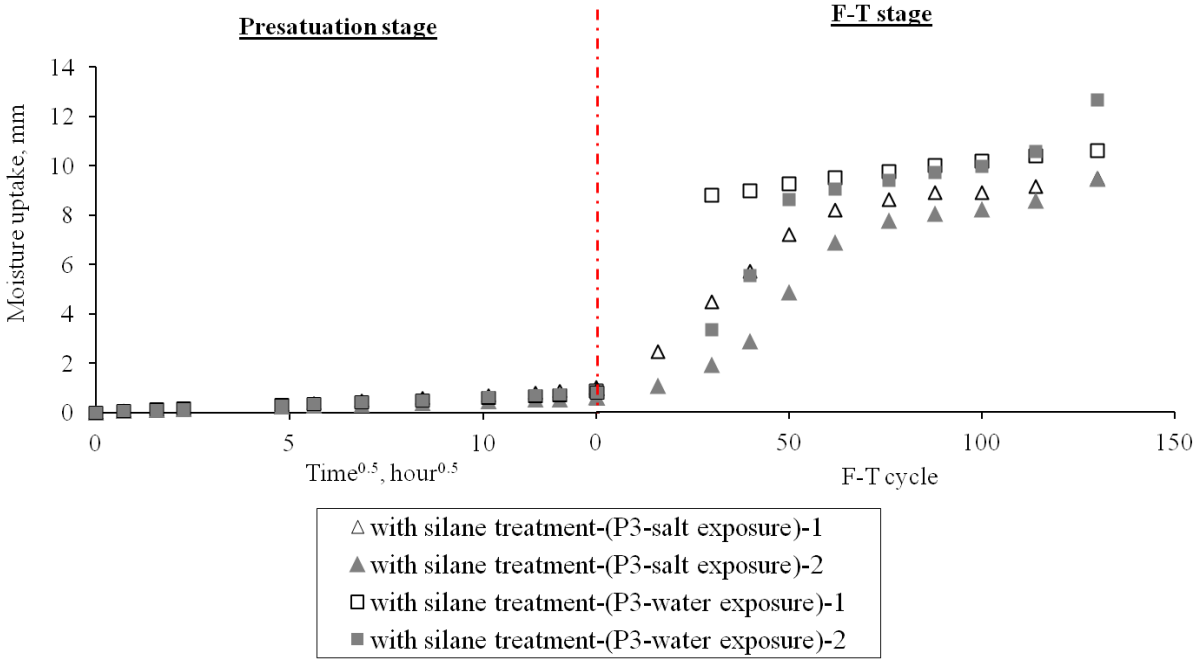

Figure 4.2 Moisture absorption in silane-treated specimens under water and salt exposures (field specimens, meaning of denotation can be found in Chapter 6)

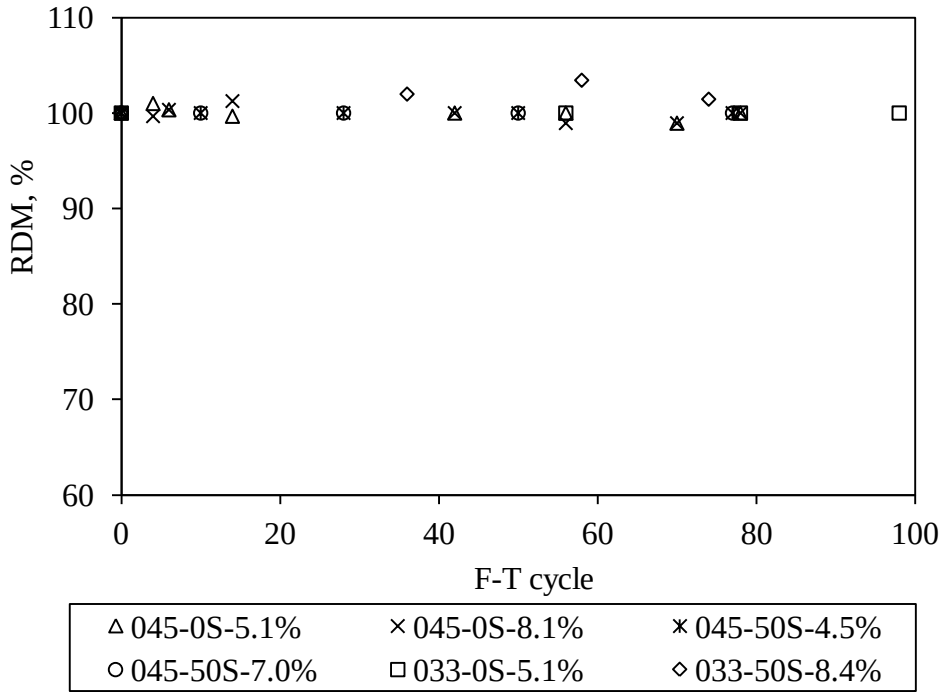

Figure 4.3 RDM change with F-T cycles in concrete exposed to 3% salt solution.

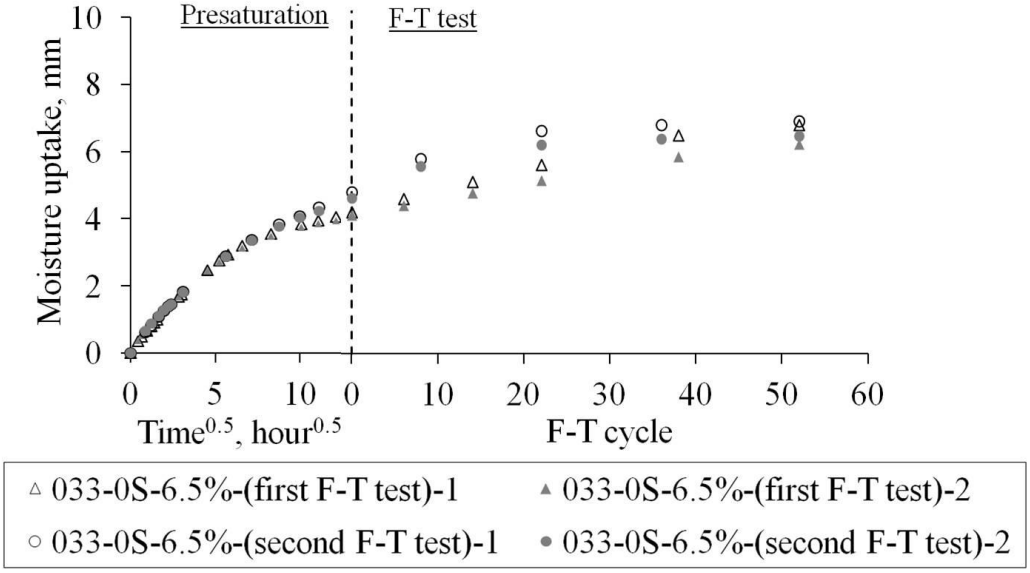

(a) 033-0S-6.5%

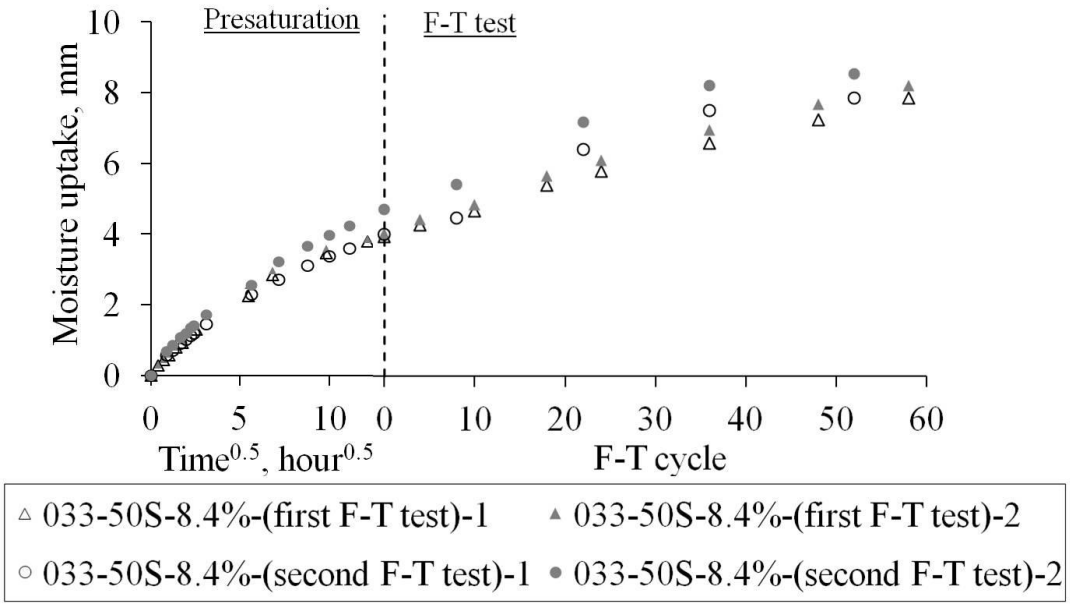

(b) 033-50S-8.4%

Figure 4.4 Moisture uptake in concrete specimens before and after F-T test in 3% salt solution

Additional moisture uptake can be also a result of internal cracking in concretes with inadequate air entrainment. This can be seen from a field concrete with poor frost resistance. There is an abrupt increase in absorption after a certain number of F-T cycles (Figure 4.5 (a)), which is accompanied by an increase in mass loss (Figure 4.5(b)) and a decrease in RDM (Figure 4.5(c)), an indication of internal damage. Coarse aggregate break-off leads to the increased mass loss (Figure 4.6 (a)) while added absorption is due to the re-saturation of the newly formed internal cracks (Bager and Jacobsen 1999), which is seen along the interface of paste and coarse aggregate and extended to the paste of the top surface that was not exposed to the salt solution during the test (Figure 4.6(b)).

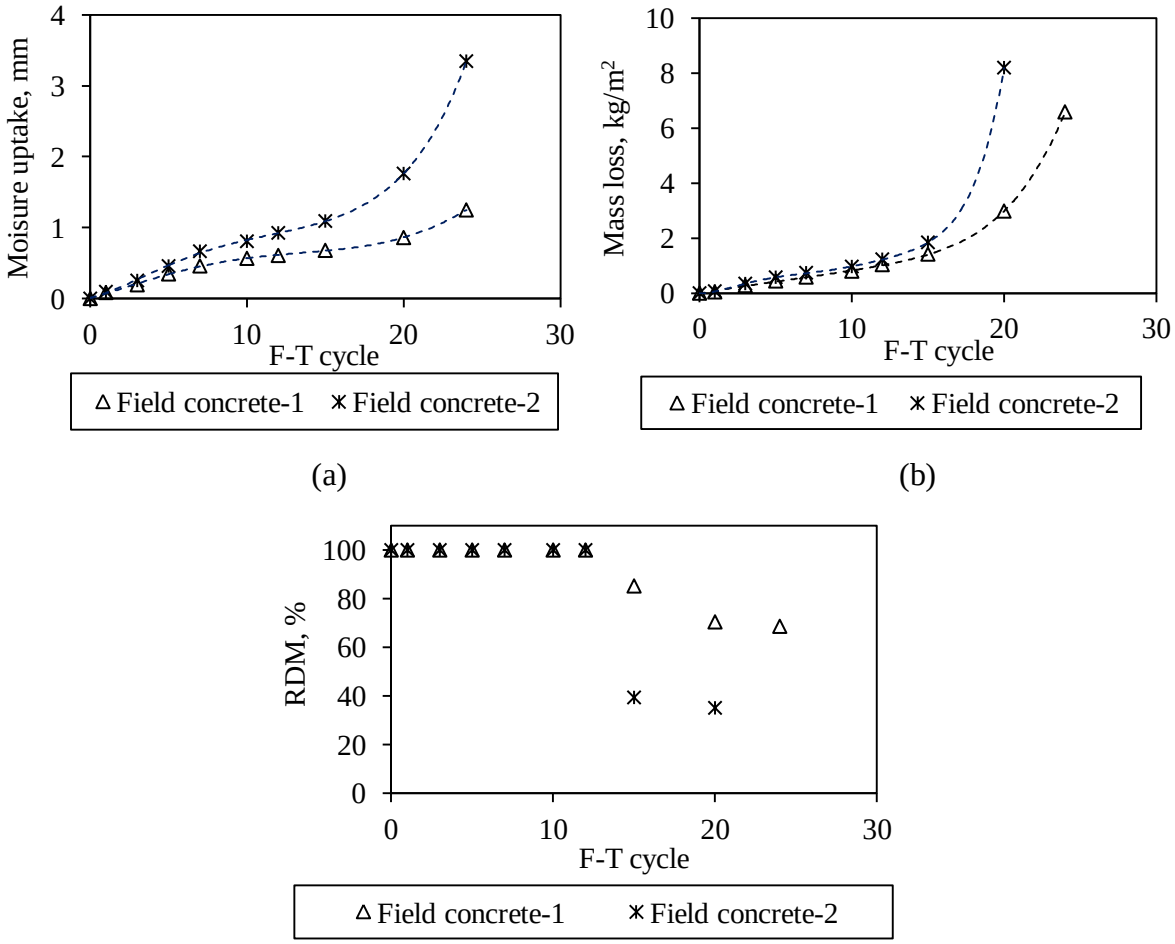

Figure 4.5 (a) Additional moisture absorption, (b) mass loss and (c) RDM change during F-T test

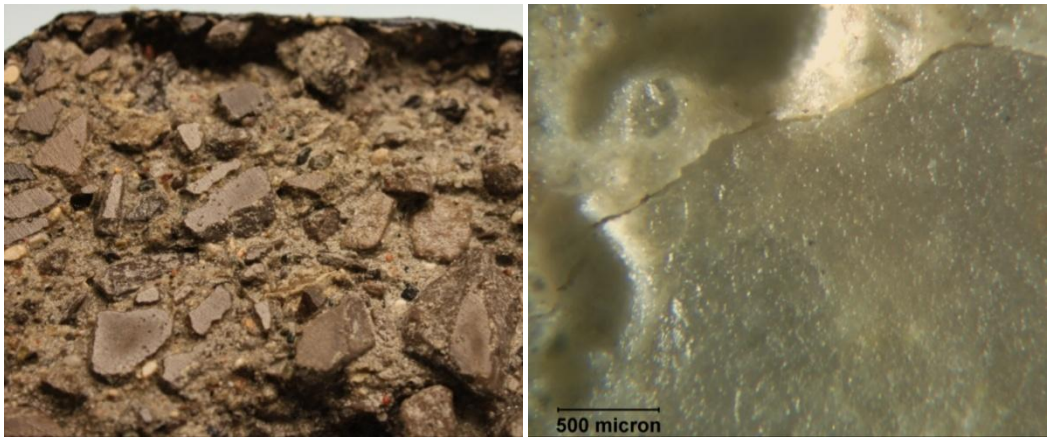

Figure 4.6 (a) Scaled surface with coarse aggregate falling off and (b) crack formation on the unexposed top surface (045-0S-2.9%-1 after 20 F-T cycles)

4.3 Air void filling in concrete under freezing

The amount of air voids that have been liquid filled can be estimated if assuming the level-off stage on the moisture uptake curve represents air void filling. This is supported by the higher absorption in concrete with more air entrained (Figure 4.7(a)&(c) and Figure 4.8(a)&(c)), regardless of the exposure condition, which is consistent with the similar size distribution in air voids of different contents (Figure 4.9). The extent of liquid diffusion into air void is clearly shown in Figure 4.7(b)&(d) and Figure 4.8(b)&(d), where typically less than 30% air volume is taken up by liquid. This gradual air void saturation effect doesn't affect the scaling performance, possibly because of the good air void system (high specific surface areas and low Powers' spacing factors, Table 5.2). This is consistent with the internal frost damage measurement in these concretes (Figure 4.3).

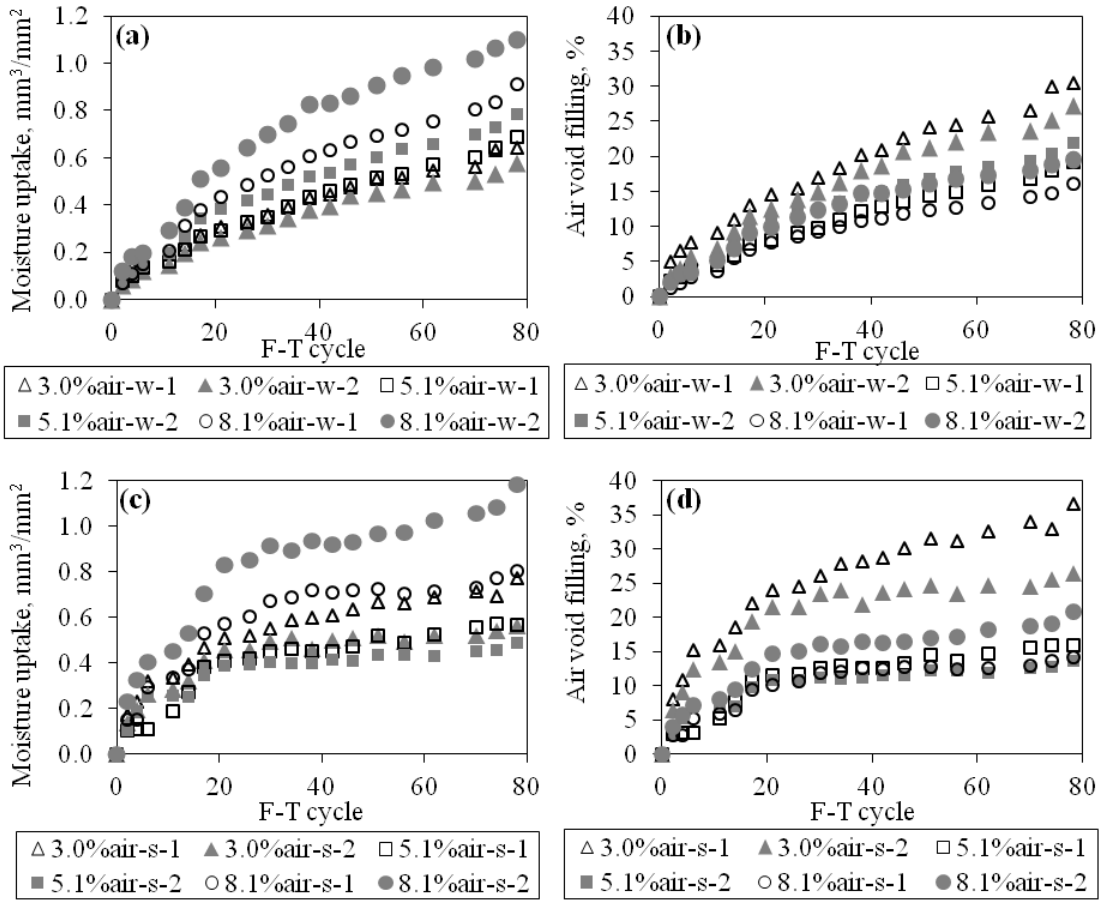

Figure 4.7 Measured moisture absorption and calculated percentage of filled air voids by volume in the level-off stage under F-T exposure to (a-b) water and (c-d) a 3% salt solution (045-0S)

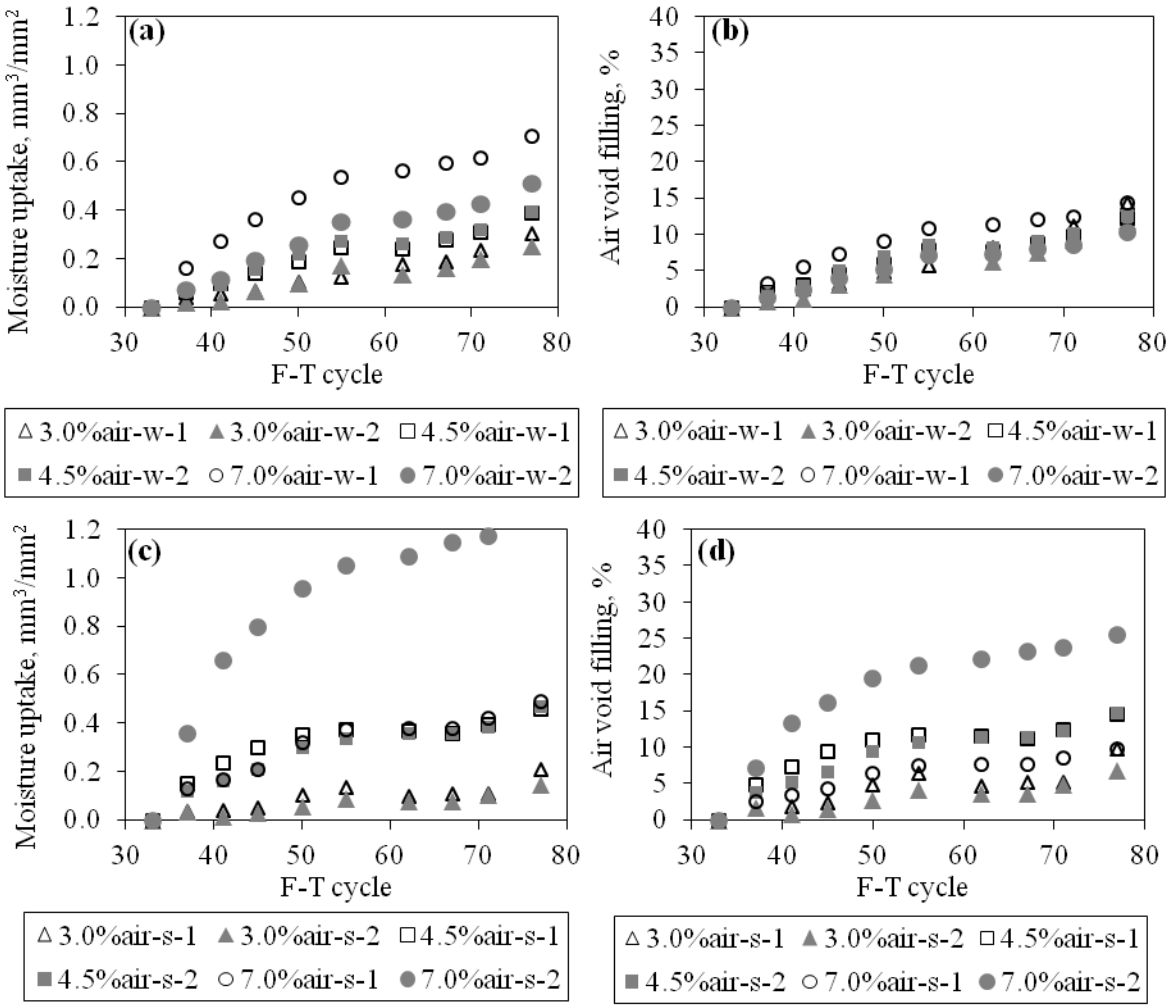

Figure 4.8 Measured moisture absorption and calculated percentage of filled air voids by volume in the level-off stage under F-T exposure to (a-b) water and (c-d) a 3% salt solution (045-50S)

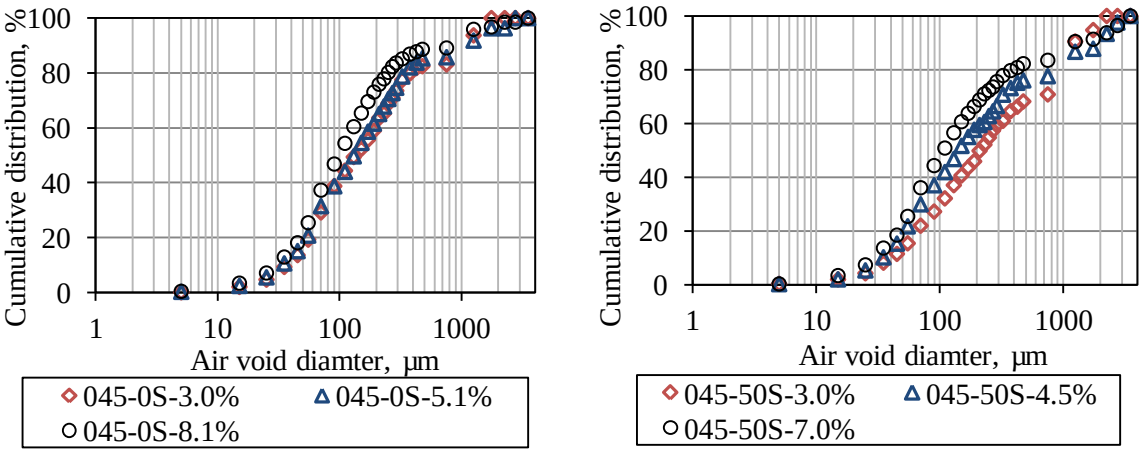

(a) (b)

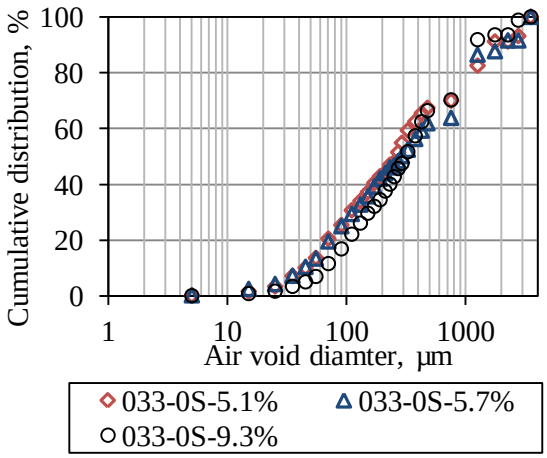

(c)

Figure 4.9 Cumulative air void size distribution in different concretes.

4.4 Relationship between permanent bulk moisture uptake and salt frost scaling

Figure 4.10 presents the mass loss vs. the additional permanent moisture uptake during the F-T test under water and 3% salt exposures for each mix on two duplicate specimens. There is no distinctive difference in the moisture absorption under the two exposure conditions for the same mix, but the mass loss differs tremendously. When comparing the moisture uptake and mass loss in different concretes exposed to a salt solution, the lack of correlation becomes more pronounced (Figure 4.11), where the 033-0S and 045-50S mixes actually has higher permanent moisture uptake than the 0.45-0S mix at the same level of scaling. In the low w/cm or slag cement systems, a big portion of the moisture uptake consists of the continuous capillary pore filling while this has been almost completed during the presaturation stage for the 0.45-0S mix. This is evidenced by the existence of a bi-linear development in the mass loss and moisture uptake curves, the clearly-defined breaking point of which coincides well with each other (Figure 4.12). Upon reaching the level-off stage in moisture uptake, mass loss is accelerated while internal cracking has been shown not to be a factor, which is consistent with other studies (Hammer and Sellevold 1990, Petersson 1986). In the case of the 0.45-0S mix, the breaking point is reached within a few F-T cycles due to the well-connected pore system, whereas it takes more than 50 F-T cycles for the 0.33-0S mix to reach the breaking point when the saturation of connected pores is completed. The reason for the higher rate of mass loss may be associated with the increased amount of internal moisture (or more ice formation) and the reduced pore space to accommodate the pressure buildup, which will be illustrated in Chapter 5.

Furthermore, the bulk moisture content distribution along the depth of two concrete specimens was measured right after the F-T test by cutting the specimens into thin slices that were oven dried at 105 ℃ to constant weight. Results show that there exists no noticeable moisture gradient (Figure 4.13), indicating internal stress distribution due to moisture difference along the depth of the specimen (Bager 2000) may not be a factor for surface scaling.

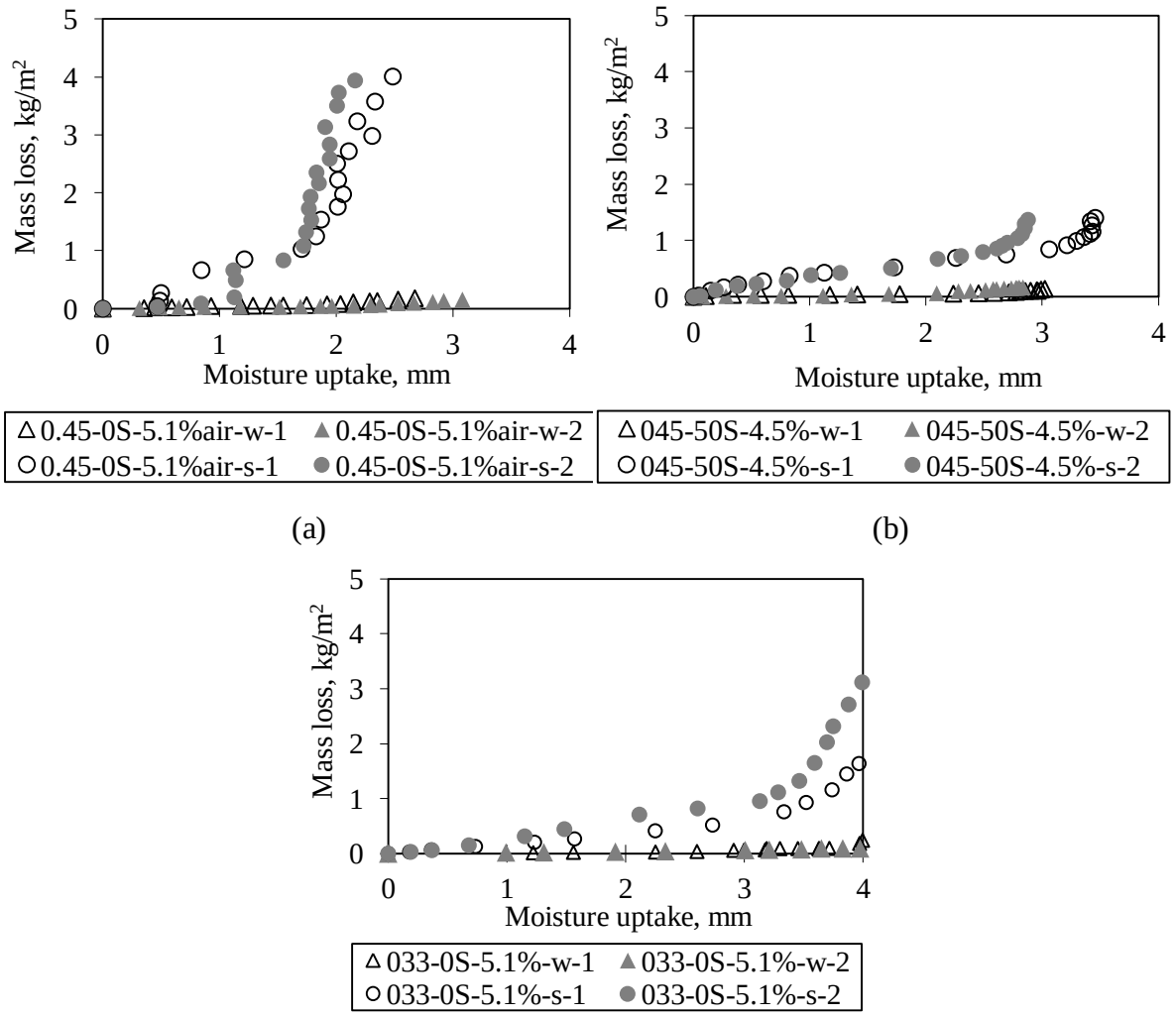

Figure 4.10 Mass loss vs. additional permanent bulk moisture uptake under water and 3% salt exposure for different concretes

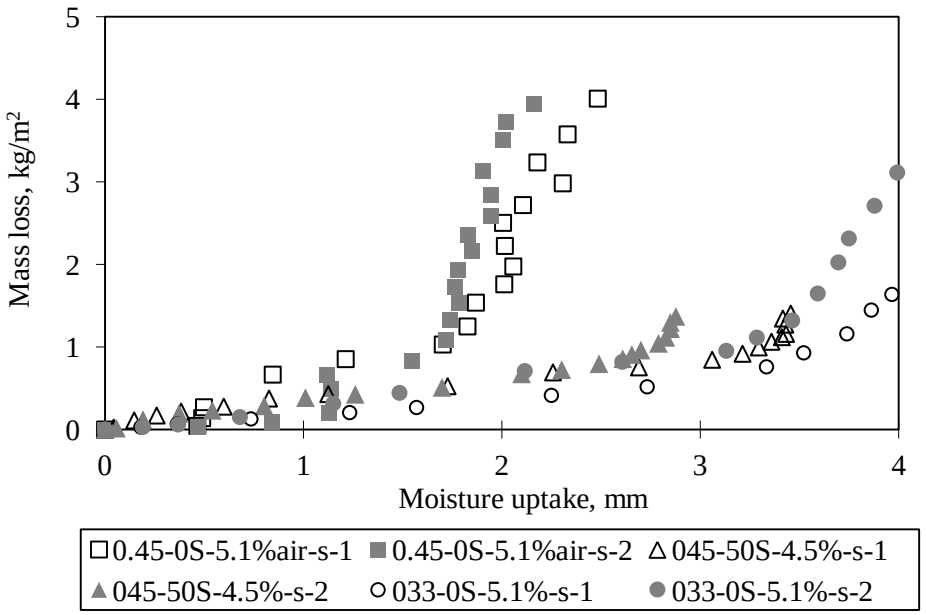

Figure 4.11 Mass loss vs. permanent bulk moisture uptake under 3% salt exposure for different concretes

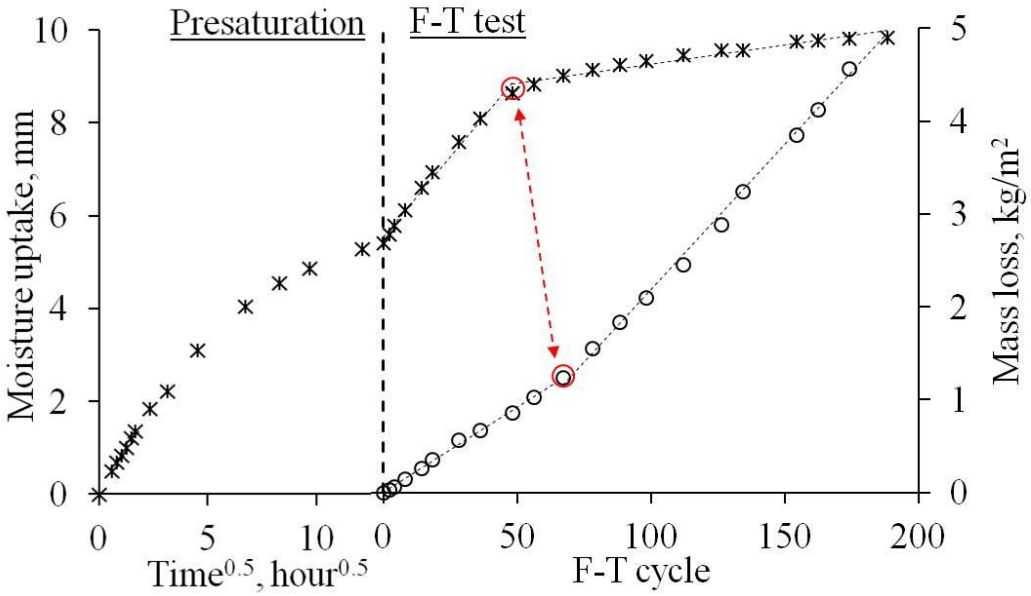

(a) 033-0S-5.1%

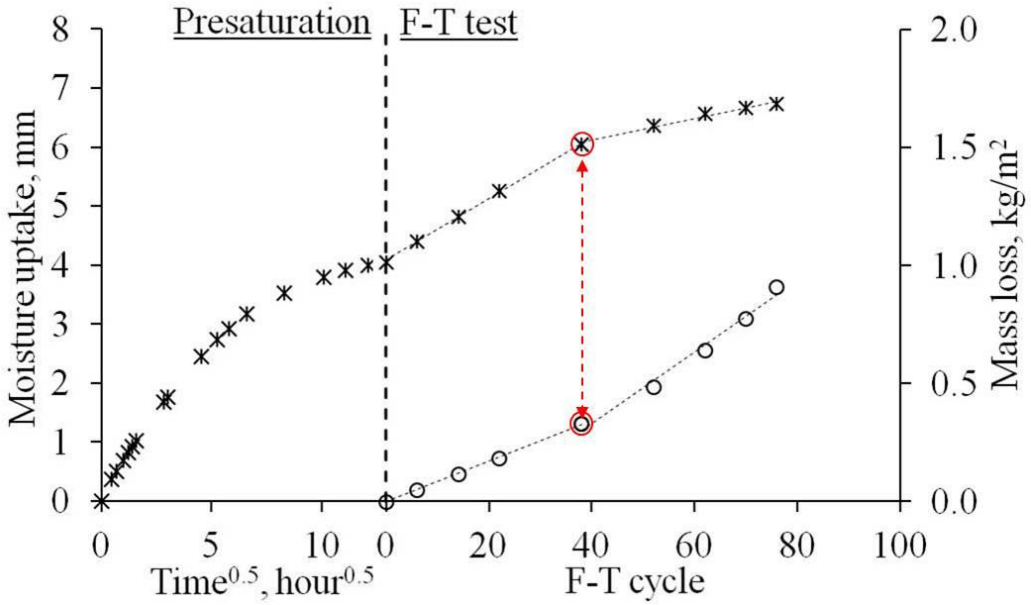

(b) 033-0S-6.5%

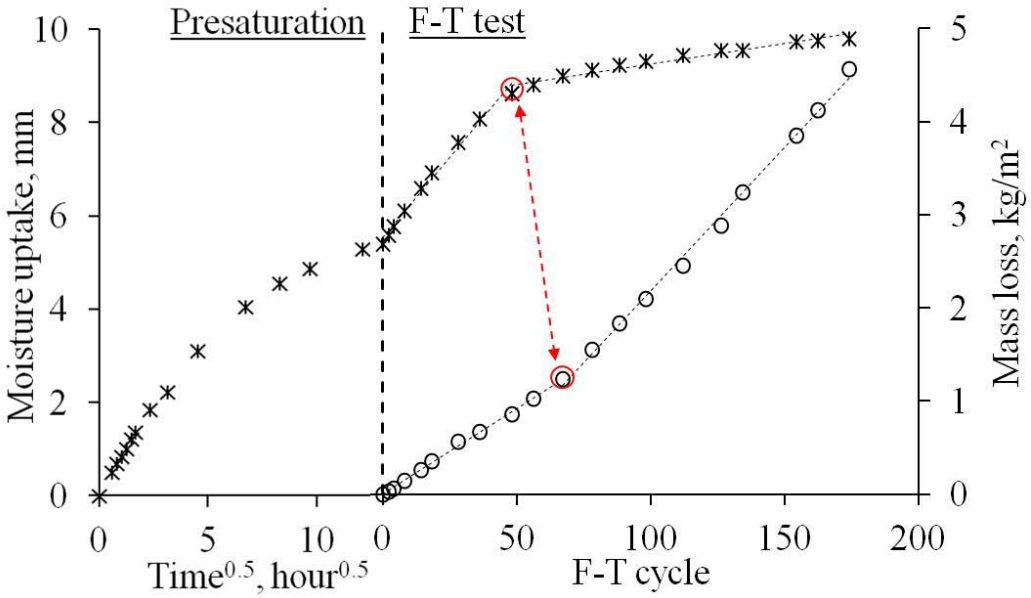

(c) 033-0S-9.3%

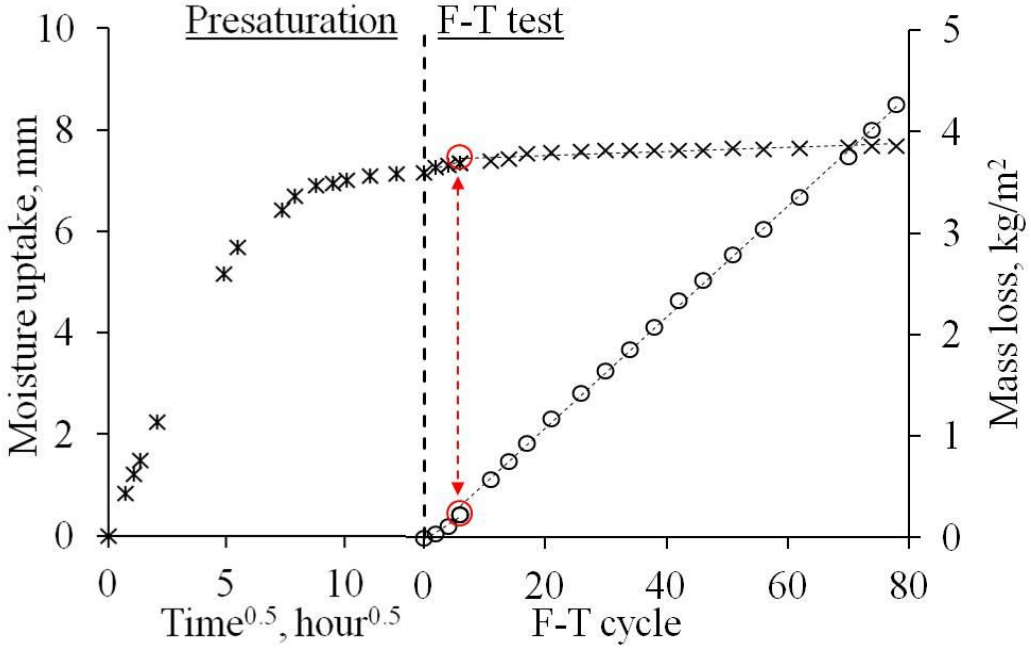

(c) 045-0S-5.1%

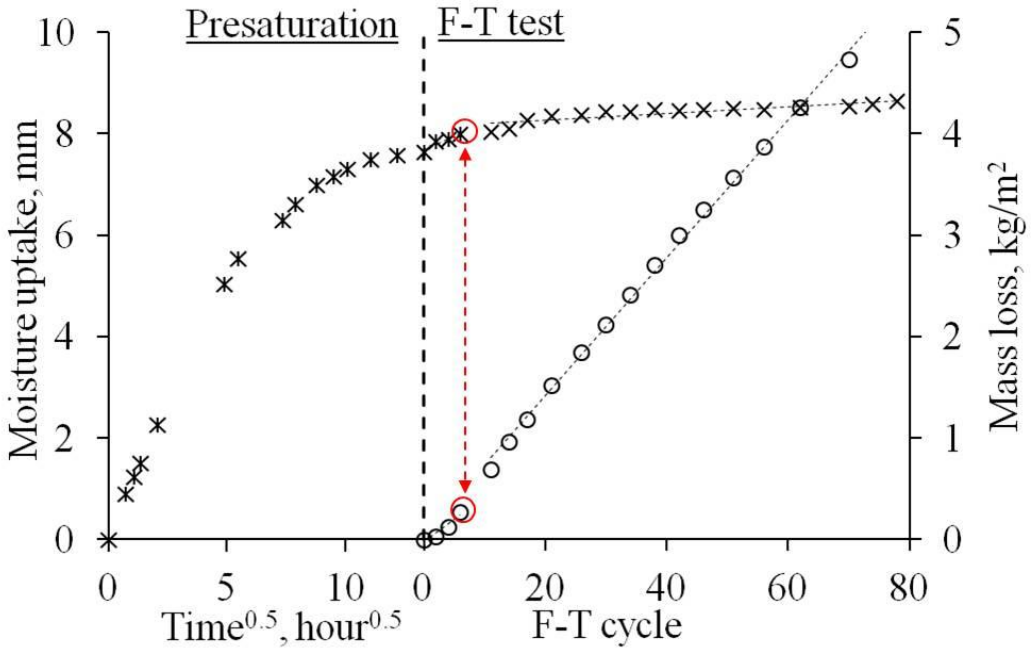

(d) 045-0S-8.0%

Figure 4.12 Breaking point on the mass loss and moisture uptake curves for different concretes

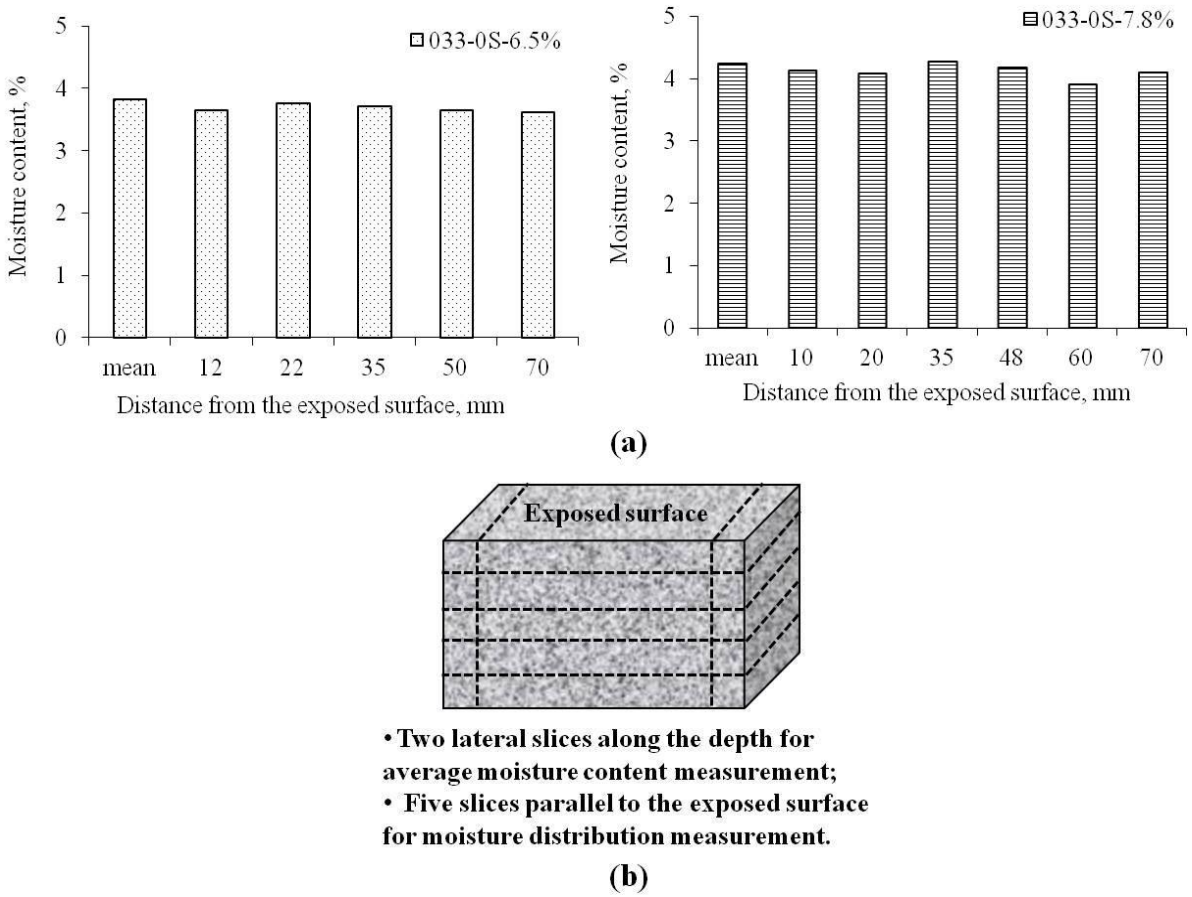

Figure 4.13 (a) Moisture distribution in concrete specimens (b) at different locations after the F-T test

Salt frost scaling as a surface phenomenon occurs within a 300 μm paste region, as shown by the thickness measurement on the scaled-off materials collected from different concretes during the F-T test (Figure 5.2). The amount of extra moisture needed to critically saturate this extremely thin surface layer may be too small to be accurately detected by the measurement of weight gain on the remaining bulk specimen at the end of an F-T cycle. This critical moisture uptake can be estimated based on the knowledge of mix design and air void characteristics with an example shown in Table 4.1. Detailed calculation procedure can be found in the Appendix.

As a result, the cumulative bulk moisture uptake is only a measure of the degree of saturation in the intact "torso", not on the scaled-off part (Fagerlund 1997), thus may not be reliable as an indicator for salt frost scaling resistance. Moreover, it is experimentally challenging to measure this added surface absorption, which is further compounded by the fact that the oversaturated

layer is removed from the surface before the weight measurement and the actual moisture content in the scaled-off materials is an unknown.

Table 4.1 Calculation on moisture needed to reach a critical spacing factor in a concrete slice of 0.3 mm

	045-0S-5.1%	033-0S-5.1%
Mix composition and air void system	P_{air}=5.12%, α=45.3 mm^{-1}, $\bar{L}$=104 μm P_{paste}=22.5%	P_{air} =5.10%, α =32.9 mm^{-1}, $\bar{L}$ =138 μm P_{paste}=24.3%
Remaining air content with α unchanged*	$P'_{air} = P_{paste}/\left[\left(\frac{(\alpha\bar{L})/3+1}{1.40}\right)^3 - 1\right]$ =0.99%,	$P'_{air} = P_{paste}/\left[\left(\frac{(\alpha\bar{L})/3+1}{1.40}\right)^3 - 1\right]$ =2.24%
Liquid filled air content	ΔP_{air}=5.12-0.99=4.13%	ΔP_{air}=5.10%-2.24%=2.86%
Moisture needed to reach $\bar{L}$=200 μm	$\Delta i = \Delta P_{air} \times h$=4.13%×0.3 =0.012 mm	$\Delta i = \Delta P_{air} \times h$=2.86%×0.15 =0.0086 mm

* This is a conservative assumption that air voids of different size classes are liquid filled simultaneously. The calculated moisture uptake will be much smaller if assuming smaller air voids are filled up first.

4.5 Summary of findings

This study investigates the moisture absorption in a range of concrete mixes and its correlation to salt frost scaling resistance. The major conclusions are:

- The measured permanent moisture uptake in concrete subjected to repetitive F-T cycles is an indication of the moisture condition in the bulk specimen and is not explicitly related to salt frost scaling. It is mostly a result of the accelerated saturation of yet empty capillary pores and the slow diffusion of liquid to entrained air voids, or the filling of newly formed micro cracks in concrete with internal damage.
- The rapid increase in bulk moisture uptake is shown to be governed by the expulsion of water into the still unsaturated region in concrete due to the transient formation of external ice. This is evidenced from moisture measurement on silane-treated specimens which have accelerated uptake even when there is a limited amount of internal moisture during the presaturation stage. Thus suction due to the melting of internal ice is not a factor.

- No moisture gradient along the depth of the specimen is found by measuring the moisture content in different slices parallel to the test surface after F-T test. In addition, the moisture needed to critically saturate the surface region where scaling occurs is calculated to be too small to be detected by existing experimental methodology. This necessitates a better criterion to evaluate scaling resistance of concrete.

Appendix

Calculation of moisture absorption needed to critically saturate a concrete slice

The moisture absorption ($i, mm^3/mm^2$) through the surface of a thin concrete slice can be determined as

$$i = \frac{V_{water}}{A_c} \tag{A.1}$$

where V_{water} is the volume of absorbed water during the test.

On the other hand, if the mixture composition of the concrete (paste content, air void system) is known, moisture uptake can be back-calculated that is needed to fill partial air voids such that a critical spacing factor (200-250 μm) is reached.

$$\Delta i = \frac{\Delta V_{water}}{A_c} = \frac{(\Delta P_{air} \times V_c)}{A_c} = \frac{(\Delta P_{air} \times A_c h)}{A_c} = \Delta P_{air} \times h \tag{A.2}$$

CHAPTER 5 CRYOGENIC SUCTION AS THE MAJOR SALT FROST SCALING MECHANISM

5.1 General

Salt frost deterioration has been recognized as one of the major concerns in concrete structures for a few decades in North America and Northern Europe where freezing temperature is prevalent and widespread use of deicing salts is common in winter. Given its importance, a great amount of research has been devoted to this subject in the past few decades and different deterioration mechanisms and models have been proposed (Litvan 1976, MacInnis and Whiting 1979, Harnik et al. 1980, Lindmark 1998, Bager and Jacbosen 1999, Setzer 2009, Kaufmann 2004, Valenza and Scherer 2006), among which, there exists one similarity that all the researchers tried to decipher the role of salt physically or chemically, which leads to various interpretations. It has been hypothesized that the central role of salt is to maintain a liquid reservoir on the concrete surface under freezing which is in connection with near-surface pore solution, thus, the micro ice bodies formed therein can be continuously re-supplied by a suction force (Lindmark 1998).

The main purpose of this chapter is to further identify and confirm the major mechanism of salt frost scaling, based on which some of the experimental observations can be accounted for. The scope of the study is experimental in nature considering a range of materials and test methods where the material level variables include water-cement ratio, air content, and slag cement and test variables include salt scaling and internal frost deterioration measurement, length change measurement, optical microscopy, air-void analysis, room-temperature capillary absorption and nitrogen sorption test. This work will set the foundation for the performance-based evaluation of scaling resistance in the next chapter.

5.2 Commonly observed features

In this section, a compilation of some frequently observed phenomena related to salt frost deterioration is listed below.

5.2.1 A surface phenomenon

Salt frost scaling is a superficial damage consisting of paste welling and flaking (Figure 5.1), which occurs within a narrow surface region, as illustrated by the microscopic evaluation of the thickness distribution of the scaled-off materials (Figure 5.2). The flake thickness is typically between 50-300 μm.

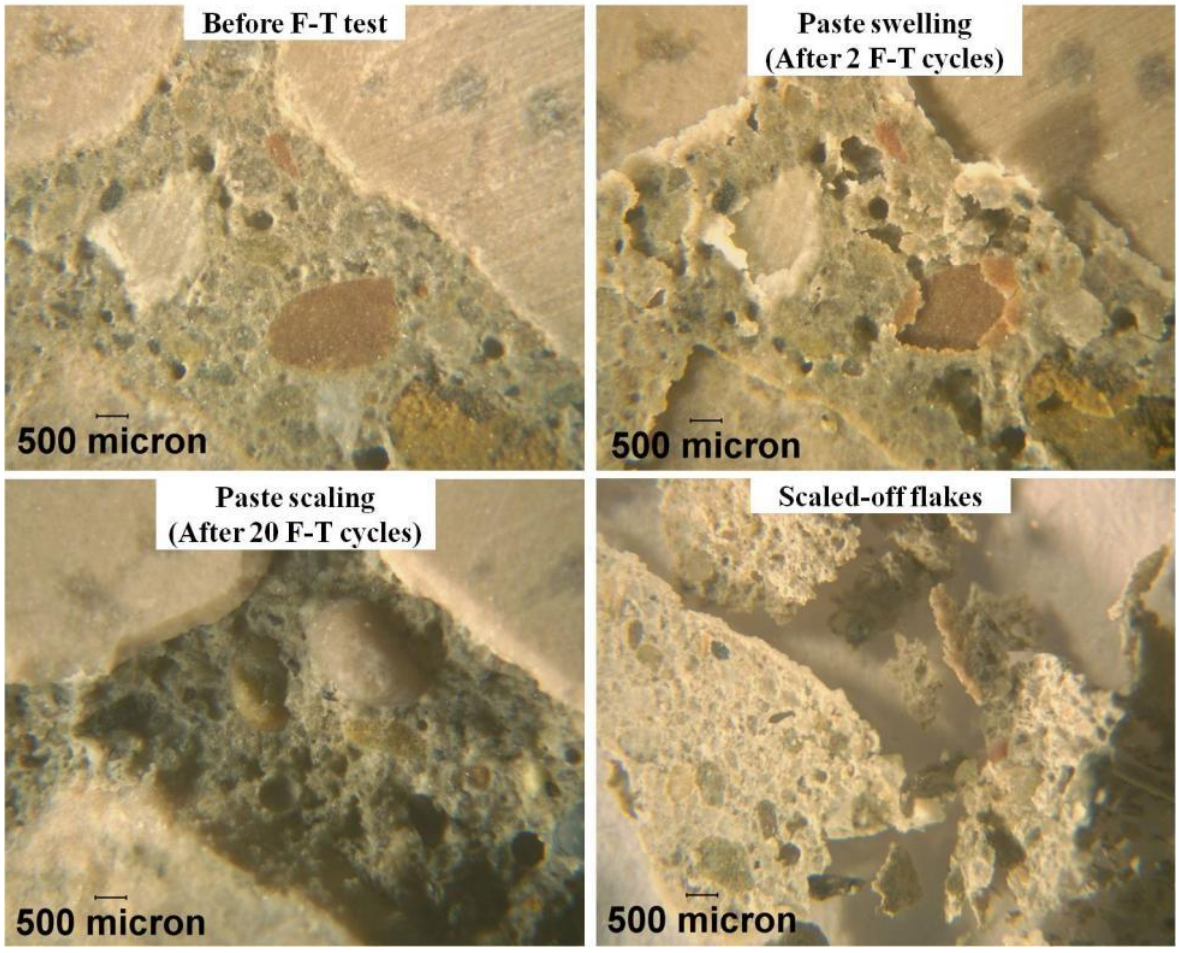

Figure 5.1 Damage pattern of salt frost scaling (045-0S-5.1%)

At the macroscopic level salt frost scaling is characterized by the normalized mass loss of scaled-off materials per exposed surface area and it typically shows a linear development with the number of F-T cycles (Figure 5.3(a)). Furthermore, the damage zone does not spread beyond this narrow surface region as long as the concrete is adequately air-entrained, as evidenced by the almost constant RDM with F-T cycles measured in the mid-height of the specimens (Figure 5.3(b)). The absence of internal damage can be also detected by the nitrogen sorption measurement on mortar samples obtained at three different locations along the depth of a tested concrete sample, which shows similar pore volume for various concrete mixes (Figure 5.4).

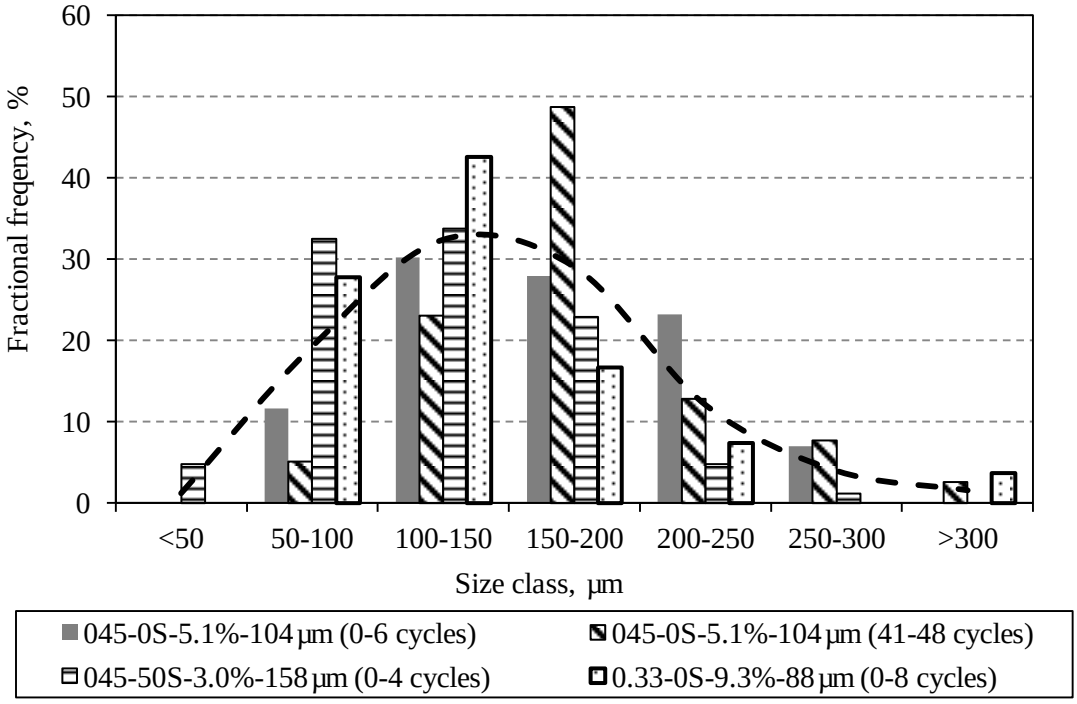

Figure 5.2 Thickness distribution of scaled-off materials

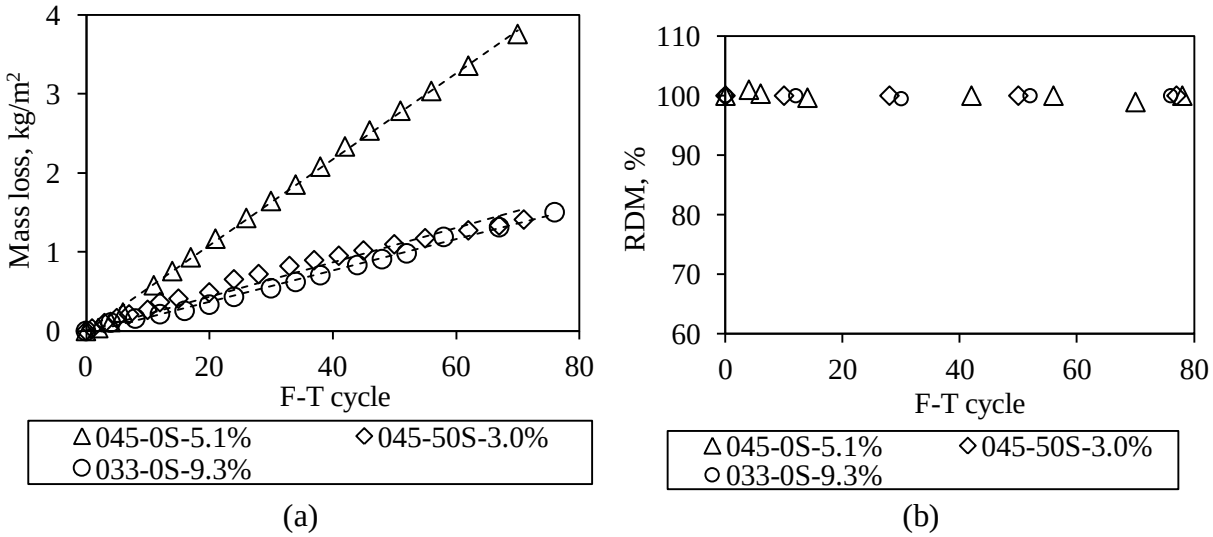

Figure 5.3 (a) Cumulative mass loss and (b) internal damage measurement by RDM with F-T cycles

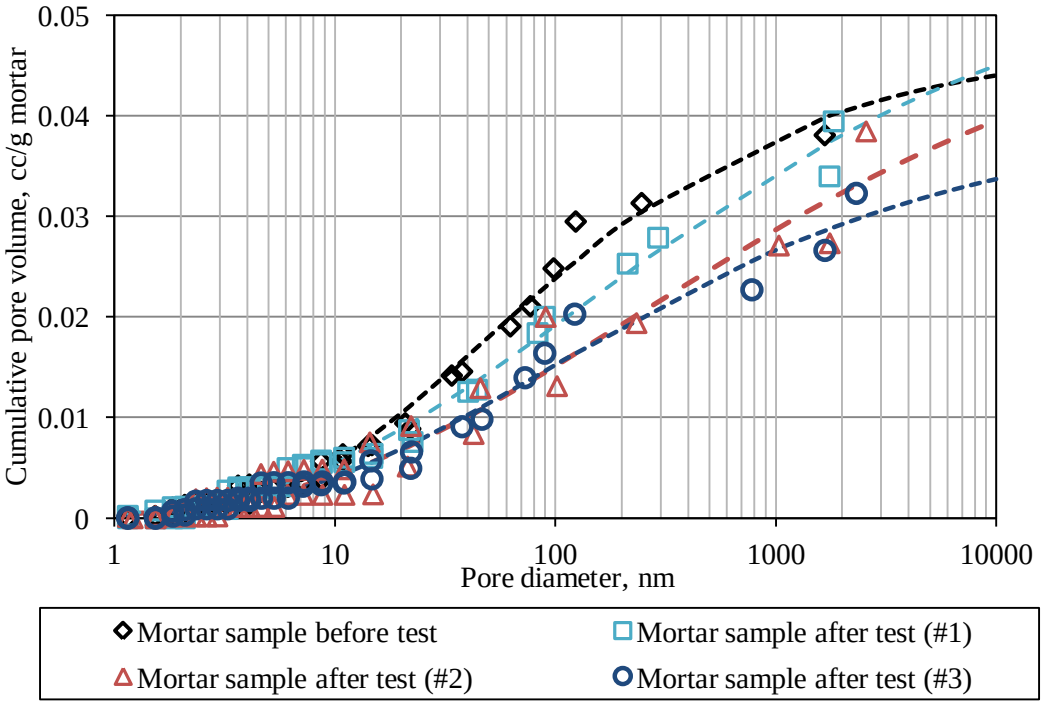

(a) 045-0S-5.1%

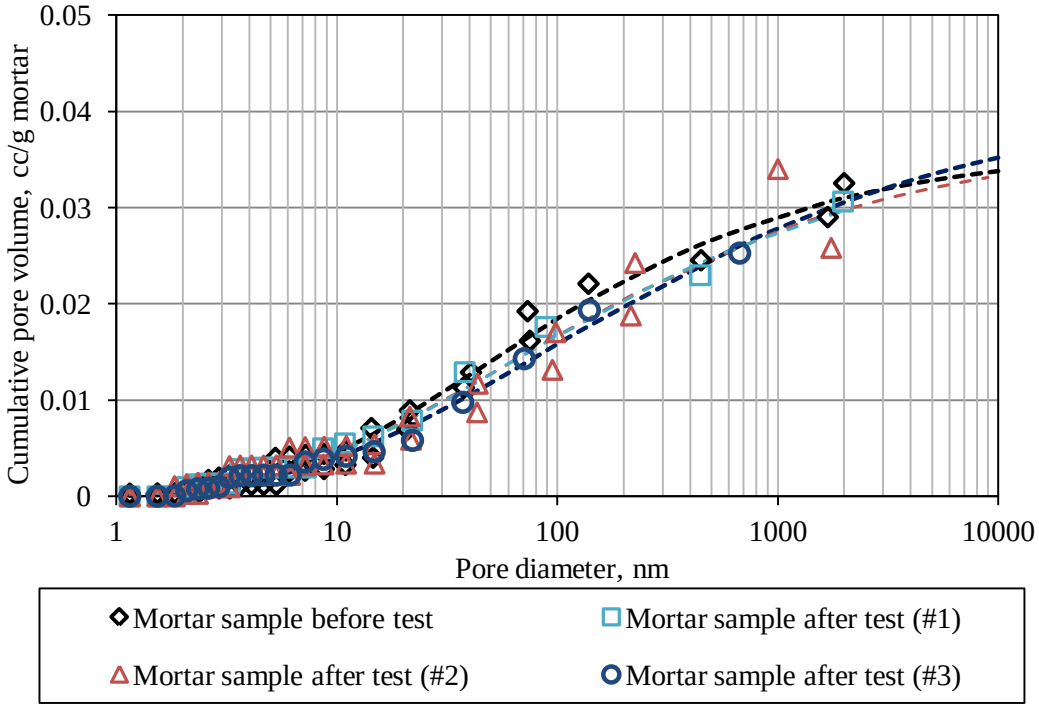

(b) 045-50S-3.0%

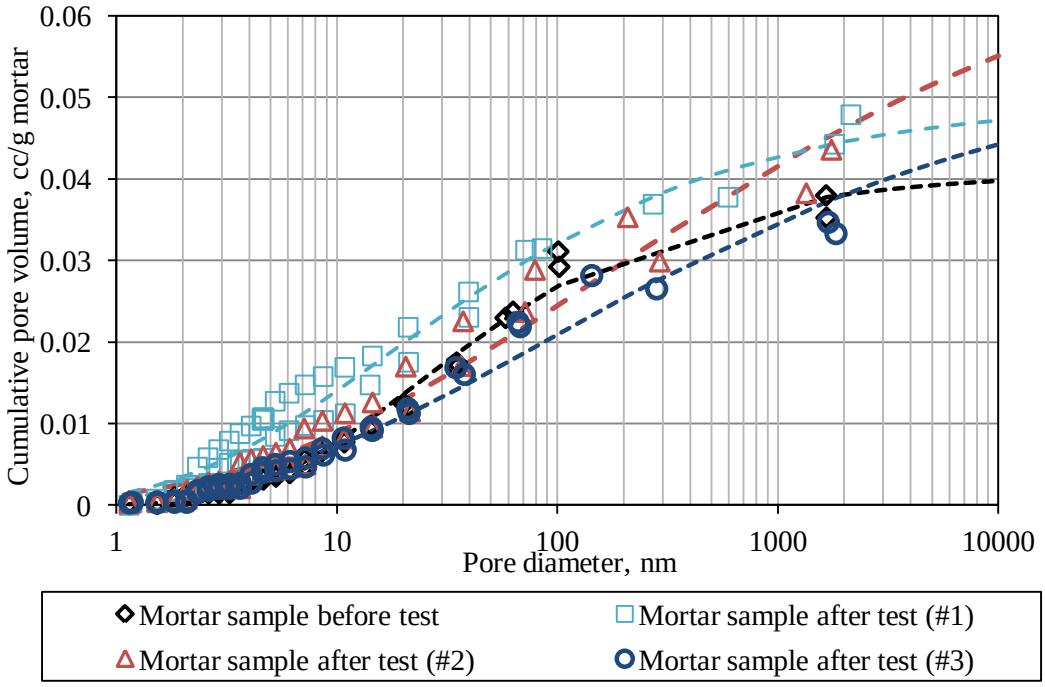

(c) 033-0S-3.0%

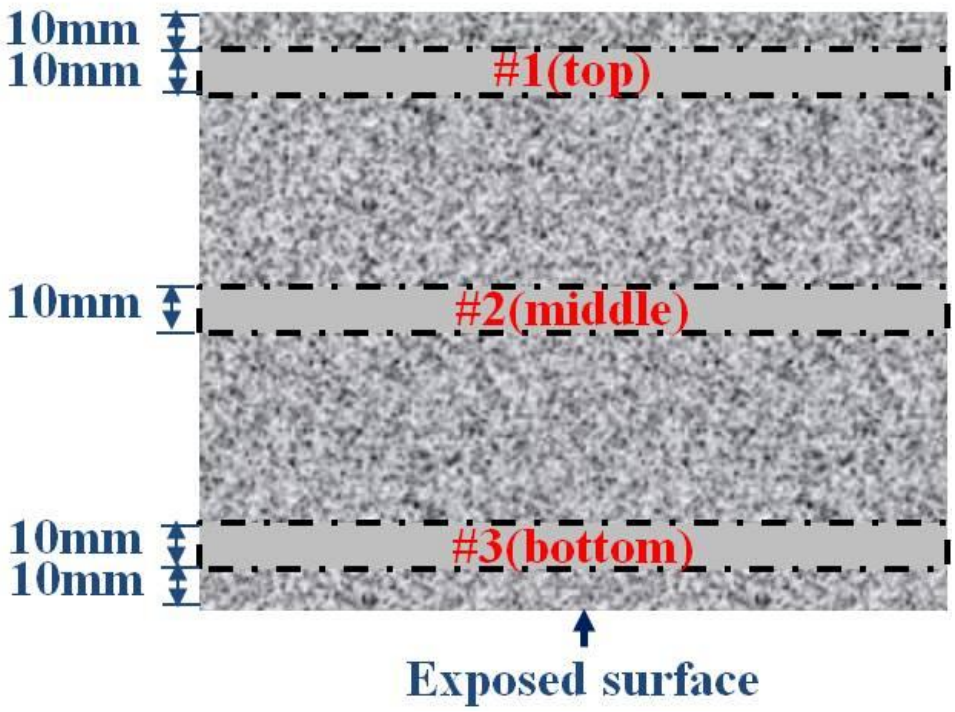

(d)

Figure 5.4 (a-c) Cumulative pore volume in mortar samples (d) obtained from thin slices of concrete at different locations after salt frost scaling test

5.2.2 Paste swelling

Another notable characteristic is discovered upon the close examination of the exposed surface of concrete in both laboratory and field conditions. It shows the swelling of the whole paste region around the periphery of coarse aggregate particles in concrete mixes with either high w/c ratio or insufficient air entrainment (Figure 5.5). The collected scaled materials are mostly flat flakes with close-up view of one flake in Figure 5.6 revealing more details on both the cut-surface side and the breaking-off side with the embedment of sand particles in the cement paste, and the lateral side as well. This indicates that stresses causing the scaling stem from beneath the surface in the paste phase and it is supported by the length change measurement perpendicular to the concrete surface which demonstrates that "expansions in the outermost concrete layer are volume dilatations and probably isotropic" (Kaufmann 2000). Paste welling has been reported in different research work, which is listed in Table 5.1. It is noted that concrete mixes displaying paste swelling generally have low air content and relatively high w/c ratio.

Table 5.1 Literature description on paste swelling

Source	Mix detail	Description
Cordon 1966	Concrete (cement content =230 kg/m^3 and no entrained air).	"Upon freezing, ice in more numerous capillaries immediately under the surface "skin" grow to such proportions by accretion that the surface of the slab is lifted."
Lindmark 1998	Mortar (0.65 w/c ratio and no entrained air)	"After each cycle, an almost coherent layer of scaled-off material could be lifted off."
Kaufmann 2000	Concrete (w/c ratios from 0.45 to 0.63 and air content from 1.0-3.7%)	"The scaled (removed) material in laboratory frost deicing salt resistance tests mostly consists of flat particles (ca. 5×5×0.2 mm), which may be a result of significant expansion perpendicular to the frost medium surface."

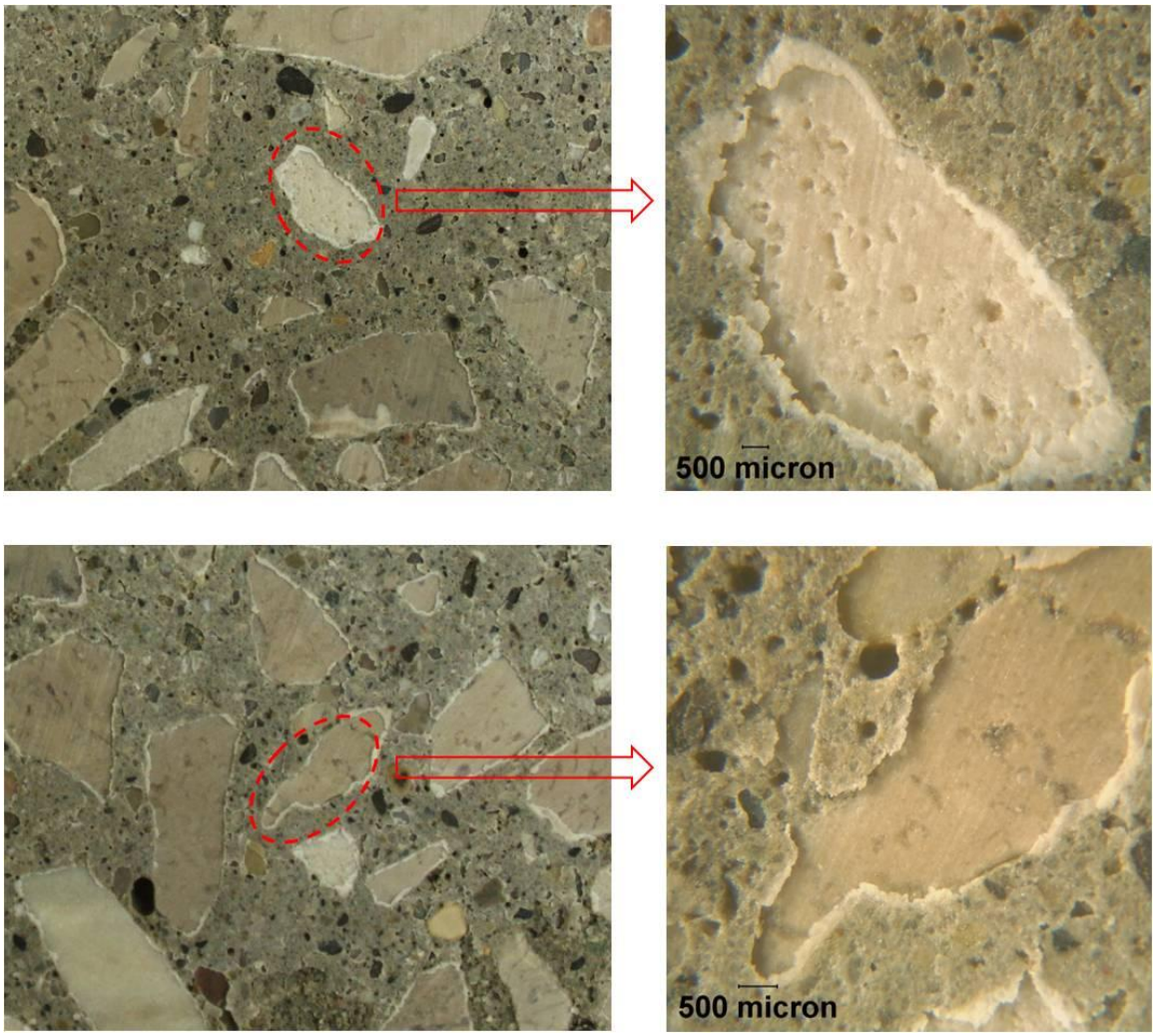

(a) 0.45-0S-5.1% after 2 F-T cycles

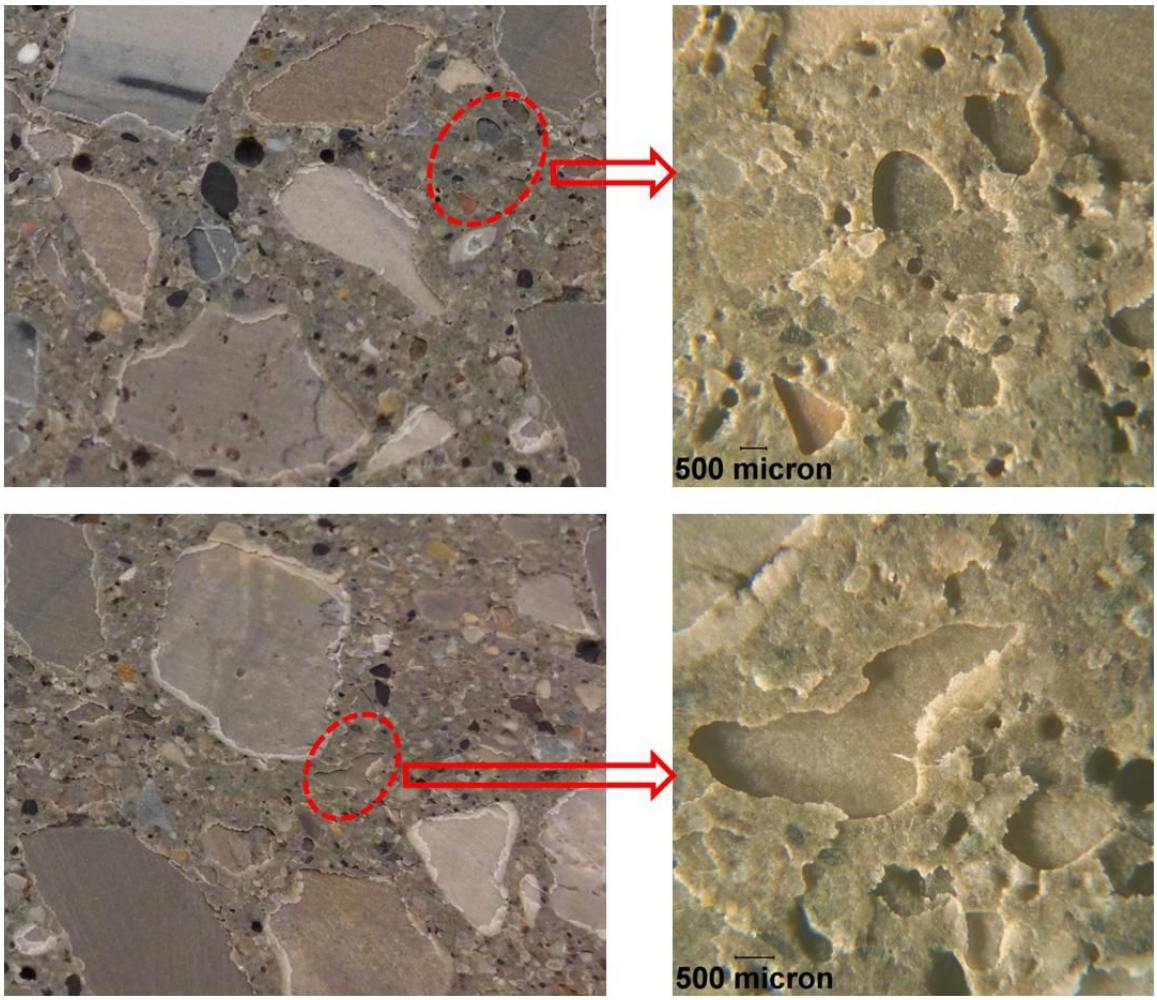

(b) 0.33-0S-non air entrained mix after 2 F-T cycles

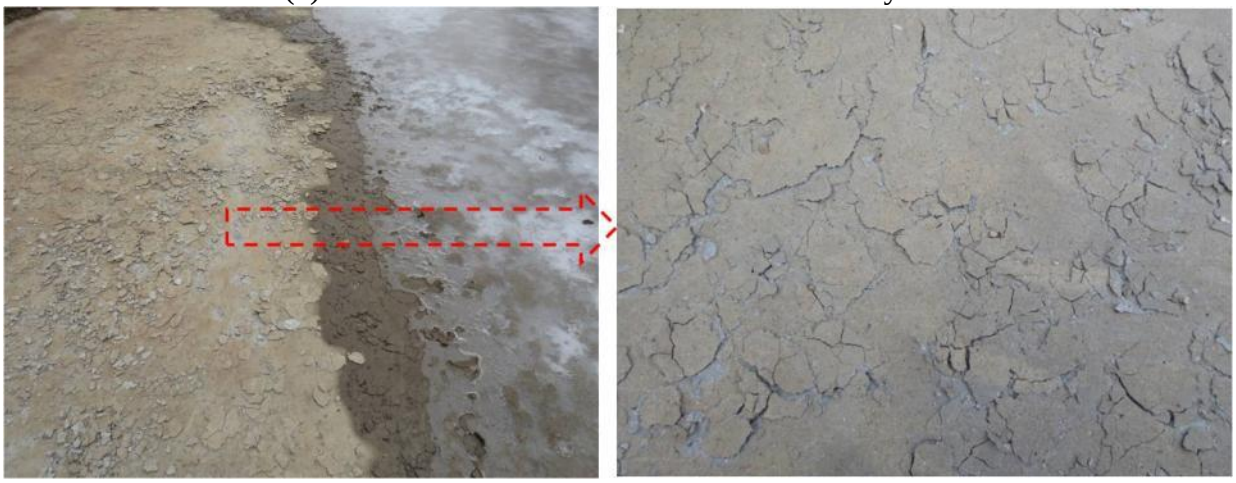

(c) 0.51-35S-non air entrained concrete in a shipyard

Figure 5.5 Swelling of paste around coarse aggregate particles under salt exposure

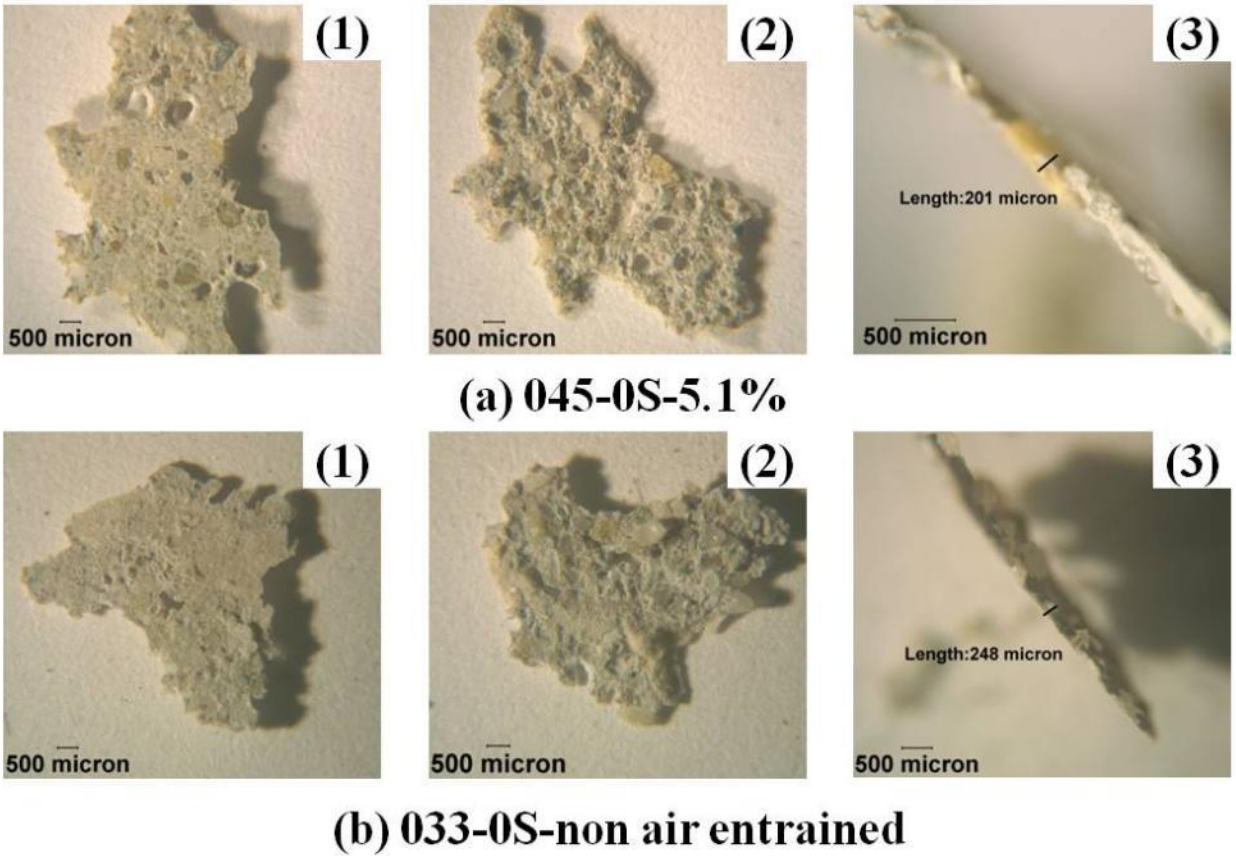

Figure 5.6 Microscopic pictures of flakes showing (1) the cut surface, (2) the scaled surface and (3) the lateral surface with thickness annotation in the two concretes

5.2.3 Existence of "pessimum" salt concentration

One of the frequently observed features of salt frost scaling is that the presence of a salt solution of a certain concentration range causes the most severe damage to concrete surface than pure water, which is known as the "pessimum" phenomenon (Figure 5.7). A wealth of research has been devoted to this subject (Arnfeldt 1943, Verbeck and Klieger 1957, Sellevold 1991, Lindmark 1998, Marchand et al. 1999, Powers 1965, Harnik et al. 1980, MacInnis and Whiting 1979, Fagerlund 1975, 1992, Litvan 1975, Wang et al. 2014). However, some of them omitted an indispensable feature of salt scaling in their tests: the presence of surface liquid, thus making their conclusion unsound (Litvan 1975, MacInnis and Whiting 1979, Fagerlund 1975, 1992, Harnik et al,).

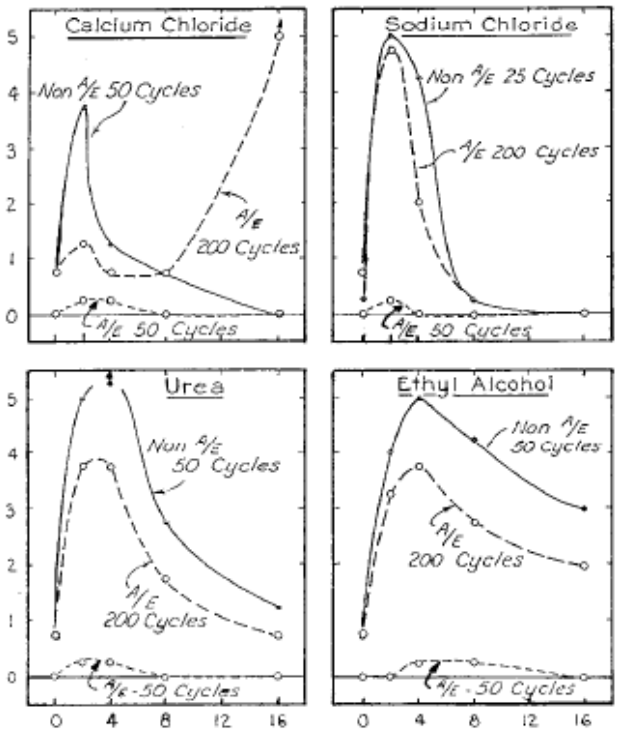

Figure 5.7 Effect of salt concentration on scaling from visual examination (Verbeck and Klieger 1957)

In order to get a better understanding of this phenomenon, the data of mass loss from some researchers are assembled and normalized with respect to the highest amount of mass loss and compared that with our result. Despite the big dispersion due to discrepancies in test method and concrete quality, the "pessimum" lies roughly in a concentration range of 0.5-6%, above which, there is an appreciable reduction in scaling (Figure 5.8). One surprising aspect of our results is the significant scaling upon the addition of a tiny amount of salt. This is consistent with (Sellevold 1991 and Setzer 2009) and will be explained later.

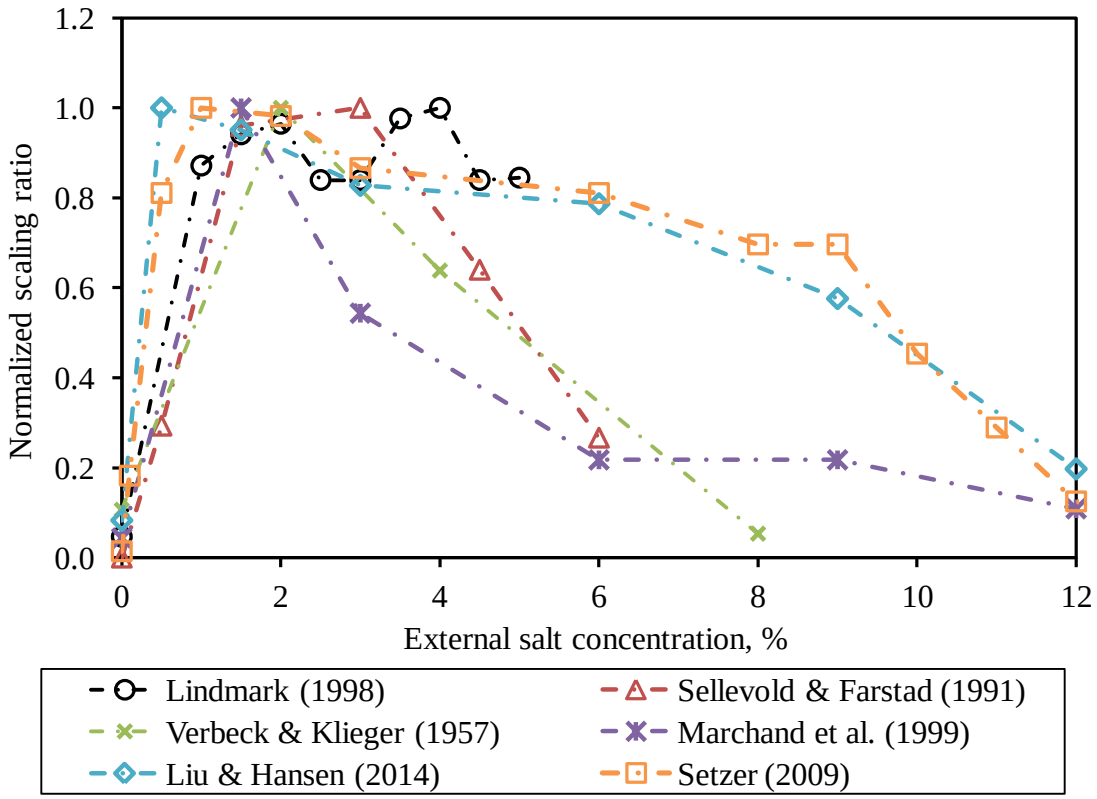

Figure 5.8 Normalized scaling ratio vs. salt concentration of surface liquid (NaCl) from various sources

5.2.4 Added moisture uptake under salt/frost exposure

It was reported that additional moisture uptake occurs in concrete under salt/frost exposure. However, mixed results were found on the magnitude of moisture absorption under water and a salt solution and its correlation to salt scaling (Fagerlund 1992, Jacobsen and Sellevold 1994, Rønning 1999), which was attributed to a variety of factors such as mix composition (Jacobsen et al. 1997), interference with internal frost damage (Jacobsen et al. 1997, Auberg and Setzer 1997) and preconditioning method (Jacobsen et al. 1997). Interpretation is further complicated by the remaining debate over the major mechanism on salt frost scaling. In the previous chapter, results show no explicit correlation between permanent bulk moisture uptake and scaling resistance.

5.3 Salt frost scaling properties of air-entrained concrete

In this section, a wide range of mixes with different material variables and air contents were investigated in internal frost damage and surface scaling by the modified RILEM CIF test procedure (Section 3.2). Results are presented as follows.

5.3.1 Internal frost resistance

Air entrainment is an important technique in protecting concrete from frost deterioration (Powers 1949). Air void characteristics were determined on the hardened concrete specimens according to the linear traverse method i(ASTM C457), as listed in Table 5.2. The mixes studied have a total air content ranging from 2.6%-9.3% and a Powers' spacing factor of 60-500 μm. The air voids on a polished concrete section show a uniform distribution (Figure 5.9). The majority void size ranges between 50-150 μm (Figure 5.10).

Table 5.2 Characteristics of hardened air void in air-entrained concrete specimens

mix	air content (%)		Powers' spacing factor (μm)	specific surface (mm^{-1})	average chord length (μm)
	total	entrained (<0.5mm)			
045-0S-1.9%	1.88	0.97	265	15.2	264
045-0S-3.0%	3.02	2.49	135	43.1	93
045-0S-5.1%	5.12	4.37	104	45.3	88
045-0S-8.1%	8.08	7.16	64	53.5	75
045-50S-3.0%	3.04	2.08	158	36.0	111
045-50S-4.5%	4.51	3.43	114	42.8	93
045-50S-7.0%	7.04	5.79	81	51.8	77
045-50S-3.8%	3.83	3.01	148	38.8	103
045-50S-7.7%	7.74	5.63	105	31.1	129
033-0S-2.5%	2.53	0.99	479	13.7	292
033-0S-5.1%	5.10	3.44	138	32.9	122
033-0S-5.7%	5.70	3.53	117	33.8	118
033-0S-8.7%	8.65	7.18	61	51.2	78
033-0S-9.3%	9.32	6.19	88	24.9	161

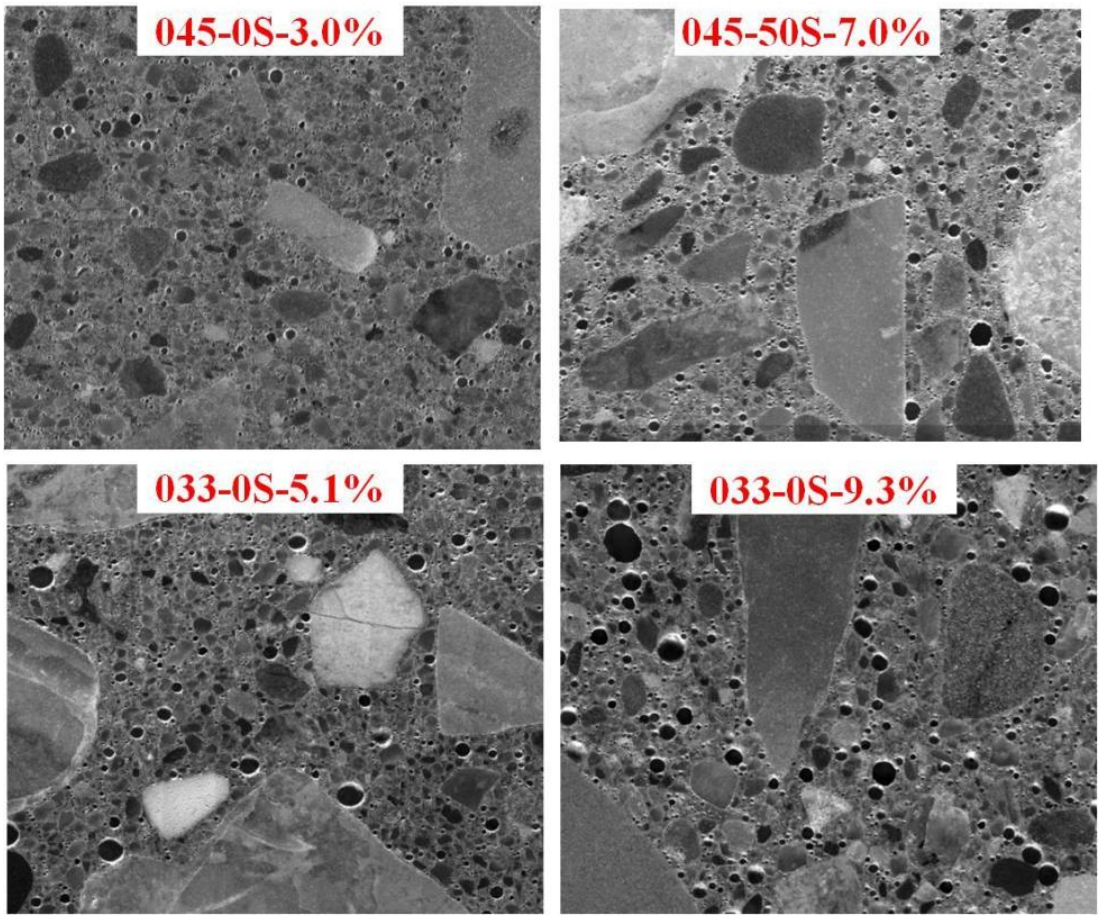

Figure 5.9 Typical air void profiles in air-entrained concrete

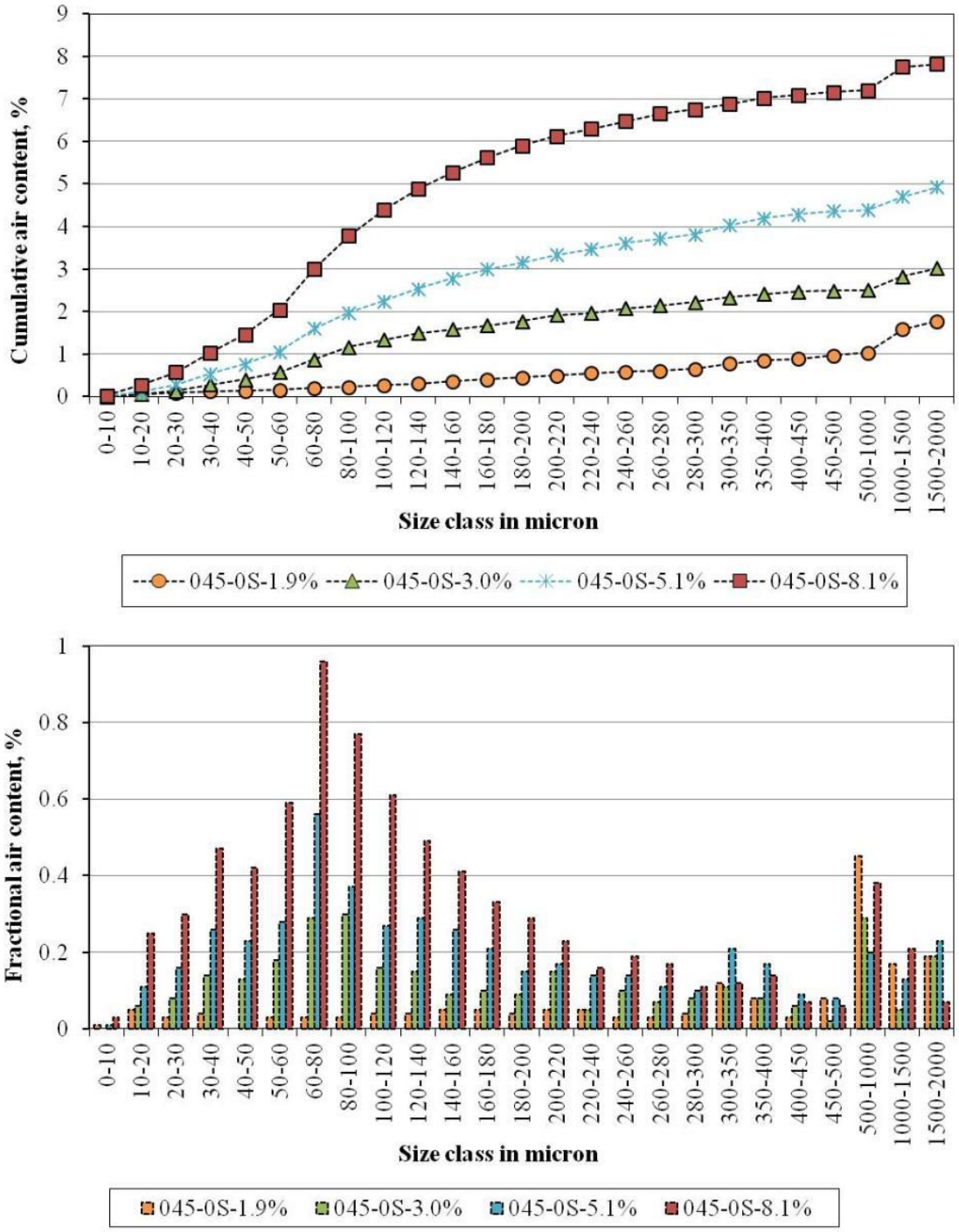

Figure 5.10 Typical air void distribution in air-entrained concrete

The internal frost durability reflected by the change in RDM is reported. No internal damage is noted in any of these mixes, except for the non-air entrained concrete mix with a Powers' spacing factor of 479 μm, as detected by the RDM with F-T cycles shown in Figure 5.11 for the

salt exposure condition. Microscopic examination of the 033-0S-2.5% mix further demonstrates the formation of cracking and the removal of coarse aggregate as a result of internal cracking (Figure 5.12), which leads to exacerbated mass loss (Figure 5.13). This is consistent with the requirement on critical spacing factor for regular frost resistance (200-250 μm) (Pigeon et al. 1996) and eliminates the interference of internal bulk cracking on the surface scaling and moisture uptake results.

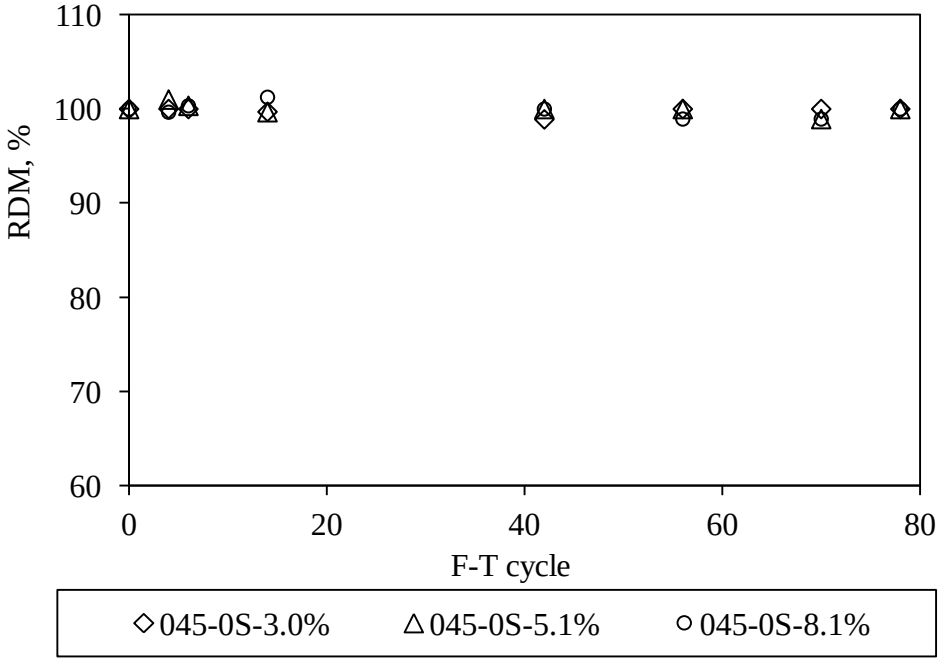

(a)

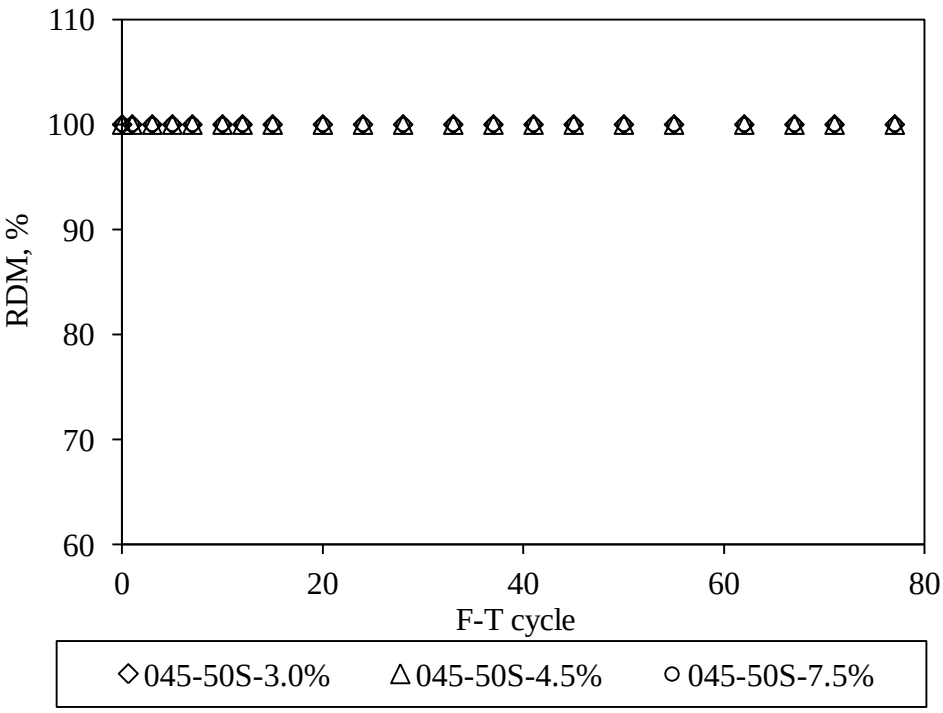
110
100
90
80
70
60
RDM, %
0
20
40
60
80
F-T cycle
045-50S-3.0%
045-50S-4.5%
045-50S-7.5%

(b)

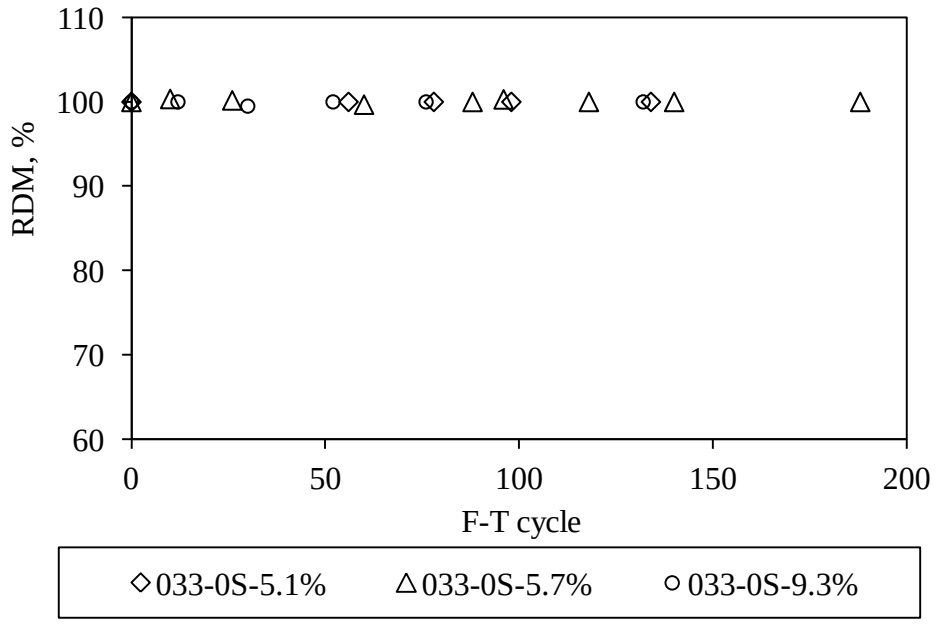
110
100
90
80
70
60
RDM, %
0
50
100
150
200
F-T cycle
033-0S-5.1%
033-0S-5.7%
033-0S-9.3%

(c)

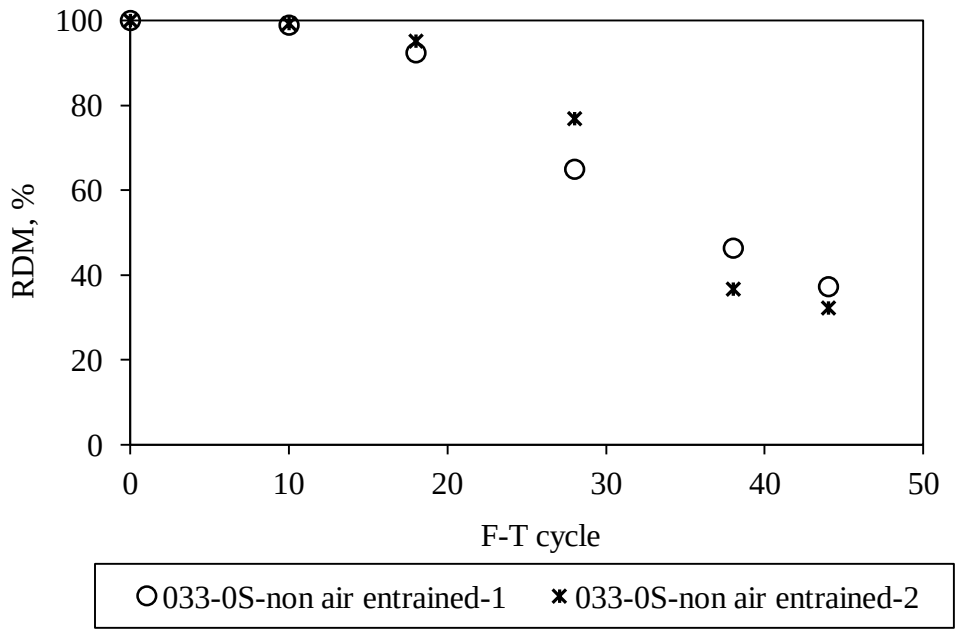

(d)

Figure 5.11 Measurement of internal damage in concrete mixes exposed to a 3% salt solution by the change in RDM

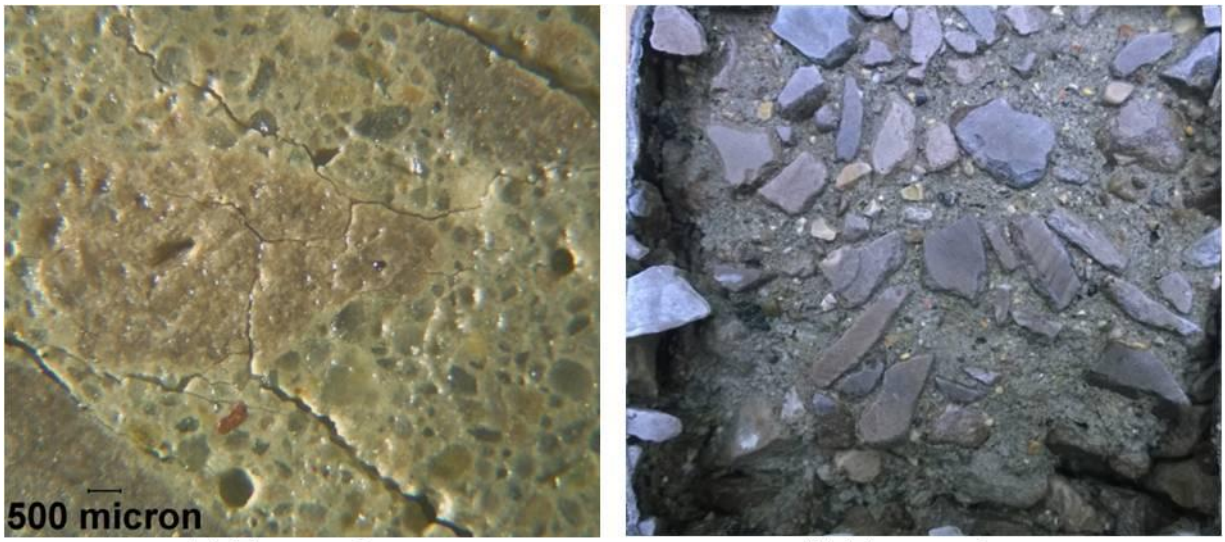

(a) Top surface (b) Test surface

Figure 5.12 (a) Crack formation on the top unexposed surface due to internal damage and (b) scaling surface profile of a non-air entrained concrete (033-0S-2.5%)

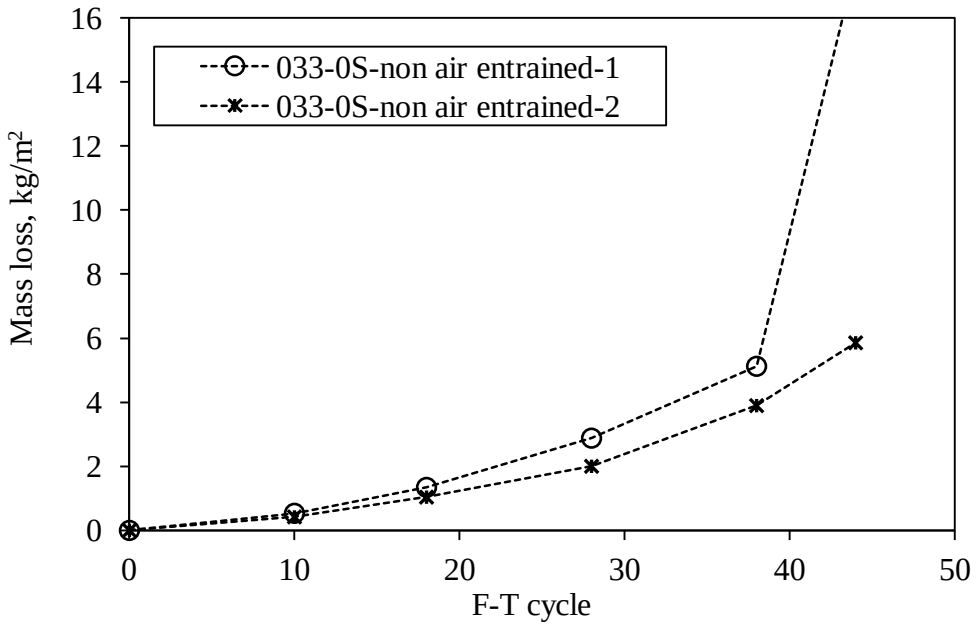

Figure 5.13 Mass loss in a non-air entrained concrete mix suffering internal damage

5.3.2 Surface scaling

The surface scaling results under water and 3% salt exposures are summarized in Figure 5.14 and the test surface profiles are shown in Figure 5.15 and Figure 5.16. The presence of salt in the surface liquid substantially amplifies scaling. In the case of salt exposure, there is a significant reduction in mass loss in concretes with 50% slag cement addition (045-50S) or with a lower w/b ratio (033-0S), compared with 045-0S. This is readily observed from the scaled surfaces at different F-T cycles. The collected scaled-off materials are mostly composed of cement paste and sand particles while the coarse aggregates remain in-situ. For a concrete system with the same w/b ratio or slag cement content, varying air content doesn't affect its scaling performance.

Furthermore, there is an almost linear development in mass loss with the progression of F-T cycles (Figure 5.14) in the case of 045-0S and 045-50S mixes, while a bi-linear pattern is noted for the 033-0S mix in the long term, which is separated by a breaking point after around 100 F-T cycles. This has been suggested to be associated with the change in degree of saturation in the specimens during continuous F-T exposure (Sellevold and Farstad 1991), as will be further explained in the following sections.

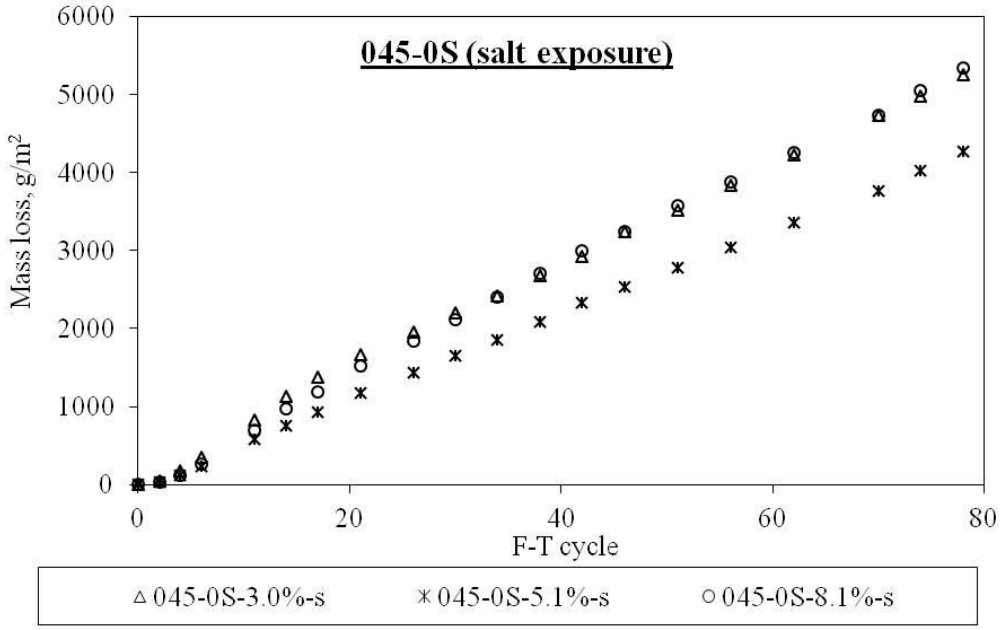
045-0S (salt exposure)
Mass loss, g/m2
6000
5000
4000
3000
2000
1000
0
0
20
40
60
80
F-T cycle
△ 045-0S-3.0%-s
✳ 045-0S-5.1%-s
○ 045-0S-8.1%-s

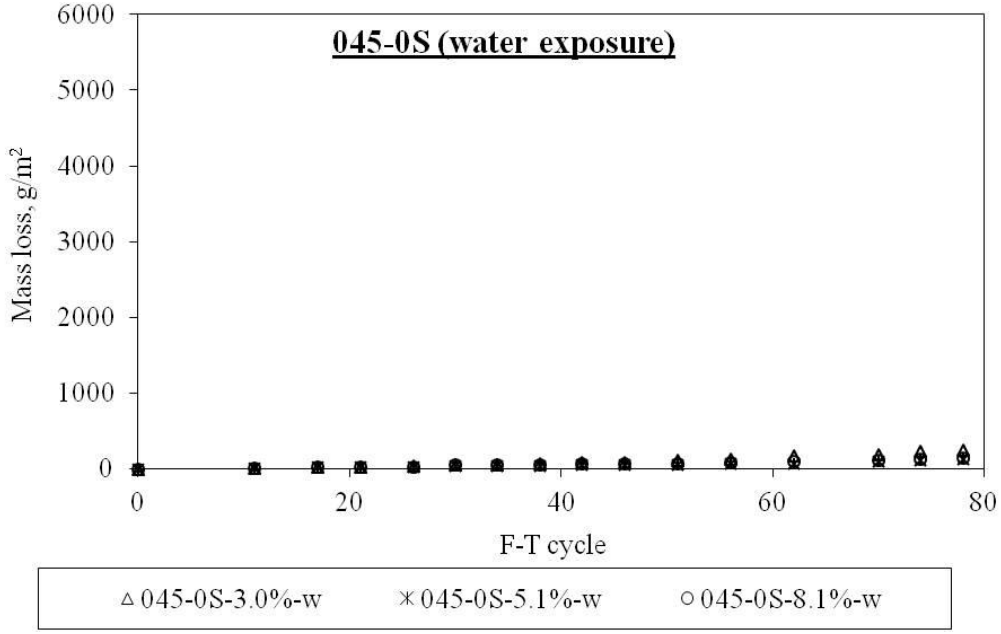
045-0S (water exposure)
Mass loss, g/m2
6000
5000
4000
3000
2000
1000
0
0
20
40
60
80
F-T cycle
△ 045-0S-3.0%-w
✳ 045-0S-5.1%-w
○ 045-0S-8.1%-w

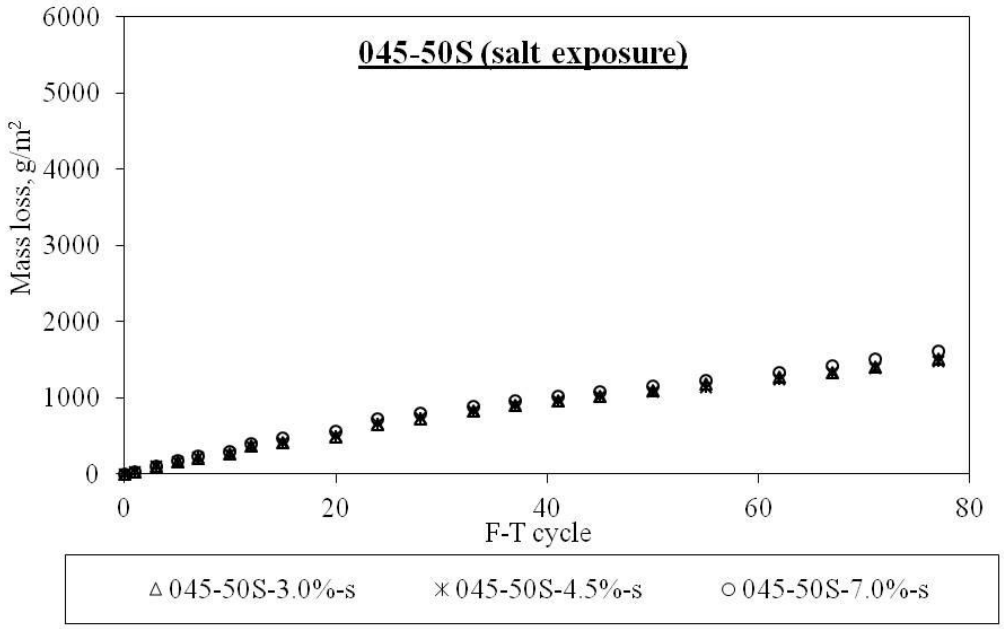
045-50S (salt exposure)
Mass loss, g/m2
6000
5000
4000
3000
2000
1000
0
0
20
40
60
80
F-T cycle
△ 045-50S-3.0%-s
✳ 045-50S-4.5%-s
○ 045-50S-7.0%-s

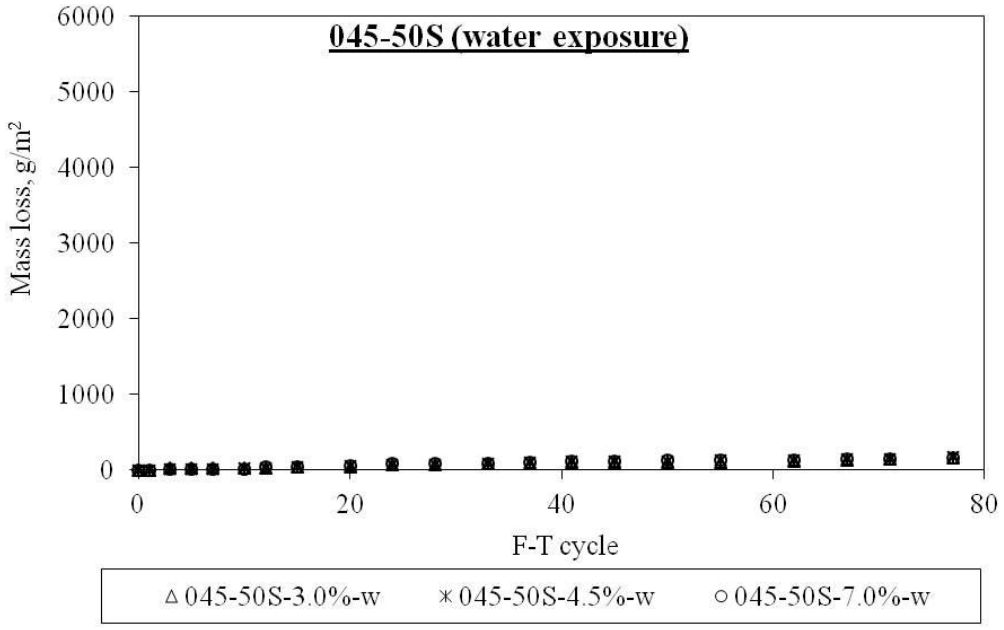
045-50S (water exposure)
Mass loss, g/m2
6000
5000
4000
3000
2000
1000
0
0
20
40
60
80
F-T cycle
△ 045-50S-3.0%-w
✳ 045-50S-4.5%-w
○ 045-50S-7.0%-w

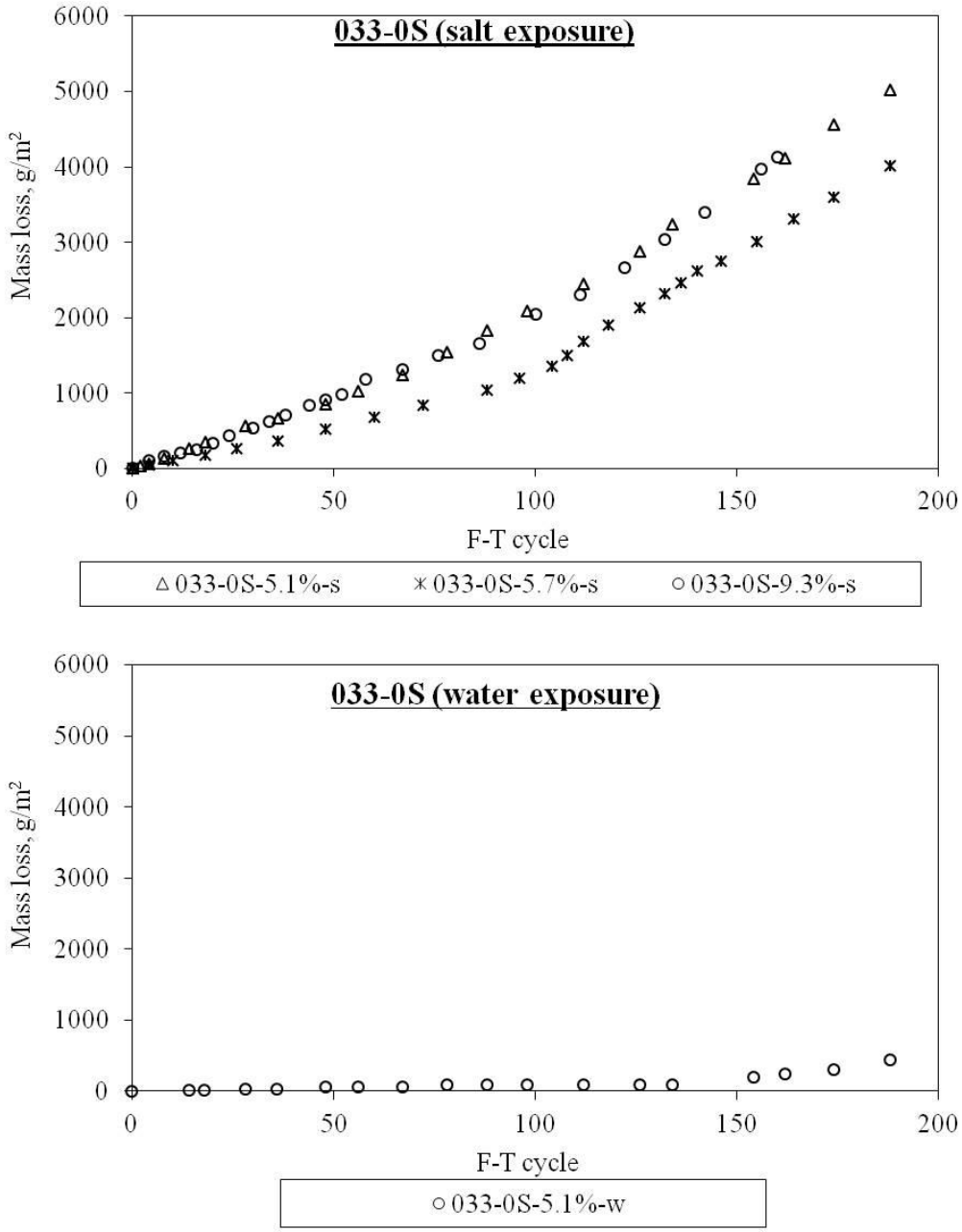

Figure 5.14 Mass loss with F-T cycles for different concrete mixes under water and salt exposures

(a) 045-0S-3.0% (salt exposure)

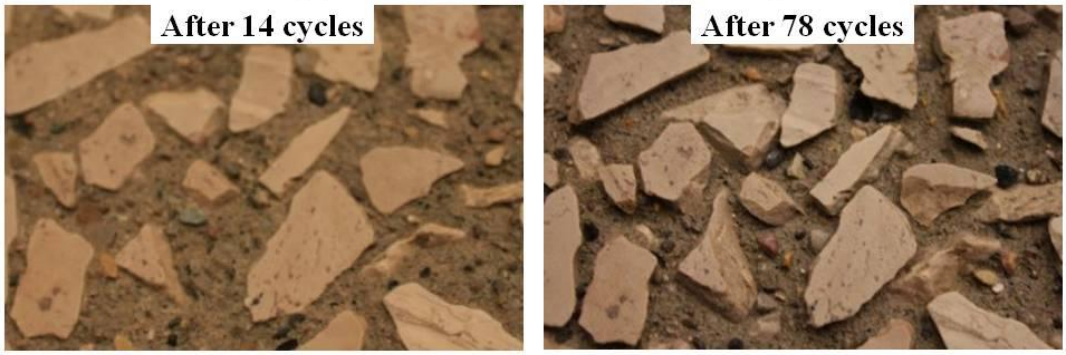

(b) 045-0S-5.1% (salt exposure)

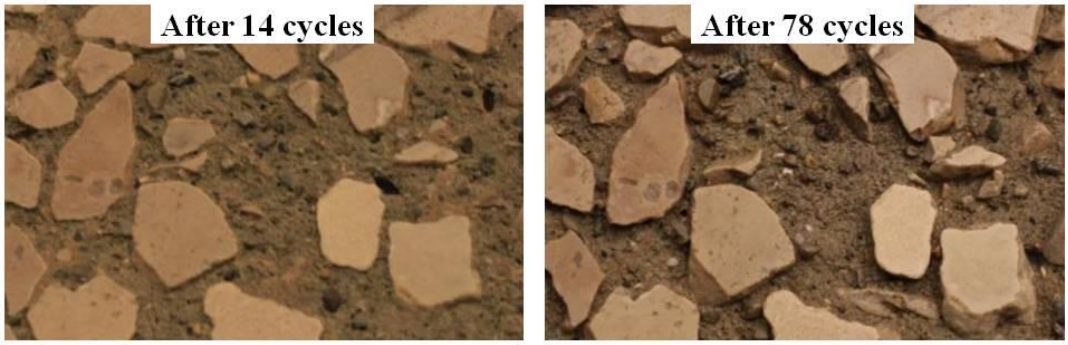

(c) 045-0S-8.1% (salt exposure)

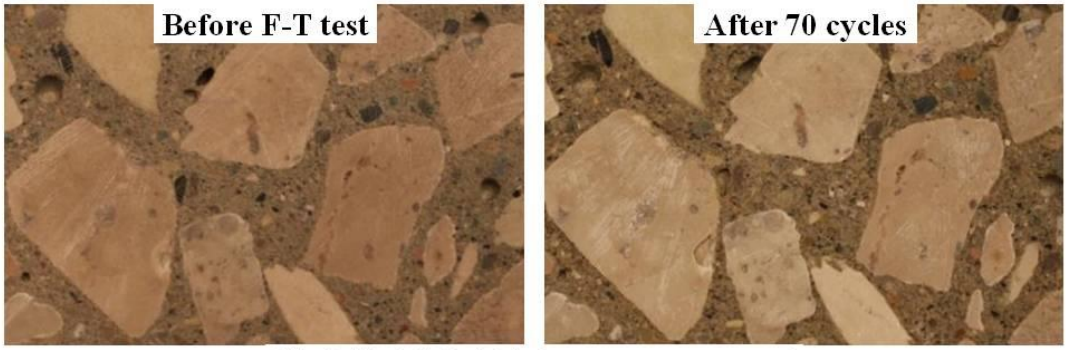

(d) 045-0S-8.1% (water exposure)

Figure 5.15 Scaled surface profiles under water and salt exposures (045-0S)

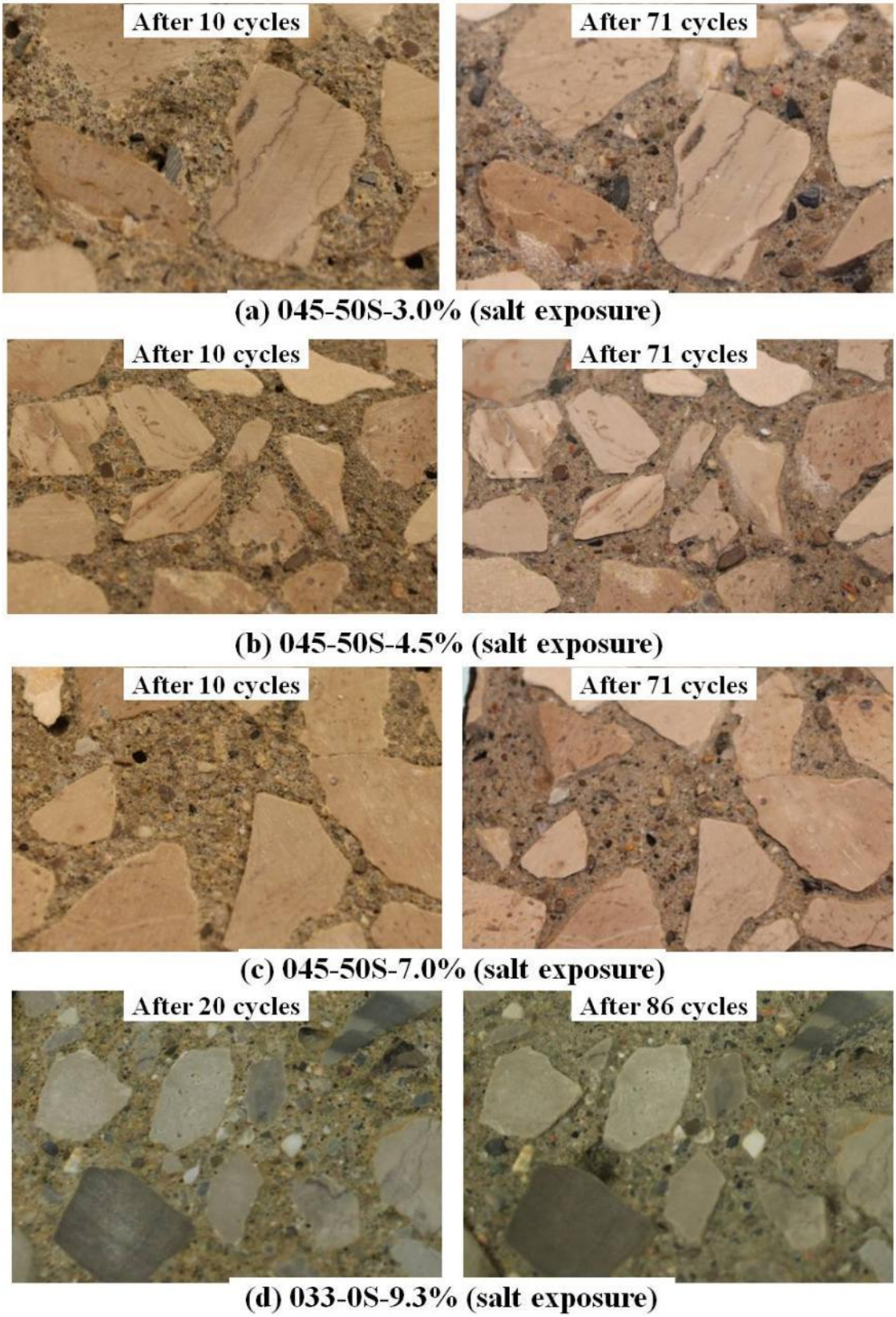

Figure 5.16 Scaled surface profiles under salt exposure (045-50S and 033-0S-9.3%)

5.4 Thermodynamic characterization of moisture flow in concrete under freezing

Freezing of water can be explained by the thermodynamic properties of the water due to the influence of temperature, pressure and special effects such as surface tension and salt solution. The equilibrium phase of the water is determined by the minimum of the partial Gibbs function (chemical potential) which we can write as

$$g = g_0 - \int s dT + \int v dP + \int \sigma dA + RT \ln y \quad (5\text{-}1)$$

g_0: Reference Gibbs function

g: Gibbs function due to the effect of surface tension and salt with a change in pressure and temperature

$-\int s dT + \int v dP$: Gibbs function change due to a change in pressure and temperature

$\int \sigma dA$: Effect of surface tension, the integral is evaluated from a cylindrical geometry neglecting the end effects which explains the variation with radius

$RT \ln y$: Effect of salt, y is the mole fraction of solvent. In the case of ice, y =1

The following three sections present the Gibbs function for water in two different forms with no consideration for the ionic effect (Borgnakke et al. 2012).

(1) Gibbs function for the solid phase

Using the standard IAPWS formulations for water, we can describe the Gibbs function for saturated solid water (ice) as a function of temperature and then add on the changes due to a higher pressure and a surface tension. For this we need the variation of the specific volume (or density ρ) which is

$$v_{sat\,T} = v_0(1 + \alpha T_C)^3 = 1/\rho \quad (5\text{-}2)$$

where α = 53 $\times 10^{-6}$ K^{-1}, v_0 = 0.0010908 m^3/kg and T_C is in degrees Celsius. The isothermal compressibility $\beta_T = -(1/v)(\frac{\partial v}{\partial P})_T$= 250 $\times 10^{-9}$ kPa^{-1} is then used to give

$$v_{solid} = v_{sat\,T}(1 - \beta_T(P - P_{sat\,T})) \quad (5\text{-}3)$$

The saturated Gibbs function at the saturated pressure is calculated using fundamental thermodynamic relations.

$$g_{sat\,T} = h_{sat\,T} - Ts_{sat\,T} \tag{5-4}$$

The final expression for the Gibbs function of ice in a pore of radius r is

$$g = g_{sat\,T} + v_{sat\,T}(P - P_{sat\,T})\left[1 - \frac{1}{2}\beta_T(P - P_{sat\,T})\right] + \sigma_{s-l}\frac{2v_{sat\,T}}{r} \tag{5-5}$$

where σ_{s-l} is the surface energy change when liquid is spread over the matrix surface. The surface tension is developed assuming there is a very thin layer of liquid covering the solid phase and the surface energy of the matrix-air is approximated to be equal to that of liquid-air (Lindmark 1998).

(2) Gibbs function for the liquid phase

A special treatment is done for the subcooled liquid, which is not an equilibrium state for pure bulk liquid water, and this was developed by (Pátek et al. 2009). Liquid at P_0=100 kPa was curve fitted as a polynomial in temperature which we then correct for the actual pressure and the presence of a surface tension and a salt solution.

The Gibbs function for the pure bulk liquid water is expressed as:

$$g_{liq\,T,P_0} = RT_R(c_1 + c_2\tau + c_3\tau\ln\tau + \sum_{i=1}^{3} a_i\alpha^{n_i} + \sum_{i=1}^{4} b_i\beta^{m_i}) \tag{5-6}$$

where R=461.51805 J kg^{-1}K^{-1}, T_R=10K, dimensionless coefficients a_i, b_i, c_i, n_i, and m_i are tabulated. Dimensionless temperature coefficients

$$\tau = \frac{T}{T_R}, \alpha = \frac{T_R}{T_a - T}, \beta = \frac{T_R}{T - T_b} \tag{5-7}$$

where T_a=593K, T_b=232K, which is the valid range of application.

The correction for liquid water at pressure P different from 100kPa is realized by using an approximated relation:

$$g \approx g_{P_0} + v_{l0}(P - P_0) \tag{5-8}$$

For a salt solution in a pore of radius r, the Gibbs function is the form of the following:

$$g = g_{liq\,T,P} + \sigma_{l-v}\frac{2v_{l0}}{r} + RT\ln y \tag{5-9}$$

It can be seen in Figure 5.17(a) that the freezing of liquid in concrete pores is a gradual process with ice formed first in larger pores, where the effect of surface tension is less significant and the

Gibbs free energy of ice is much lower than water; in addition, water in pores less than 10 nm (mostly gel pores) stays unfrozen at -20 ℃ due to the strong surface tension, which indicates that gel pore system is an crucial source of liquid to promote ice accretion (Powers and Helmuth 1953, Pickett 1953). It is noted in Figure 5.17(b) that a Gibbs free energy reduction in water and ice is observed with temperature decrease and the reduction rate is much faster in ice than water, which enhances the driving potential of the spontaneous liquid transport.

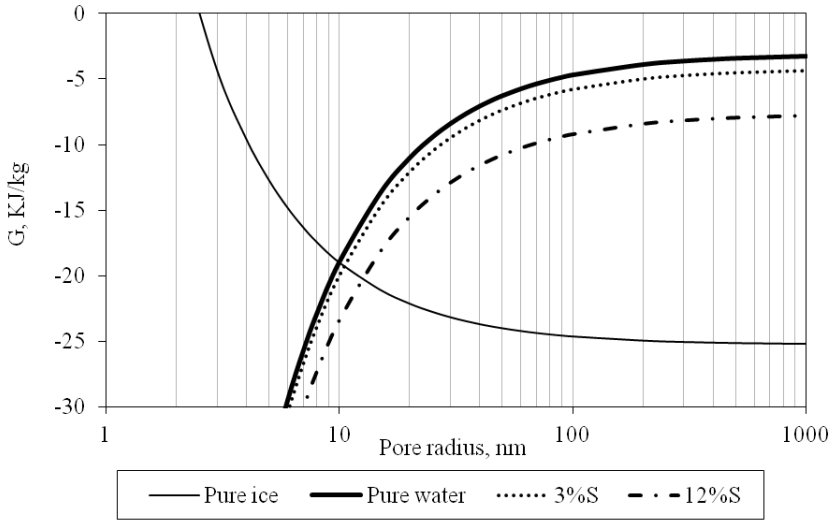

(a)

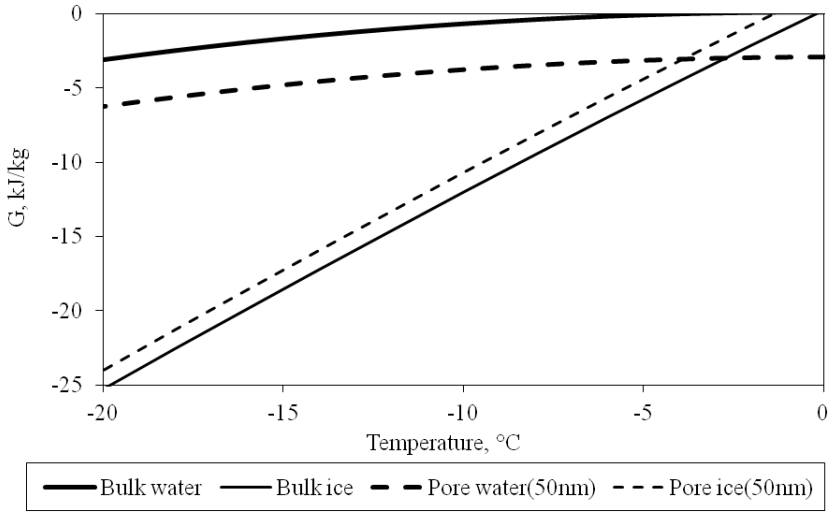

(b)

Figure 5.17 Gibbs free energy of water and ice as a function of (a) pore size at -20 ℃ and (b) temperature

The following two sections deal with the salient features of the length change measurements with our own interpretation in order to confirm that the added cryogenic suction into concrete from its surface is the major factor in salt frost deterioration. We have no intension to claim complete originality for some of the ideas presented herein. As a matter of fact, our work is built upon those previous theories (Powers and Helmuth 1953, Lindmark 1998, Bager and Jacobsen 1999).

5.5 Length-change measurement to characterize moisture flow in concrete under freezing

Moisture flow in a porous body towards the sites of ice formation under freezing has long been identified as the main cause of frost heave (macro ice lens, Taber 1930, Blanchard and Frémond 1982) and also an important addition to the well-known hydraulic pressure hypothesis (HPH) to account for the frost damage of concrete (Micro ice segregation, Powers 1945, Powers and Helmuth 1953). The driving force behind this liquid transport lies in the Gibbs free energy difference between ice and unfrozen water that is facilitated by the wide distribution of pore size and the presence of dissolved salt (Powers and Helmuth 1953, Pickett 1953, Helmuth 1960, Everett 1961, MacInnis and Whiting 1979, Harnik et al 1980).

Experimentally it is not practical to monitor the moisture movement in concrete during freezing. However, this moisture redistribution and the concomitant ice accretion can lead to volumetric deformation: shrinkage due to pore drying and dilation due to unaccommodated ice growth, and the net deformation depends on the relative magnitude of the two effects (Powers 1945, Powers and Helmuth 1953, Fridh 2005). Thus, simultaneous measurement of the uniaxial length change and the temperature profile during a F-T cycle, which has been extensively used in the laboratory to study frost damage (Powers and Helmuth 1953, Fagerlund 1992, Fridh 2005, Penttala and Al-Neshawy 2002, Kaufmann 2004, Litvan 1975, MacInnis and Whiting, 1979, Sun and Scherer 2010, Bager 2000), is empolyed in this investigation.

In our work, the length change of a $90 \times 10 \times 10$ mm prism is monitored for 1-3 freezing-thawing cycles, in addition to the conventional mass loss measurement. In order to retain liquid on the surface of the small specimen, saturated sponge pads were placed on the top surface of the specimen while the other surfaces were kept wet due to the dripping from the sponge pads, then the specimen was wrapped up by a plastic foil before test. As a result, the deformation along the cross-section of the specimen is almost uniform without the need to consider warping. This is confirmed by visual examination of the specimen surfaces before and after 3 F-T cycles (Figure

5.18). All the lateral surfaces demonstrate equally severe scaling damage and only some minor deterioration occurs on the two end surfaces which are not covered by the wrapping and thus have reduced moisture content due to evaporation.

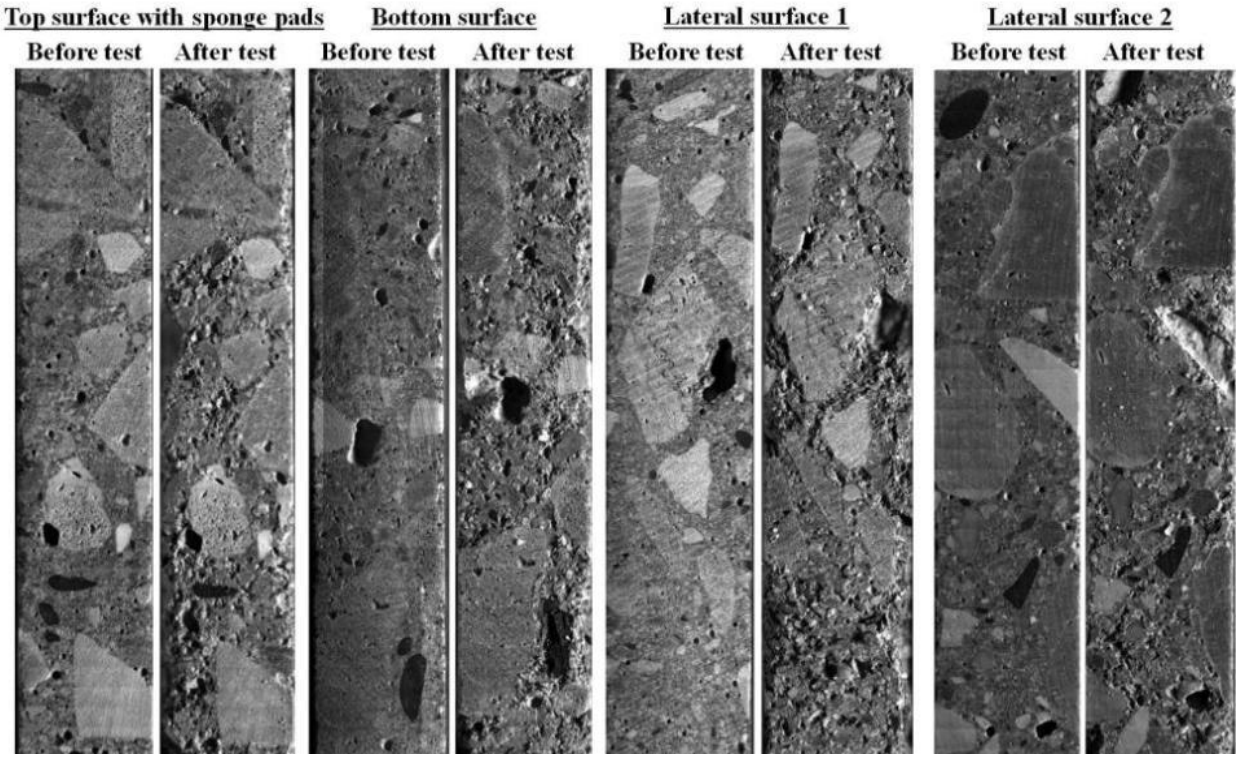

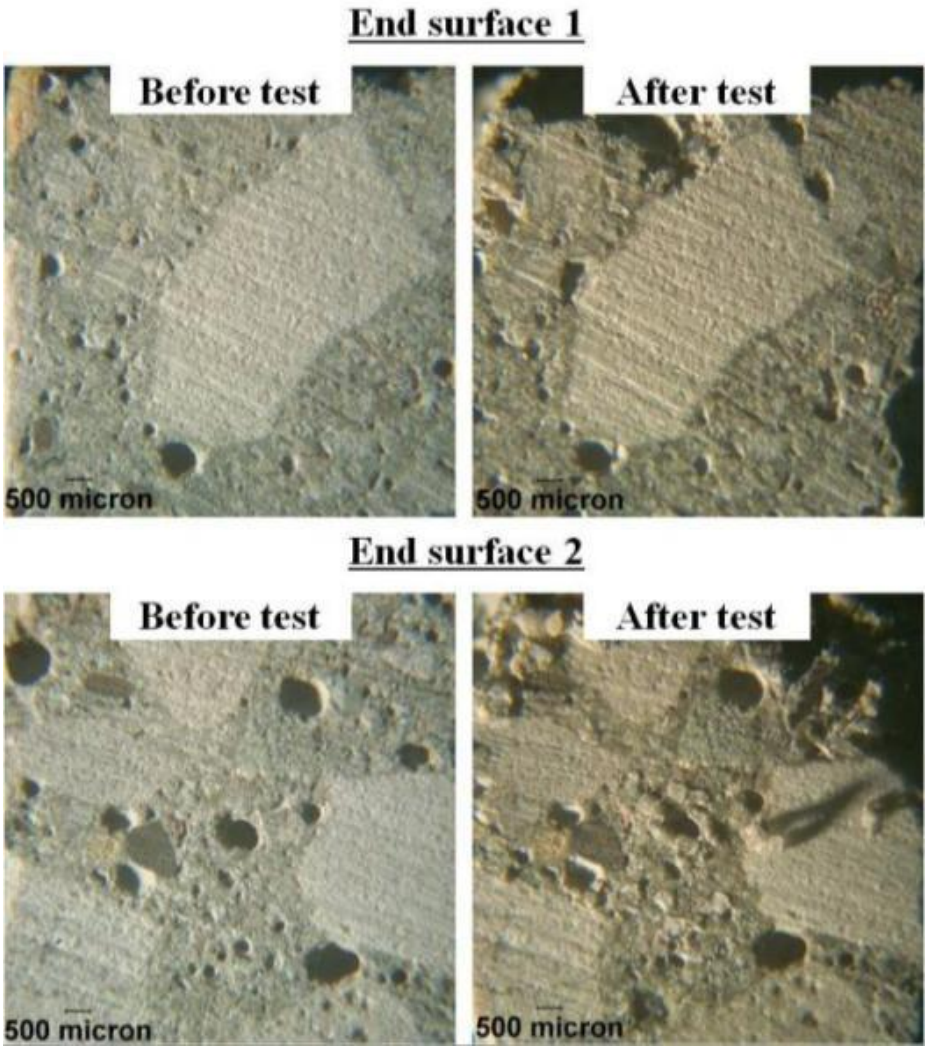

Figure 5.18 Surface profile before and after test in a LTD test under salt exposure (045-0S-3.0%)

5.6 Freezing deformation in concrete with no surface liquid

In a pre-wetted cementitious material (paste, mortar or concrete) under freezing, ice body growth occurs in pores or voids of the cementitious matrix once nucleation commences which is associated with the spontaneous movement of unfrozen water to the micro ice bodies (Powers and Helmuth 1953, Pickett 1953, Everett 1961). This typically leads to two scenarios of volumetric deformation.

- If the material is adequately air entrained with low degree of void filling, shrinkage occurs more than can be accounted for by the thermal contraction alone, which is known as “pore drying” (Fridh 2005) or “desiccation of paste” (Powers and Helmuth 1953).

- If the material is non-air entrained or most of its air voids have been saturated, significant secondary dilation occurs, since it reaches a critical degree of saturation and there is no sufficient space to accommodate the continuous ice accretion.

This is clearly shown in the length-change measurement on a concrete specimen with an air content of 8.1% at different levels of air void saturation (Figure 5.19 and Figure 5.20). The initial dilation is a result of the hydraulic pressure due to the instant ice nucleation upon termination of supercooling, which is accompanied by a temperature rise caused by the release of latent heat of fusion (Powers and Helmuth 1953). It is increased gradually with the degree of saturation in air voids (Figure 5.21). The added shrinkage strain is noted in the first three saturation points when the unfilled air voids are still able to provide room for the ice growth without causing expansion (Figure 5.22(a)). After reaching a critical saturation point, the continuous ice body growth starts to create pore pressure buildup that leads to excessive secondary dilation (Figure 5.20(d) and Figure 5.22(b)).

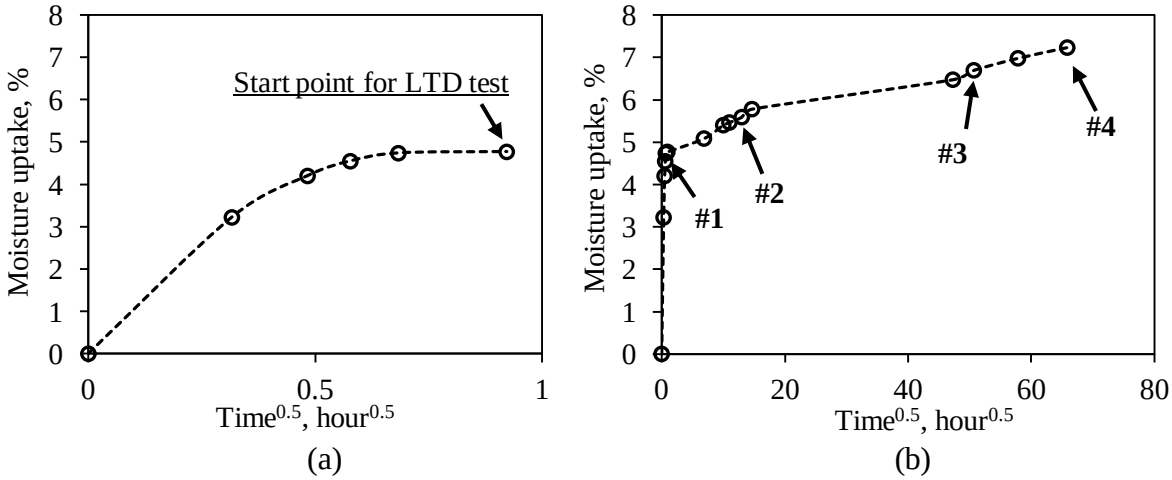

Figure 5.19 Moisture uptake during presaturation. (a) Moisture uptake up to the first test point that is a little beyond the nick point indicating capillary pore saturation and the start of slow filling of air voids (Fagerlund 2004); (b) continuous moisture uptake due to gradual air void filling

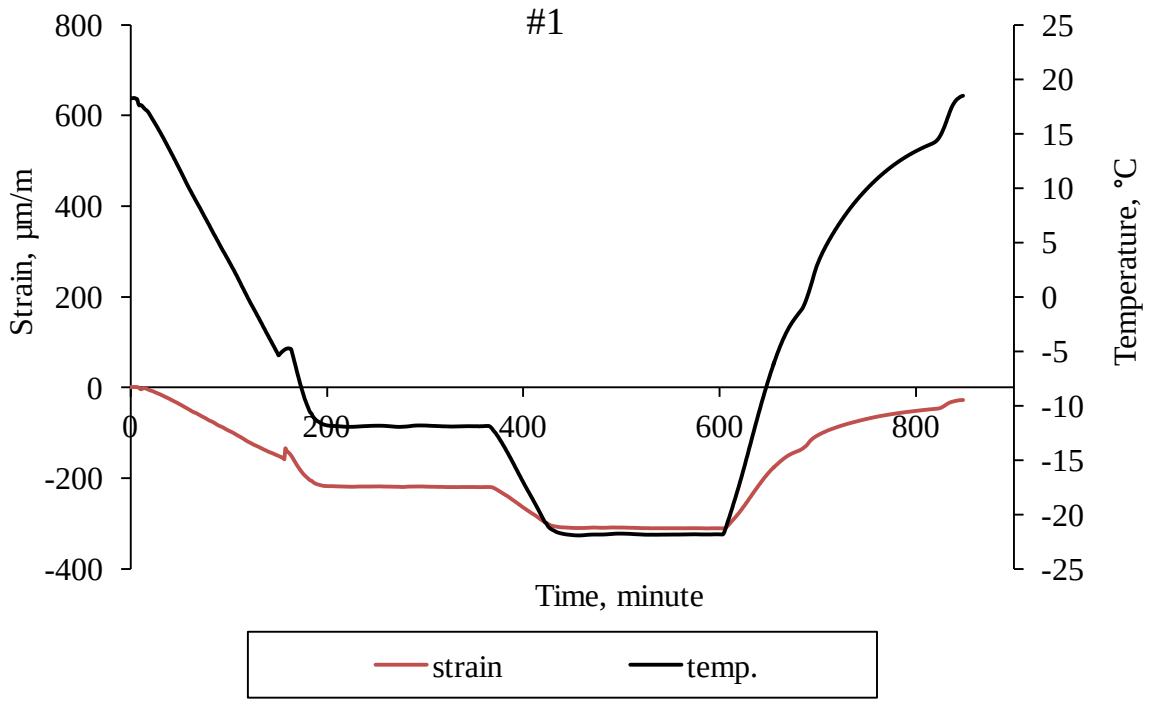
#1
800
600
400
200
0
-200
-400
Strain, μm/m
25
20
15
10
5
0
-5
-10
-15
-20
-25
Temperature, °C
0
200
400
600
800
Time, minute
strain
temp.

(a)

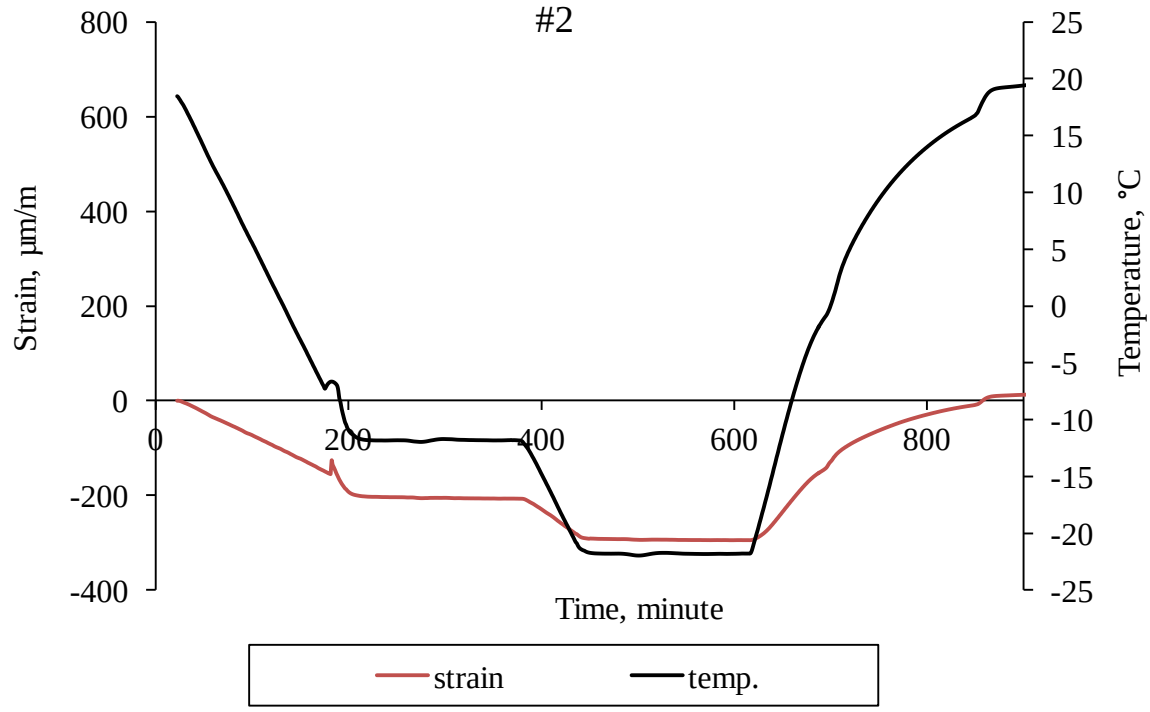
#2
800
600
400
200
0
-200
-400
Strain, μm/m
25
20
15
10
5
0
-5
-10
-15
-20
-25
Temperature, °C
0
200
400
600
800
Time, minute
strain
temp.

(b)

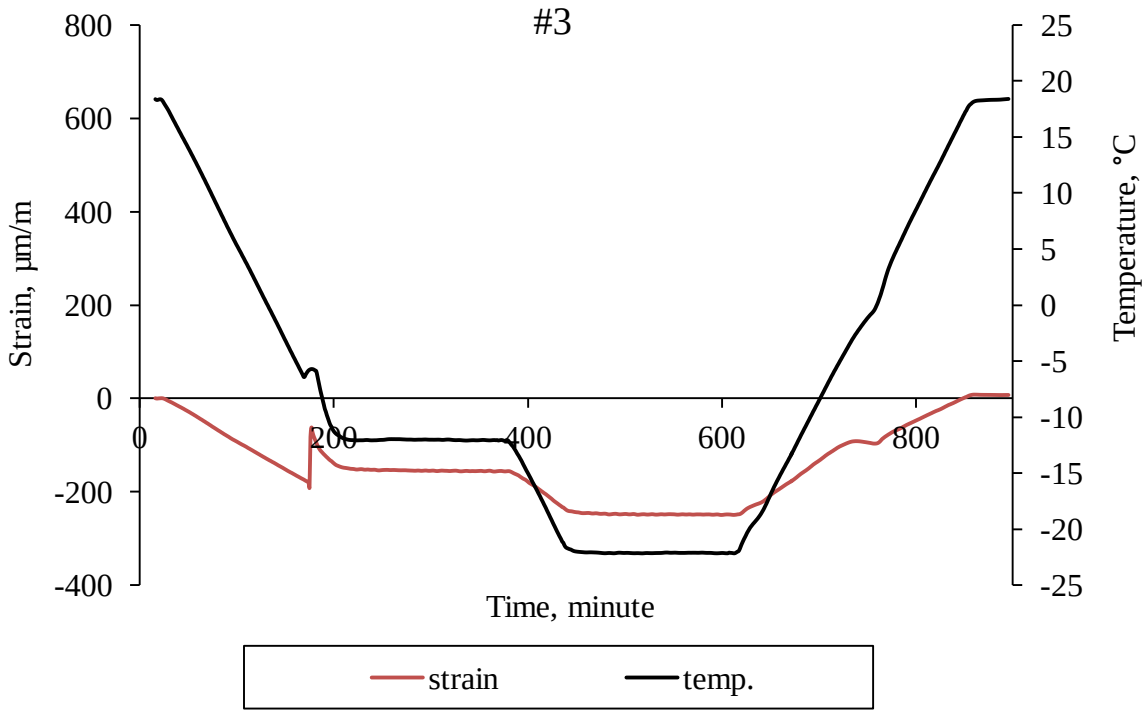

(c)

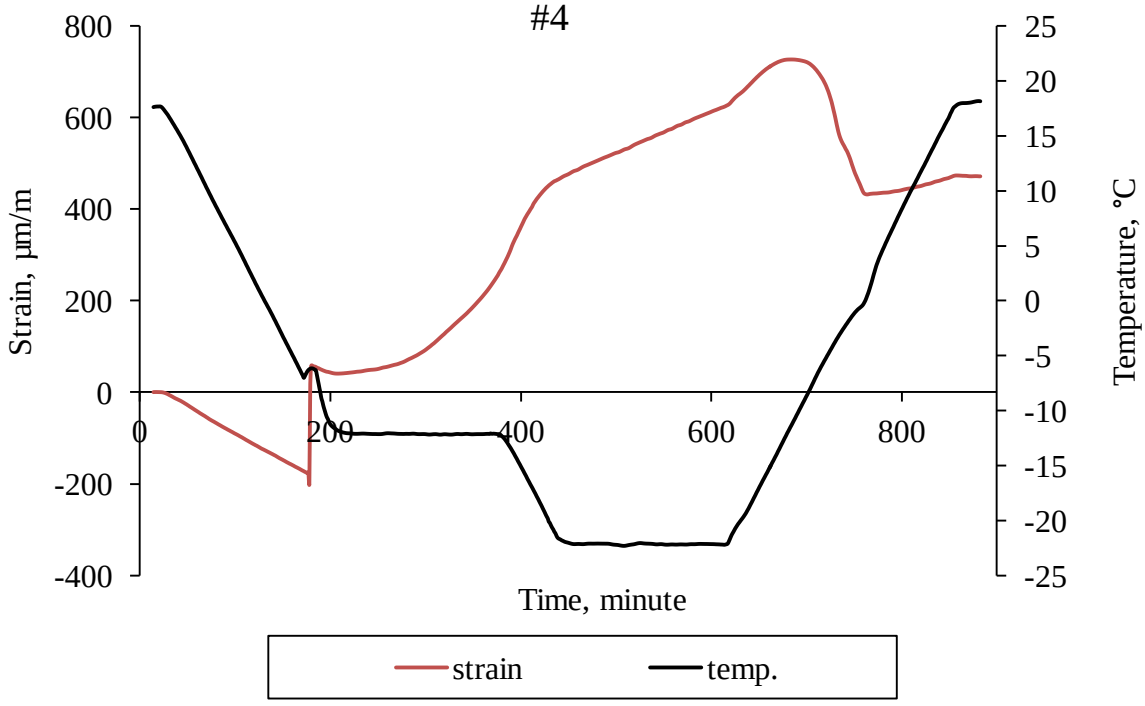

(d)

Figure 5.20 Length and temperature change with time in concrete specimens under different degrees of air void saturation

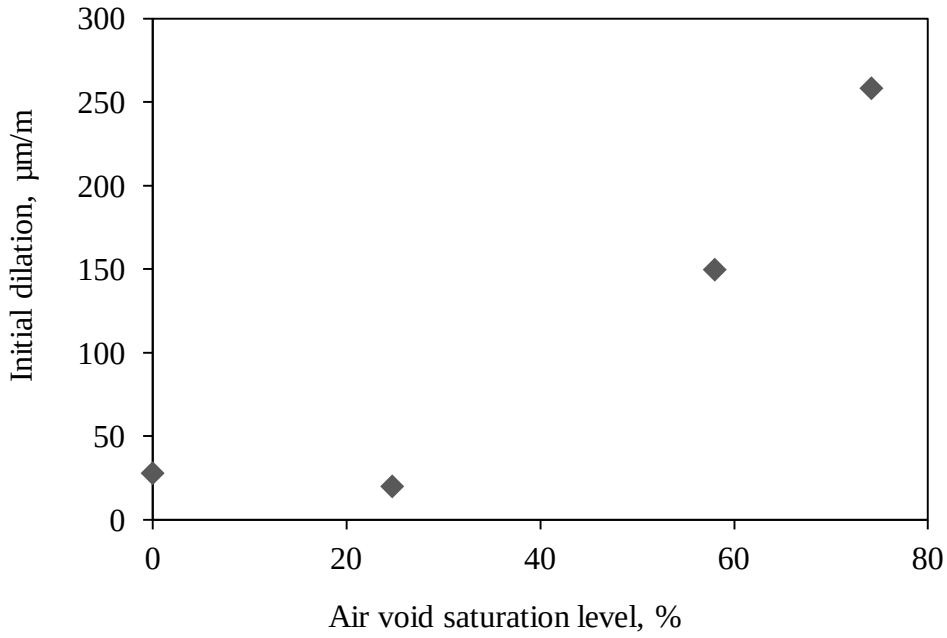

Figure 5.21 Effect of air void saturation level on the initial dilation

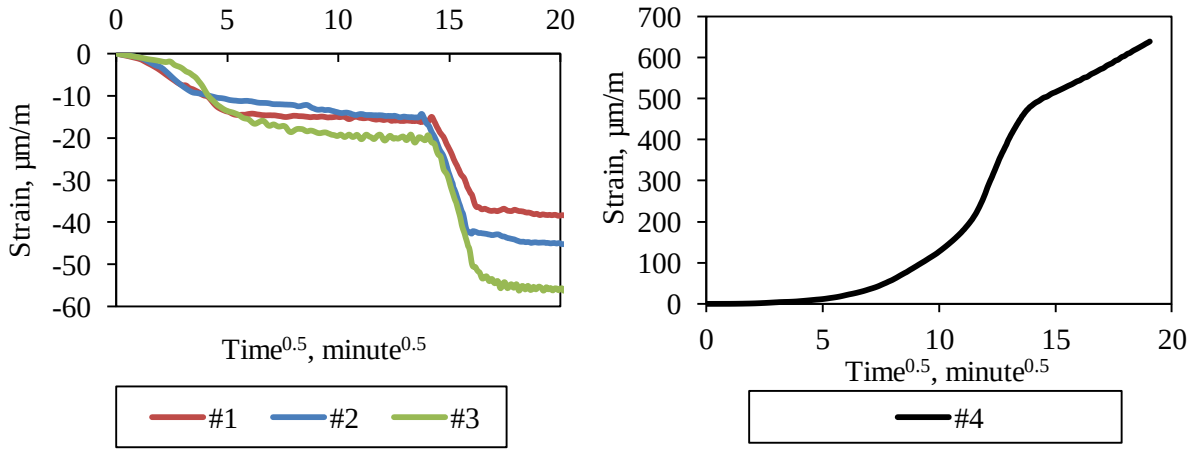

Figure 5.22 The added freezing strain by accounting for the thermal contraction of the concrete specimen (045-0S-8.1%) under prolonged water saturation (no surface liquid present)

5.7 Added dilation by cryogenic suction of unfrozen surface liquid under salt exposure

In Figure 5.23(a), a similar secondary dilation is noted even in an adequately air entrained concrete specimen (045-0S-3.0% with a Powers' spacing factor of 135 µm) that is only capillary saturated before the test, when it is exposed to a 3% salt solution. Meanwhile, added shrinkage occurs under water exposure, since all the surface liquid is frozen when reaching the freezing point, resembling a surface dry condition.

However, in the case of salt exposure, additional unfrozen liquid is still present on the surface due to the unique feature of freezing a salt solution: a mixture of solid ice and liquid brine co-exists as long as its temperature stays between the freezing and eutectic point (Lindmark 1998, Weissenberger et al. 1992). Upon instant ice nucleation, transient expansion of capillary pores occurs which creates an unsaturated pore condition and triggers cryogenic suction. The additional external liquid will be drawn into the surface region, which counteracts pore drying and amplifies continuous ice growth therein (Lindmark 1998). This causes specimen shrinkage within the bulk and expansion within a narrow surface region (Bager and Jacobsen 1999). The extensive dilation under the 3% salt exposure condition indicating a rapid liquid transport process, when combined with the linear development of the freezing strain with the square root of time at different temperature regimes (Figure 5.23(b)), confirms that cryogenic suction is the primary transport mechanism in concrete in contact with a salt solution during an F-T cycle.

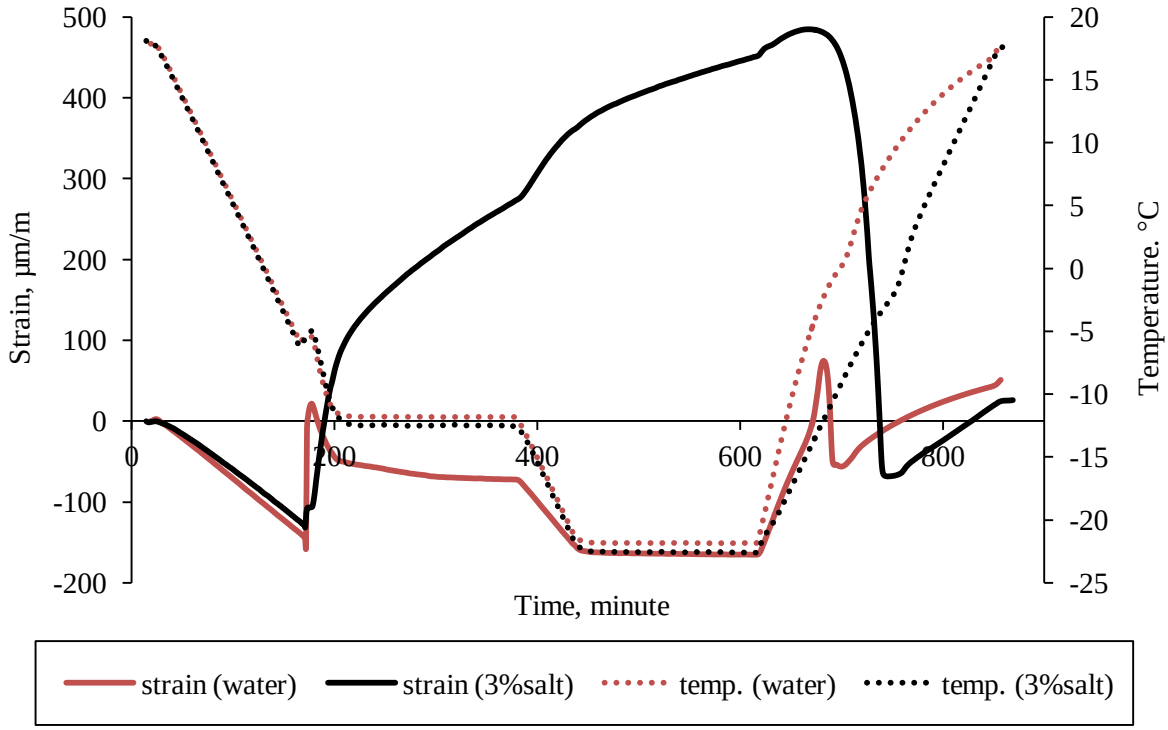

(a) Length & temperature change with time

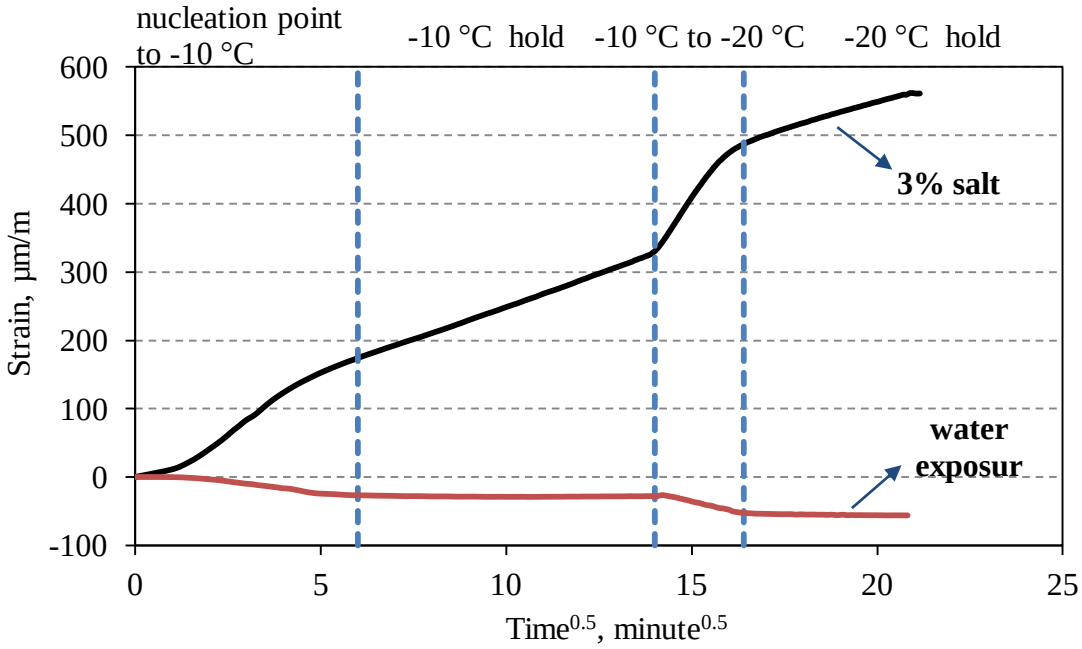

(b) Isothermal freezing strain vs. the square root of time

Figure 5.23 Length-change measurement on a concrete specimen exposed to water and a 3% salt solution, respectively (045-0S-3.0%)

From a practical point of view, this additional unfrozen liquid can be more readily realized in the field. The application of de-icing agent always follows extensive snow precipitation or severe ice formation while concrete surface is under freezing. The de-icing agent will melt the snow and ice, thus providing extra surface moisture (Cordon 1966). This is worsened when poor drainage condition exists in a pavement joint that entraps liquid (Hansen and Yang 2010). Another possible contribution of moisture-uptake may come from early freezing and the thawing periods in several ways (Bager 2000) and this is explained with the aid of Figure 5.24: (1) Pore water in #3 freezes preceding that farther away from the surface (#1 and #2), inducing moisture transport towards #3; (2) surface ice melts prior to pore ice in some small capillary pores, causing moisture flow into those remaining frozen sites; (3) The melting of pore ice causes a relaxation of the porous matrix, which in turn sucks liquid from the surface and increases the degree of saturation before next F-T cycle. The temperature distribution in locations of a dummy concrete specimen is measured and shown in Figure 5.24. It verifies the existence of a temperature gradient along the depth of the specimen. At the same time, it shows that the span of time for step (1) and (2) is relatively brief (less than 30 minutes) while it has sufficient time for step (3) to take place. However, this process may contribute only to the global moisture uptake, as has been

shown in Chapter 4 that the bulk absorption, although accelerated under F-T, is similar between water and salt exposure, while the mass loss is quite different. Moreover, there is no dilation occurring during thawing in the length-change measurement under either exposure conditions (Figure 5.23(a)). Thus, the moisture absorption due to the sequence of ice formation or melting is not a factor for scaling.

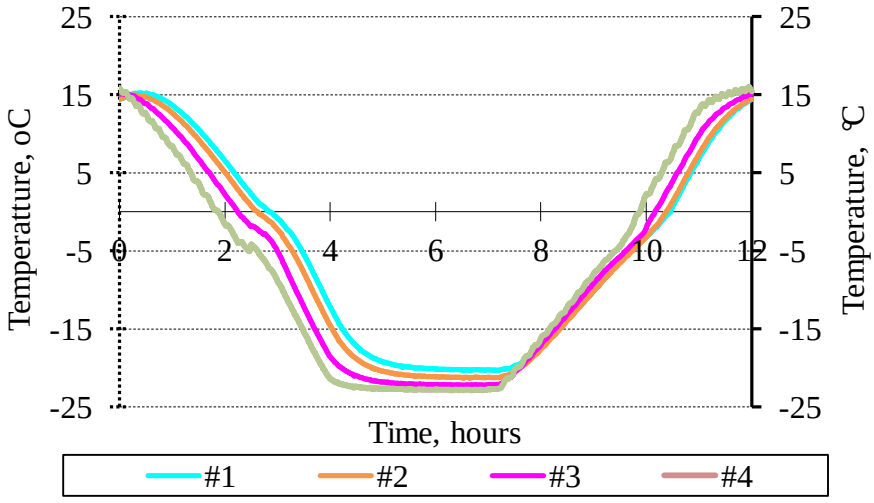

(a)

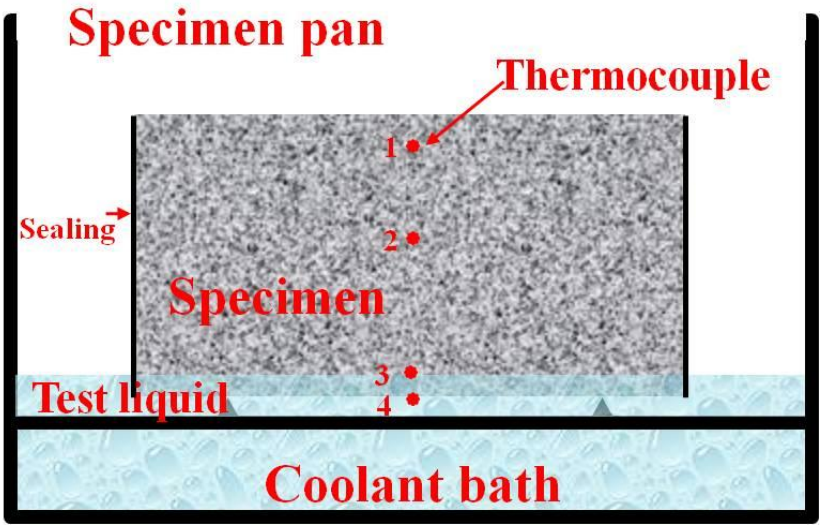

(b)

Figure 5.24 Temperature measurement in RILEM CIF test specimen at different locations

In order to provide more insight into what happens at each step of an F-T cycle, a detailed breakdown of the length change process with temperature is presented on the water-presaturated specimen with and without 3% salt on surface in Figure 5.25, followed by a tabulated comparative description of the two cases (Table 5.3).

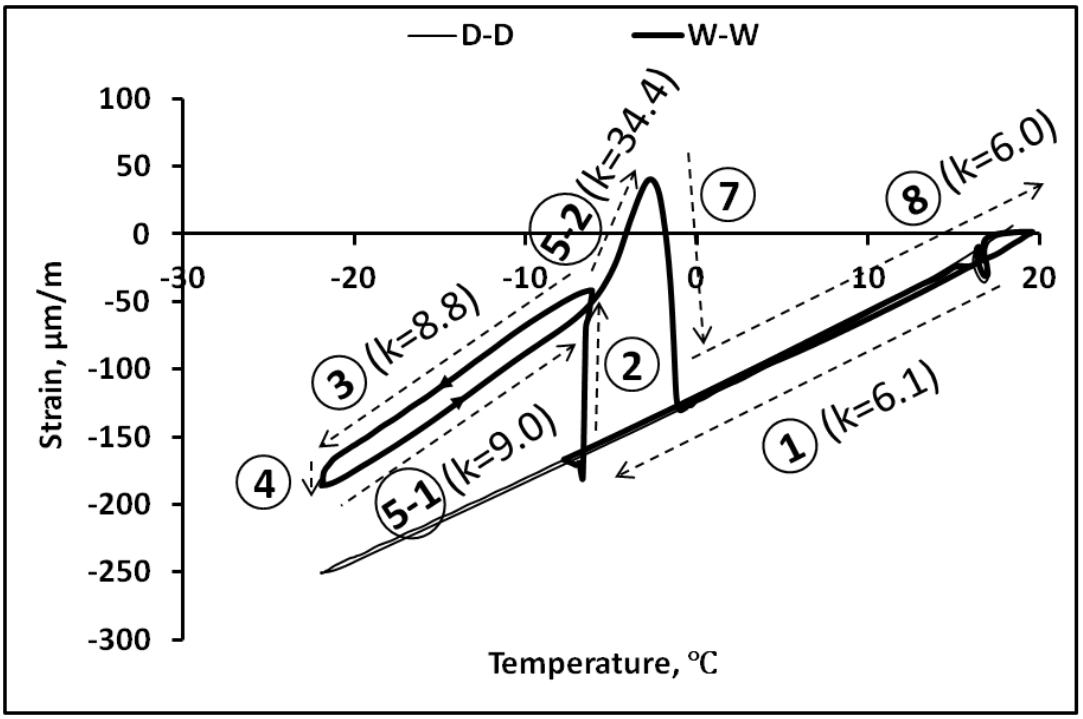

(a) dry surface

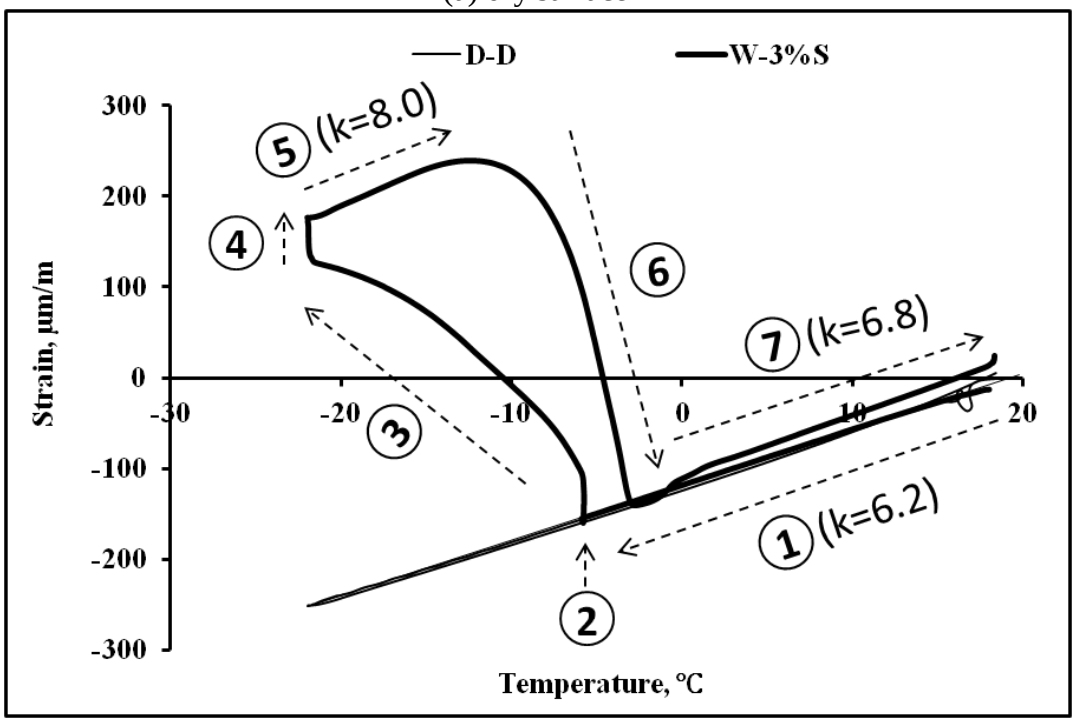

(b) 3% salt on surface

Figure 5.25 A breakdown of the length change process (*k denotes the length change rate*)

Table 5.3 Detailed description of length change steps

<table>
<tr><th colspan="2" rowspan="2">Step</th><th colspan="3">Description</th></tr>
<tr><th colspan="2">Water saturation-water on the surface</th><th>Water saturation-3%salt on the surface</th></tr>
<tr><td>1</td><td>20 ℃-nucleation point</td><td colspan="3">Linear thermal contraction close to that of the dry concrete.</td></tr>
<tr><td>2</td><td>At nucleation point</td><td colspan="3">Initial dilation due to the rapid ice formation in concrete pores as a result of the supercooling, augmented by ice formation on the surface. The amount of ice formation is higher and the bonding of ice layer with concrete surface is stronger in the case of pure water, leading to higher initial dilation.</td></tr>
<tr><td>3</td><td>Nucleation point to -20 ℃</td><td colspan="2">Shrinkage due to the coupling effect of thermal contraction of solid matrix and ice, and pore drying caused by the migration of liquid towards the frozen sites.</td><td>Secondary dilation due to the internal pressure build-up caused by the continuous growth of ice bodies by the cryogenic suction of surface liquid.</td></tr>
<tr><td>4</td><td>Isothermal range (-20 ℃)</td><td colspan="2">Isothermal shrinkage due to the persistent pore drying.</td><td>Isothermal dilation similar to step 3. Magnitude is suppressed possibly due to the diminishing amount of surface liquid available and the reduced liquid transport rate caused by the pore blockage from ice formation and a reduced difference in Gibbs free energy.</td></tr>
<tr><td rowspan="2">5</td><td rowspan="2">-20 ℃-melting point</td><td>5-1</td><td>Ice in concrete pores and on the surface expands to the original volume. Meanwhile, some of the pore ice under high pressure starts melting, causing shrinkage.</td><td rowspan="2">Concrete has been saturated completely or partially due to the added moisture flow. Some of the air voids have been filled with ice whose thermal expansion is much bigger than the matrix.</td></tr>
<tr><td>5-2</td><td>Ice in concrete pores and on the surface starts causing dilation of the concrete, coupled with the thermal expansion of the matrix.</td></tr>
<tr><td>6</td><td>Melting range</td><td colspan="3">Most of the ice crystals start melting, causing a redistribution of the moisture and a relaxation in strains.</td></tr>
<tr><td>7</td><td>End of melting range to 20 ℃</td><td colspan="3">Linear thermal expansion with a length change rate close to the initial thermal shrinkage.</td></tr>
</table>

5.8 Cryogenic suction mechanism for salt frost scaling

5.8.1 Pore damage associated with continuous ice growth under salt exposure

The observed swelling of the whole paste around the periphery of coarse aggregates shown in Figure 5.5 is sound evidence of excessive pore pressure buildup beneath concrete surface. This is further substantiated by an apparent volume increase of 50%-100% in the mortar flakes for all size classes, compared to the control mortar (Figure 5.26). This suggests pore pressure buildup occurs in the capillary pore system of the surface region. These results are also consistent with the length-change measurement on small-scale concrete prisms, as shown in Figure 5.23.

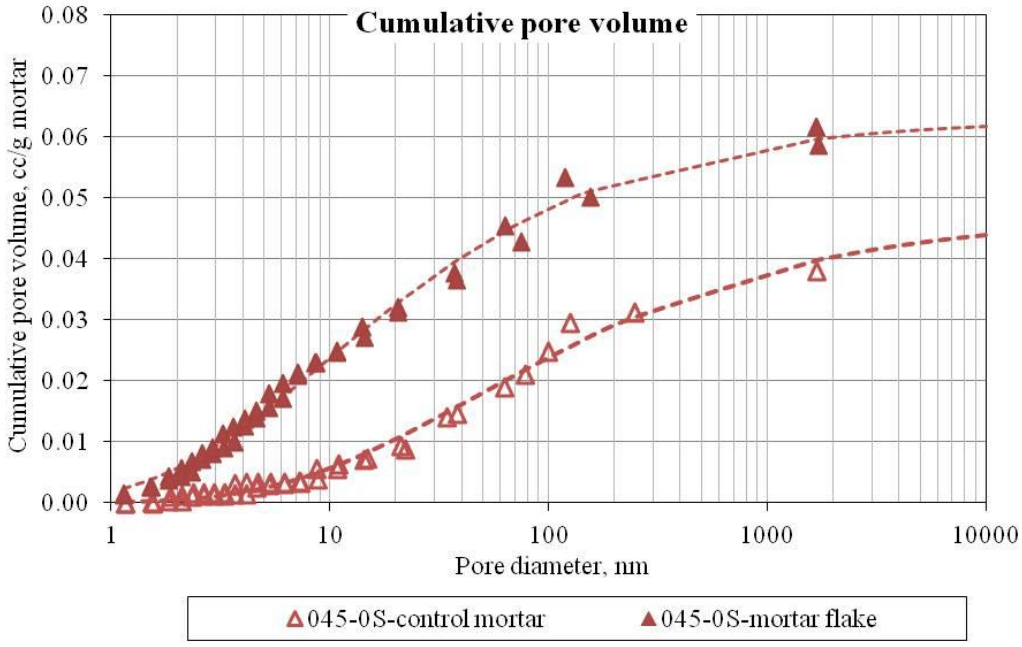
Cumulative pore volume
Cumulative pore volume, cc/g mortar
0.08
0.07
0.06
0.05
0.04
0.03
0.02
0.01
0.00
1
10
100
1000
10000
Pore diameter, nm
045-0S-control mortar
045-0S-mortar flake

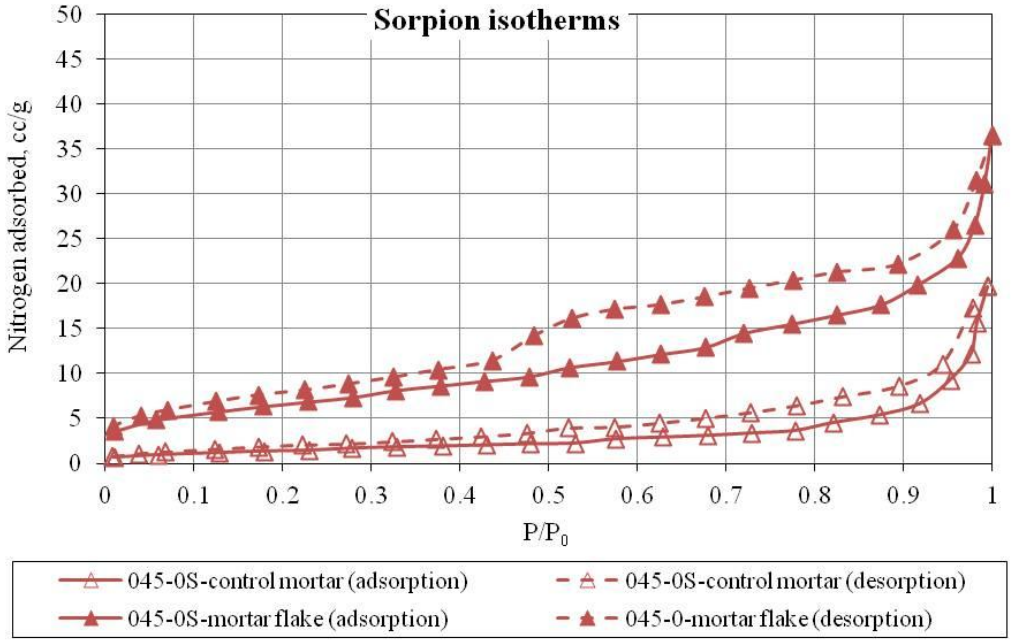
Sorpion isotherms
Nitrogen adsorbed, cc/g
50
45
40
35
30
25
20
15
10
5
0
0
0.1
0.2
0.3
0.4
0.5
0.6
0.7
0.8
0.9
1
P/P0
045-0S-control mortar (adsorption)
045-0S-control mortar (desorption)
045-0S-mortar flake (adsorption)
045-0-mortar flake (desorption)

(a) 045-0S-5.1%

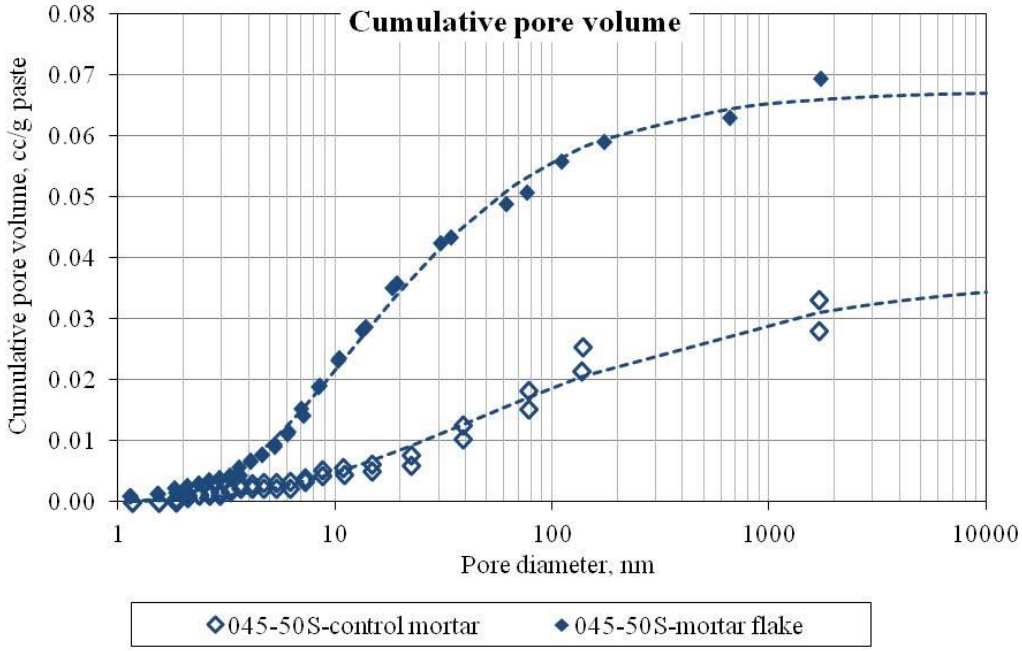
Cumulative pore volume
Cumulative pore volume, cc/g paste
0.08
0.07
0.06
0.05
0.04
0.03
0.02
0.01
0.00
1
10
100
1000
10000
Pore diameter, nm
045-50S-control mortar
045-50S-mortar flake

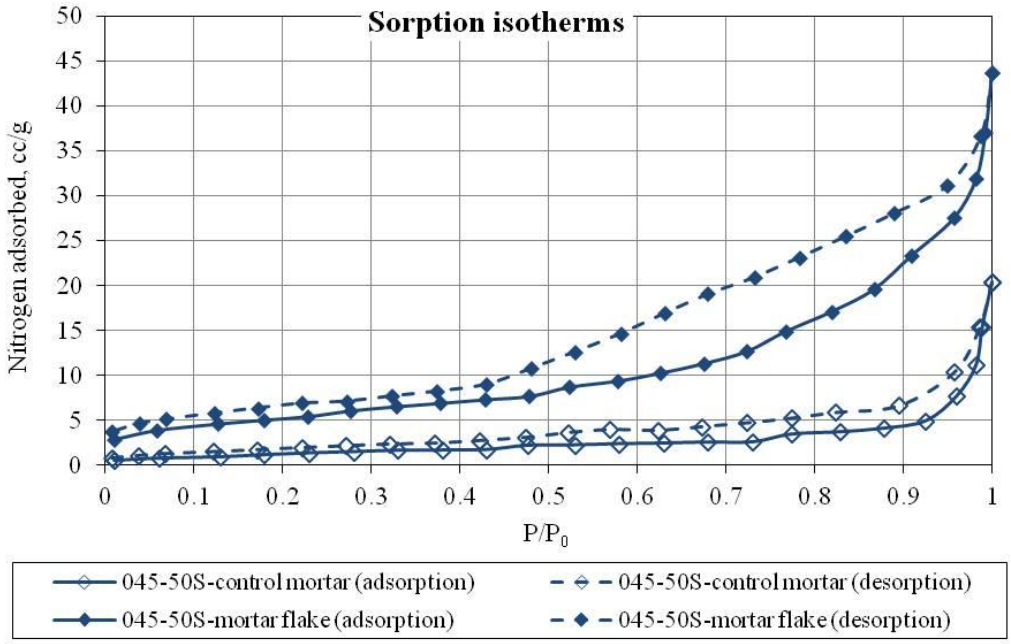
Sorption isotherms
Nitrogen adsorbed, cc/g
50
45
40
35
30
25
20
15
10
5
0
0
0.1
0.2
0.3
0.4
0.5
0.6
0.7
0.8
0.9
1
P/P0
045-50S-control mortar (adsorption)
045-50S-control mortar (desorption)
045-50S-mortar flake (adsorption)
045-50S-mortar flake (desorption)

(b) 045-50S-3.0%

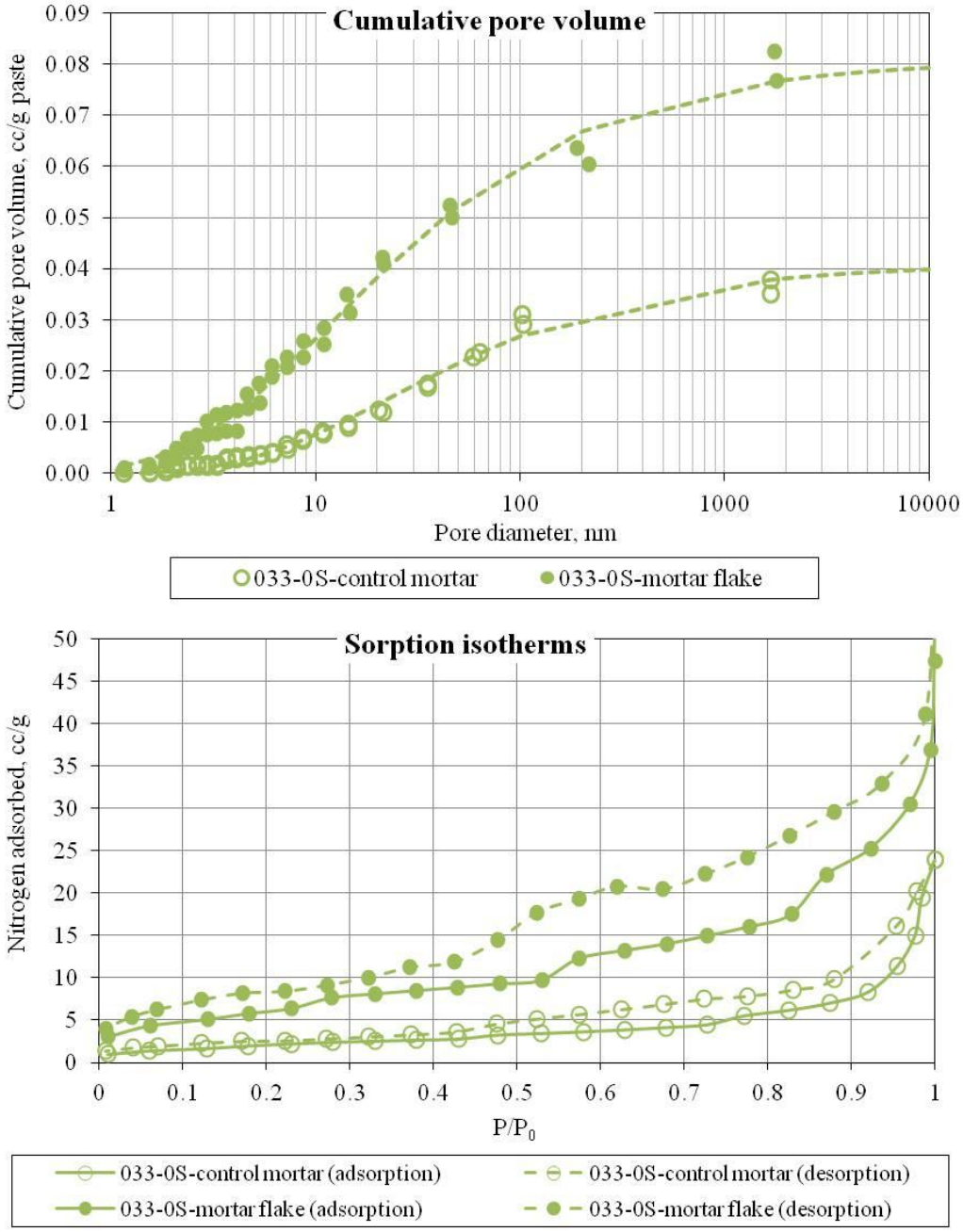

(c) 033-03-3.5%

Figure 5.26 Nitrogen sorption results different mixes before and after F-T exposure compression

5.8.2 A conceptual model for surface scaling

As shown in Figure 5.27, cryogenic suction mechanism consists of three indispensible components: (I) the amount of initial ice formation in capillary pores and (II) the presence of unfrozen moisture transported through (III) the capillary network. (I) is the driver to initiate capillary suction while (II) guarantees the continuous ice growth. The presence of salt in the surface liquid provides the unfrozen moisture. Capillary pore system controls both the rate of capillary suction and the amount of freezable water (or the initial ice nucleation).

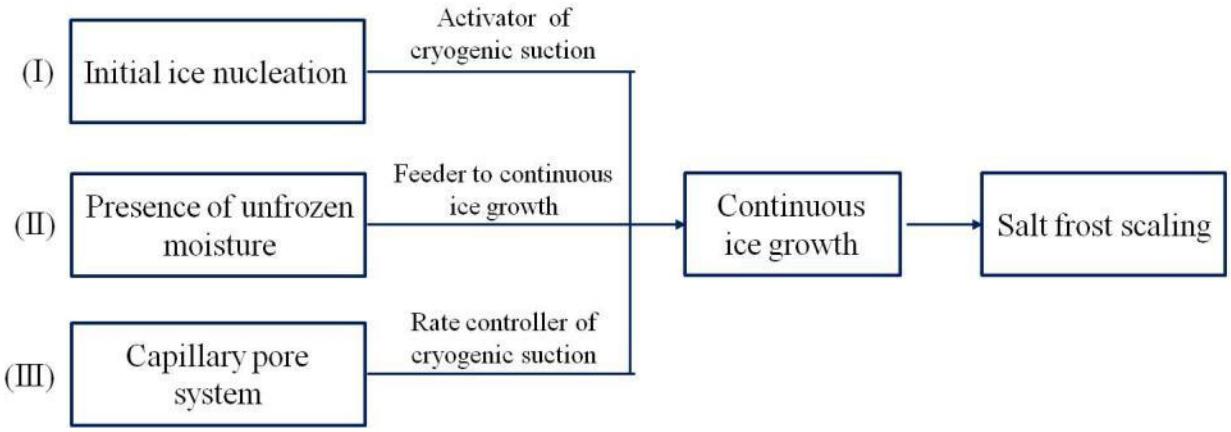

Figure 5.27 Schematic representation of cryogenic suction mechanism

The pore expansion in scaled-off flakes shown in Figure 5.26 further explains the activation of cryogenic suction even when the surface region has a saturated capillary pore condition prior to F-T exposure. As illustrated in Figure 5.28, (I) for a capillary saturated concrete with a salt solution on the surface, (II) the instant ice nucleation upon the termination of supercooling creates a transient unsaturated pore condition. This initiates cryogenic suction, which starts drawing liquid from adjacent pores and external surface layer (a composite of ice and interweaved brine pockets Weissenberger et al. 1992). (III) The subsequent ice growth leads to extra unsaturated pore space by compressing the interlayer space of adjacent pores, which in turn enhances the suction and further facilitates continuous ice growth. (IV) This causes expansion of the surface region, which is restrained by the remaining bulk concrete, and thus induces compressive stresses in the two lateral sides. The unrestraint top surface is under increasing tension due to Poisson's effect. This stress condition favors generation of cracks parallel to concrete surface, ultimately leading to paste swelling and scaling (Figure 5.5). This process is depicted in more detail in Figure 5.29.

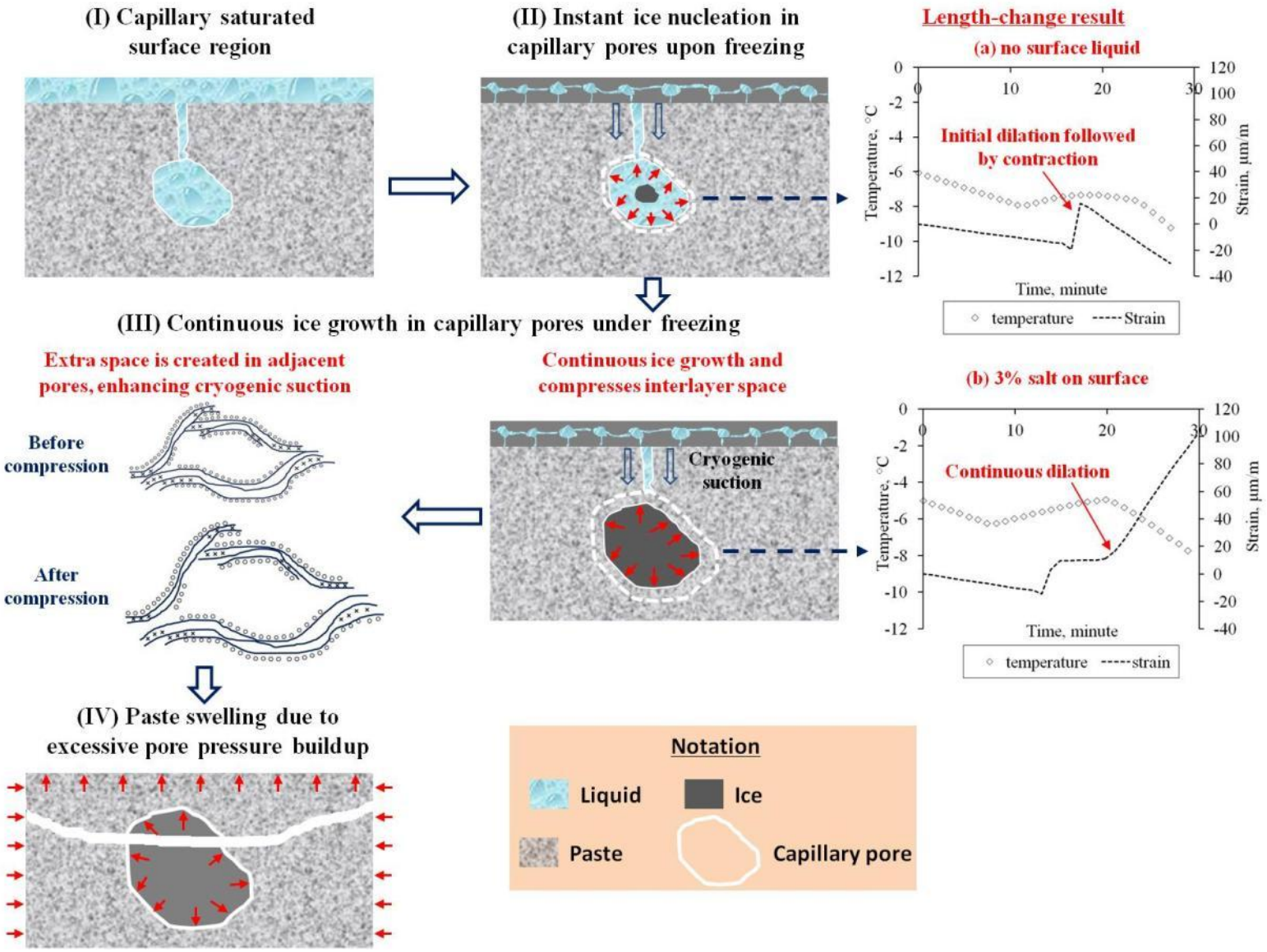

Figure 5.28 A conceptual model for salt frost scaling

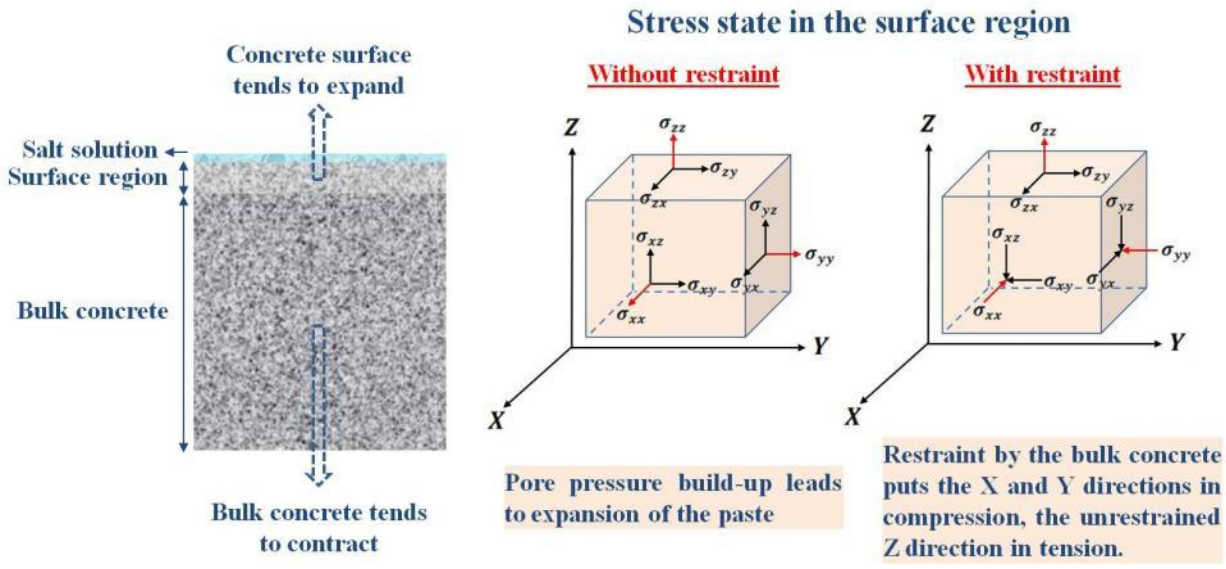

Figure 5.29 Stress condition in concrete specimen exposed to a salt/freezing condition

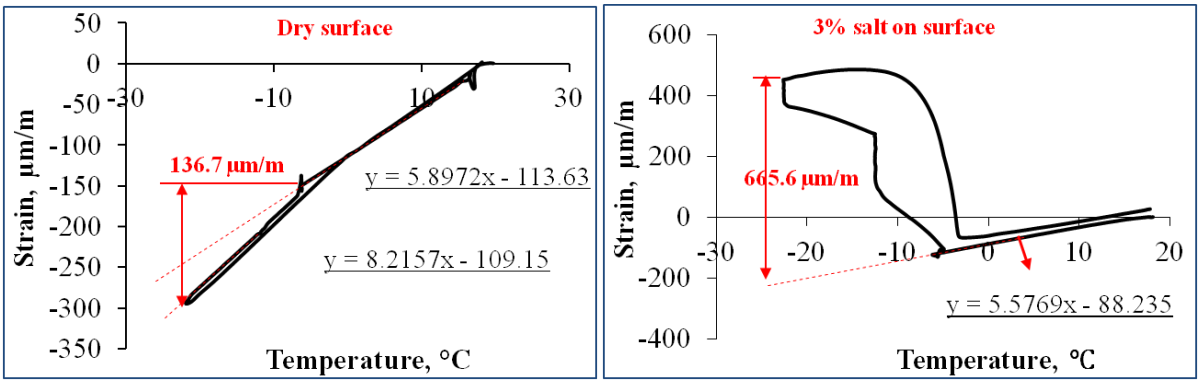

(a) no surface liquid (b) 3% salt solution on surface

Figure 5.30 Length-change in concrete under freezing (045-0S-3.0%)

- In concrete under freezing, moisture flow towards ice crystals formed in big capillary pores is a spontaneous process driven by the Gibbs free energy difference between liquid and ice (Powers and Helmuth 1953, Coussy 2005).
- This accretion process will persist until thermodynamic equilibrium is reached, while the drainage of those smaller pores causes a drying effect, leading to shrinkage of the matrix (Figure 5.30(a)) (Sun and Scherer 2010, Fridh 2005), as in the case of bulk concrete where no additional unfrozen liquid is available.
- For the thin surface region (~0.3 mm) in direct contact with a salt solution, pore drainage is constantly replenished by drawing the surface liquid via cryogenic suction. This

continuously promotes ice crystallization and expands the pore walls, which creates an unsaturated pore condition and enhances cryogenic suction mechanism. The resultant pore pressure build-up causes dilation in the paste (Figure 5.30(b)).

- As seen from Figure 5.29, the remaining bulk concrete imposes restraint on the dilation tendency of the surface region. This induces residual compressive stresses in the X and Y directions, which is exacerbated by the shrinkage of the bulk concrete, while the unrestraint Z direction is under increasing tension due to Poisson's effect. This stress condition favors generation of cracks parallel to concrete surface, ultimately leading to paste swelling and scaling.

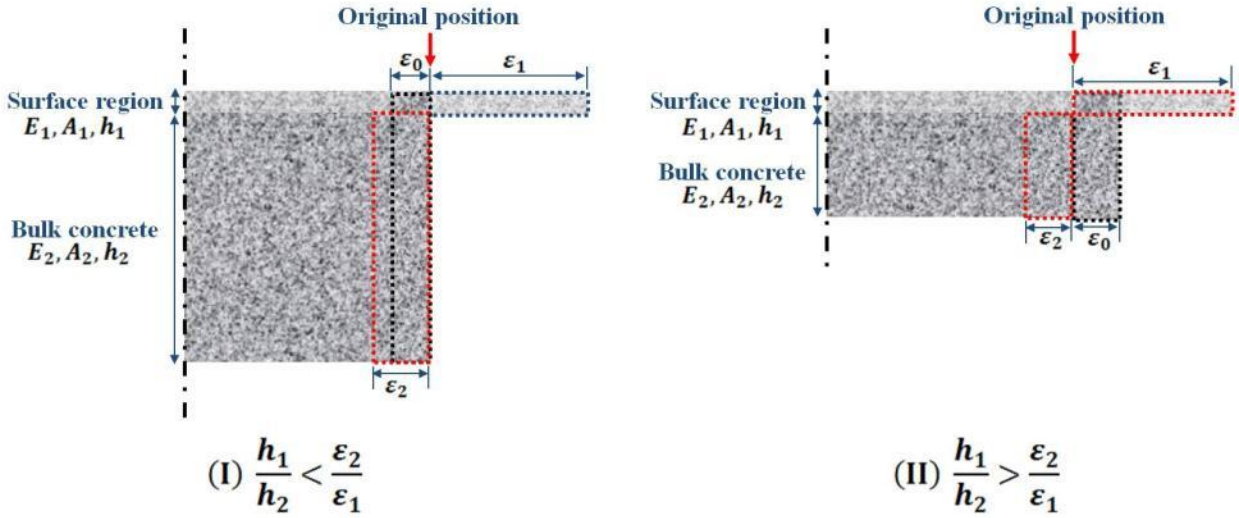

Figure 5.31 Strain compatibility between the surface region and bulk concrete.

In order to calculate the unstrained tension strain ε_z perpendicular to the top surface, strain compatibility between the surface region and the remaining bulk concrete is imposed. As seen from Figure 5.31, the surface region tends to expand by ε_1 while the bulk concrete tends to contract by ε_2 under free restraint. The ultimate deformation ε_0 can be either expansion (case I) or contraction (case II), depending on the restraining effect of the bulk concrete.

Given strain compatibility, force equilibrium analysis yields,

$$E_1(\varepsilon_1 + \varepsilon_0)A_1 = E_2(\varepsilon_2 - \varepsilon_0)A_2 \qquad \text{(case I)} \qquad (5\text{-}10)$$

Or

$$E_1(\varepsilon_1 - \varepsilon_0)A_1 = E_2(\varepsilon_2 + \varepsilon_0)A_2 \qquad \text{(case II)} \qquad (5\text{-}11)$$

Since $E_1 = E_2$, $A_1/A_2 = h_1/h_2$

Thus,

$$\varepsilon_0 = \frac{\varepsilon_2 h_2 - \varepsilon_1 h_1}{h_1 + h_2} \quad \text{(case I)} \quad (5\text{-}12)$$

$$\varepsilon_0 = \frac{\varepsilon_1 h_1 - \varepsilon_2 h_2}{h_1 + h_2} \quad \text{(case II)} \quad (5\text{-}13)$$

where E_1, E_2 are the elastic moduli, A_1, A_2 are the cross-sectional areas and h_1, h_2 are the thicknesses of the surface region and remaining bulk concrete, respectively.

Assuming the surface region of concrete is subjected to a state of triaxial stress (σ_x, σ_y, σ_z), the associated normal strains (ε_x, ε_y, ε_z) can be determined by the generalized Hook's law.

$$\varepsilon_x = \frac{1}{E}(\sigma_x - \mu(\sigma_y + \sigma_z)) \quad \text{(compression)} \quad (5\text{-}14)$$

$$\varepsilon_y = \frac{1}{E}(\sigma_y - \mu(\sigma_x + \sigma_z)) \quad \text{(compression)} \quad (5\text{-}15)$$

$$\varepsilon_z = \frac{1}{E}(\sigma_z - \mu(\sigma_x + \sigma_y)) \quad \text{(tension)} \quad (5\text{-}16)$$

Since

$\varepsilon_x = \varepsilon_y$, σ_z=0 for a square-shaped free surface (5-17)

Thus,

$$\sigma_x = \sigma_y \quad (5\text{-}18)$$

$$\varepsilon_z = -2\,\mu\frac{\sigma_x}{E} \quad (5\text{-}19)$$

Since

$$\sigma_x = \frac{E\varepsilon_x}{1-\mu} \quad (5\text{-}20)$$

Thus,

$$\varepsilon_z = -\frac{2\mu}{1-\mu}\varepsilon_x \quad (5\text{-}21)$$

Since ε_x=$-(\varepsilon_1 + \varepsilon_0)$ for case I or ε_x=$-(\varepsilon_1 - \varepsilon_0)$ for case II

$$\varepsilon_z = \frac{2\mu}{1-\mu}(\varepsilon_1 + \varepsilon_0) = \frac{2\mu}{1-\mu} \times (\varepsilon_1 + \frac{\varepsilon_2 h_2 - \varepsilon_1 h_1}{h_1 + h_2}) = \frac{2\mu}{1-\mu} \times \frac{h_2}{h_1 + h_2} \times (\varepsilon_1 + \varepsilon_2) \text{ (case I)} \quad (5\text{-}22)$$

$$\varepsilon_z = \frac{2\mu}{1-\mu}(\varepsilon_1 - \varepsilon_0) = \frac{2\mu}{1-\mu} \times (\varepsilon_1 - \frac{\varepsilon_1 h_1 - \varepsilon_2 h_2}{h_1+h_2}) = \frac{2\mu}{1-\mu} \times \frac{h_2}{h_1+h_2} \times (\varepsilon_1 + \varepsilon_2) \text{ (case II)} \quad (5\text{-}23)$$

The tensile strain of the bulk concrete is

$$\varepsilon_t = \varepsilon_2 - \varepsilon_0 = \varepsilon_2 - \frac{\varepsilon_2 h_2 - \varepsilon_1 h_1}{h_1+h_2} = \frac{h_1}{h_1+h_2} \times (\varepsilon_1 + \varepsilon_2) \quad \text{(case I)} \quad (5\text{-}24)$$

$$\varepsilon_t = \varepsilon_2 + \varepsilon_0 = \varepsilon_2 + \frac{\varepsilon_1 h_1 - \varepsilon_2 h_2}{h_1+h_2} = \frac{h_1}{h_1+h_2} \times (\varepsilon_1 + \varepsilon_2) \quad \text{(case II)} \quad (5\text{-}25)$$

From LTD measurement in Figure 5.30, ε_1=665.6 μm/m, ε_2=136.7 μm/m, $t_1 + t_2$=70 mm. If we assume h_1=0.3 mm, h_2=69.7 mm and μ=0.2, then ε_z=399.4 μm/m, which exceeds the tensile strain capacity of concrete, while the tensile strain of the bulk concrete is ε_t =3.4 μm/m. This, again, accords with the pore volume measurement in Figure 5.4, showing no internal cracking.

5.9 Effect of air entrainment on salt frost scaling

Mixed results have been reported on the correlation between scaling resistance and air void properties in laboratory test where the surface is in constant contact with a salt solution (Setzer 1997, Fagerlund 1993, Stark 1997, Petersson 1991, Pigeon and Pleau 1995 Tremblay et al. 2007). In this section, laboratory and filed concrete samples with a wide range of air entrainment characteristics were tested on the frost scaling performance and its relation to air void properties was explored.

5.9.1 Effect of air content

Air entrainment has been generally accepted as the most efficient method to protect concrete against frost deterioration. Powers quantified the role of microscopic air voids with the proposal of spacing factor to indicate the hydraulic pressure-accommodating capacity of the air void system (Powers 1949). Normally, a minimum spacing factor of ~200 μm (or equivalently around 3% air in concrete) is required to arrest the internal microcracking due to freezing-thawing action (Powers 1949, Backstrom et al. 1958). The initial dilation, which is believed to be a result of hydraulic pressure upon the termination of supercooling, is measured at different levels of air entrainment. The importance of air entrainment in internal frost damage has been seen in Figure 5.20 and Figure 5.21 and is further shown in Figure 5.32 and Figure 5.33. It can be seen that the initial dilation is substantially suppressed with an entrainment of 3% air and the reduction is not discernible when the air content reaches 5%. Thus, the air void system is a key factor in

controlling the instant ice nucleation expansion which is related to F-T resistance to bulk specimen cracking in a laboratory test.

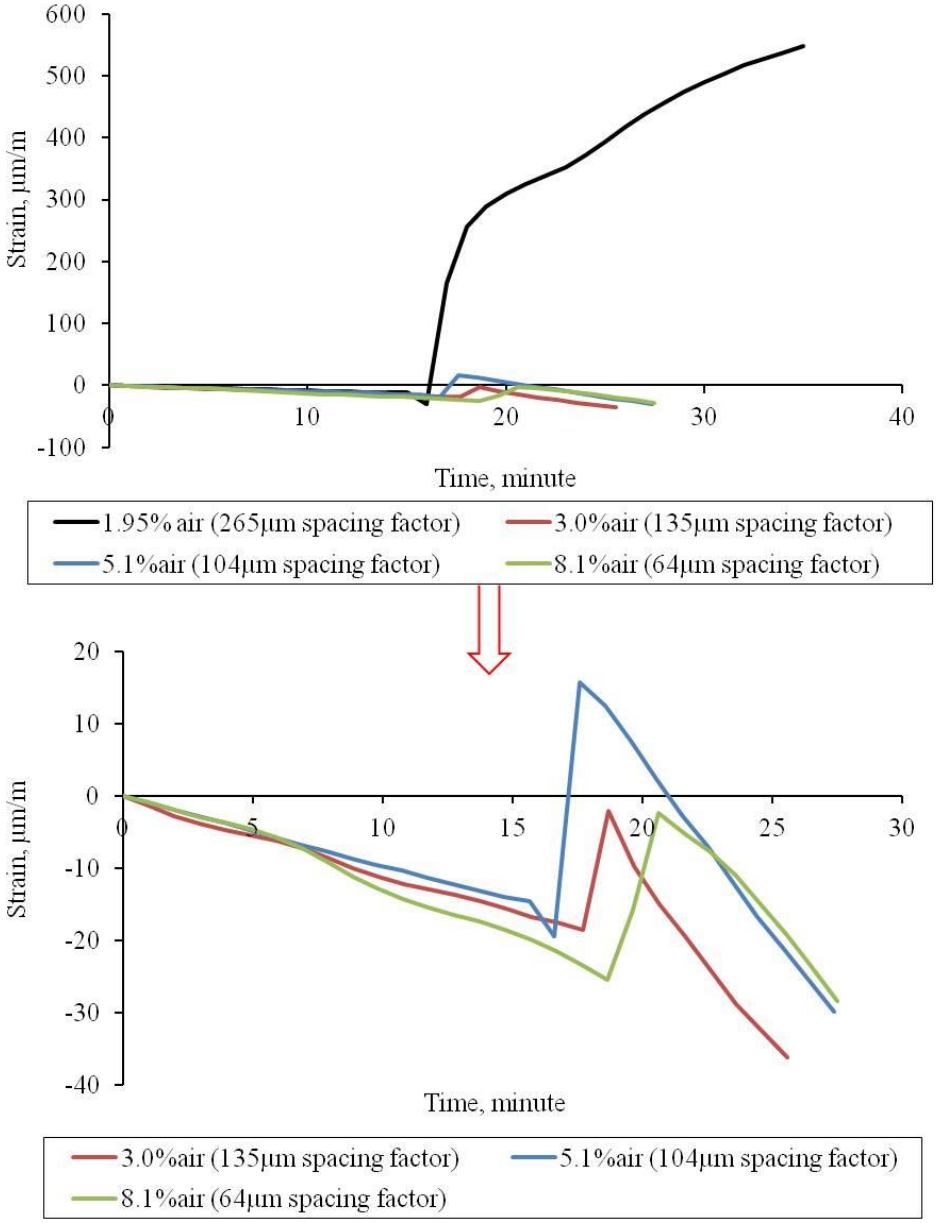

Figure 5.32 Effect of air content on the initial dilation

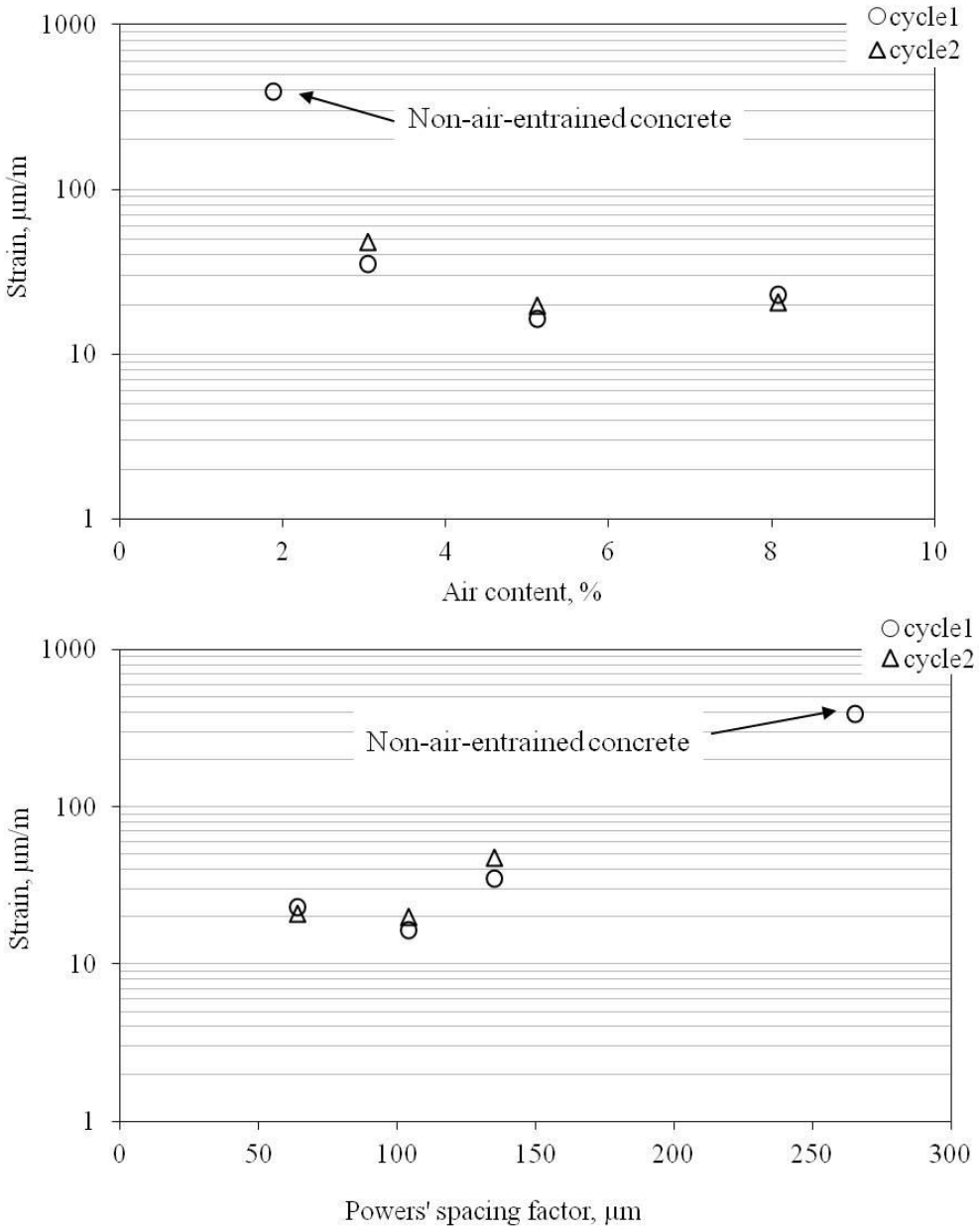

Figure 5.33 Effect of air void system on instant dilation strain associated with ice nucleation

Other studies have found that the air void system, although needed for field resistance to salt scaling, is not a strong predictor in laboratory test procedures where the surface is in constant contact with a salt solution (Setzer 1997, Pigeon and Pleau 1995, Petersson 1991,Tremblay et al. 2007). This has been shown by the scaled surface profiles previously (Figure 5.15 and Figure 5.16). It is further evidenced by a poor relationship between mass loss and air content (Figure 5.34 (a)). No added benefit is achieved in scaling resistance beyond a critical air level, which is

~2% entrained air (<500 μm). This correponds to a Powers' spacing factor of 200 μm (Figure 5.34 (b)) and a specific surface of ~25 mm^{-1} (Figure 5.34 (c)).

In concretes with internal damage problems, as indicated by the dashed circle in Figure 5.34, scaling is substantially exacerbated (Figure 5.13(a)). In this case, scaling is coupled with internal cracking, evidenced by the decrease in RDM (Figure 5.11(d)) and the propagation of cracks to the unexposed top surface (Figure 5.12(a)). The accelerated mass loss at later F-T cycles is associated with the removal of coarse aggregate (Figure 5.12 (b)).

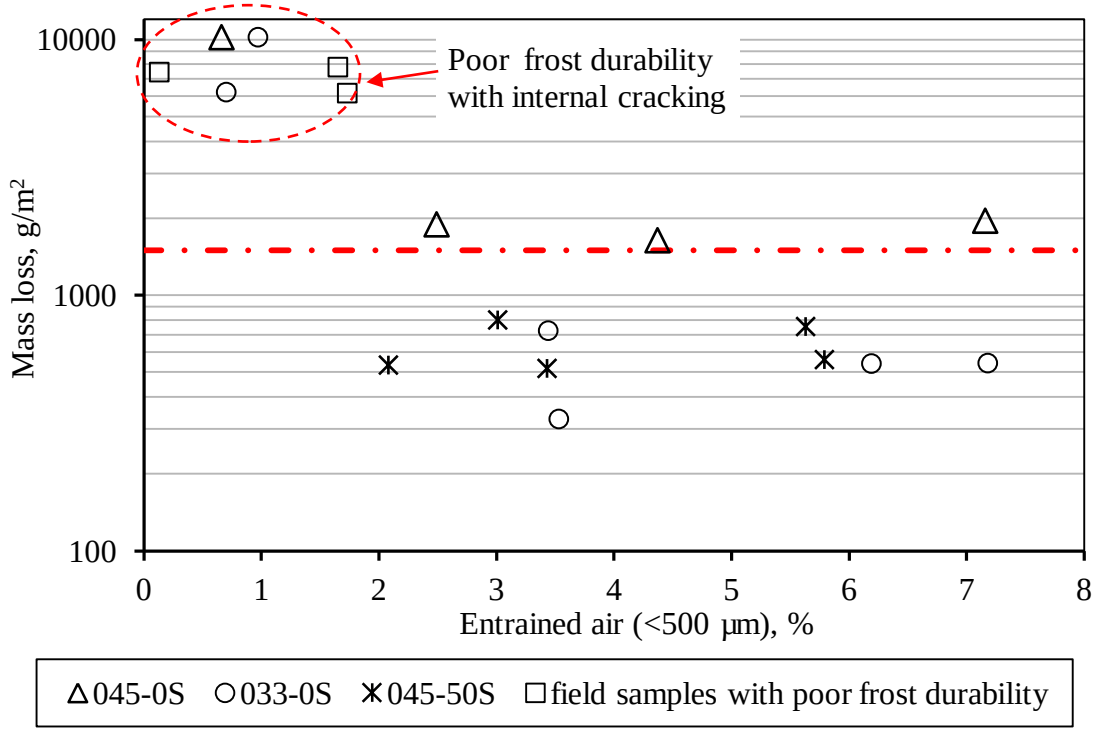

(a) Entrained air (<500 μm) vs. mass loss after 28 F-T cycles

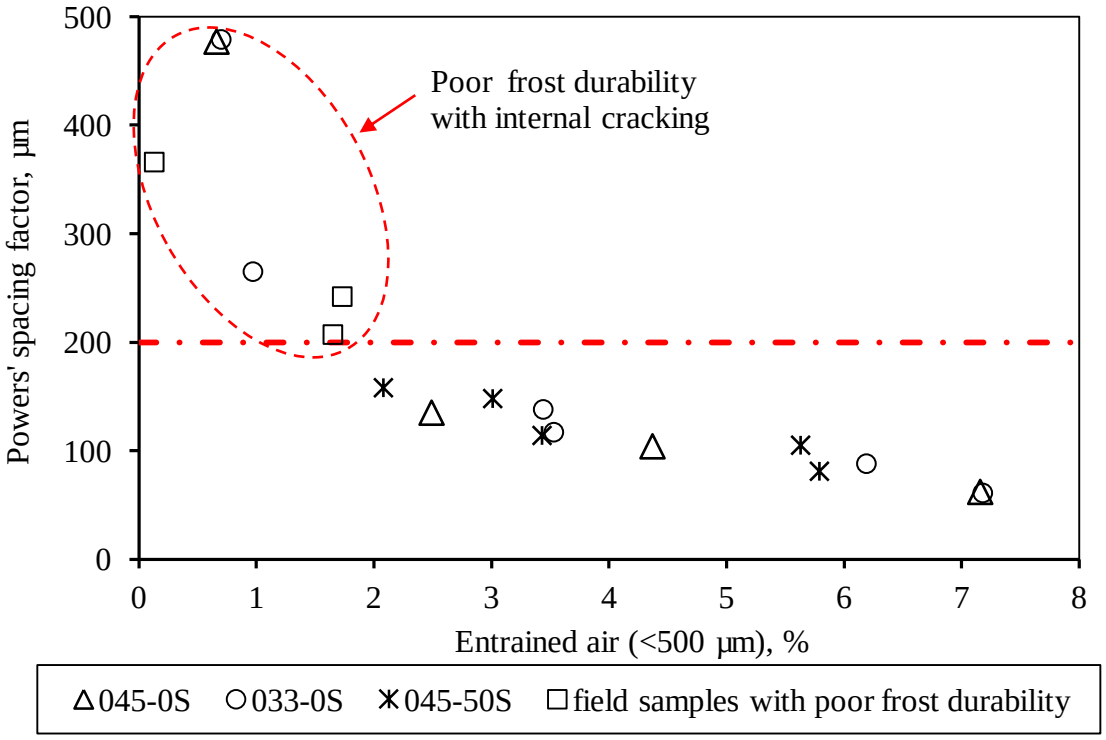

(b) Entrained air (<500 µm) vs.Powers' spacing factor

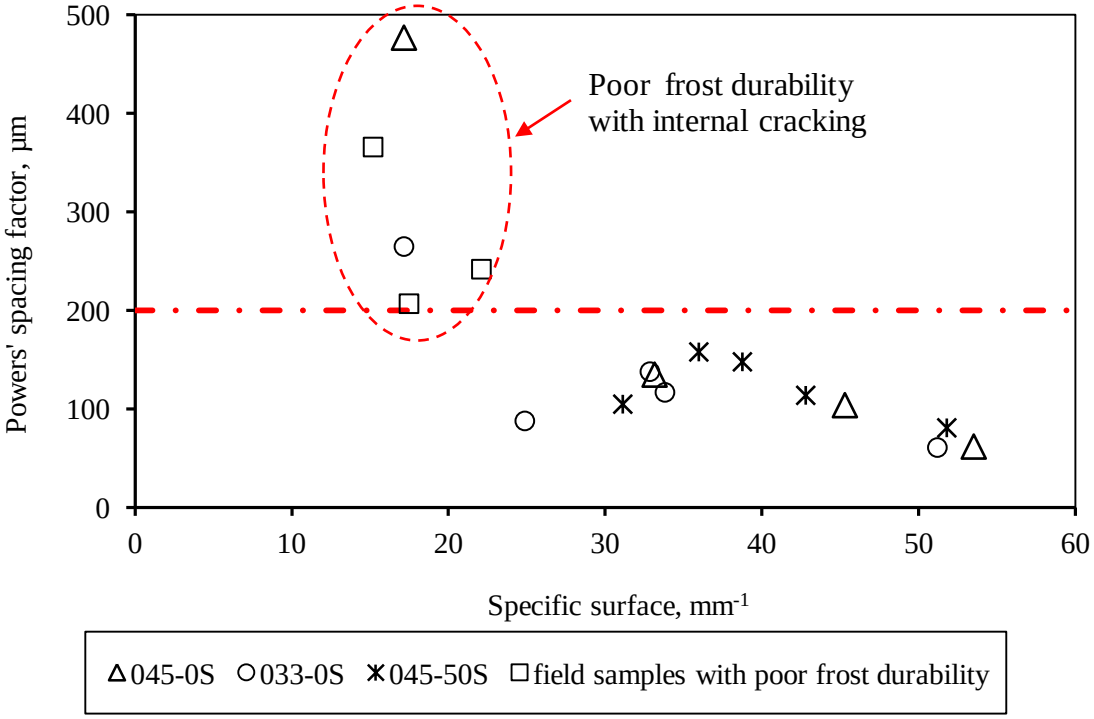

(c) Specific surface vs.Powers' spacing factor

Figure 5.34 Air void properties and their relation to salt frost scaling

Furthermore, the air content has only limited effect on sorptivity (Figure 5.35). These results are consistent with the hypothesis that cryogenic suction is the dominating factor.

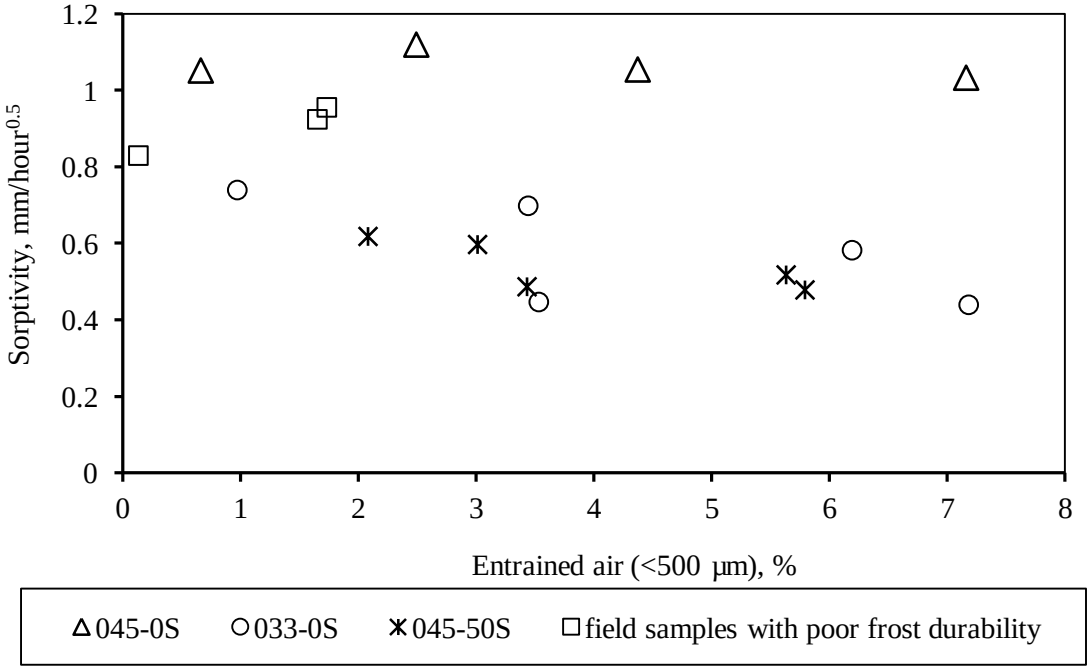

Figure 5.35 Effect of air content on scaling resistance and capillary transport rate

5.9.2 Effect of void size distribution

Void size effect of air entrainment was studied on 0.33 w/c concrete mixes using two different air entrainers while maintaining similar total air content. Both the fractional and cumulative void size distributions by linear traverse method are shown in Figure 5.36. It can be seen that AEA-1 entrains more small air bubbles (<500 μm), which is clearly shown in Figure 5.37. The coarser void distribution by AEA-2 leads to larger Powers' spacing factor and smaller specific surface at the same air level (Figure 5.38).

Nevertheless, all these mixes show excellent scaling performance without discernible difference being noted in Figure 5.39.

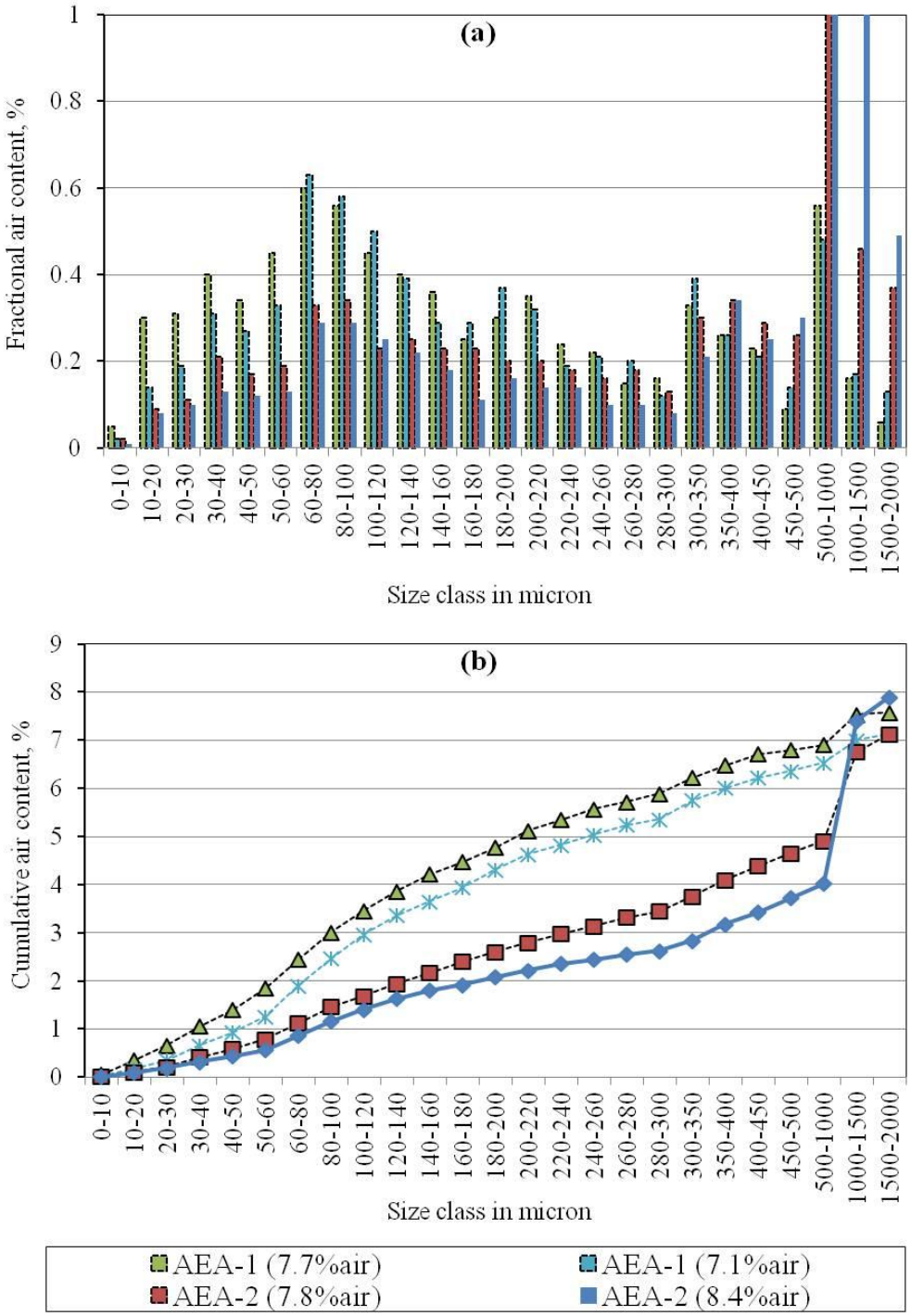

Figure 5.36 Air void size distribution in concrete mixes using different air entrainer

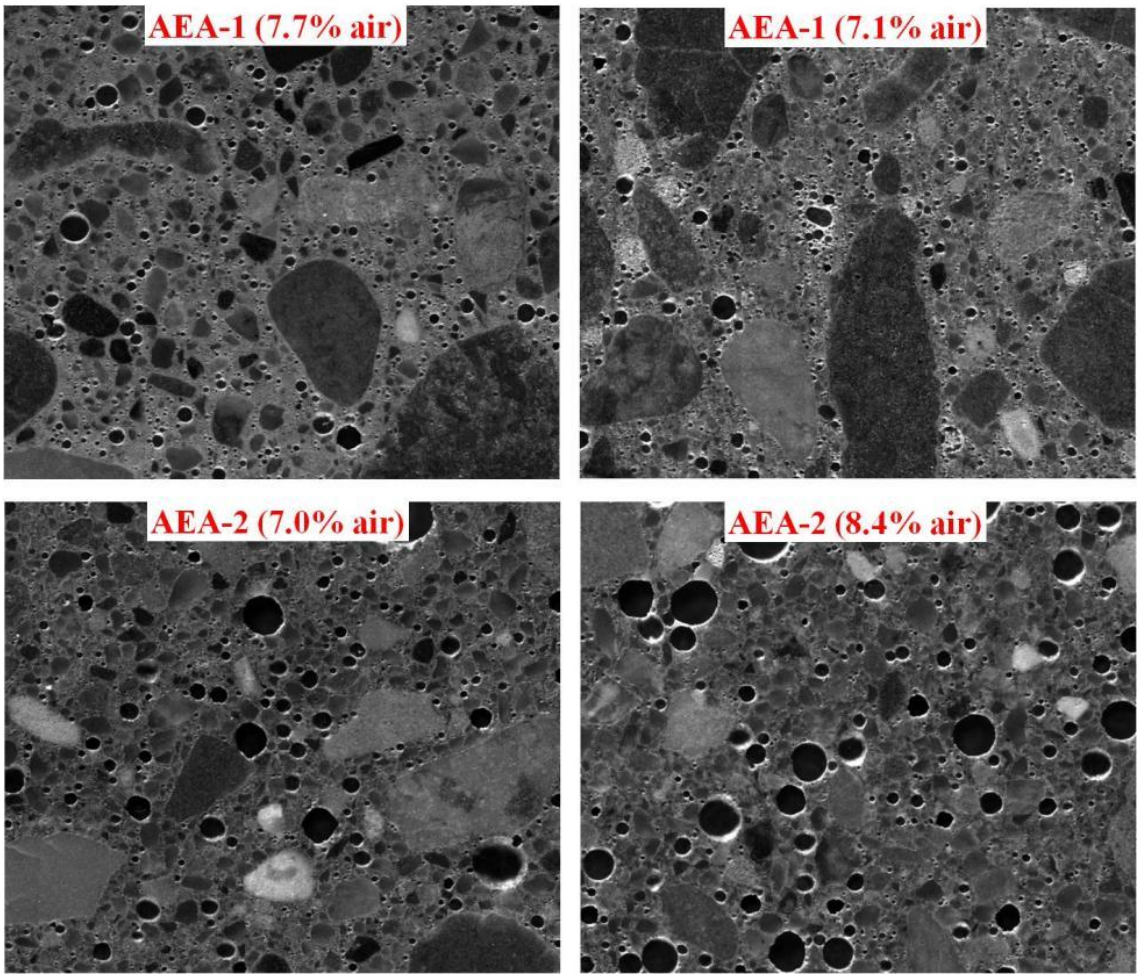

Figure 5.37 Air void profiles in concrete mixes using different air entrainer

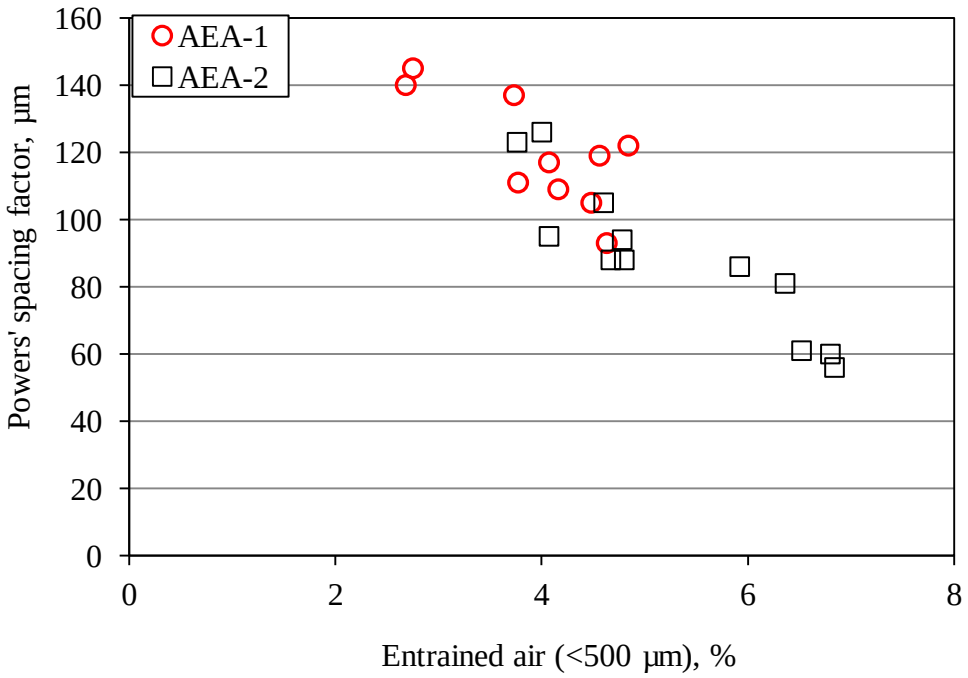

(a)

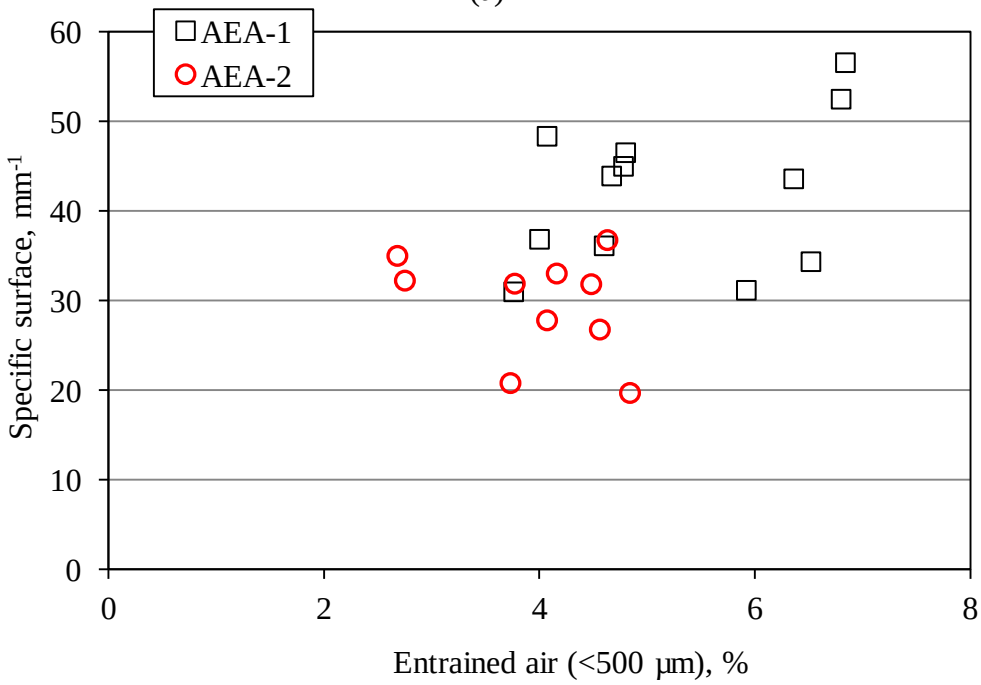

(b)

Figure 5.38 Air void properties in concrete mixes using different air entrainer

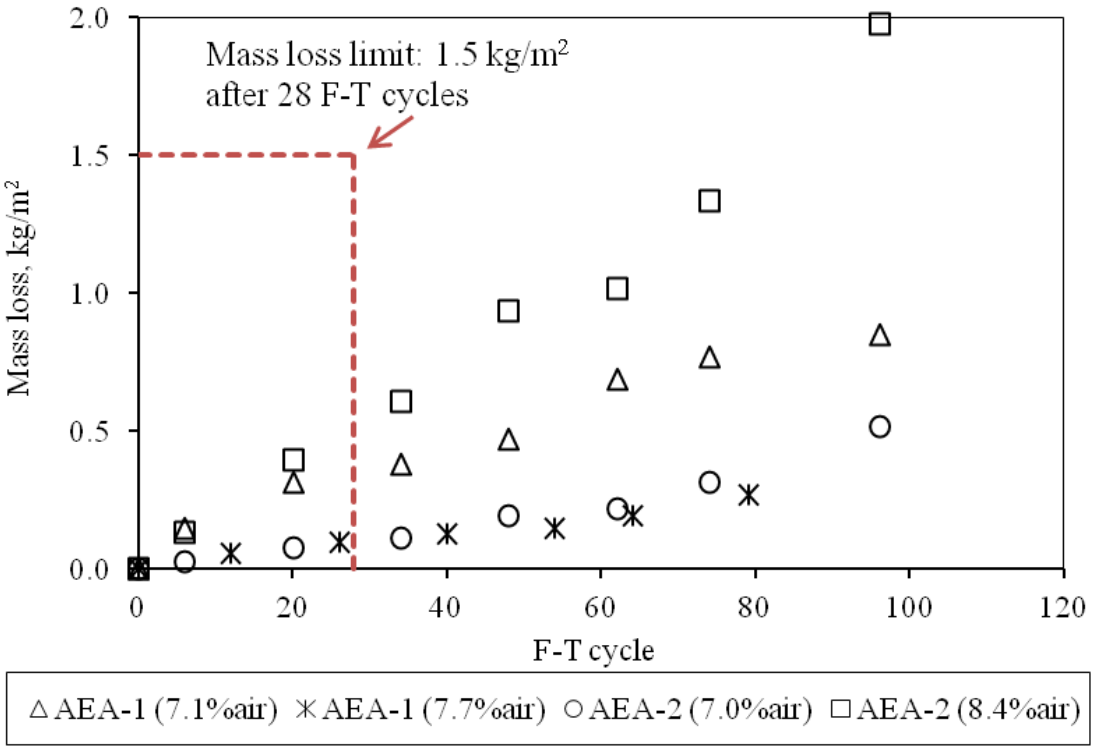

Figure 5.39 Mass loss vs. F-T cycles for concrete with different air entrainer

5.9.3 Restraint-relief effect of air entrainment

The conceptual model proposed above may partially explain the lack of correlation between air content and scaling resistance. Length-change measurement on capillary saturated concrete prisms of different air contents shows that the coefficient of thermal expansion (CTE) of concrete under freezing is 9-10×10^{-6}/℃ (Figure 5.40), which is far below the CTE of ice (~50×10-6/℃). This is contradictory to the proposed glue-spall theory which attributes the improvement by air entrainment to the contraction of concrete that alleviates the mismatch stress due to the CTE difference between concrete and ice (Sun and Scherer 2010). The calculated cumulative contraction between the freezing point and the minimum temperature further illustrates that there is a marginal increase in freezing contraction with increased air content, which has limited effect on the bulging strain (Figure 5.41).

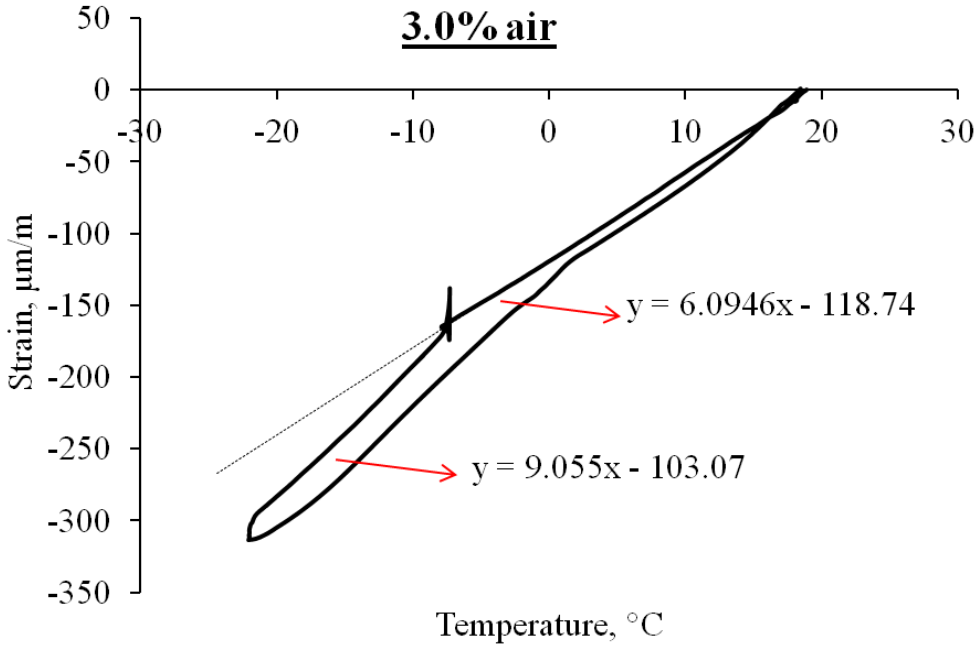
3.0% air
50
0
-50
-100
-150
-200
-250
-300
-350
-30
-20
-10
0
10
20
30
Strain, µm/m
Temperature, °C
y = 6.0946x - 118.74
y = 9.055x - 103.07

(a)

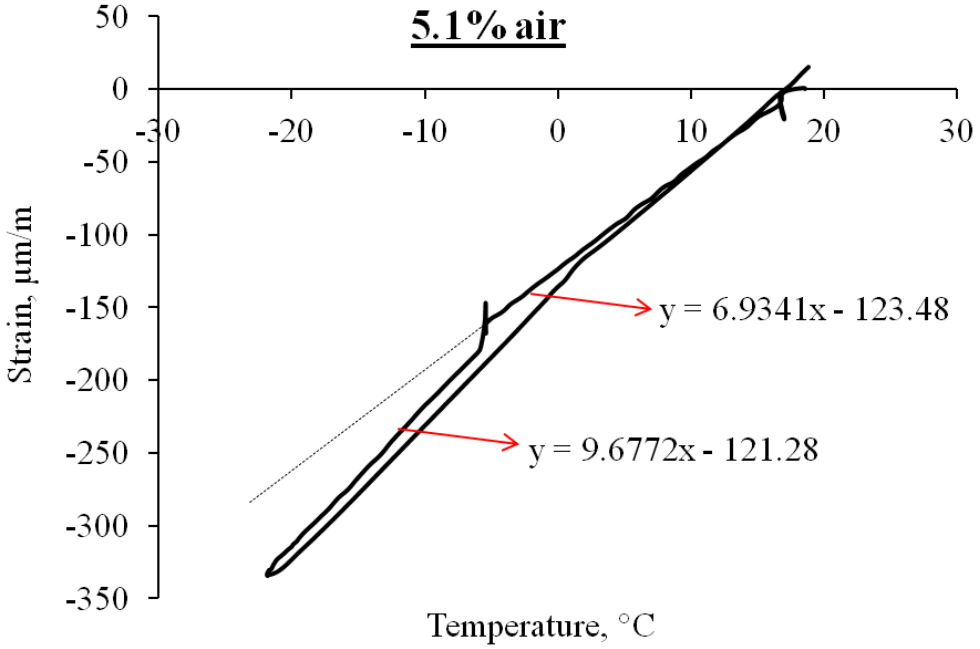
5.1% air
50
0
-50
-100
-150
-200
-250
-300
-350
-30
-20
-10
0
10
20
30
Strain, µm/m
Temperature, °C
y = 6.9341x - 123.48
y = 9.6772x - 121.28

(b)

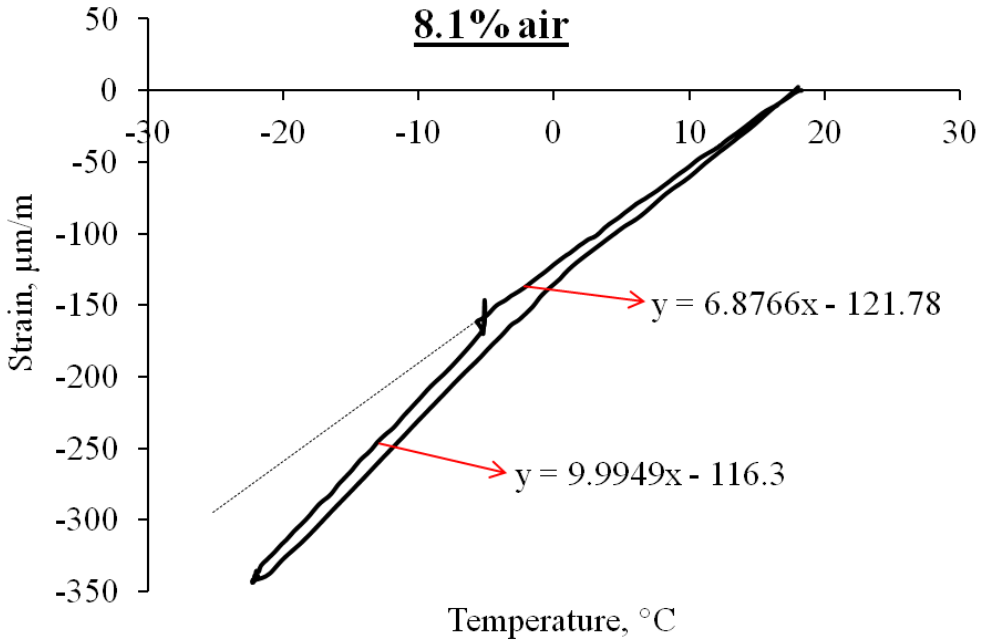

(c)

Figure 5.40 Effect of air content on the freezing contraction of concrete specimens that are capillary presaturated with water

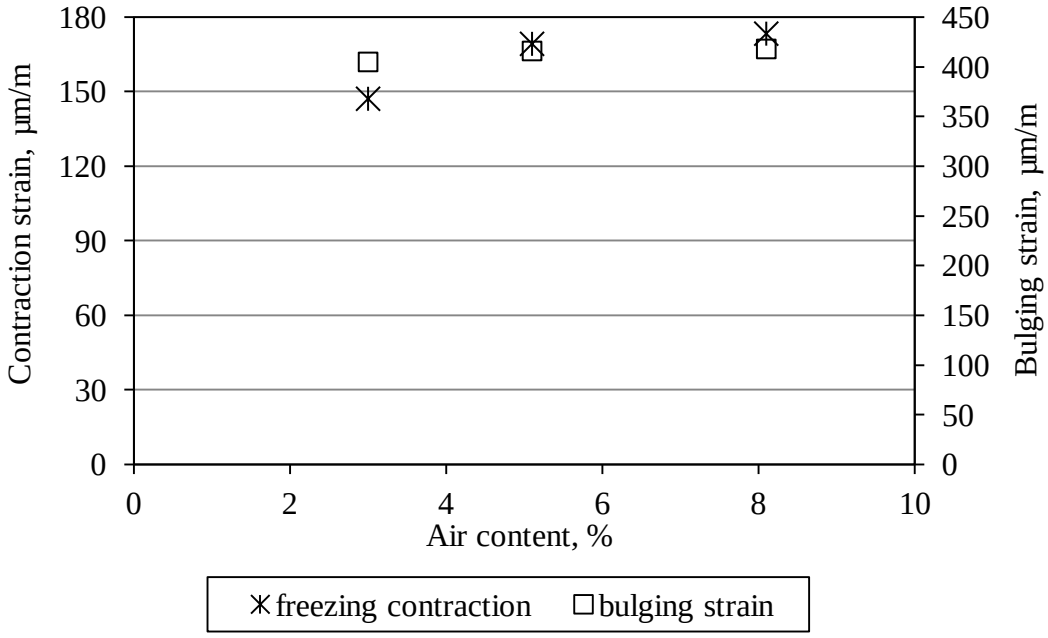

Figure 5.41 Contraction strain of concrete with different air contents under sub-freezing cooling stage

5.10 Salt effect

It has been previously shown that reduction in capillary size and continuity restrains the initial nucleation of ice crystals, thus reducing the potential of crogenic suction. Another alternative on regulating this sequence of events is the incorporation of varied concentrated salt solution, which will ultimately lead to an interpreation of the "pessimum" phenomenon (Figure 5.42).

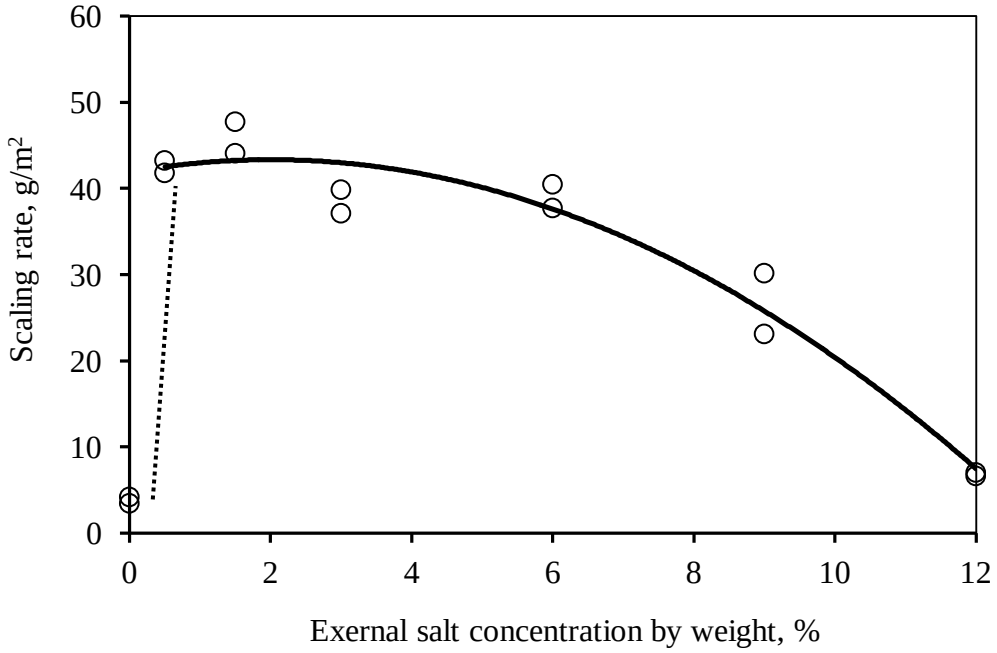

Figure 5.42 Effect of external salt concentration on the mass loss of concrete (045-0S-3.0%)

The salt effect on internal ice formation pattern has been studied extensively (Powers 1975, Litvan 1976, Harnik et al. 1980, Sellevold and Farstad 1991) and it is well known that salt solution in concrete pores can depress the freezing point and reduce the rate of ice nucleation and growth (Kaufmann 2000, Karlsson 1994, Bauerecker et al. 2008). This is elucidated by investigating the length change and associated temperature profiles of concrete specimens saturated with variedly concentrated salt solutions. As seen from Figure 5.43, immediately upon the arrival of freezing point, there is a transient dilation and a gradual temperature rise associated with internal ice formation and both are attenuated with increased strength of salt solutions. In order to quantify this effect, the maximum temperature rise and the instant dilation are computed and plotted, together with the freezing point, against salt concentrations in Figure 5.44.

Now, with the confirmation of added moisture movement from outside to surface pores as aforementioned, a new revealing window can be offered. First and foremost, the presence of salt solution on concrete surface makes available the liquid during freezing and keeps the moisture flow active. Second, the amount of both the unfrozen liquid on the surface and the ice formation in the pores under freezing depends on the concentration of the salt solution and temperature. This is elucidated by the reduced secondary dilation when concrete is either exposed to or presaturated with a salt solution of high concentration (9% NaCl solution) (Figure 5.45(a) and (b), respectively). This demonstrates that the inner salt concentration is equally important as the outer salt concentration, which is consistent with the majority of the results reported in the literature review by (Lindmark 1998). This makes sense considering the fact that the concentration of the outer salt solution will equilibrate with the inner salt solution in pores of concrete surface in a short period of time (Valenza and Scherer 2006, Marchand et al. 1999), depending on the diffusion coefficient of salt ions (typically 10^{-11}-10^{-10} m^2/s for chloride ions) and the thickness of the surface region (Valenza and Scherer 2006). As seen from Figure 5.46, it takes less than 3 hours for the outer salt solution to penetrate into concrete surface of ~300 μm thick and reach equilibrium. This explains why similar dilation suppression occurs no matter if the 9% salt solution is applied on concrete surface or located within concrete pores.

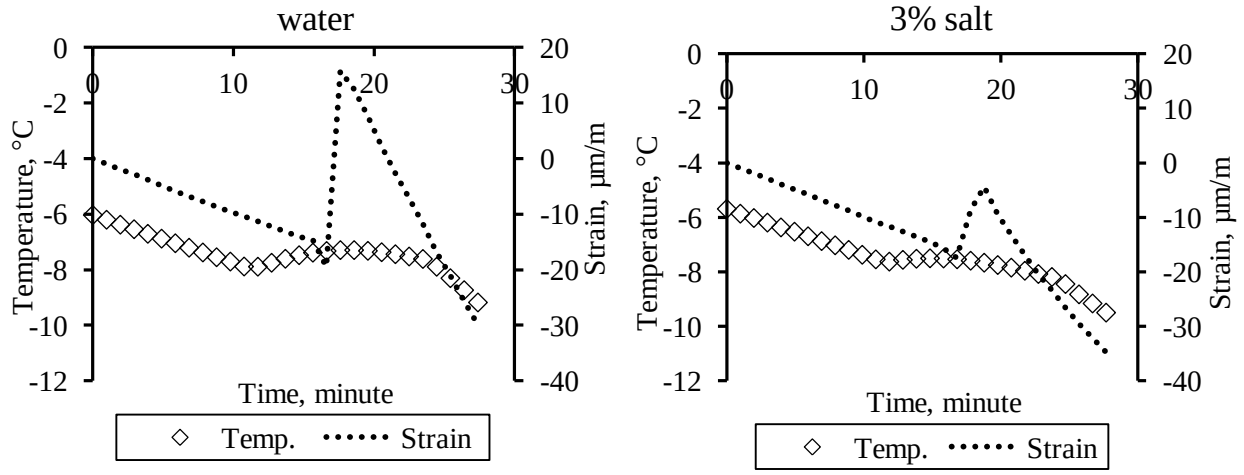

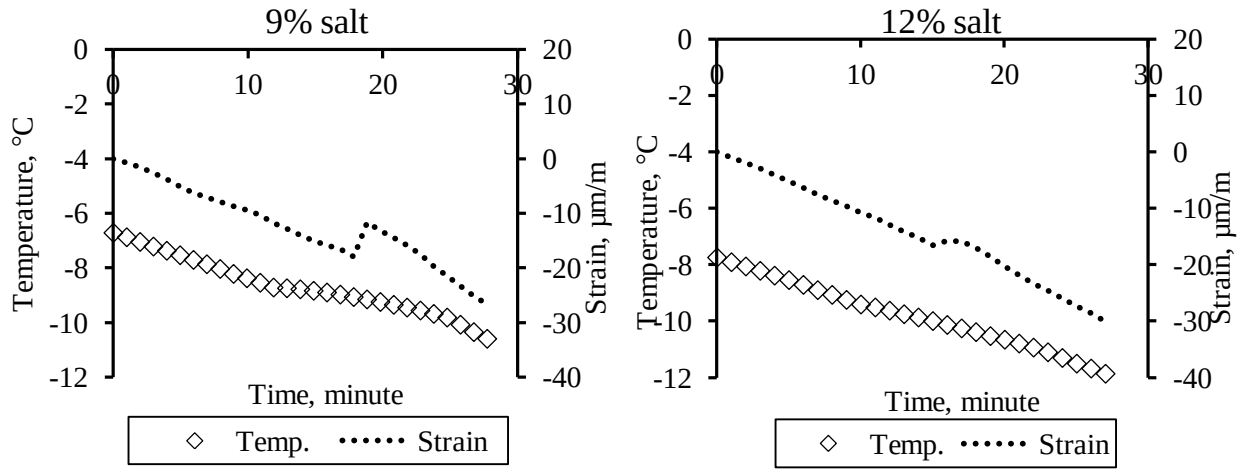

Figure 5.43 Length and temperature change curves due to ice formation (cycle 1)

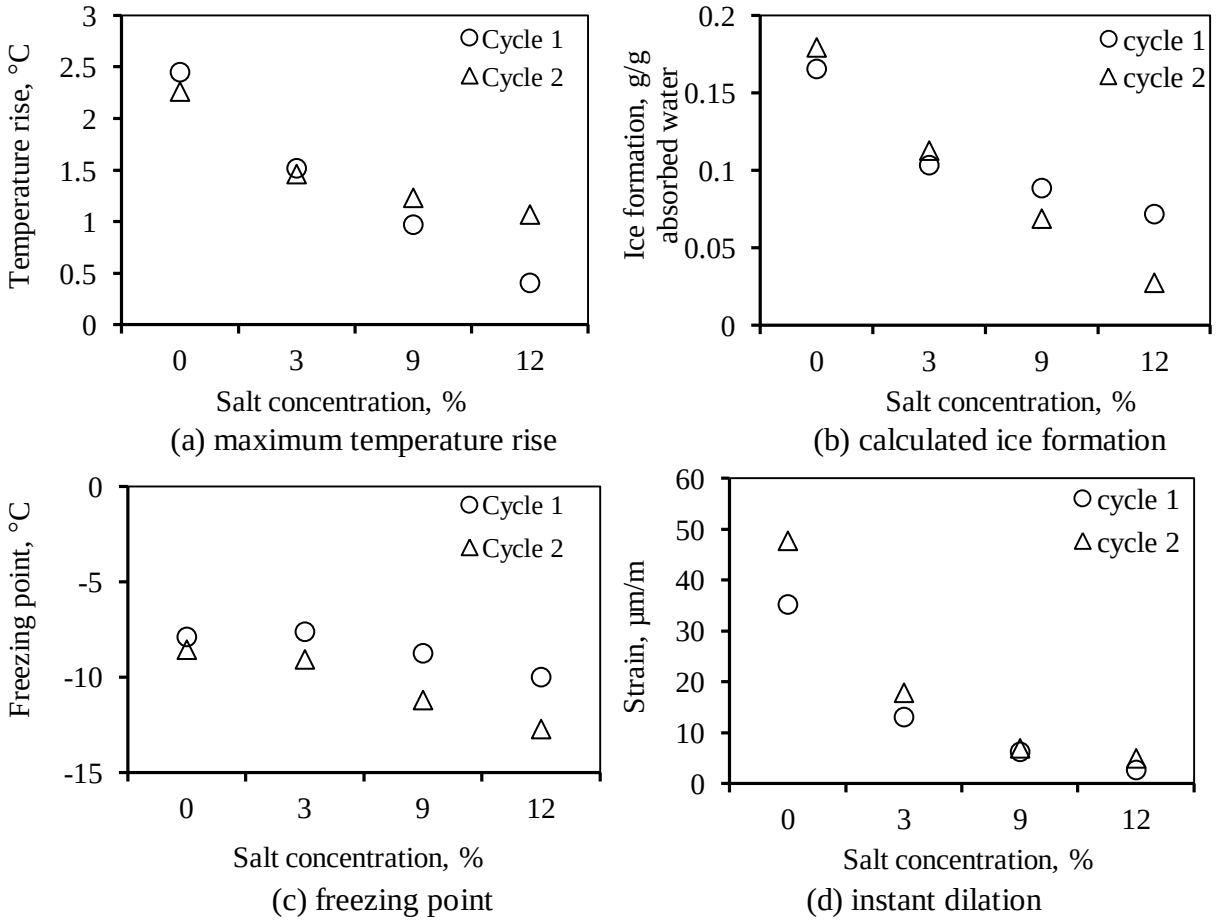

(a) maximum temperature rise

(b) calculated ice formation

(c) freezing point

(d) instant dilation

Figure 5.44 Effect of internal salt concentration on ice formation pattern of concrete

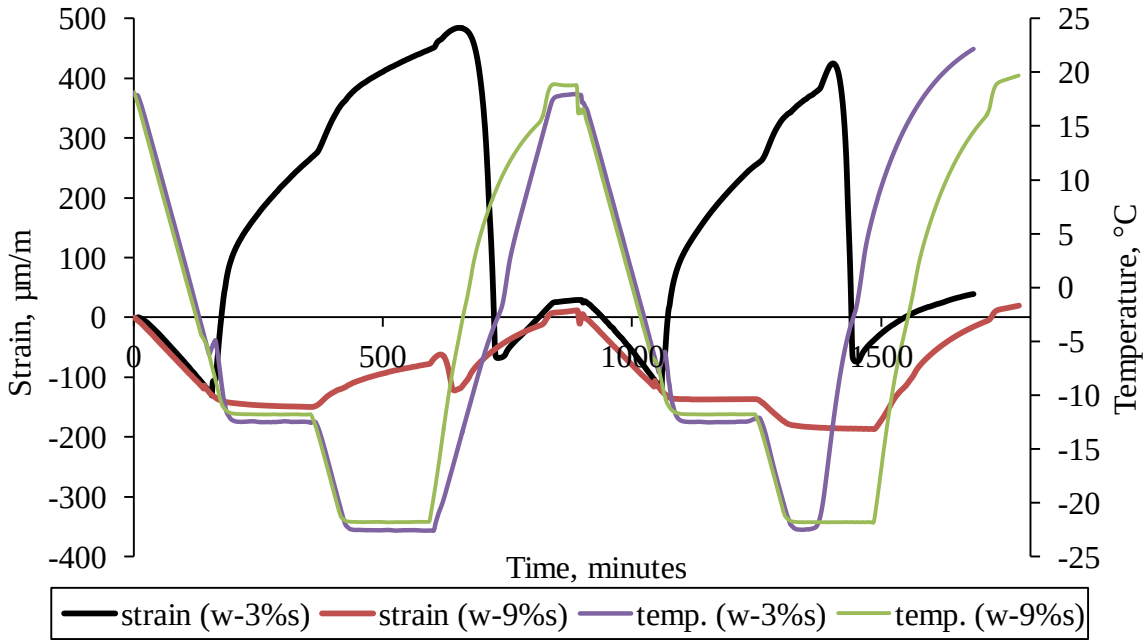

(a)

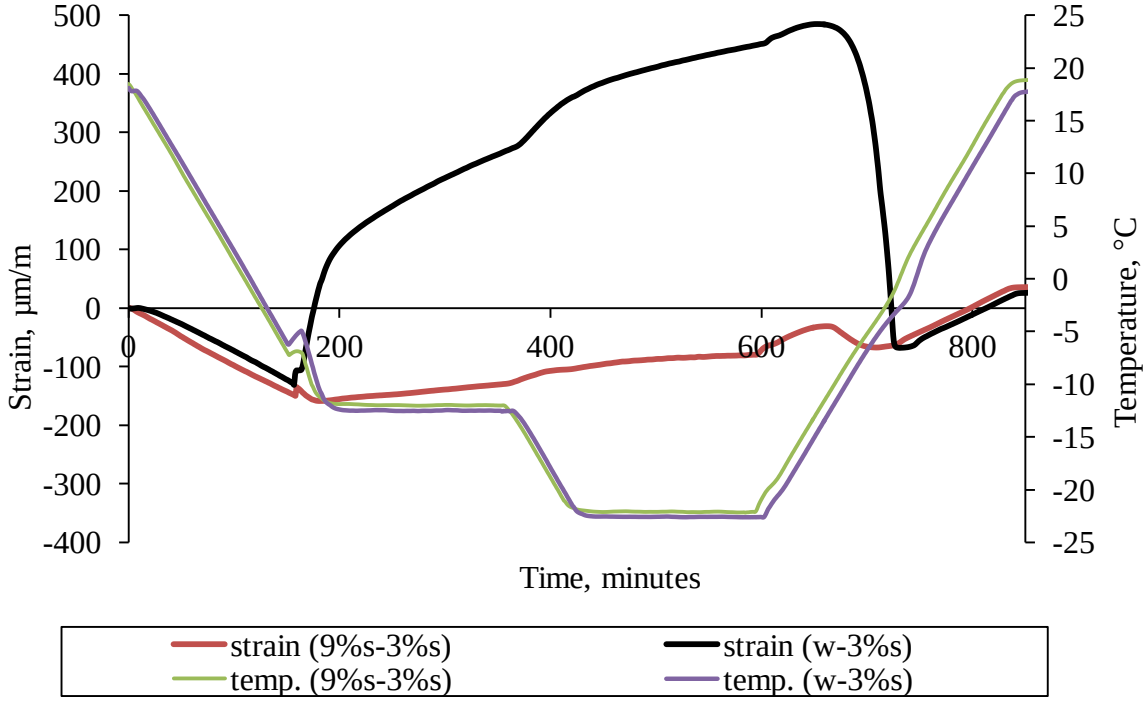

(b)

Figure 5.45 Effect of salt concentration on the ice growth in concrete pores (a) Length and temperature change with time for concrete specimens (045-0S-3.0%) presaturated with water and exposed to 3% and 9% salt solutions, respectively (In the second cycle for the 3% salt exposure, the -20 °C isothermal stage was less than 3 hours due to a malfunction of the temperature control system) (b) Length and temperature change with time for concrete specimens (045-0S-3.0%) presaturated with water and 9% salt solution respectively, and exposed to 3% salt solution

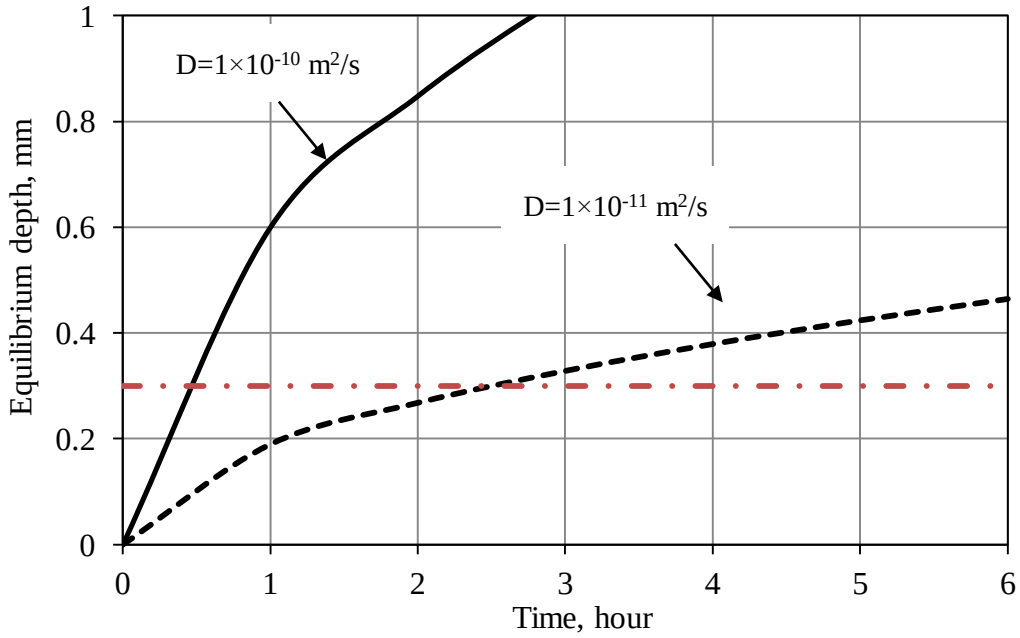

Figure 5.46 Calculated equilibrium depth with time at two diffusion coefficients for the diffusion of NaCl ions into concrete surface assuming similar diffusion coefficient for chloride and sodium ions

The length change curves of concrete exposed to four different salt concentrations are shown in Figure 5.47. It is interesting to note that when the surface liquid is weakly concentrated (such as 0.5% and 3% salt solution), significant dilation occurs below and at -10 ℃, after which, dilation is substantially reduced, even some shrinkage is observed. This is because when the temperature stays not too low from freezing point, both the amount of internal ice and surface liquid is sufficient to maintain the moisture flow; when the temperature drops below -10 ℃, the availability of surface liquid is so limited, albeit more inner ice growth (which possibly increases the pore blockage and thus resistance to the liquid transport), that the moisture flow is diminished or even discontinued. When the surface liquid is very strongly concentrated (such as 9% salt solution), the amount of internal ice formation dominates, which is suppressed markedly. Thus, the "engine power" to activate the cryosuction is insufficient, but it gains momentum gradually with further temperature decrease which is evidenced by a small dilation after -10 ℃.

In addition, as mentioned previously, the difference in Gibbs free energy between the surface liquid and the pore liquid is reduced at higher salt concentrations, which decreases the driving force of moisture flow as well. This opposing effect becomes more self-evident by plotting the isothermal dilations at both -10 ℃ and -20 ℃ for different salt concentrations (Figure 5.48). As

can be seen, the isothermal dilation at -10 ℃ is reduced with more salt present, which indicates it is dominated by the amount of internal ice formation. When temperature stays at -20 ℃, the isothermal dilation becomes much smaller and is increased with more salt present and it is controlled by both the availability of unfrozen surface liquid and the pore blockage due to excessive ice formation.

In summary, "pessimum" salt concentration is a cause of the synergic effect of salt on the dominant factors, "the availability of unfrozen surface liquid and internal ice formation and the magnitude of cryogenic suction".

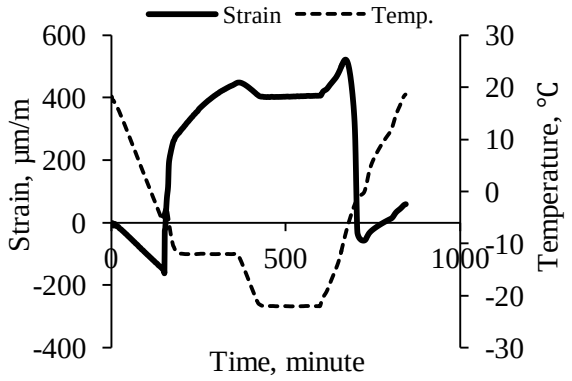

(a) strain & temperature vs. time

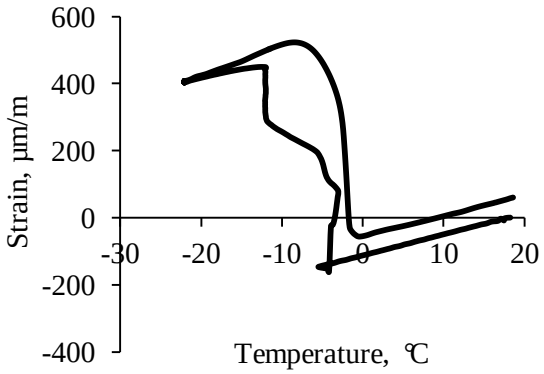

(b) strain vs. temperature

(0.5% salt)

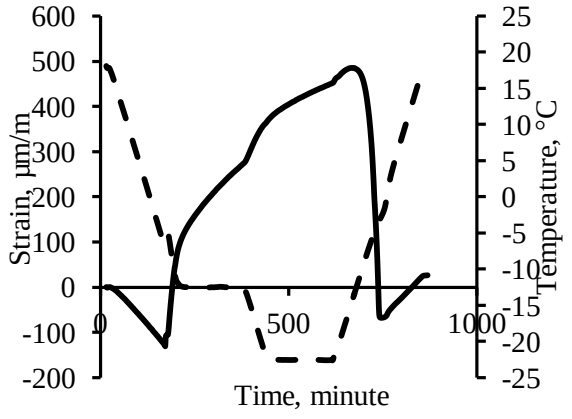

(a) strain & temperature vs. time

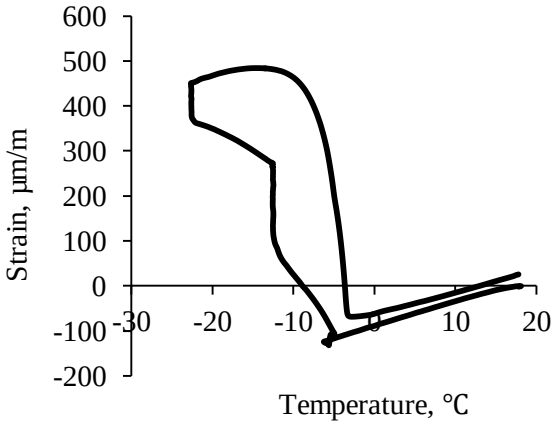

(b) strain vs. temperature

(3.0 % salt)

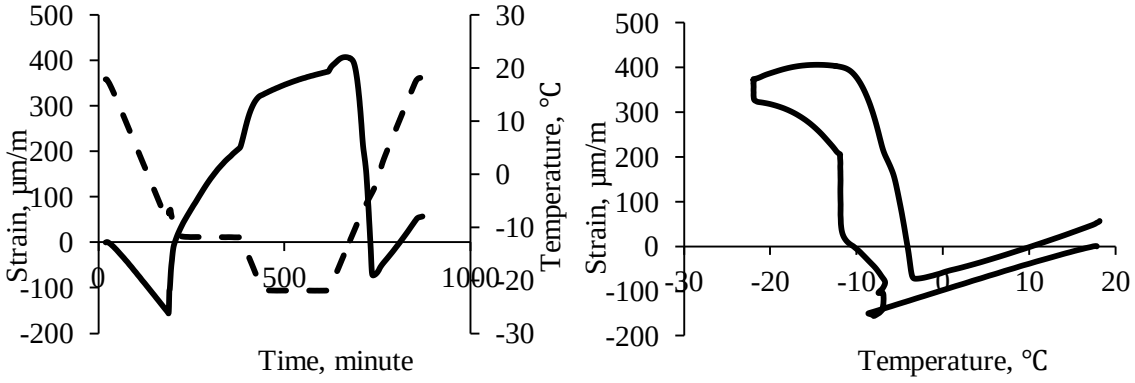

(a) strain & temperature vs. time (b) strain vs. temperature

(6.0 % salt)

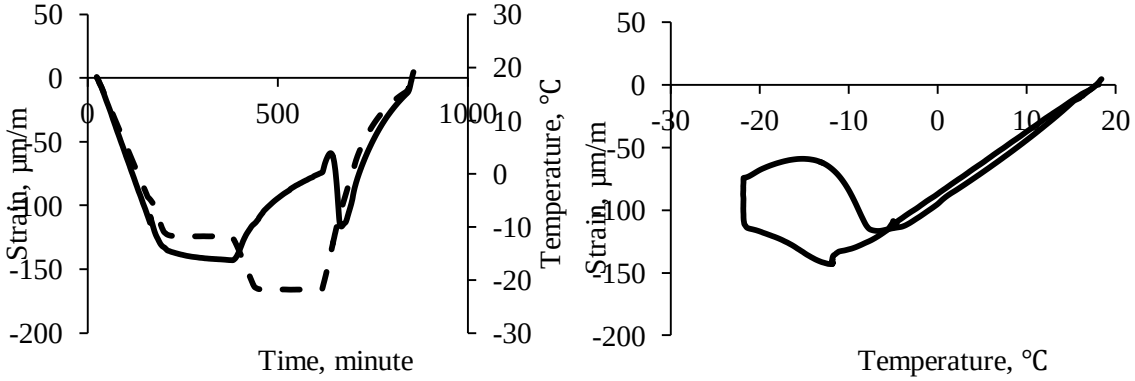

(a) strain & temperature vs. time (b) strain vs. temperature

(9.0 % salt)

Figure 5.47 Length change profile in concrete exposed to different salt concentrations

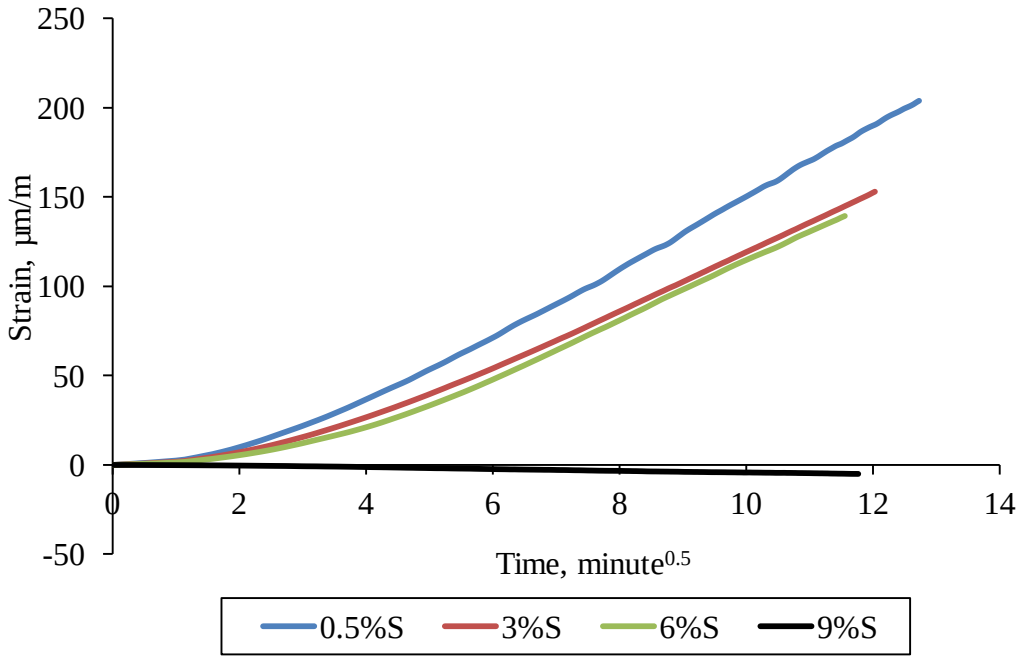

(a) -10 ℃

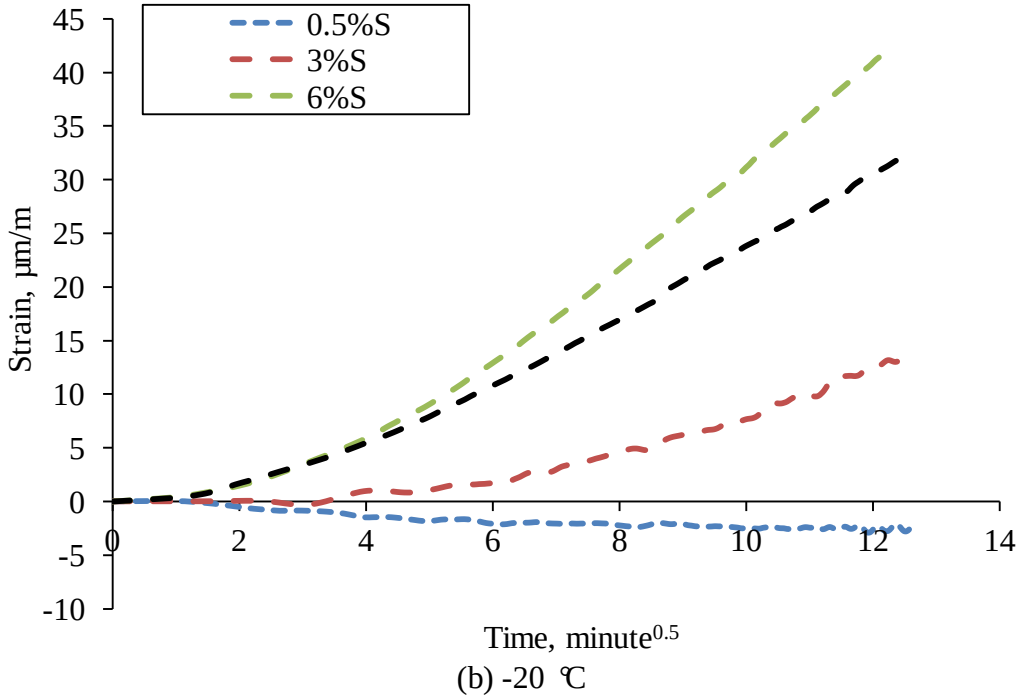

(b) -20 ℃

Figure 5.48 Isothermal dialtions of concrete exposed to different salt solutions

5.11 Thickness effect

Concrete disks of different thicknesses (12mm, 25mm, 45mm and 70mm) are tested in salt scaling test. All the disks reach capillary saturation before being exposed to F-T cycles and the saturation level is similar to one another (Figure 5.49(a)). It is shown in Fig. that the mass loss during the salt scaling test is increased with a thicker specimen (Figure 5.49(b)).

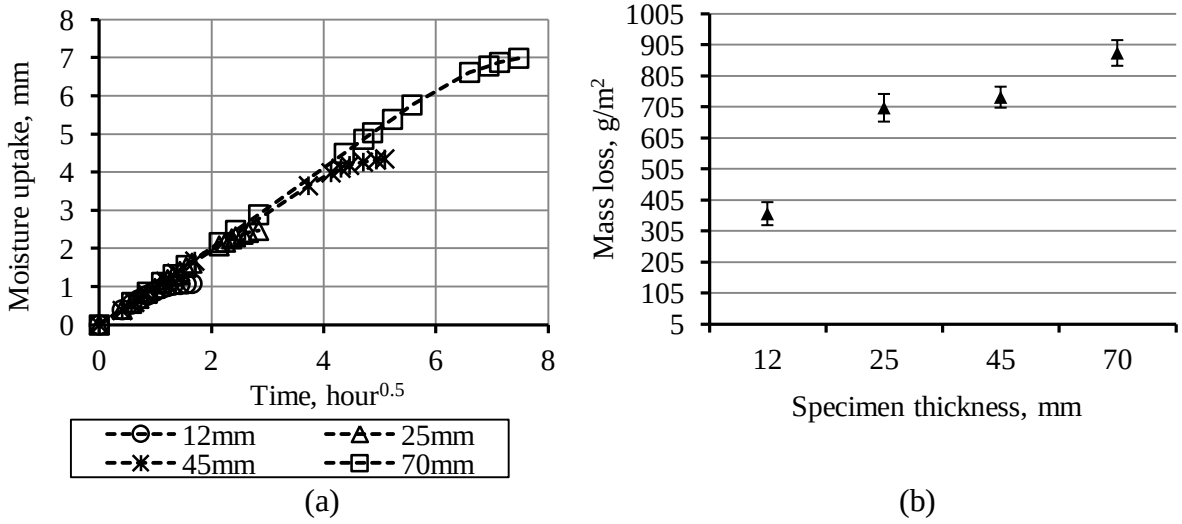

Figure 5.49 Moisture uptake curves of concrete disks with varied thicknesses and (b) correlation between concrete thickness and mass loss at 28 cycles

This feature may be a result of specimen size effect on internal ice formation. Ice formed in concrete pores or air voids is the engine to initiate the unsaturated moisture flow. More ice formation means more power to attract the surface liquid. In concrete of varied sizes with the same degree of liquid saturation, the total amount of internal ice formation is decreased in a thinner specimen (Figure 5.50). In addition, the diffusion of salt solution into concrete pores to equilibrate with pore water tends to suppress internal ice formation as well, and the reduction percentage is more significant when concrete specimen is thinner. An effort is made to quantify this effect. We assume a layer-by-layer diffusion front of the salt solution gradually moving inward and the equilibrium depth can be calculated by Eq. 7-1 (Valenza and Scherer 2006) where D is the coefficient of diffusion. With the knowledge of ice formation from low temperature dilatometer test, the amount of ice can be calculated that is formed at different penetration depth of a specific salt solution (3% NaCl solution in this case) (Table 5.4) and the fraction of ice formation normalized with respect to that of water saturated concrete. It can be

seen in Figure 5.51 that the degree of ice formation suppression is increased, especially at 12 mm specimen.

$$h = Dt^2 \tag{5-26}$$

Both of these two effects lead to a reduction in the driving force to draw surface liquid into concrete pores. The other factor may be that the generation of hydraulic pressure is more readily dissipated to the top surface when the thickness is smaller.

Table 5.4 Calculated ice formation rate in concrete

Saturation liquid	Ice formation in LTD test g/per specimen	LTD specimen volume, cm^3	Ice formation g/cm^3 concrete	Ice formation g/(mm penetration·m^2 concrete)
water	0.182	10.52	0.01726	17.26
3% salt	0.108	10.02	0.01082	10.82

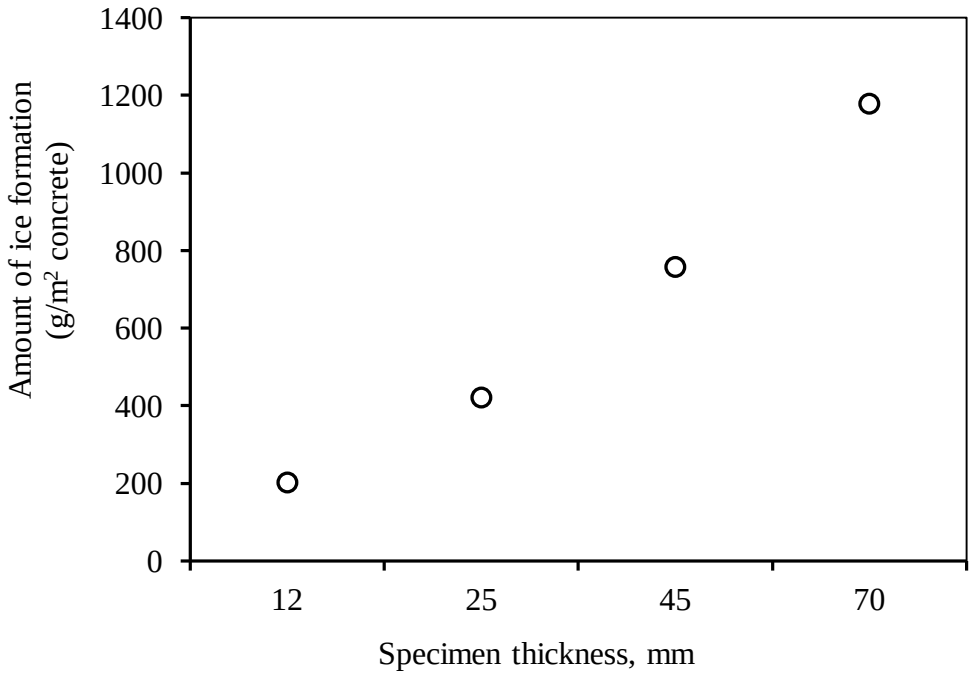

Figure 5.50 Amount of total ice formation per unit area of concrete of different thicknesses

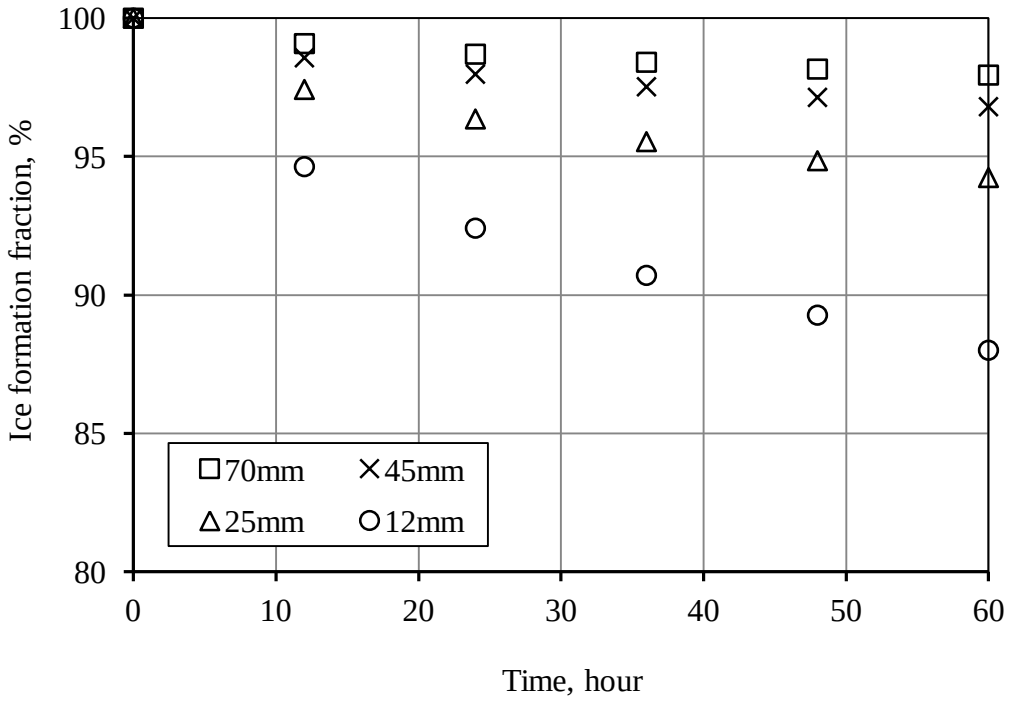

Figure 5.51 Fractional ice formation in concrete exposed to 3% salt solution

5.12 Summary of findings

This chapter consolidates the cryogenic suction theory for salt frost scaling in air-entrained concrete and the major conclusions are as follows

- Some common features associated with salt frost scaling are reviewed with experimental observations. Scaling is shown to be a paste deterioration restricted within a thin surface region (~50-300 μm) and the destruction stress is originated from beneath the surface. The "pessimum" salt concentration range is found to be 0.5-6% based on several different investigations.
- Internal damage and surface scaling are studied extensively. A critical amount of air entrainment (Powers' spacing factor< 200 μm) is required for bulk cracking prevention. Otherwise, salt scaling is markedly increased when coupled with internal damage, which is characterized by the falling of coarse aggregate particles. Nevertheless, no added benefit is gained in salt scaling resistance with a further increase in air content beyond the critical value.
- Moisture flow in moisture-isolated concrete under freezing is shown to cause both shrinkage and dilation, depending on the competing effect of ice accretion and the associated pore drying. A thermodynamic approach incorporating the effect of liquid supercooling is

proposed to account for the spontaneous movement of pore moisture and effect of salt concentration.

- Ice growth in capillary pores is found to be substantially augmented when a salt solution is present on concrete surface, which is evidenced by the significant secondary dilation immediately after the nucleation temperature in length-change measurement and the almost doubled pore volume increase in scaled-off materials from nitrogen sorption test. This serves as strong indication that there is added moisture transported into concrete pores to promote the ice growth therein. The central role of salt in the surface liquid is to maintain a fraction of interconnected unfrozen brine pockets embedded in the ice when the salt solution is under freezing. The major transport mechanism is believed to be cryogenic capillary suction from the rapid and linear development of dilation strain against the square-root of time.
- A conceptual model is proposed to account for the paste swelling and flaking due to a combined salt-frost attack. Ice-growth creates the 3-D pore stresses in the surface zone which results in residual compressive stress within the two confined directions (length and width) because of the restraint from the bulk specimen. Thus, a net tensile stress in the unconfined direction is resulted which causes "popout" if the tensile capacity of cement paste is exceeded.
- Air entrainment is shown to have negligible effect on both the capillary suction rate and the contraction strain under freezing, which explains the lack of its correlation to scaling resistance. Increasing the salt concentration in the surface liquid has counterbalancing effect in the pore ice growth: more unfrozen moisture is available while the penetration of salt into concrete pores tends to suppress the ice formation and growth. This results in the "pessimum" effect.

CHAPTER 6 PERFORMANCE-BASED EVALUATION OF SCALING RESISTANCE

6.1 General

Typical laboratory assessment of concrete scaling resistance consists of regularly measuring the weight gain and mass loss of a specimen under cyclic salt/F-T exposure, which is a laborious and time-consuming process. Nowadays, there is an increasing interest in the investigation of concrete transport properties as the performance-based criteria that facilitate rapid evaluation and innovative design in concrete durability at the material level (Hooton et al. 1993, Kropp 1995, Alexander et al. 2008).

Concrete sorptivity, S, which characterizes the rate of water uptake by capillary forces, is uniquely related to capillary porosity and pore structure of the porous hydration products within the portland cement paste (Sellevold 1990). Thus, this property has been proposed as a predictor for quality control (Sellevold 1990, Taus et al. 2005) and service life design (Bentz et al. 2001) of concrete structures. Several attempts have also been made to correlate it with salt frost scaling (Liu and Hansen 2014, Chidiac and Panesar 2006, Gagné et al. 2011).

Experimental determination of sorptivity typically consists of regular measurement of cumulative moisture uptake per unit inflow surface area of a pre-dried disc specimen in contact with water on one side. Sorptivity is then obtained from the established linear moisture uptake curve against the square-root of time (Figure 6.1), which can be described as

$$Q = St^{0.5} + A \tag{6-1}$$

Q is the cumulative moisture uptake per inflow concrete area (mm^3/mm^2) in the surface region, S is the corresponding sorptivty ($mm/hour^{0.5}$). In practice, a finite, but small intercept A is usually found which is attributed to the filling of open surface pores (Hall 1989).

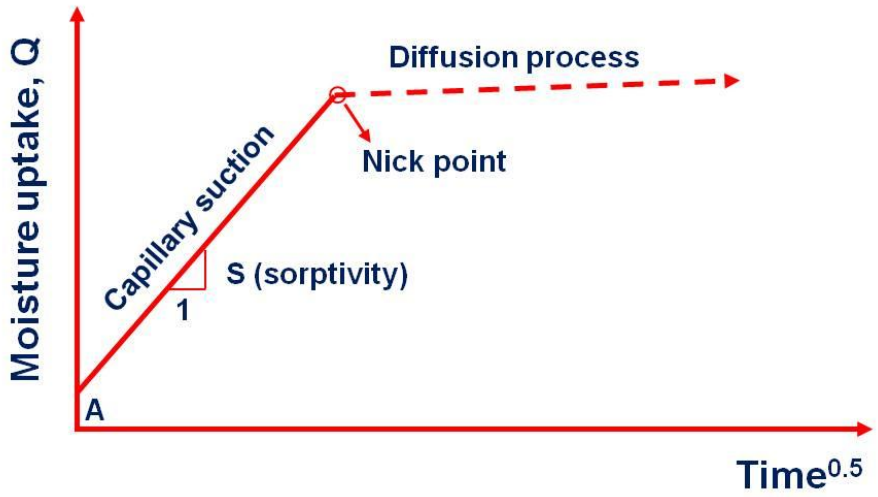

Figure 6.1 An idealized moisture uptake curve in concrete

The main objective of this chapter is to enhance the theoretical nature of sorptivity and evaluate its role with respect to salt frost scaling by a refined model for calculating sorptivity, combined with pore structure measurements from nitrogen adsorption isotherms. In the meantime, surface treatment using silanes is also explored as a mitigation technique to improve the service life of existing concrete structures. By validating sorptivity as an effective indicator of scaling resistance, this work will hopefully advance the application of performance-based specifications for concrete durability evaluation in actual construction practices.

6.2 Empirical correlation between sorptivity and scaling resistance

It is seen from Figure 6.2 that surface scaling resistance is strongly correlated with sorptivity. Such a relationship was reported by (Gagné et al. 2011) as well. These results suggest that the pore structure of the paste hydration products plays a decisive role with respect to salt frost scaling, since concrete sorptivity is an indicator of capillary suction which has been proposed to be the primary transport mechanism under sub-freezing condition in promoting ice growth in the surface-region capillary pores that eventually leads to scaling (Liu and Hansen 2014). While air entrainment, as shown before, is needed to prevent internal cracking (Pigeon and Pleau 1995) (Figure 6.3 (a)), no added benefit is achieved for scaling resistance at a higher air content (>4%) when the Powers' spacing factor is below 200 μm (Figure 6.3(b) and Figure 6.4), which is consistent with the negligible effect of air content on sorptivity (Chapter 5). The presaturation curves further reveal the major factors controlling pore structure include w/b ratio,

supplementary cementitious materials (such as slag cement) (Pigeon and Pleau 1995, Manmohan and Mehta 1980).

Therefore sorptivity is an effective parameter in evaluating scaling resistance and its theoretical aspect will be further explored in the next section. In the following sections, theoretical nature of capillary suction will be reviewed and simplified model on concrete sorptivity will be constructed, which provides quantification efforts to sorptivity as a scaling resistance predictor.

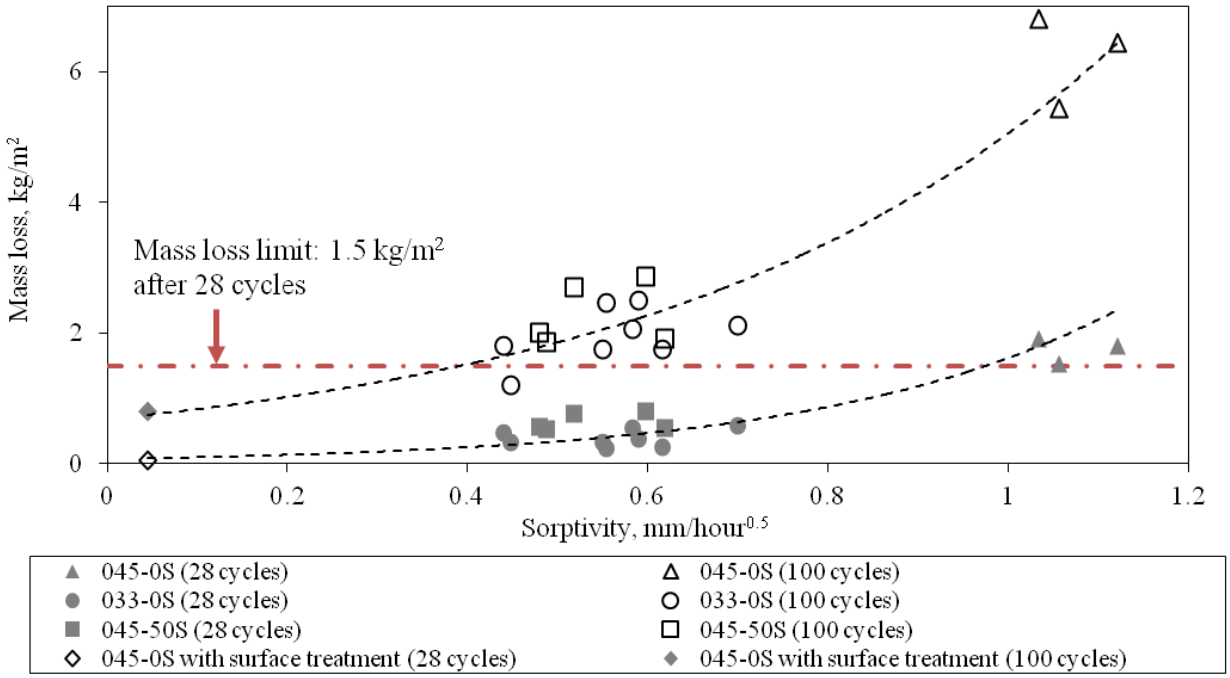

Figure 6.2 Correlation between sorptivity and mass loss at different cycles

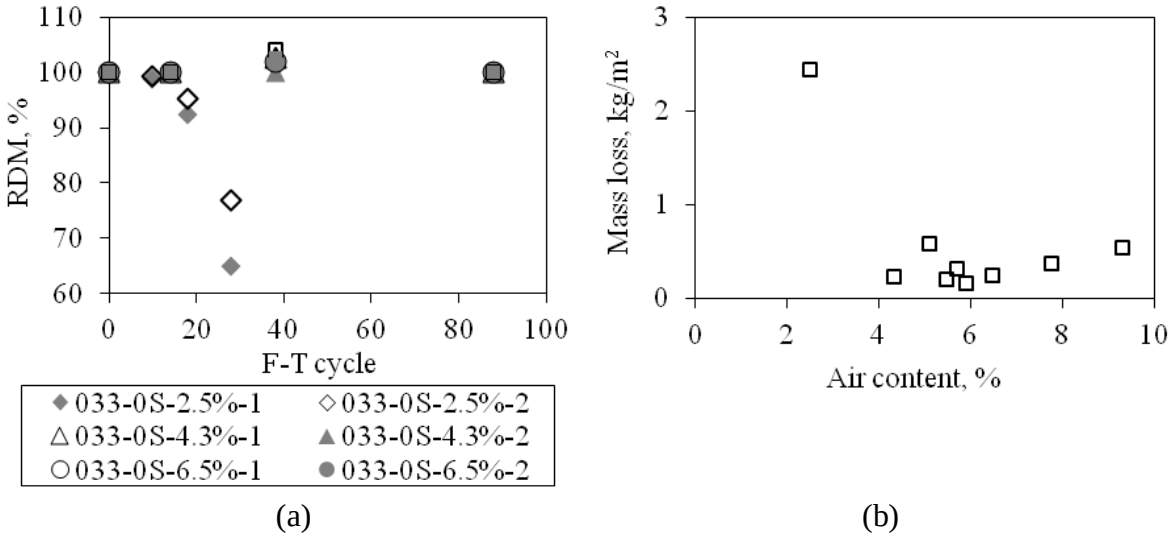

(a) (b)

Figure 6.3 (a) RDM vs. F-T cycles and (b) mass loss after 28 F-T cycles vs. air content (033-0S mixes)

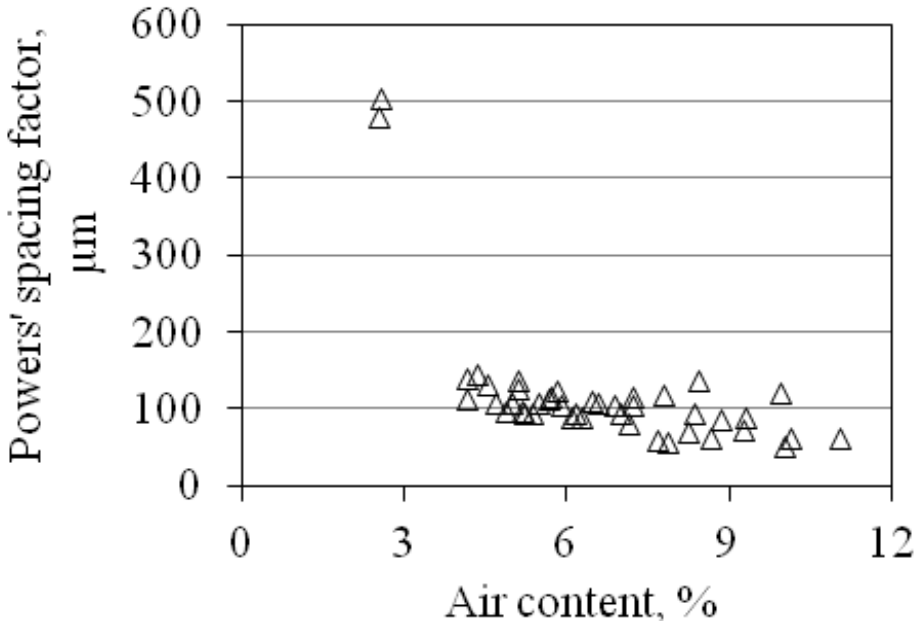

Figure 6.4 Measured Powers' spacing factor and total air content (033-0S mixes)

6.3 Kinetics of capillary suction

When a cylindrical tube of small diameter (a capillary) is in contact with free water, a meniscus forms in the tube due to the contact angle between water and the tube walls and minimum surface energy requirements. The pressure at the water side is lower than the atmospheric pressure. This pressure difference causes a water rise in the tube until the capillary pressure is

balanced out by the weight of the water column. The static equilibrium height can be calculated as follows.

The upward capillary pressure is

$$\Delta P = \frac{2\pi r\sigma \cos\theta}{\pi r^2} = \frac{2\sigma \cos\theta}{r} \tag{6-2}$$

where σ is the surface tension of the liquid and is liquid and is 0.07272 N/m for water at 20 ℃, θ is the contact angle and is normally about 0 °for water.

This is the famous Laplace equation.

The ultimate capillary rise can be calculated by force equilibrium.

$$\Delta P = \frac{2\sigma \cos\theta}{r} = \rho g h \tag{6-3}$$

$$h = \frac{2\sigma \cos\theta}{\rho g r} \tag{6-4}$$

This indicates that water rise by capillary force is higher, the smaller the tube is.

However, this equilibrium height of water movement in a capillary tube doesn't impart any information regarding the rate of rise and the associated time scale, which is of great significance in the unsaturated water movement in concrete. Washburn is among the first to give an analytic explanation of the rate of liquid rise in a capillary tube and he considers a flow regime where the influence of inertia and the influence of gravity can be neglected (Washburn 1921).

Poiseuille's law

$$\frac{dV}{dt} = \frac{\pi \Delta P}{8\eta x}(r^4 + 4\varepsilon r^3) \sim \frac{\pi \Delta P r^4}{8\eta x} \tag{6-5}$$

where dV is the volume of liquid flowing through the cross-section of the capillary pore with a radius r in time dt. η is the viscosity of the liquid and is 1.002 Pa s for water at 20 ℃, x is the length of the column of liquid in the capillary pore, ΔP is the pressure head along the liquid column, ε is the slip factor and is assumed to be zero.

Since $dV = \pi r^2 dx$,

$$\frac{dV}{dt} = \frac{\pi r^2 dx}{dt} = \frac{\pi \Delta P r^4}{8\eta x} \tag{6-6}$$

Thus,

$$\frac{dx}{dt} = \frac{\Delta P r^2}{8\eta x} \tag{6-7}$$

Plugging Eq. (6-2) into Eq. (6-7) yields

$$\frac{dx}{dt} = \frac{\Delta P r^2}{8\eta x} = \frac{\sigma r}{4\eta x} \tag{6-8}$$

Taking the integration produces the Washburn's equation

$$x = (\frac{\sigma r}{2\eta})^{0.5} \cdot t^{0.5} \tag{6-9}$$

6.4 Modelling of Concrete sorptivity

Concrete sorptivity is the representation of the kinetics of capillary suction in its pore system. Theoretical computation of concrete sorptivity was proposed in a model by Sellevold that correlates sorptivity to the total capillary pore volume (Sellevold 1990). He simplified capillary pore structure to one straight circular tube with an average pore radius r (Figure 6.5) and sorptivity S is a function of capillary porosity ϵ_0 and the average pore radius r of the paste pore system (Eq. 6-10).

$$S = (\frac{\sigma r}{2\eta})^{0.5} \epsilon_0 \tag{6-10}$$

where σ and η are the surface tension and viscosity of the liquid, which are 7.272×10^{-5} N/mm and 1.002×10^{-3} N s/m^2, respectively, for water at 20 ℃.

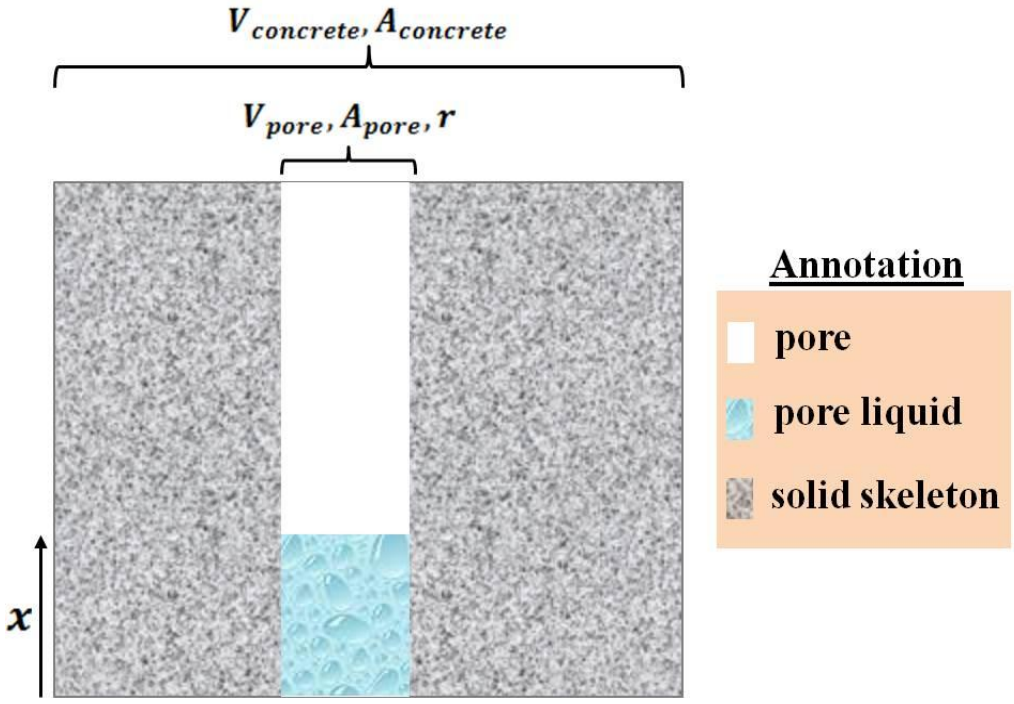

Figure 6.5 Simplification of concrete pore structure in Sellevold's model (Sellevold 1990)

Two pore properties (ϵ_0, r) are needed for sorptivity calculation, both of which can be obtained from the nitrogen adsorption measurement, as shown in Figure 6.6. An S-curve is used to model the cumulative pore size distribution (Eq. 6-11).

$$\mathcal{E} \sim \frac{\epsilon_0}{\exp\left(\frac{\tau}{x}\right)^{n}} \tag{6-11}$$

where ϵ_0 is the total pore volume in the paste, which can be estimated by extrapolating the size range to 10 μm as the upper limit for capillary pores (Mindess et al. 2002). τ and n are curve fitting parameters by the method of least squares. The average pore radius is estimated by the Mean Value Theorems for Integrals.

As seen from Table 6.1, the predicted sorptivity is much higher than the measured, which is attributed to the single pore assumption with the same straight and circular shape. In reality, the pore structure in concrete is more complicated in shape, thus increasing the resistance to moisture uptake by capillary forces.

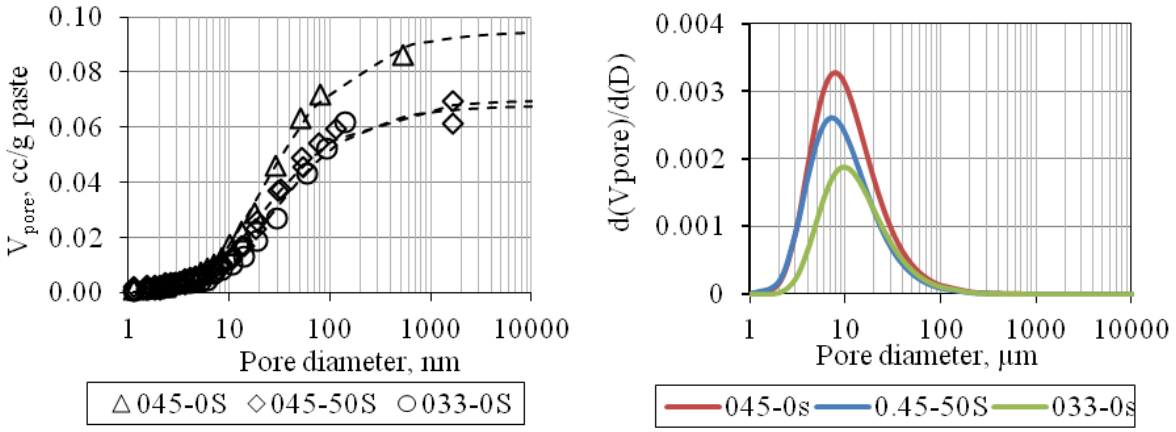

(a) (b)

Figure 6.6 (a) Cumulative and (b) differential pore size distribution in paste samples

Table 6.1 Calculated average pore radius and the sorptivity

	r, nm	ϵ_0, cc/g bulk paste	$\rho_{bulk\ paste}$, g/cc	ϵ_0, cc/cc concrete	S, mm/hour$^{0.5}$	
					predicted	measured
045-0S	86	0.0964	1.68	0.0405	4.3	1.0
045-50S	86	0.0699	1.77	0.0309	3.2	0.55
033-0S	62	0.0680	1.74	0.0296	2.7	0.53

In the following section, Sellevold's model is adapted to include the size distribution effect by the construction of a multitude of pore clusters. In this model, a cement paste specimen with a cross-section area of A_p and a height of h is idealized to be composed of solid paste phase and n clusters of straight circular pores with a radius of r_i and a volume of $V(r_i)$ (cc/cc paste) (Figure 6.7).

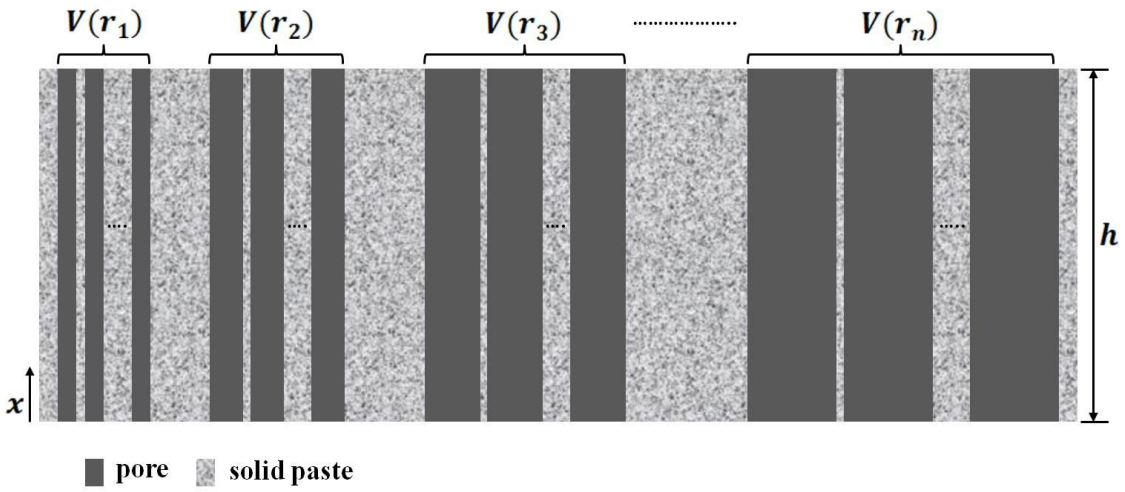

Figure 6.7 Simplification of pore geometry and its distribution in paste

Upon contact with water, a wet front rises through the pores. The capillary rise x_i in the pore cluster with a radius r_i can be computed by Washburn's equation, as shown before.

$$x_i = (\frac{\sigma r_i}{2\eta})^{0.5} \cdot t^{0.5} \tag{6-12}$$

In order to calculate the volume of water uptake, the cross-section area of the aggregated pores in each cluster $\mathrm{A(r_i)}$ is needed.

$$\mathrm{V(r_i)} = \frac{\text{Pore volume } (\mathrm{r_i})}{\text{Paste volume}} = \frac{\text{Pore area } (\mathrm{r_i}) \times \mathrm{h}}{\text{Paste area} \times \mathrm{h}} = \frac{\mathrm{A(r_i)}}{\mathrm{A_p}} \tag{6-13}$$

So

$$\mathrm{A(r_i)} = \mathrm{V(r_i)A_p} \tag{6-14}$$

Thus, the water uptake in each pore cluster is

$$\mathrm{V_w(r_i)} = \mathrm{A(r_i)x_i} = \mathrm{A_pV(r_i)x_i} \tag{6-15}$$

The cumulative water uptake in all pores is

$$V_{w,total} = \sum_{i=1}^{n} V_w(r_i) = \sum_{i=1}^{n} A_p V(r_i) r_i = A_p[\sum_{i=1}^{n} V(r_i) x_i] \tag{6-16}$$

The cumulative water uptake per unit cross-section area of concrete A_c is

$$Q(t) = \frac{V_{w,total}}{A_c} = \frac{A_p[\sum_{i=1}^{n} V(r_i) x_i]}{A_c} = P_{paste} \sum_{i=1}^{n} V(r_i) x_i \tag{6-17}$$

where P_{paste} is the paste content determined from point count method.

Plugging Eq. (6-12) into Eq. (6-17) yields

$$Q(t) = P_{paste}(\frac{\sigma}{2\eta})^{0.5}[\sum_{i=1}^{n} V(r_i) r_i^{0.5}\, t^{0.5}] \quad (6\text{-}18)$$

This clearly shows the strong dependence of sorptivity on the pore size distribution and the total pore volume of concrete. It also demonstrates moisture uptake in large capillary pores is faster.

In order to construct the moisture uptake curve as the basis for sorptivity prediction, the incremental pore volume $V(r_i)$ at the pore radius r_i is extracted from Figure 6.6(a). When a series of time points are assigned, the respective cumulative moisture uptake $Q(t)$ can be computed from Eq. (6-18). As seen from Figure 6.8 for the modelled moisture uptake curve of a 70 mm thick concrete specimen, there is initially a linear development with the square-root of time for a short time period, within which sorptivity is typically calculated as the curve slope (Gagné et al. 2011, ASTM C1585, Hall 1989). This is followed by a gradual departure from linearity, which is associated with the incremental termination of capillary rise in pores since the water front has reached to the top. This feature enables the model to predict the observed non-linearity in some concrete mixes by capping the pores to various heights water can advance, as shown in Figure 6.9.

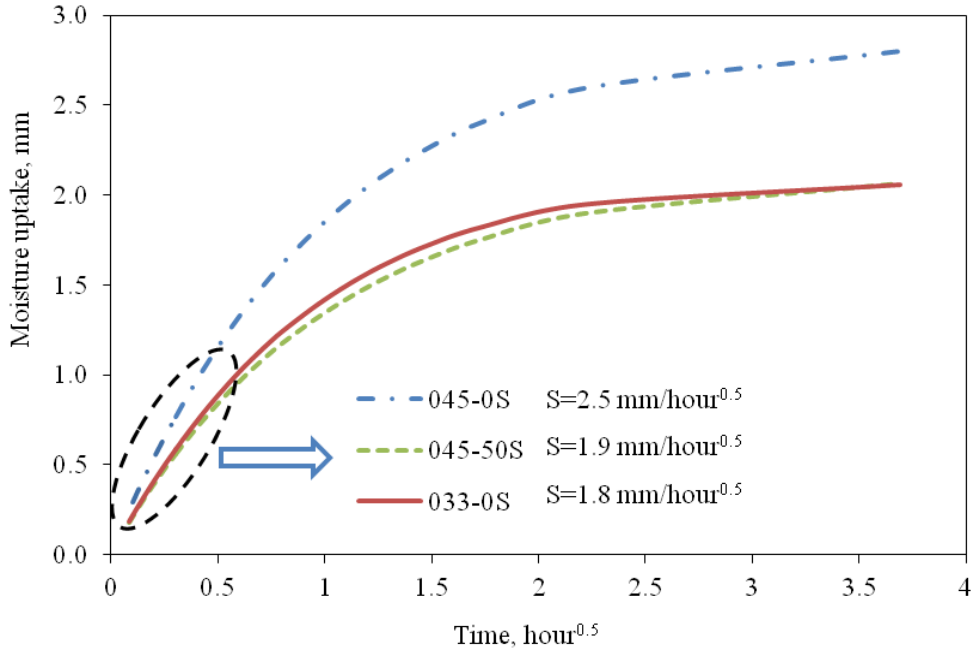

Figure 6.8 Modelled moisture uptake curve

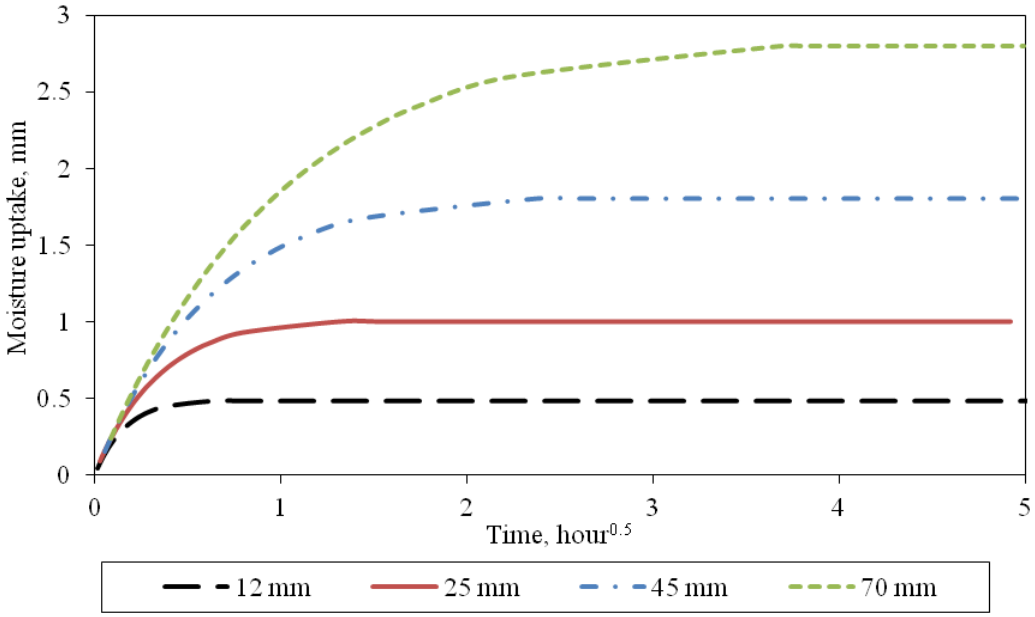

Figure 6.9 Pore discontinuity effect in the 045-0S mix

Albeit its limitations, this preliminary work yields improved prediction on concrete sorptivity and if aided with further refinement in incorporation of pore shape and continuity factors, can be a precursor to the construction of a performance-based prediction model for scaling resistance.

6.5 Salt concentration and temperature effects on sorptivity

For a paste of given pore structure, its sorptivity of a wetting liquid is affected by $(\sigma/\eta)^{0.5}$. Both the surface tension and dynamic viscosity of the liquid vary with temperature and the concentration of the solutes, as seen in Figure 6.10 and Figure 6.11. While a higher NaCl concentration increases the two parameters, a higher temperature reduces them. Their effect on calculated sorptivity is shown in Figure 6.12. A small variation in sorptivity is observed with the increase in NaCl concentration, while a reduction in sorptivity is appreciable at lower temperature. This may partially explain the reduced isothermal subfreezing dilation at -20 ℃ compared than -10 ℃ in Chapter 5.

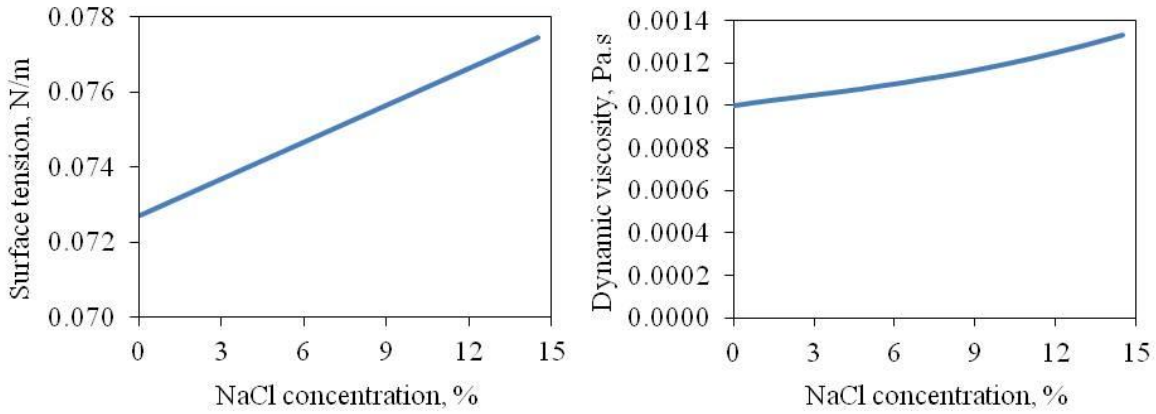

Figure 6.10 Effect of salt concentration on surface tension and dynamic viscosity of a salt solution at 20 ℃

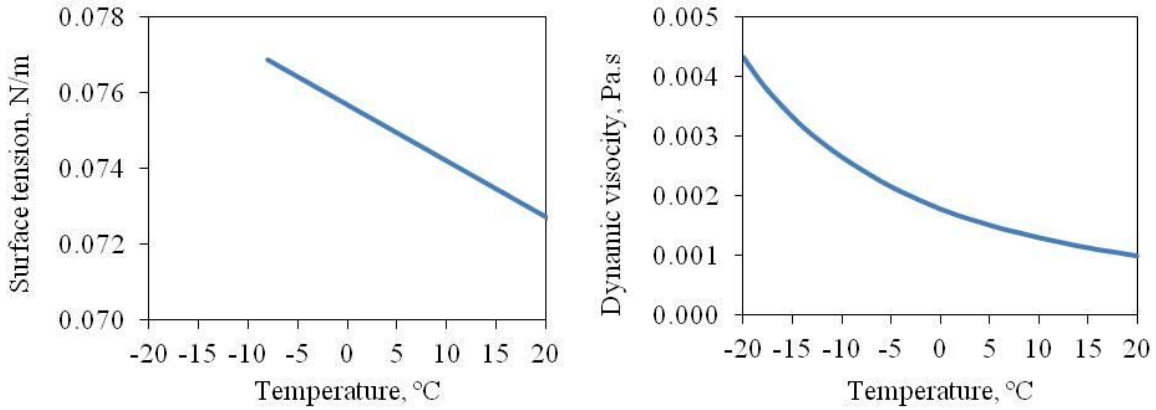

Figure 6.11 Effect of temperature on surface tension and dynamic viscosity of water

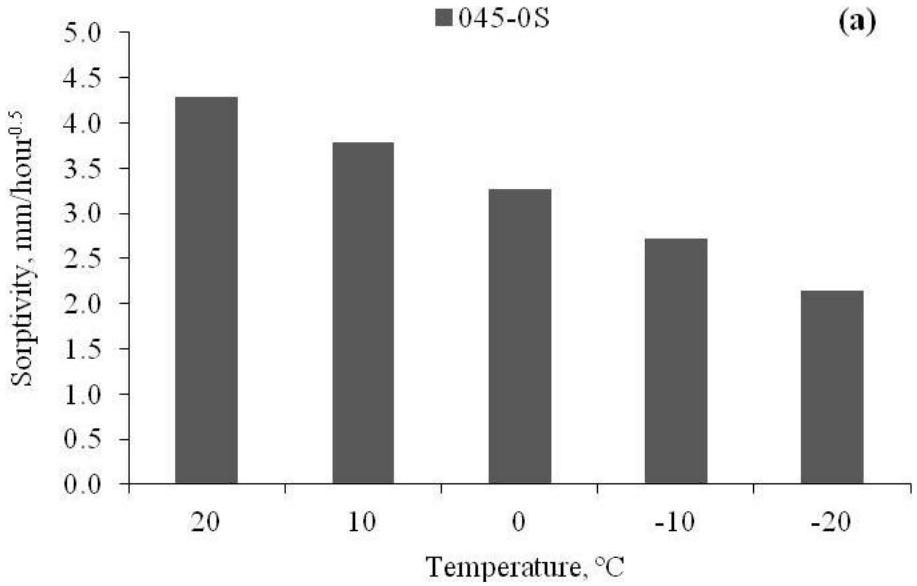

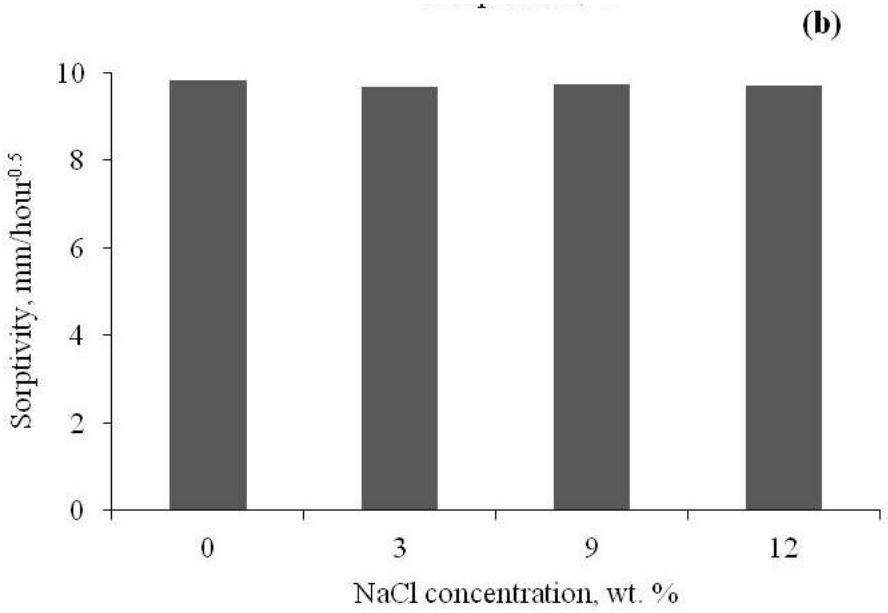

Figure 6.12 Effect of (a) temperature and (b) salt concentration on calculated sorptivity (045-0S)

6.6 Pore structure effect

Several studies have shown a close relationship between pore structure and ice formation (Machard et al. 1999, Hammer and Sellevold 1990, Sellevold et al. 1991). The amount of initial ice nucleation is mainly affected by the total porosity and pore size distribution, which is evidenced in Figure 6.13 by a good correlation between the calculated ice formation and sorptivity, a physical parameter of capillary suction rate that is uniquely related to capillary porosity and pore size distribution (Sellevold 1990, Liu and Hansen 2014). When there exists external liquid transport such as the salt frost exposure, pore continuity comes into play as well which controls the capillary suction rate, and thus the ice growth.

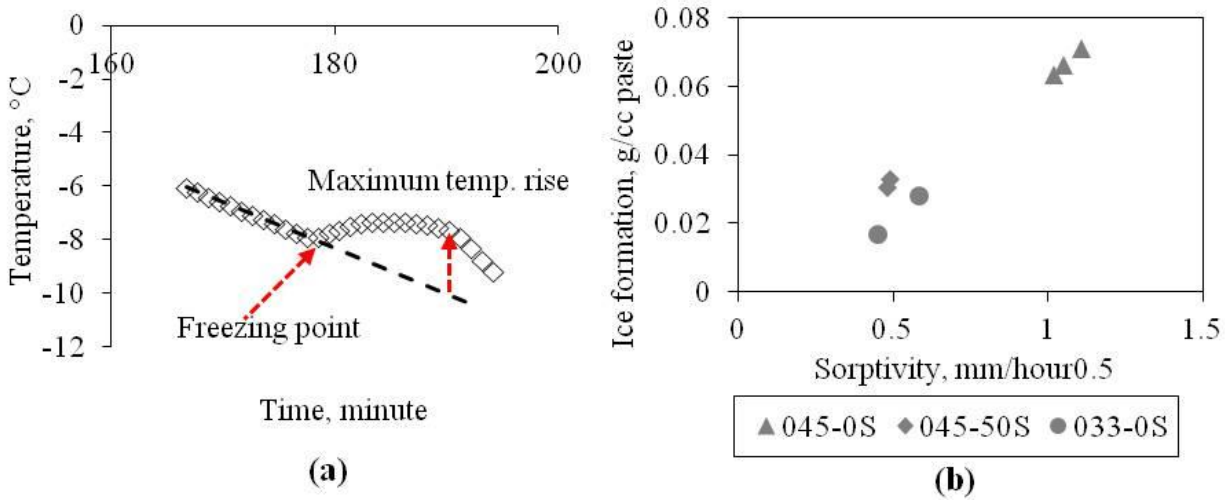

Figure 6.13(a) Temperature rise calculation from the LTD measurement for instant ice formation determination; (b) correlation between instant ice formation and sorptivity (ice amount is calculated from the temperature rise associated with the release of fusion heat (Fridh 2005)

These pore parameters can be altered by the w/c ratio or incorporation of supplementary cementitious materials (e.g. slag cement) (Marchand et al. 1999, Feldman 1983, Feldman and Sereda 1968). This is clearly demonstrated by the moisture uptake curves in pre-dried specimens for three different concretes (Figure 6.14). Both the cumulative moisture absorption (total porosity) and the rate of capillary suction (pore size distribution and connectivity) are reduced for the 033-0S-9.3% and 045-50S-3.0% mixes, which is accompanied by improved scaling resistance (Figure 6.15). In addition, these two mixes show a smooth transition between capillary suction and diffusion, while a well-defined nick point is seen for the 045-0S-5.1% mix, a typical sign of capillary saturation and good pore connectivity (Fagerlund 2004, Sellevold 1990). The pore continuity effect can be also detected by the size-dependent moisture uptake in specimens of different thicknesses (Figure 6.16). When normalizing the absorption in specimens of 12, 25 and 45 mm by a thickness multiplier (70/12=5.83, 70/25=2.80, 70/45=1.56), there is a significant discrepancy between the normalized uptake in thinner specimens and the 70-mm measured uptake for the 033-0S-9.3% and 045-50S-3.0% mixes (Figure 6.17), indicating increased pore discontinuity with thickness (Nguyen et al. 2012). It is also noted that sorptivity is independent of specimen thickness (Figure 6.18).

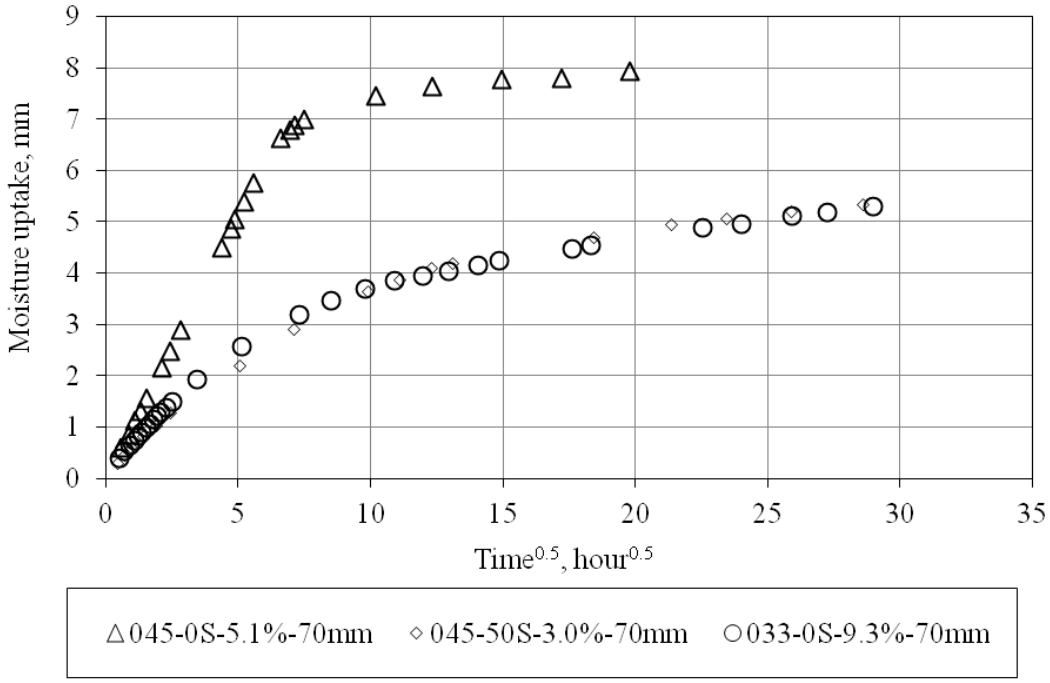

Figure 6.14 Moisture uptake curves in pre-dried specimens for different concretes at room temperature

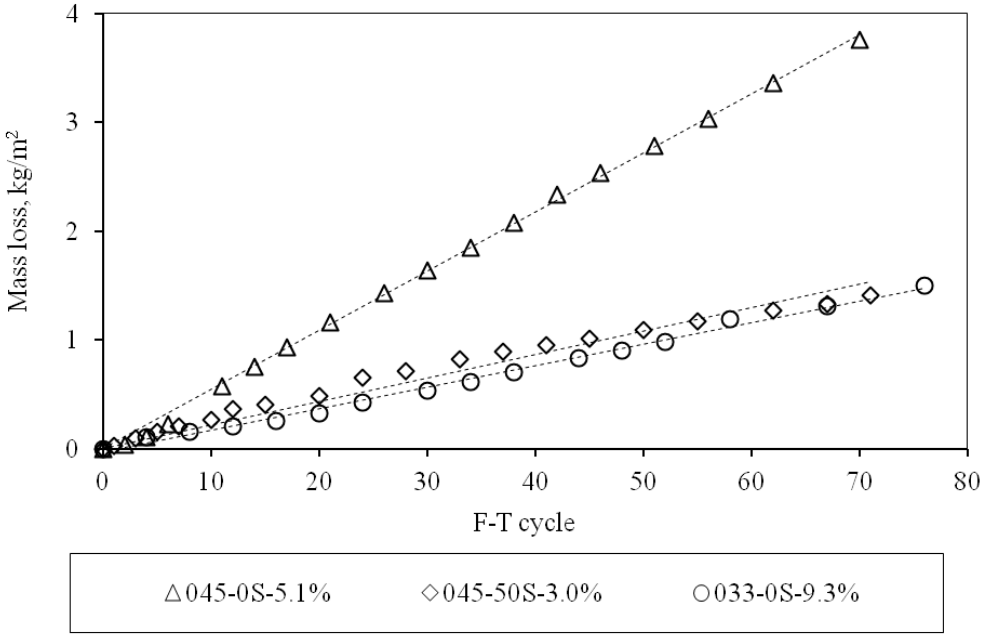

Figure 6.15 Mass loss in different concretes

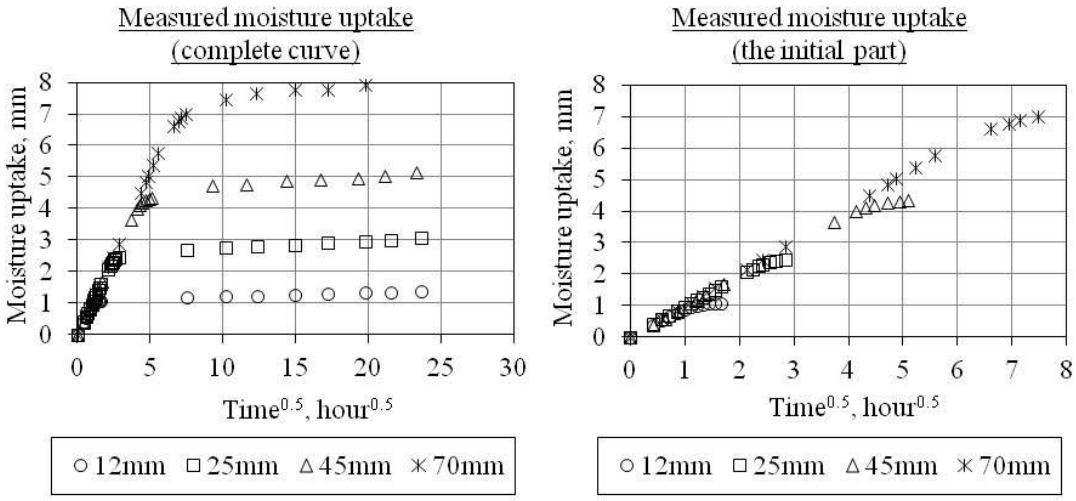

(a) 045-0S-5.1%

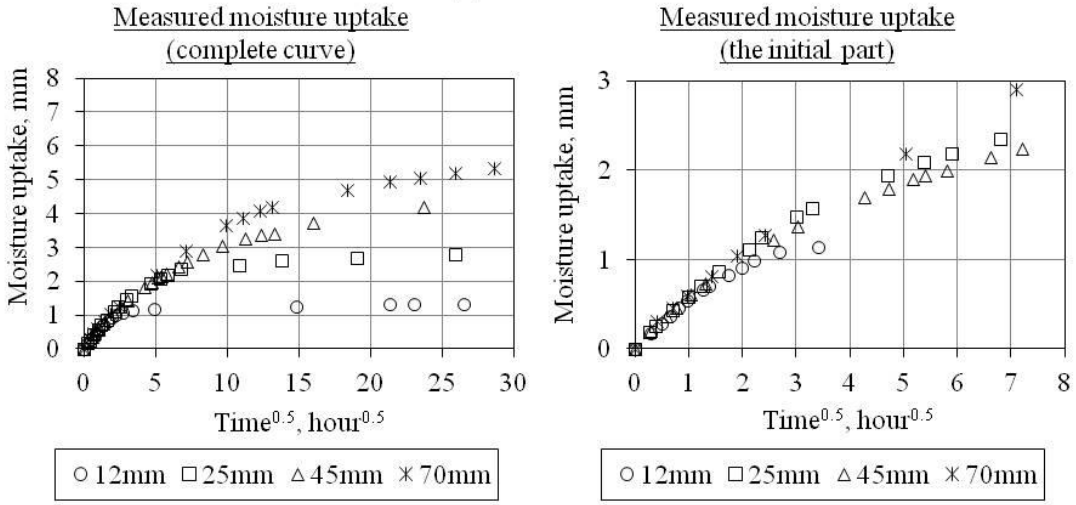

(b) 045-50S-3.0%

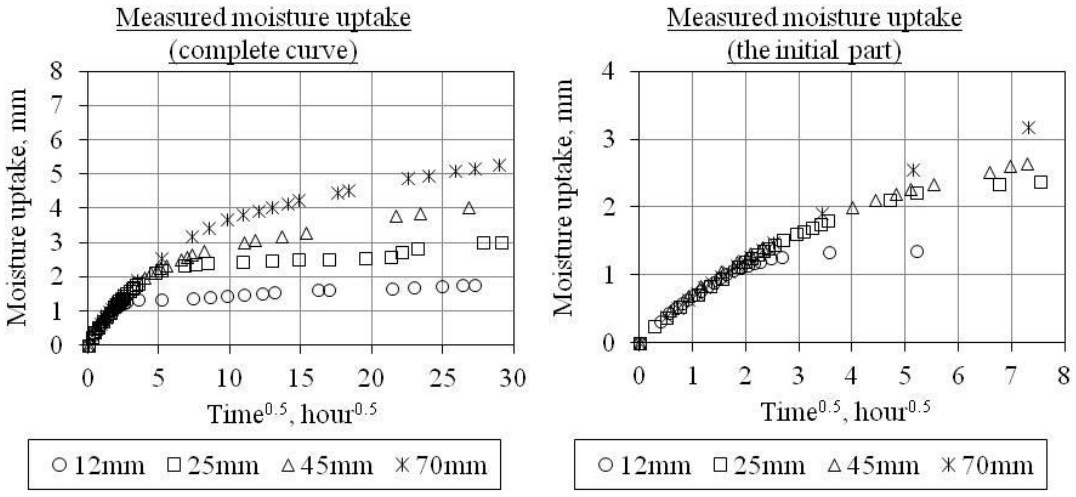

(c) 033-0S-9.3%

Figure 6.16 Moisture uptake curves in different concretes

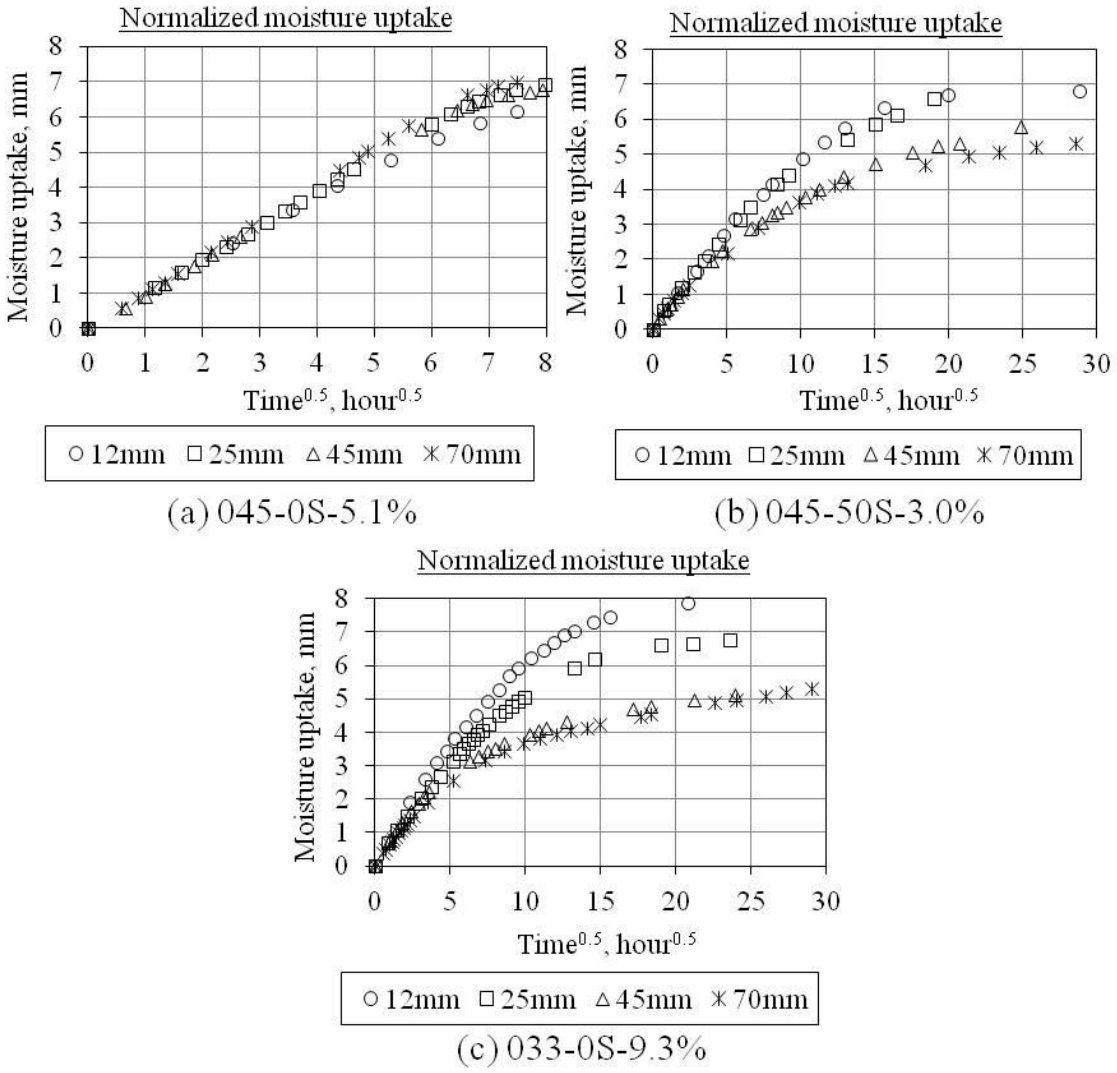

Figure 6.17 Normalized moisture uptake

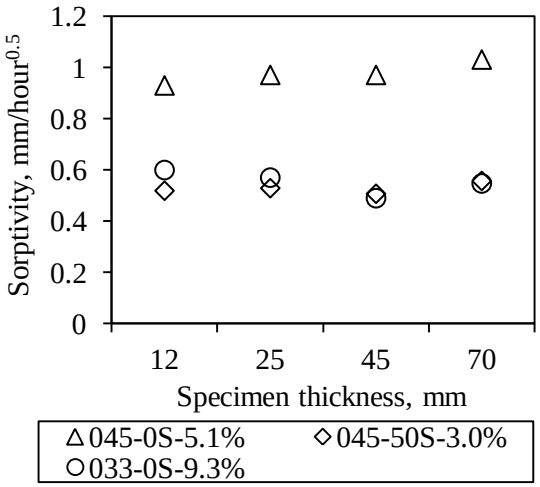

Figure 6.18 Effect of thickness on concrtete sorptivity

6.7 Moisture ingress repulsion by surface treatment

Hydrophobic surface treatment has been proven to be an effective technique to minimize moisture transport into concrete and its effect on durability improvement and service life extension is well-documented (Snyder 1965, Wong et al. 1983, Vries and Polder 1997, Hazrati et al. 1997, Basheer and Cleland 2006, Tittarelli and Moriconi 2008, Selander 2010, Freitag and Bruce 2010, Christodoulou 2013, Dang et al. 2014). There are currently three types of hydrophobic treatment methods, as illustrated in Figure 6.19.

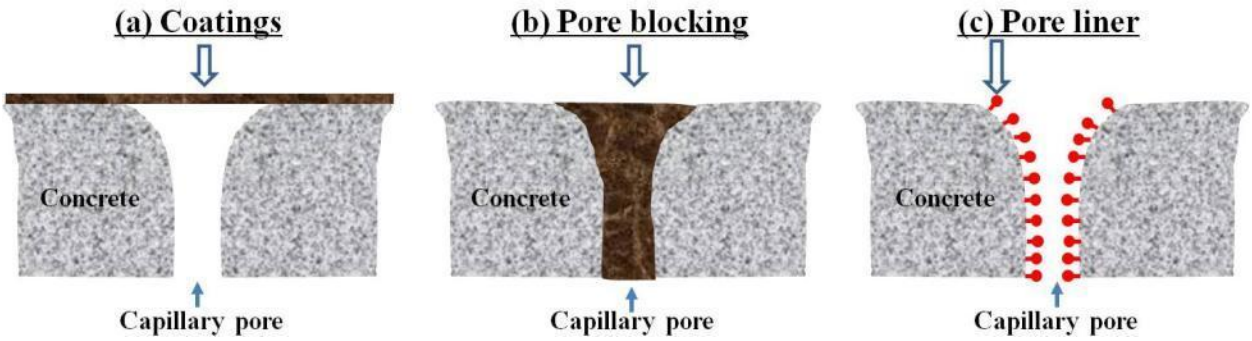

Figure 6.19 Common surface treatment techniques for concrete

Silanes are low molecular weight pore liners with a molecular size of 1-2 nm (Tittarelli and Moriconi 2008), thus they can easily penetrate capillary pores. Unlike the coating and pore blocking agents, silanes only modifies the substrate (pore walls in this case) by chemically react with the hydrated silicates via a two-step process (hydrolysis and condensation) (Wong et al. 1983, Basheer and Cleland 2006), rendering the pore hydrophobic while maintains its breathability (i.e. the slow diffusion of gas or vapor) (Basheer and Cleland 2006, Tittarelli and Moriconi 2008) (Figure 6.19(c)). This is clearly seen from the nitrogen sorption measurement in Figure 6.20 which shows similar pore volume in mortar specimens with and without silane treatment.

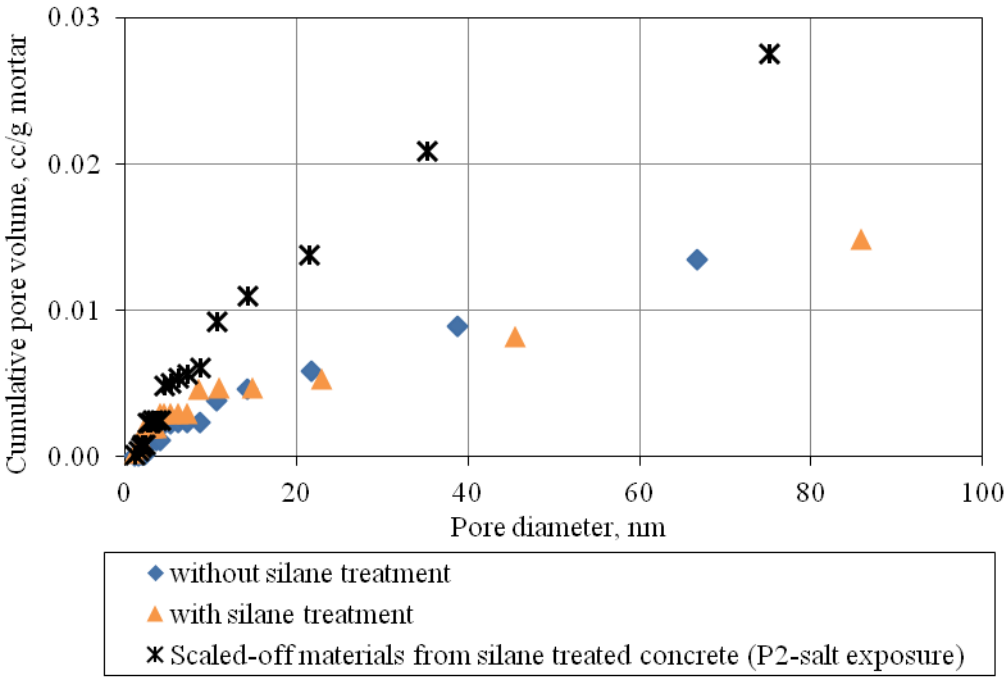

Figure 6.20 Effect of silane treatment on mortar pore volume

Capillary suction is an unsaturated transport process by means of capillary forces, which is a function of surface tension σ of the wetting liquid and its contact angle θ with a pore of a radius r.

$$\Delta P = \frac{2\sigma \cos\theta}{r} \tag{6-19}$$

It is thermodynamically a spontaneous process when θ<90 °, in which case there is a molecular attraction between the liquid and substrate, accompanied by a capillary rise and a concave meniscus (Figure 6.21(a)). silanes is able to increase the contact angle above 90 ° by forming a water repellent lining on the pore walls (Kargol et al. 2013, Tittarelli and Moriconi 2008, Basheer and Cleland 2006) (Figure 6.21(b)), such that the pressure difference is reversed and extra work is needed for moisture to penetrate the pores (de Vries and Polder 1997). Moreover, studies have shown silanes used as surface impregnators possess no surface strengthening effect (Sha'at et al. 1993, Nolan et al. 1995).

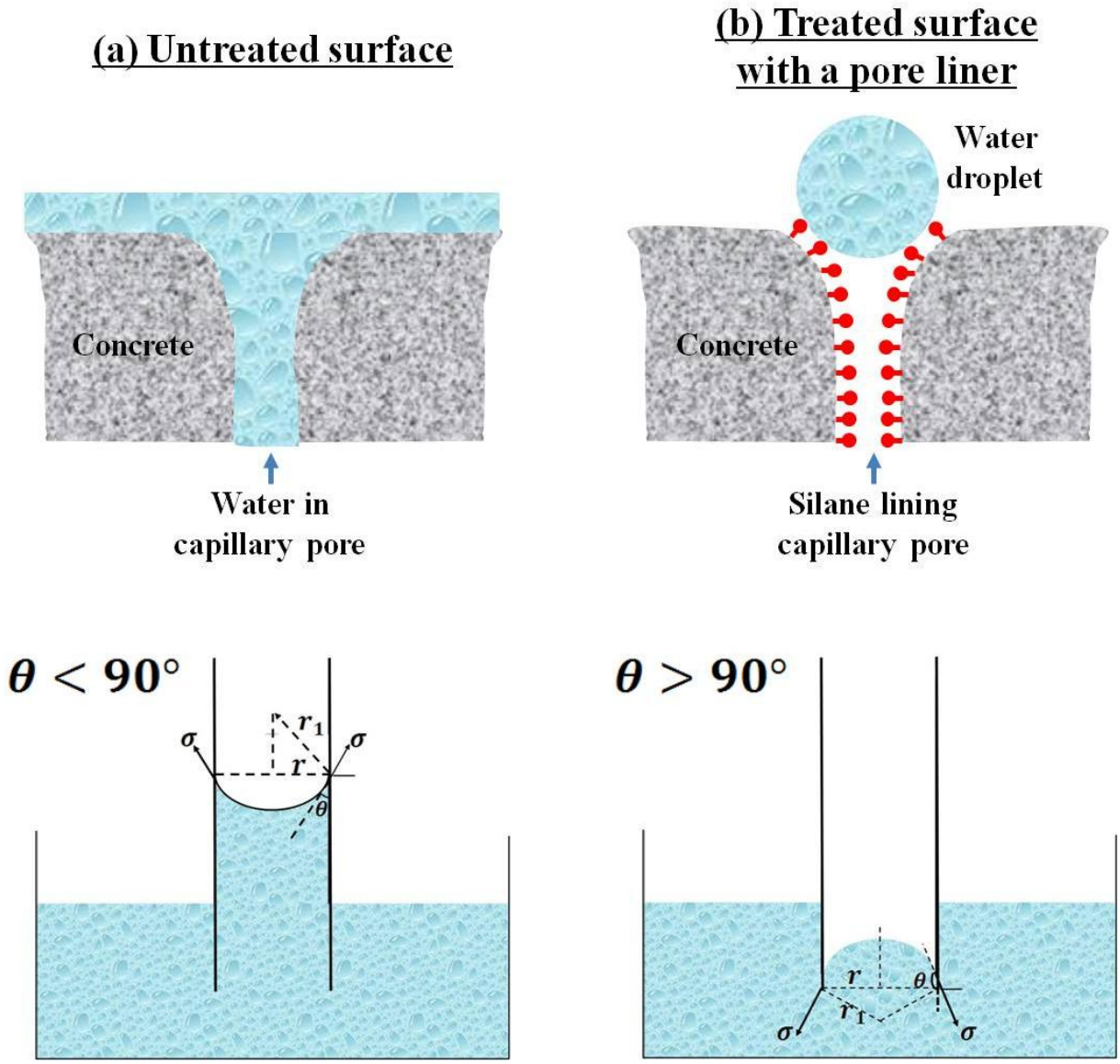

Figure 6.21 Illustration of silane pore lining effect

In this section, hydrophobic surface treatment by silanes is evaluated for mass loss, water absorption and internal damage in a salt scaling test, along with simultaneous measurement of sub-freezing length change on small-scale concrete specimens.

6.7.1 Mix characteristics and testing procedure

A 0.45 w/c ratio concrete mix was prepared in the laboratory according to ASTM C 192. 100 mm×200 mm cylindrical specimens were cast and left in the mould for 1 day before curing started, which involved 27-day immersion in tap water at 20 ℃. Concrete samples were also obtained from one section of a Michigan highway with salt frost durability issues.

Air content and Powers' spacing factor for the air void system were measured by the linear traverse method according to ASTM C457.The mix design and air void properties for lab concrete are shown in Table 6.1 and the air void properties for field concrete are shown in Table 6.3.

Table 6.2 Mix design and air void properties of concrete mixtures

Mix design						Slump
cement	gravel	sand	water	superplasticizer	air entrainer	
kg/m^3				ml/kg cement		mm
290	1115	775	130.5	4.0	0.9	80
Air void characteristics by linear traverse						
air content (%)				Powers' spacing factor, μm)		specific surface, mm^{-1}
total	entrained (<0.5mm)					
3.02	2.49			135		43.1

Table 6.3 Air void properties of field concrete specimens

air content (%)		Powers' spacing factor, μm)	specific surface, mm^{-1}
total	entrained (<0.5mm)		
2.80	1.65	207	27.5

Procedures for silane treatment are detailed below.

For untreated specimens, their lateral surfaces were sealed by the aluminum foil with butyl rubber. This was followed by a one-week presaturation test with the test surface immersed in demineralized water by 5 mm. The weight gain was regularly recorded and followed the profile shown. F-T test typically starts after the nick point.

For silane treated specimens, two different regimes were adopted, as illustrated in Figure 6.22. For the first regime, tape-sealed specimens were presaturated for 7 days. Then only the test surface was exposed to air drying at 20 ℃ and 60±5% RH for ~6 hours before silane application. The moisture loss during drying was registered and was ~0.15% of the dry weight. For the second regime, the silane was applied to the test surface of the pre-dried specimens. A 24-hour curing period was followed after silane application for both regimes. Silane application involves two-time brush coating with an interval of 6 hours. In the case of lab concrete, the silane coverage rate is 4.1 m^2/L for dried surface and 6.9 m^2/L for presaturated surface. In the case of field concrete, the silane coverage rate is 5.3 m^2/L for presaturated surface only.

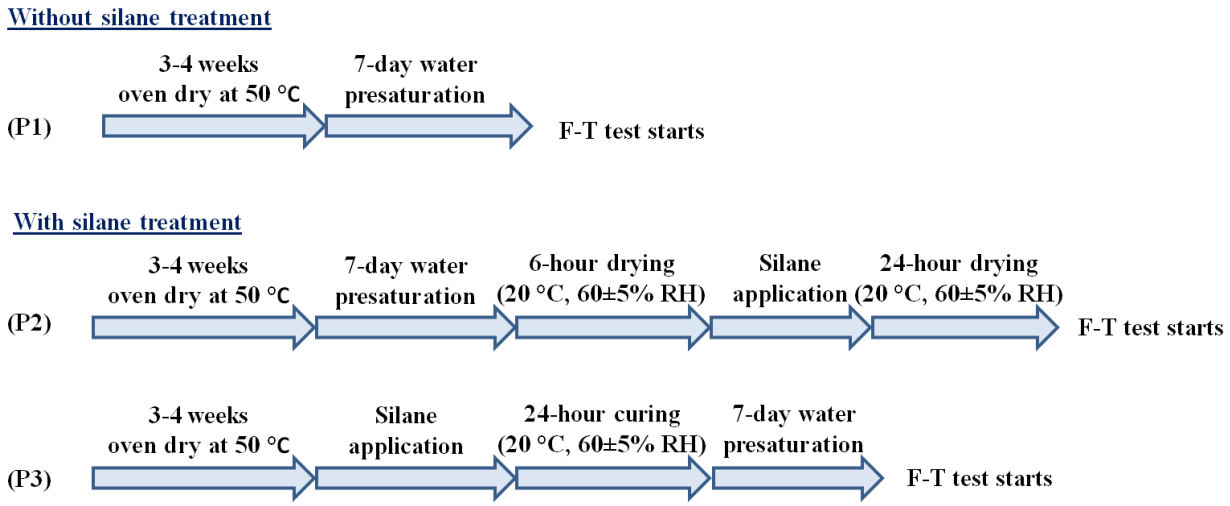

Figure 6.22 Silane treatment procedures

6.7.2 Effect of hydrophobic surface treatment on deicing salt scaling resistance

In this section, F-T test results on a 0.45 w/c ratio concrete mix with adequate air entrainment (3.0% total air and 135 μm Powers' spacing factor) is reported, including moisture uptake during the presaturation and F-T stages, mass loss and internal damage during the F-T stage (Figure 6.23 to Figure 6.28).

Under a severe salt exposure condition, silane treatment almost completely eliminates surface scaling up to more than 70 F-T cycles and the mass loss is reduced by ~95% compared with the untreated specimens, which resembles the performance of an untreated specimens under water exposure (Figure 6.23). In the long term, mass loss for silane treated specimens is accelerated gradually, approaching or even exceeding the untreated specimens, which indicates the loss of protection from silanes. Nevertheless, no bulk damage is observed in those specimens, as indicated by the almost constant RDM with F-T cycles (Figure 6.24). Examination of the deteriorated surface reveals that localized damage is observed for the surface treated specimens while mass loss is uniformly distributed for either water or salt exposure (Figure 6.25). This may be associated with the uneven distribution of silane on the surface. In addition, application of silanes onto a dry surface (P3) yields better long-term scaling resistance compared with a partially dry surface (P2), since silanes penetrates deeper into a dry surface (Basheer and Cleland 2011).

The cumulative moisture uptake is shown in Figure 6.26. During the presaturation stage in untreated specimens, the rapid capillary suction contributes most of the moisture uptake. This is followed by a well-defined nick point, indicating capillary saturation (Fagerlund 2004). Silane treatment reduces water absorption by modifying the contact angle such that capillary suction is arrested (Figure 6.21). The limited absorption may be a result of slow diffusion. However, the F-T action accelerates the bulk moisture uptake even in the P3 specimens, which has been reported in other studies (Basheer and Cleland 2006). The moisture uptake in concrete under F-T test has been attributed to a "pumping" effect that involves several different mechanisms (Jacobsen 2002). Considering the significance of the absorption, the most likely transport mechanisms are the "external ice forcing water inwards-suction due to melting of ice" as proposed by Powers and reviewed by Jacobsen (Powers 1945, Jacobsen 2002). It is hypothesized that upon freezing, the external ice formation surrounding the exposed surface generates hydraulic pressure and forces liquid into the unsaturated concrete pores; upon thawing, the melting of internal ice results in volumetric contraction and creates suction that draws liquid inwards from the surface if the ice therein melts preceding the interior (Figure 6.27). Either the hydraulic pressure expulsion or the extra suction force is able to overcome the reversed pressure difference due to hydrophobic effect (Figure 6.21(b)), thus water is able to be drawn into the unsaturated region. P3 specimens have initially limited moisture content (or internal ice formation upon freezing), thus the major transport mode may be the hydraulic pressure in silane treated specimens (P3).

When plotting the mass loss against the additional moisture absorption during F-T exposure (Figure 6.28), it clearly show that the permanent bulk moisture uptake is not correlated to scaling resistance, as has been confirmed in (Liu and Hansen 2014). This is, however, consistent with the cryogenic suction mechanism for deicing salt scaling, where continuous ice growth by cryogenic suction of surface liquid is the cause for scaling (Liu and Hansen 2014). Silane treatment sets up a hydrophobic barrier for this moisture transport, thus restricting the ice growth. This is readily seen from the length-change results on concrete specimens (Figure 6.29). Ice growth at subfreezing temperature indicated by the big secondary dilation is completely arrested by the silane treatment or water exposure, where surface liquid is either prevented from ingress or is not available at all.

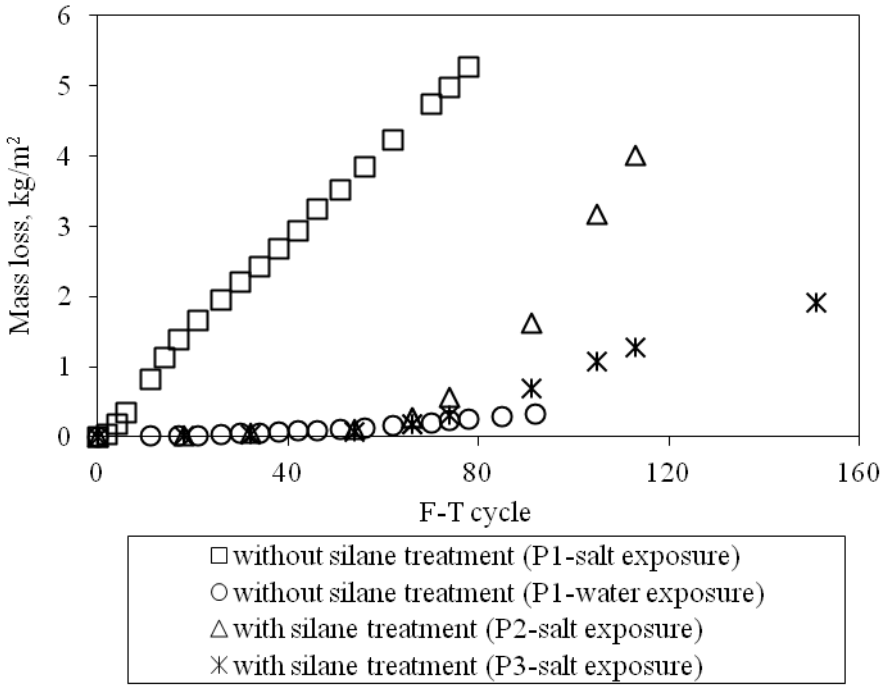

Figure 6.23 Mass loss with F-T cycles for lab concrete

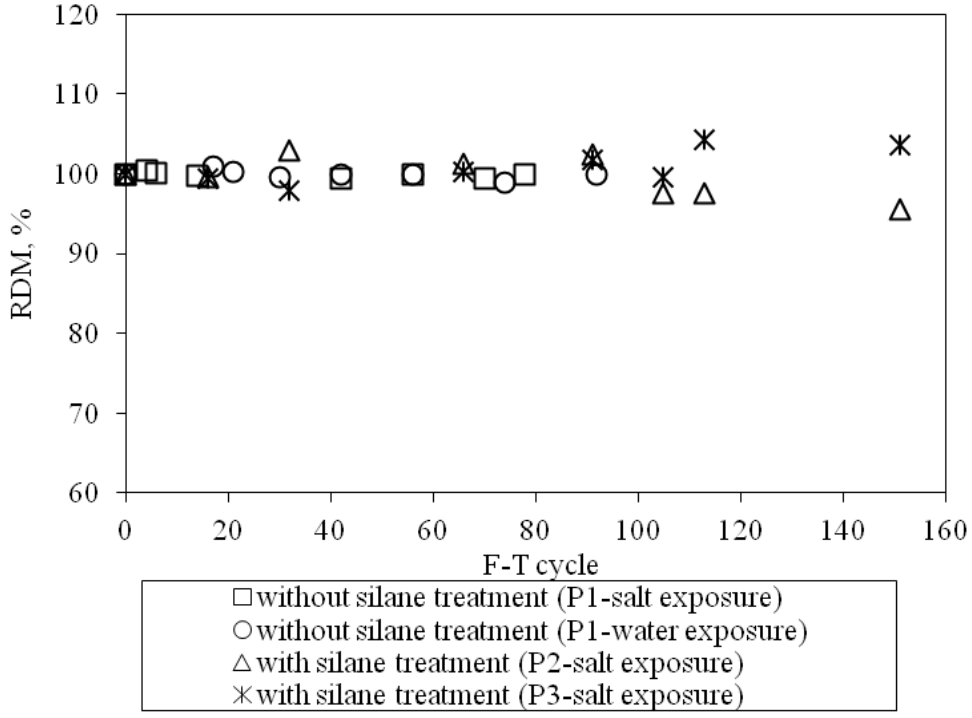

Figure 6.24 RDM change with F-T cycles for lab concrete

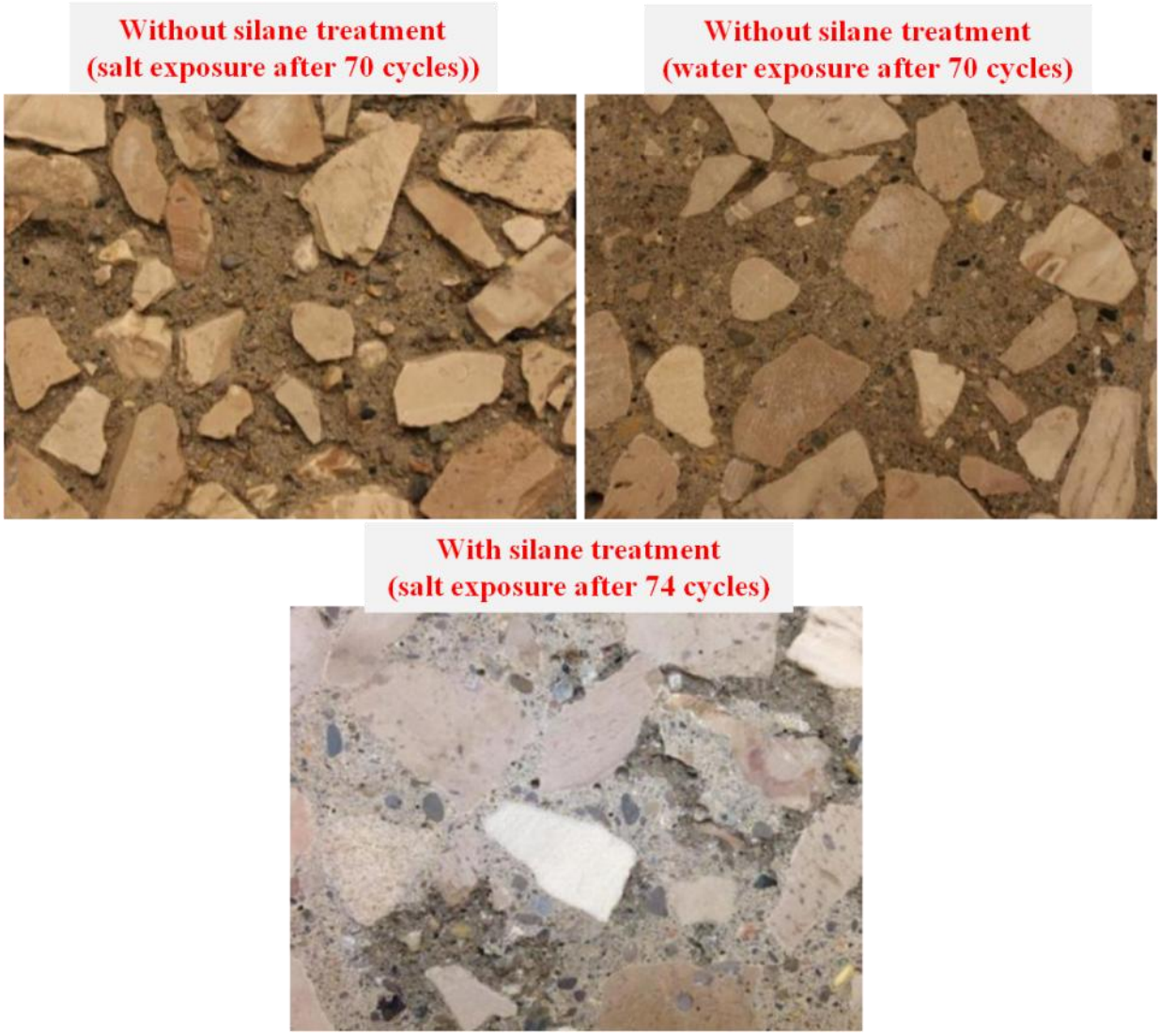

Figure 6.25 Scaled surface profiles in lab concrete specimens

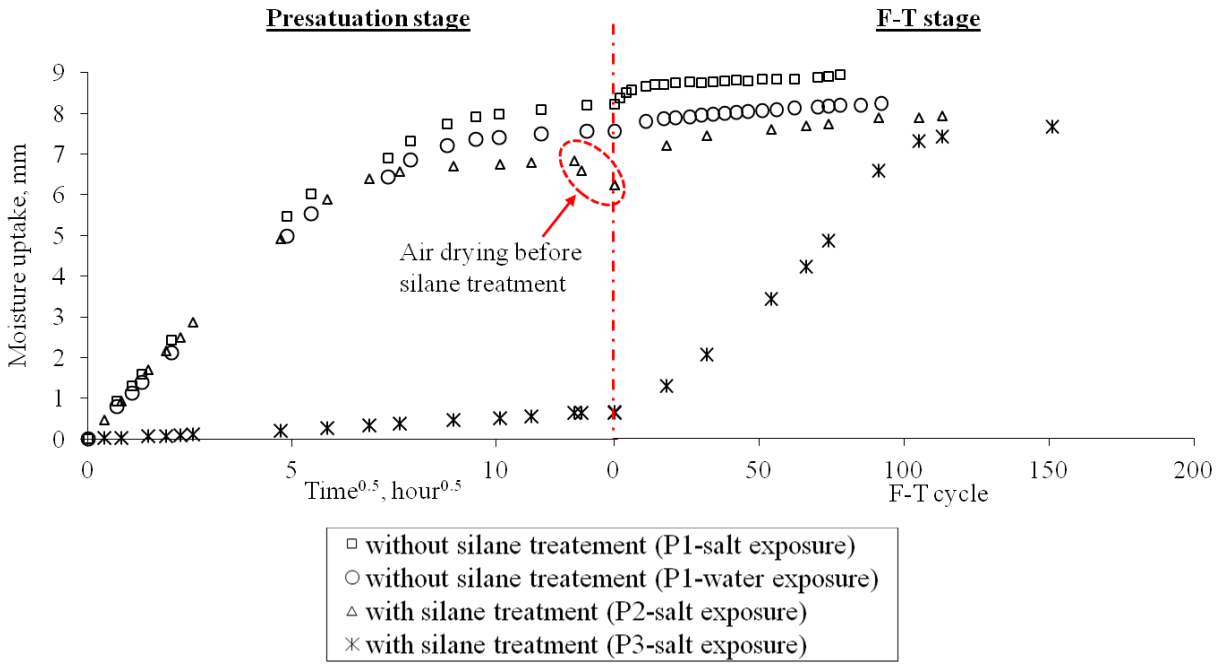

Figure 6.26 Moisture uptake during the presaturation and F-T

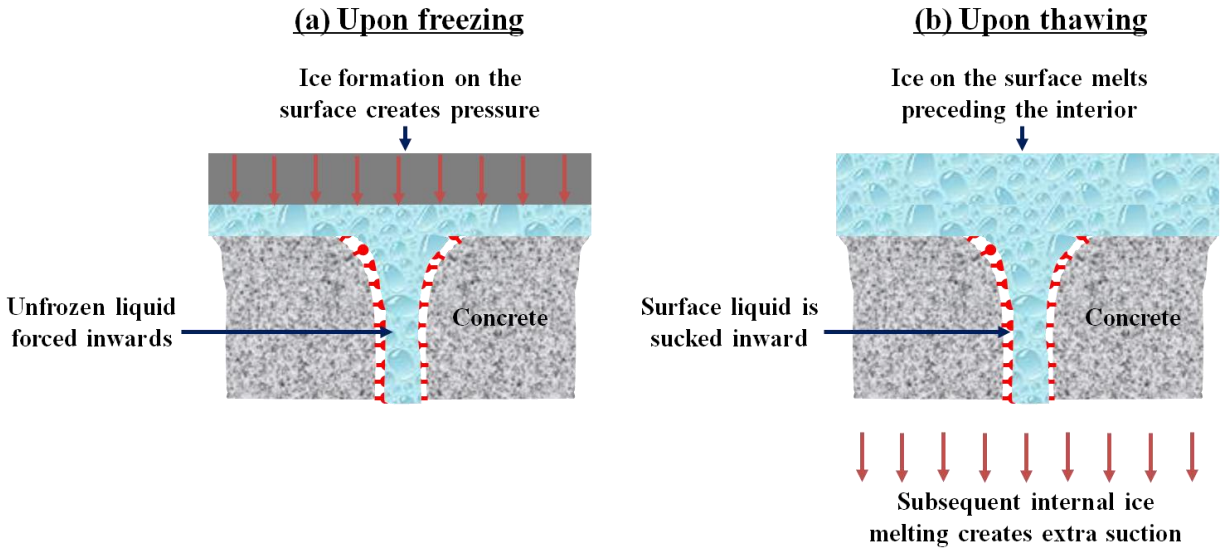

Figure 6.27 Liquid transport upon freezing of external moisture

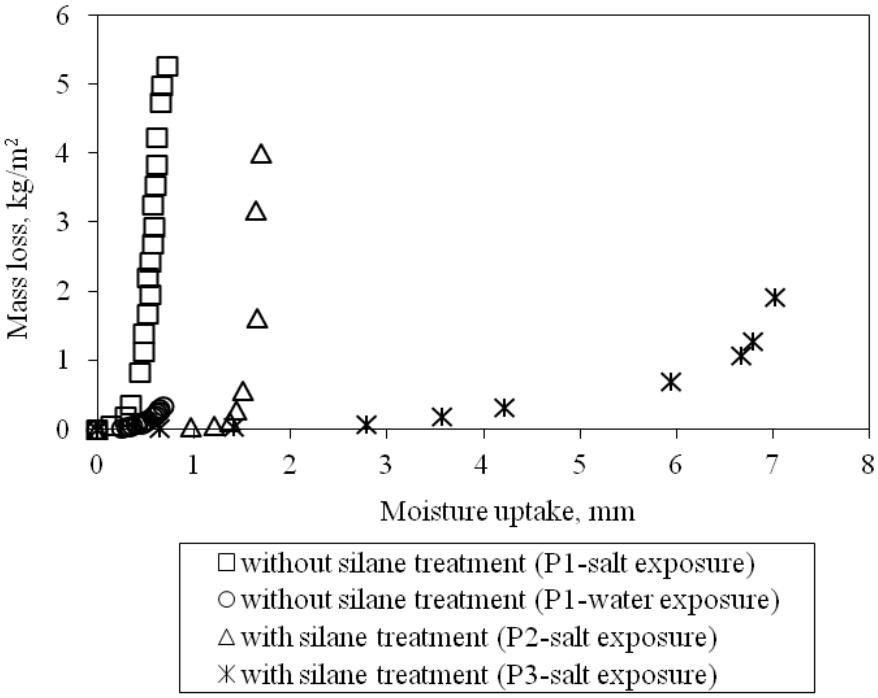

Figure 6.28 Relationship between mass loss and bulk moisture uptake during salt frost scaling test

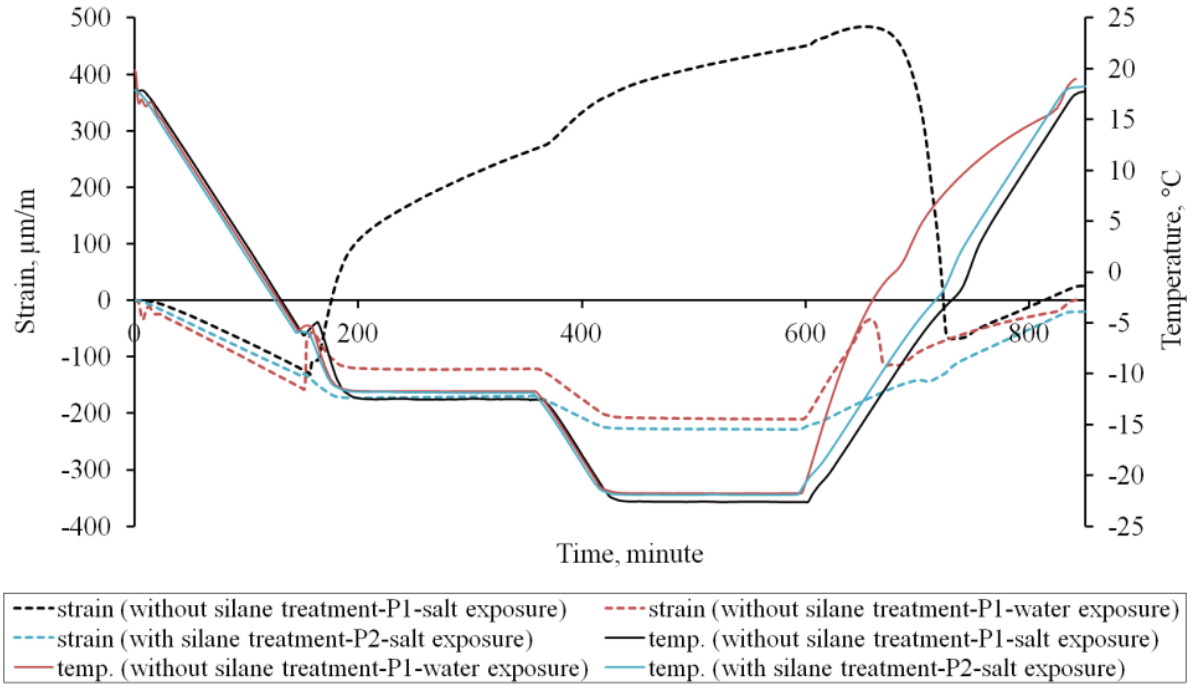

Figure 6.29 Length-change result on the lab concrete specimen surface treatment and two exposure conditions (Procedure P2 in Figure 6.22 was used for silane application and its dosage is 7.2 m^2/L).

6.7.3 Service life extension on field concrete

Surface treatment provides a promising technique to mitigate durability problems in concrete structures due to combined attack of salt and frost exposure. In this section, concrete samples were obtained from a Michigan highway that demonstrated joint deterioration (Figure 6.30(a)). Laboratory test also shows severe surface scaling and internal cracking (Figure 6.30(b), Figure 6.31 and Figure 6.32). When silane is applied, the surface scaling is substantially reduced and the F-T cycles needed to reach the 1.5 kg/m^2 mass loss is extended by more than four times (Figure 6.31). The bulk damage is delayed as well (Figure 6.32). The mass loss on silane-treated specimen is mainly a result of the localized damage which spreads gradually (Figure 6.33). It is noted the accelerated mass loss coincides well with the occurrence of bulk cracking, typically indicated by the removal of coarse aggregates (Figure 6.30(b) and Figure 6.33).

(a) Joint deterioration (b) Severe surface scaling

Figure 6.30 Field and laboratory performance of the concrete samples from a Michigan highway

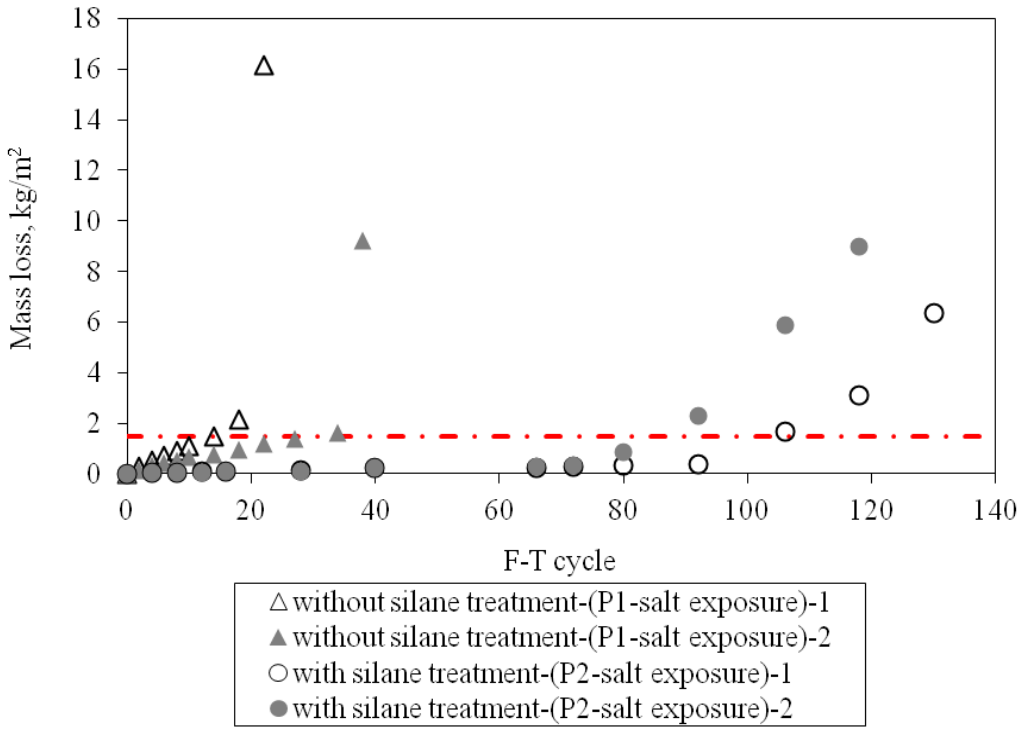

Figure 6.31 Mass loss with F-T cycles on field concrete using regime P1 and P2

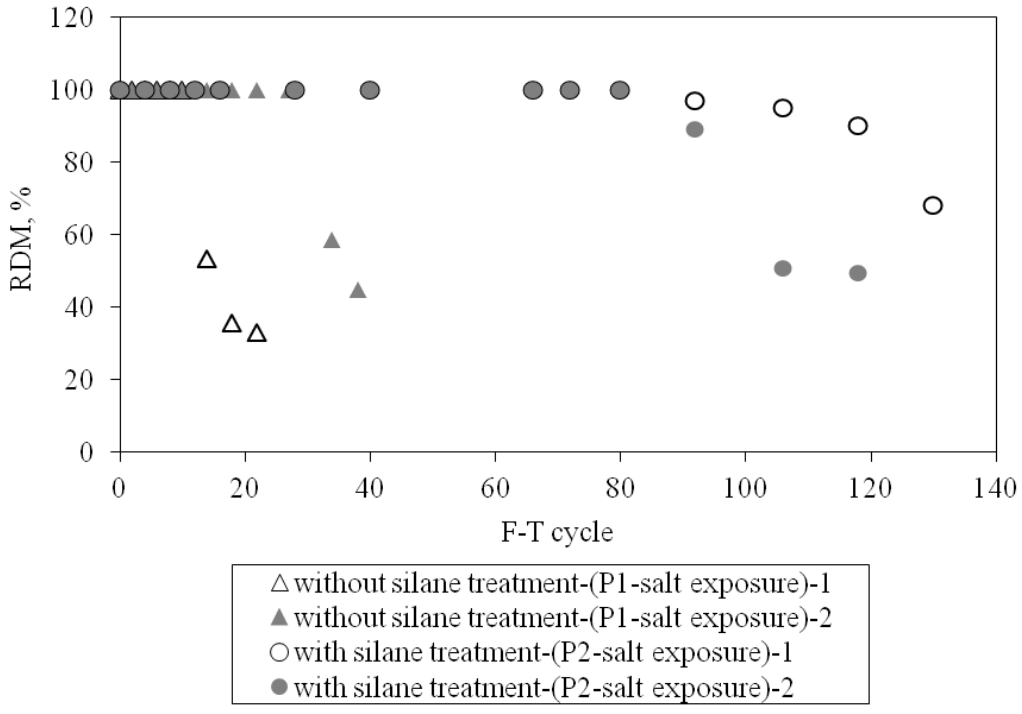

Figure 6.32 RDM change with F-T cycles on field concrete using regime P1 and P2

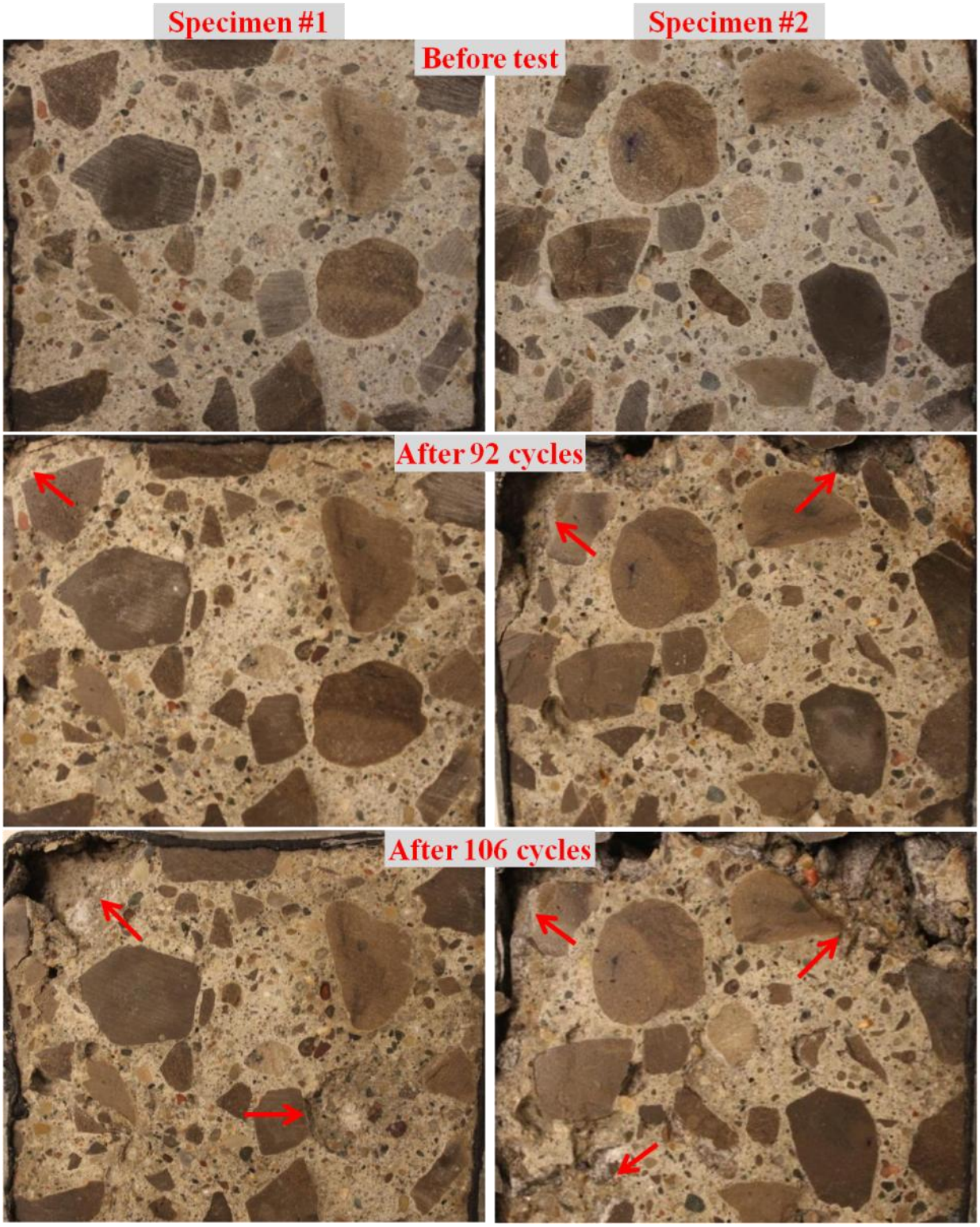

Figure 6.33 Surface profiles of field concrete specimens (localized damage marked by red arrows)

6.8 Summary of findings

In this Chapter, a performance-based methodology is proposed to evaluate scaling resistance of concrete. The following major conclusions are obtained.

- Concrete sorptivity, a transport property for capillary suction rate, is found to be correlated to salt-frost scaling resistance. In this paper, a refinement to the sorptivity model developed by Sellevold is proposed, which can account for the pore size distribution and continuity effects on sorptivitiy with the major objective to improve salt-frost scaling resistance of air-entrained concrete.
- The sorptivity model for predicting liquid transport in concrete provides a sound basis for developing performance-based quality control tests for service life design of concrete structures for severe exposure conditions (i.e. wet-freeze climate and deicer-salt application).
- Hydrophobic surface treatment is effective in practically eliminating over 90% of the surface scaling which is typically encountered in a highly salt scaling susceptible concrete (i.e. high water ratio). This technique is also applied to field samples already demonstrating frost deterioration and laboratory results show great potential in extending its service life significantly.

CHAPTER 7 PREPARATION OF CONCRETE FOR HIGH DURABILITY AND SUSTAINALBILITY

7.1 General

Nowadays, sustainability is a sustainable terminology in concrete industry which primarily involves minimizing the ecological, economic and societal impact during the entire life cycle of a concrete structure (Naik 2008). There are several aspects in the manufacture of a sustainable concrete, among which alternative binders and improved durability, thus prolonged service life are gaining special interests in concrete researchers and practitioners. This reconciles the results presented in the previous chapters which have clearly shown incorporation of slag cement and the application of surface treatment substantially increase the durability of concrete mixes.

In this chapter, a summary of results from two MDOT projects is presented regarding the development of concrete mixes for rapid repair purposes and the utilization of different sealants on field concrete samples demonstrating frost durability problems. In addition, lightweight aggregate as partial replacement of sand is investigated as an internal curing agent to counteract the negative effect of slag cement on the shrinkage induced cracking and also on its salt frost scaling performance.

7.2 High early strength concrete for rapid repair of pavement

High early strength concrete (HESC) is characterized by a lower w/b ratio (typically<0.35) and fast early strength gain realized by the addition of setting-control admixtures (accelerator and hardener). HESC has been proposed to be a good candidate for rapid repair and replacement of concrete pavement with a more flexible work window and less traffic disruption.

As part of an MDOT project on the development of an early strength full-depth and economical repair material, this study is focused on the assessment of the durability (salt frost resistance) of HESC and its influencing factors, which is extended from 2012 summer to 2014 summer.

Concrete specimens prepared in ready-mix plants were tested on the properties of salt frost scaling and air void system. A typical mix design is listed in Table 7.5 and all air void properties are shown in Table 7.6 in the Appendix.

7.2.1 Air void characteristics

The air void system was determined on both the fresh and hardened state of concrete by an air meter (ASTM C231) and an automatic air void analyzer (ASTM C 457, linear traverse and point count), respectively. It can be seen from Figure 7.1 that the total air content from linear traverse on hardened concrete is normally lower than from the air meter on fresh concrete, which may be because of the air loss during placement. Nevertheless, as for the hardened concrete, good agreement is noted between the linear traverse and point count methods (Figure 7.2). Except for one mix which yielded unexpectedly low air content (highlighted in red), the rest mixes have a total air content between 4.0% and 11.0%, among which around 70% are entrained air voids smaller than 0.5 mm (Figure 7.3). The Powers' spacing factor is between 50-150 μm (Figure 7.4) and the specific surface is between 20-60 mm^{-1} (Figure 7.5). Specific surface is an indicator of the average void size and is independent of total air content, which can be seen by its clear correlation to the average chord length (Figure 7.6) and is also illustrated in Figure 7.7.

The wide range of air void properties produced in the field concrete mixes, albeit the same dosage of air entrainer, underlines the challenge in maintaining a specific air void system in practical construction. However, it has been shown previously that air content (or Powers' spacing factor), upon a critical value, possesses no further positive contribution to scaling resistance which is dominated by the transport property of the paste structure.

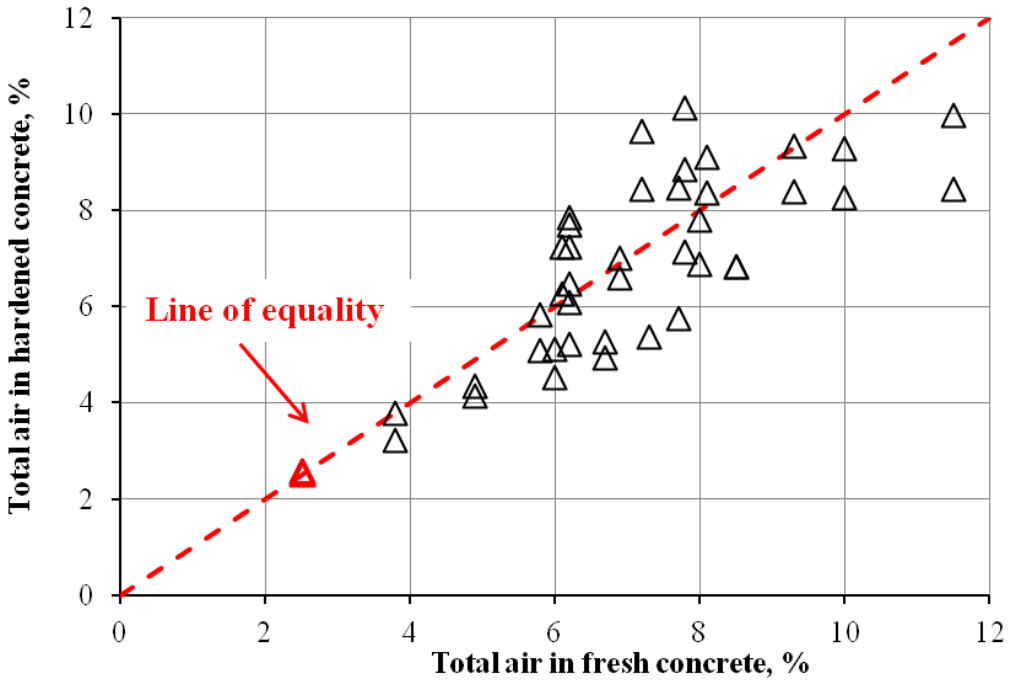

Figure 7.1 Comparison of total air content measured from the linear traverse and the air meter

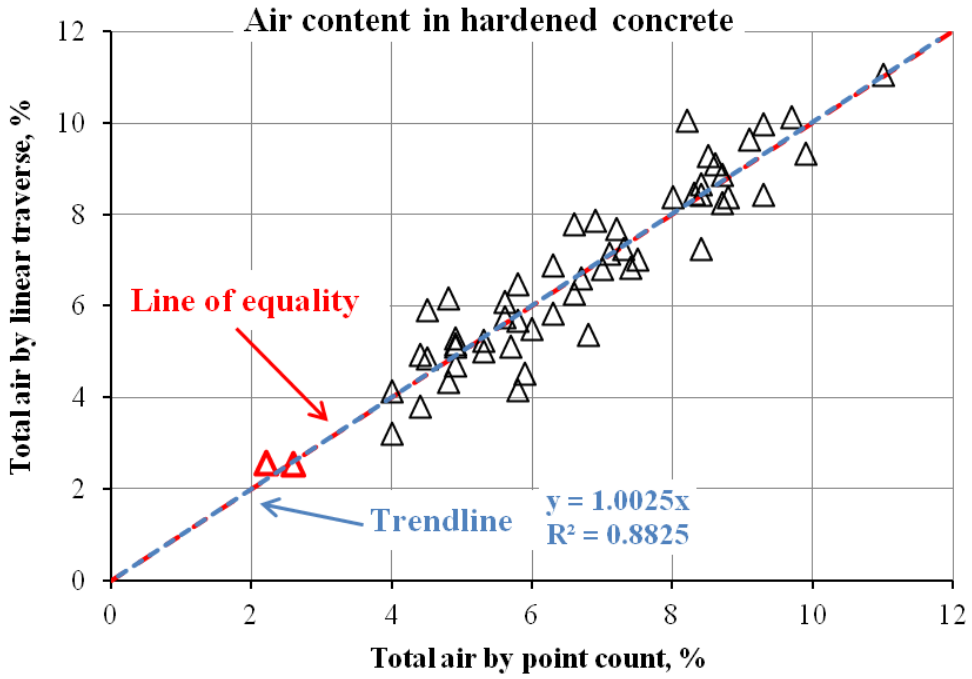

Figure 7.2 Comparison of total air content measured from the linear traverse and point count

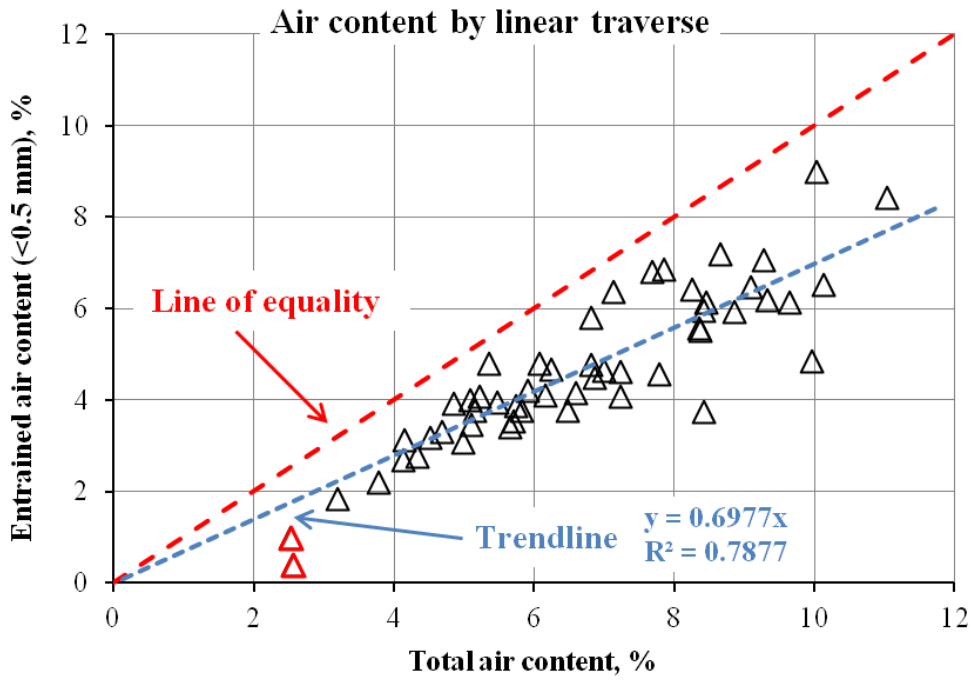

Figure 7.3 Relationship between total air content and entrained air content by linear traverse

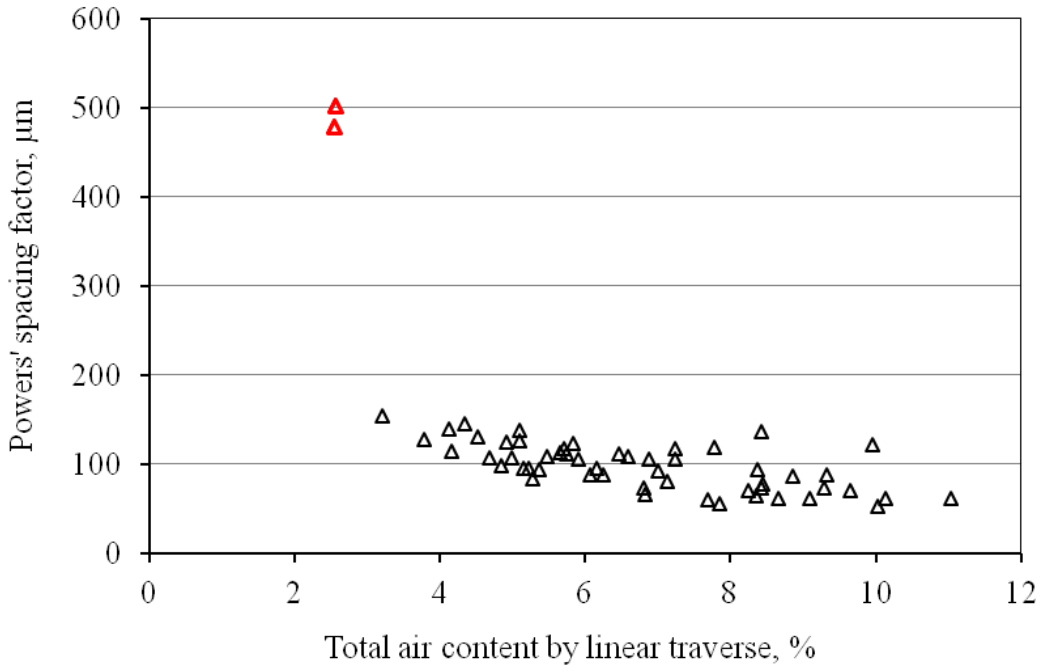

Figure 7.4 Relationship between Powers' spacing factor and total air content by linear traverse

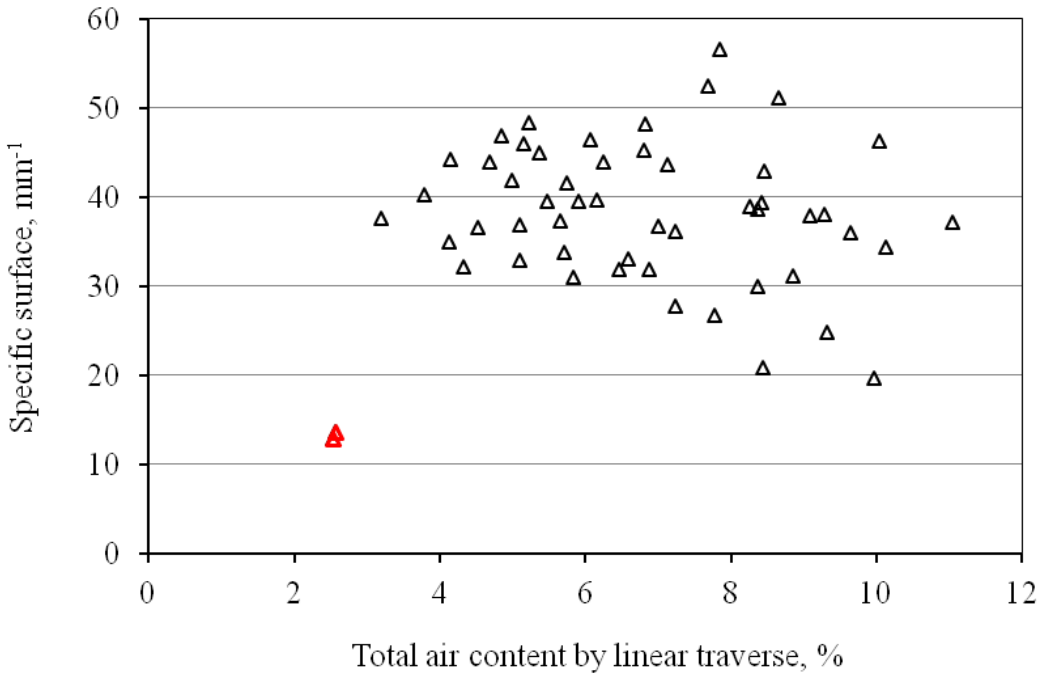

Figure 7.5 Relationship between specific surface and total air content by linear traverse

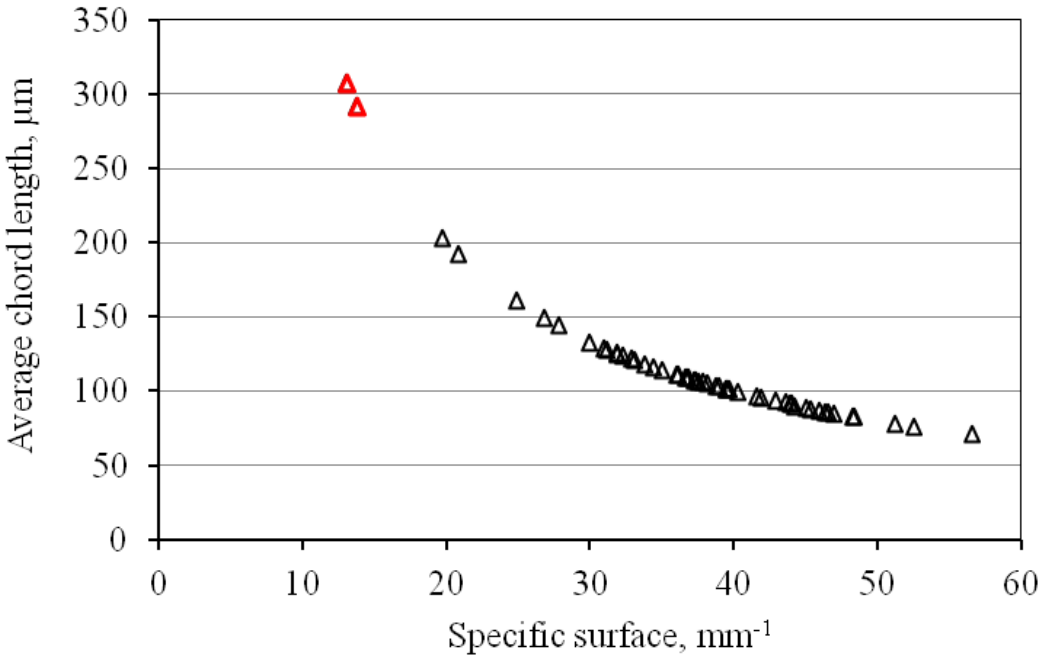

Figure 7.6 Relationship between specific surface and average chord length by linear traverse

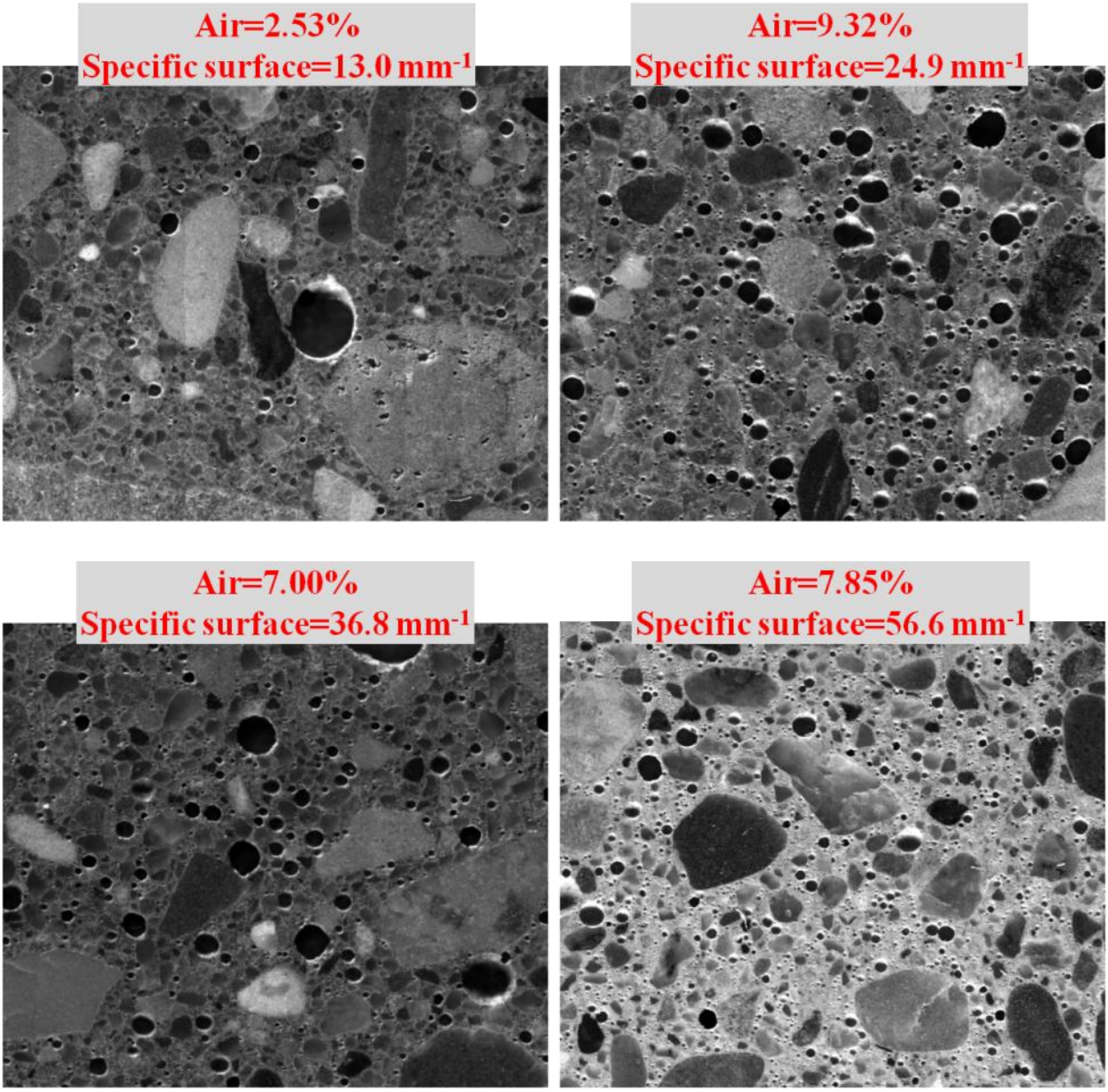

Figure 7.7 Microscopic pictures of air void systems with a range of specific surfaces

7.2.2 Salt frost scaling properties

The mass loss after 28 F-T cycles is plotted for all the mixes against air void and transport properties, as shown in Figure 7.8 to Figure 7.10. The concrete specimens tested exhibit excellent scaling resistance, except for the mix with almost no entrained air (highlighted in red). The exceptionally high mass loss, as explained previously, is because the surface scaling is coupled with the occurrence of internal cracking that leads to coarse aggregate removal. The

sorptivity of these mixes is typically less than 0.75, which is in good agreement with a result reported in (Gagné et al. 2011).

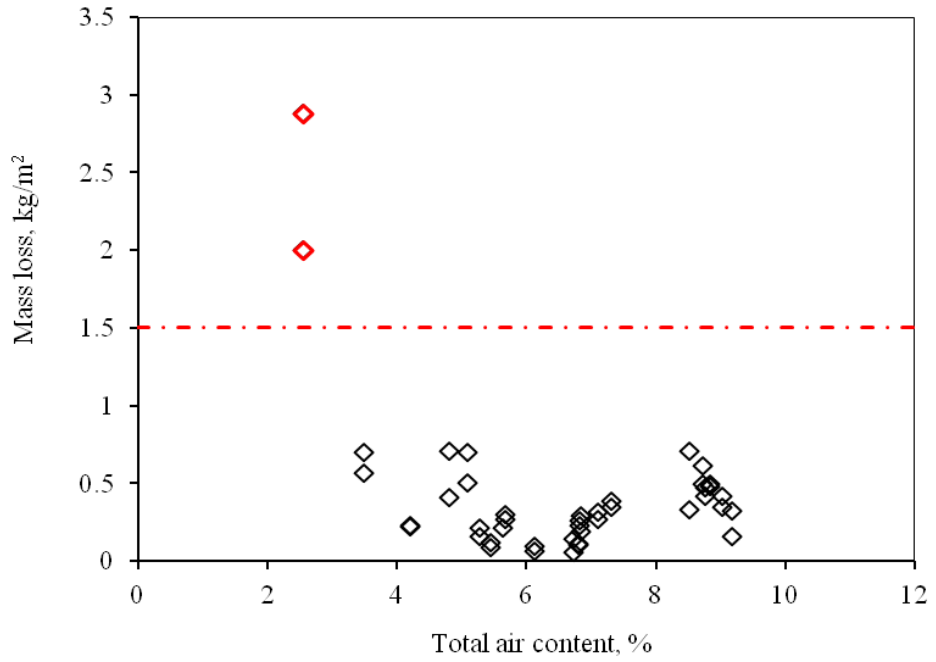

Figure 7.8 Relationship between mass loss and total air content by linear traverse

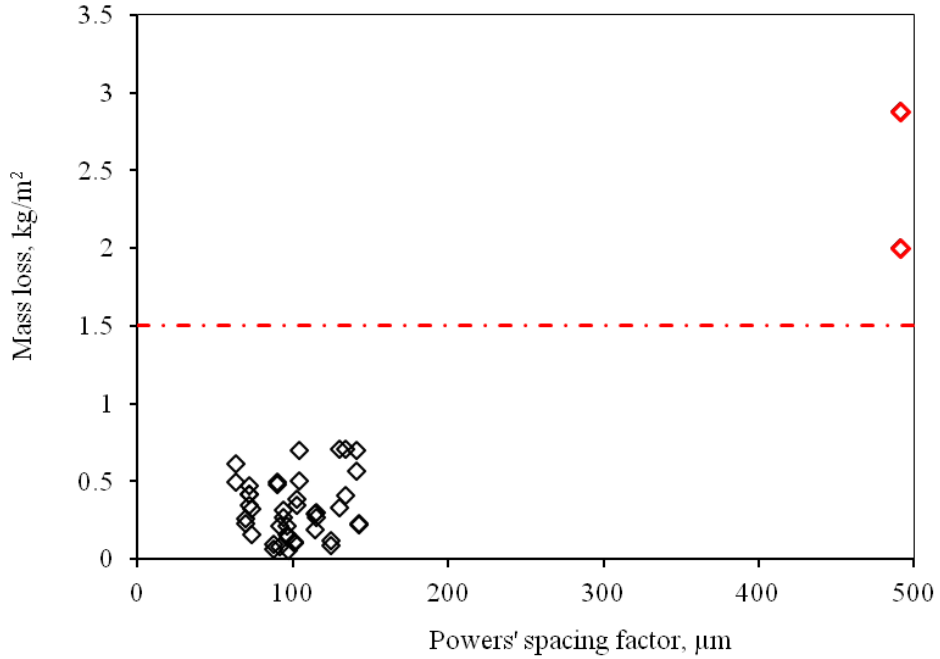

Figure 7.9 Relationship between mass loss and Powers' spacing factor by linear traverse

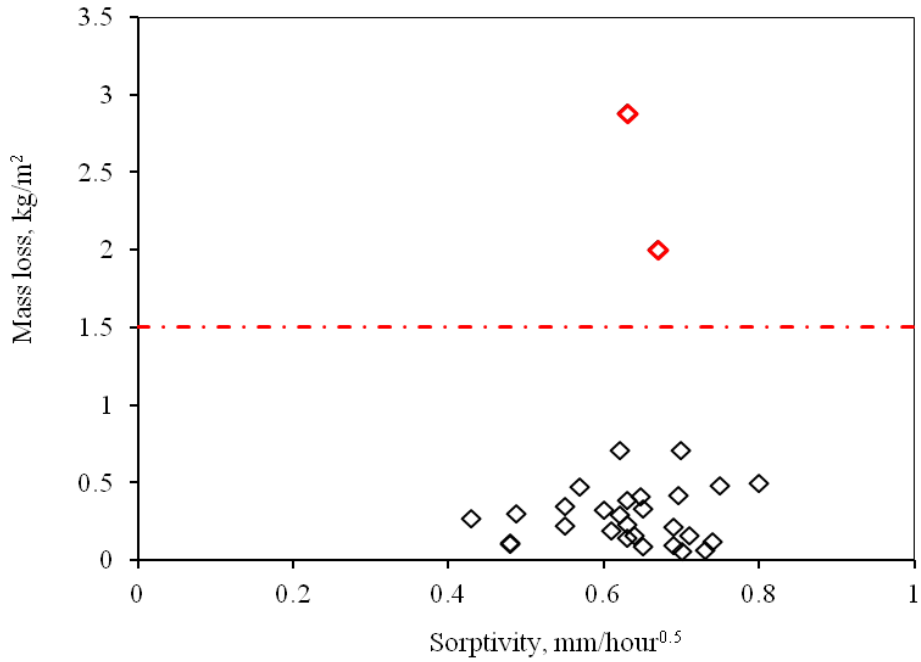

Figure 7.10 Relationship between mass loss and sorptivity

7.3 Effect of lightweight aggregate on salt frost scaling

High performance concrete (HPC) is characterized by a low water-binder (w/b) ratio and the use of supplementary cementitious materials (SCM) (A ïcin 1998). HPC is gaining more and more popularity in structures such as bridge decks, pavements and off-shore platforms due to its improved durability and sustainability. One drawback of HPC is the increased susceptibility to shrinkage induced cracking associated with the low w/b ratio, which is exacerbated by the partial replacement of portland cement with slag cement (Wei 2008). Internal curing by the incorporation of presaturated lightweight aggregate (LWA) is a well accepted remedy to reduce or even neutralize autogenous shrinkage in HPC by artificially entraining extra water to sustain cement hydration and pozzolanic reaction (Bentz et al. 2007, Lura 2003, Bentur et al. 2001).

In this study, a series of 0.33-0.35 w/b ratio HPC mixes with addition of LWA and slag cement at different volume fractions are investigated on salt frost scaling and autogenous shrinkage. In the end preliminary results were reported on a new method to evaluate the mitigation effectiveness of autogenous shrinkage by LWA.

Table 7.1 Mix design, compressive strength and air void properties of concrete mixes

Mix	Mix proportion (kg/m^3)					Air void system by linear traverse			28d compressive strength (MPa)
	portland cement	slag cement	normal sand	LWA	gravel	air content (%)	Powers' spacing factor (μm)	specific surface (mm^{-1})	
033-0S-0LWA-2.6%	390	0	695	0	1112	2.64	265	23.4	72
033-0S-0LWA-5.5%	390	0	695	0	1112	5.49	113	35.5	64
033-0S-25LWA-3.2%	390	0	521	116	1112	3.18	192	30.2	71
033-0S-25LWA-8.1%	390	0	521	116	1112	8.12	66	45.8	66
033-0S-50LWA-3.7%	390	0	348	232	1112	3.73	154	34.3	67
033-0S-50LWA-6.7%	390	0	348	232	1112	6.74	99	37.5	52
033-25S-0LWA-7.1%	292	98	691	0	1106	7.07	84	41.2	69
033-50S-0LWA-8.4%	195	195	690	0	1103	8.42	104	25.6	74

Table 7.2 Mix design of mortar mixes (kg/m^3)

Mix	portland cement	slag cement	normal sand	LWA	water
035-0S-0LWA	1515	0	1786	0	530
035-0S-25LWA	1515	0	1339	298	530
035-0S-50LWA	1515	0	893	595	530
035-50S-0LWA	757	757	1823	0	530
035-50S-25LWA	757	757	1367	304	530
035-50S-50LWA	757	757	911	607	530

7.3.1 Effect of LWA on compressive strength of concrete

The compressive strength of 6 by 12 in. cylindrical concrete made by partial replacement of fine aggregate by LWA at equal volume was tested at different ages. It can be seen in Figure 7.11 that addition of 25% LWA actually improves the strength of concrete slightly while a noticeable reduction in strength is observed when the replacement ratio is increased to 50%. This can be explained by the opposing effects of LWA. On the one hand, saturated LWA has a much higher absorption capacity (13.6%) than normal sand (1.4%), which means the effective w/c ratio is increased (from 0.33 to 0.36 at 25% LWA and 0.40 at 50% LWA); on the other hand, the so-called internal curing provided by LWA promotes cement hydration and strengthens the interfacial transition zone (ITZ) which is believed to be the weak link in stress-bearing capacity of concrete. From the perspective of compressive strength, a replacement level of 25% LWA seems to be the optimal choice.

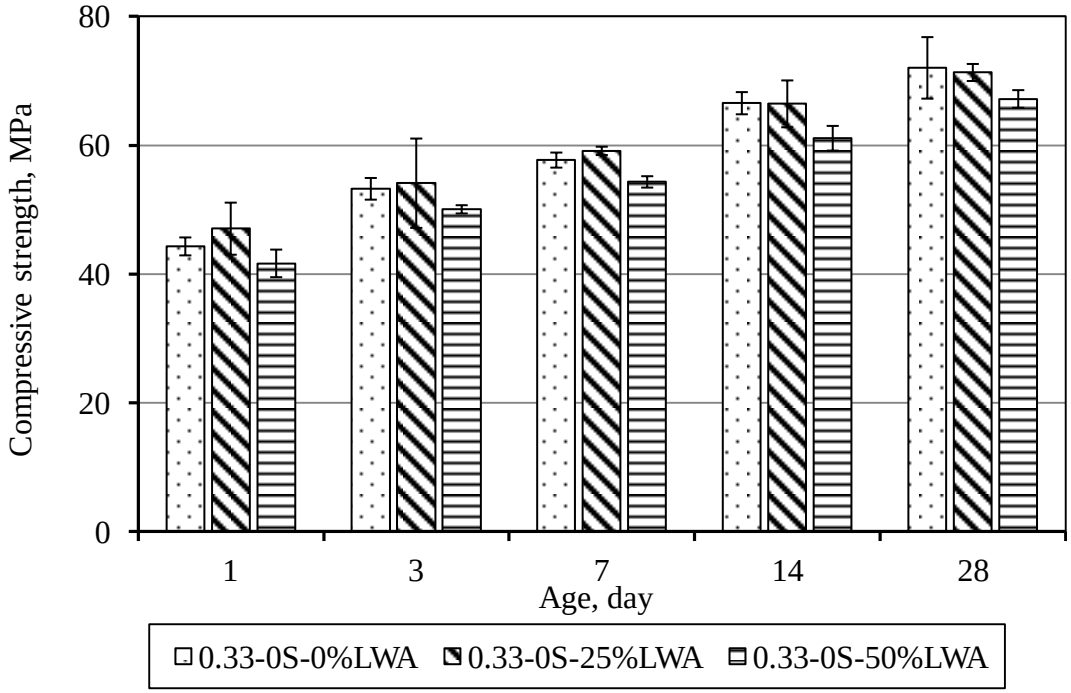

Figure 7.11 Effect of LWA addition on compressive strength of concrete

7.3.2 Mitigating autogenous shrinkage by LWA entrainment.

Incorporation of LWA in concrete mix has been proved to be an effective approach to reduce autogenous shrinkage by acting as a water storage agent that replenishes the consumption of pore water via the continuous release of retained moisture in LWA (Bentz et al. 2007, Lura 2003, Bentur et al. 2001). This is clearly shown in Figure 7.12 that the autogenous shrinkage of a 0.35 w/c mortar with LWA is substantially reduced. Description of the test method can be seen from (Liu and Hansen 2014). As for the blended mix with 50% slag cement replacement, the autogenous shrinkage is increased significantly, possibly due to the refined pore structure and the pozzolanic raction in a blended cement paste (Wei 2008). In this case, an addition of 25% LWA is not sufficient to mitigate the development of autogenous shrinkage (Figure 7.12).

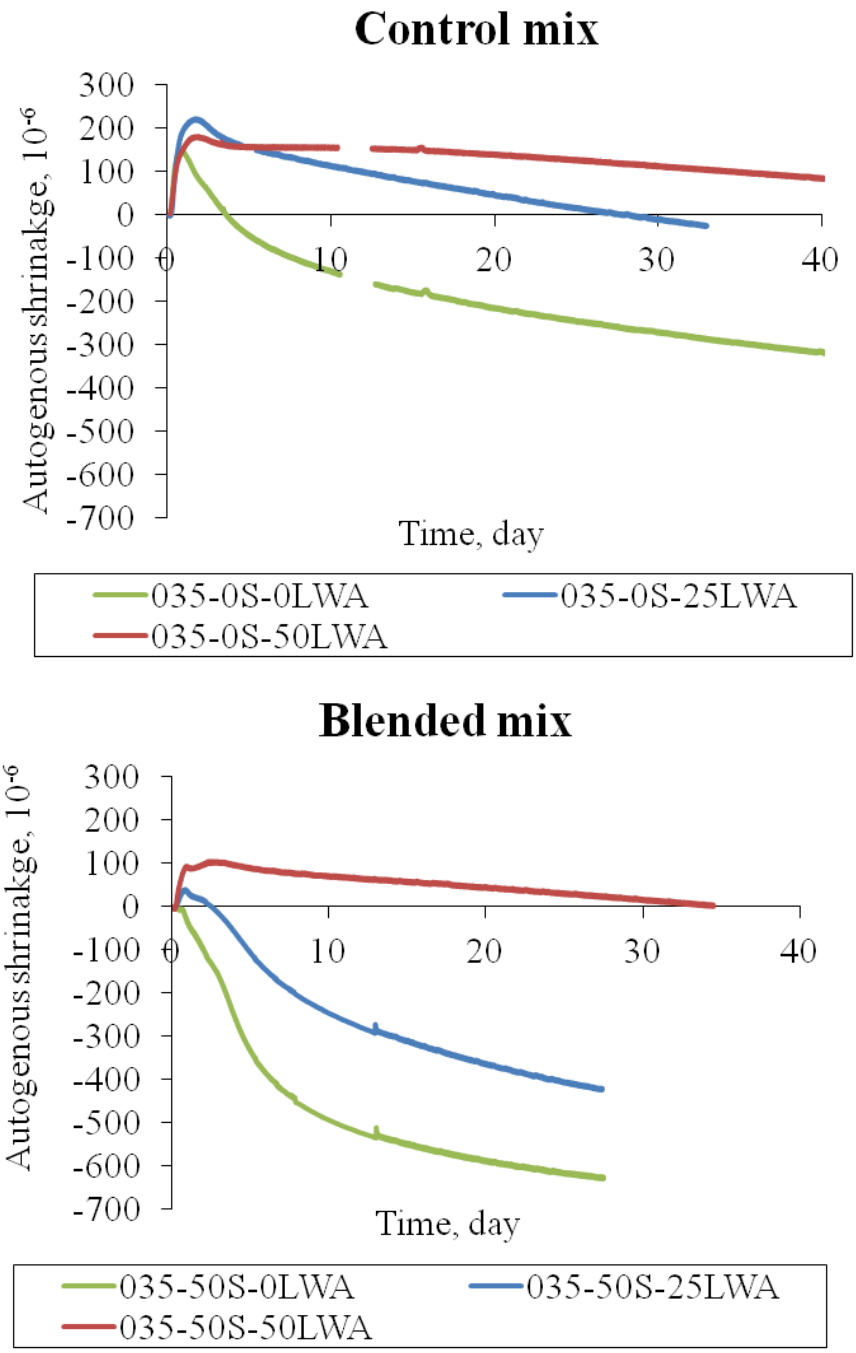

Figure 7.12 Autogenous shrinkage development in cementitious mortar

The working mechanism of LWA repalcement by water entrainment resembles the air entrainment as the hydraulic pressure relief to protect concrete from frost damage, as illustraed in Figure 7.13. It has been well accepted that the distance between air bubbles is a reliable indicator to assess frost resistance in concrete (Powers 1945), which serves as an inspiration to

characterize the effectiveness of LWA on mitigating autogenous shrinkage by how far the retained water in LWA is able to travel to the adjacent paste (Bentz et al. 2007).

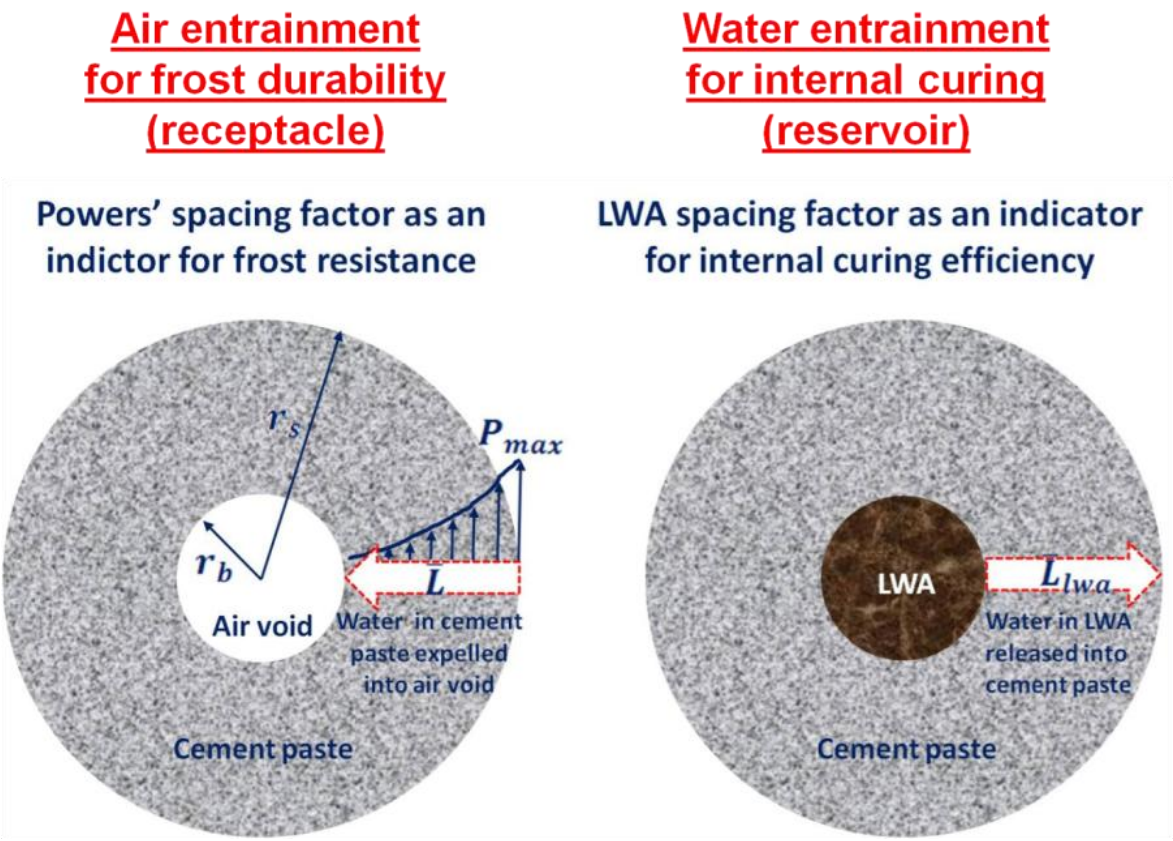

Figure 7.13 Mechanism comparison between internal curing by LWA and air entrainment

A 0.35 w/c control specimen was polished to clearly distinguish each component (Figure 7.14). Then only the LWA particles were made white by a permanent marker while the other part of the specimen was dark (Figure 7.14). An automatic image analyzer will scan the whole surface while measuring the fractional and cumulative chord length of the white dots, from which the "spacing factor" can be calculated. The water flow distance in cement paste at different curing ages was estimated by a model developed by Bentz et al. (Bentz et al. 2007). As seen in Figure 7.15, the water flow distance is larger than the LWA spacing at both 25% and 50% LWA addition during the early and middle ages when the majority of autogenous shrinkage occurs, which means that internal curing is effective throughout the cement paste.

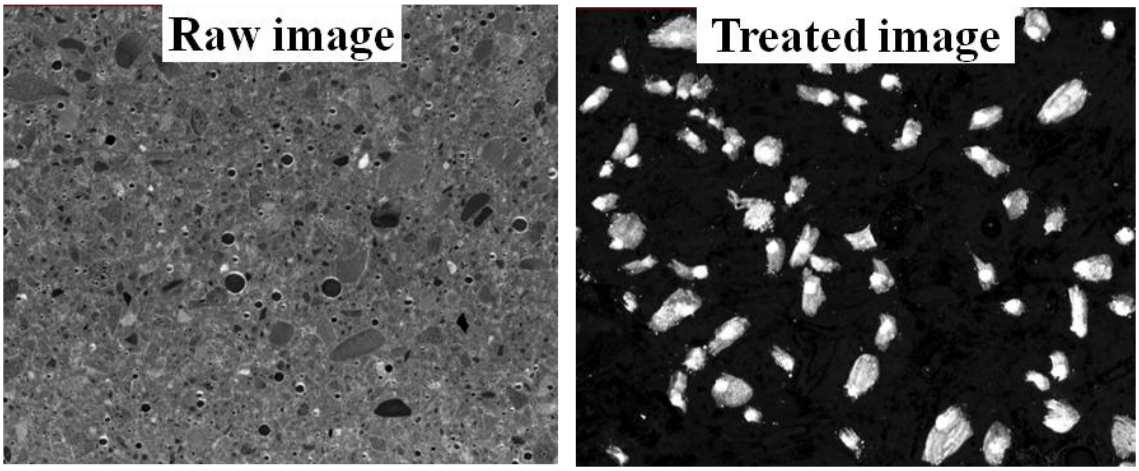

Figure 7.14 Composite image of polished mortar with 50% LWA

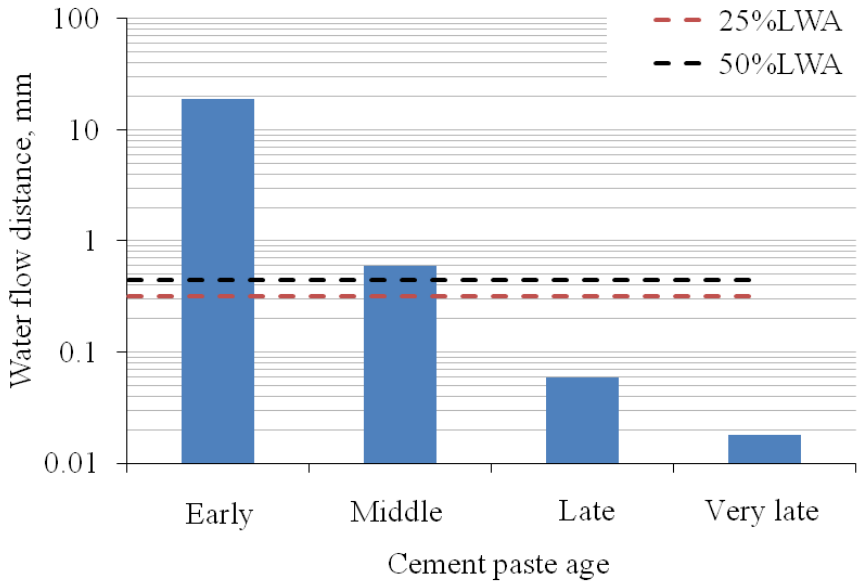

Figure 7.15 Estimated water flow distance with cement paste age and the effect of LWA

7.3.3 Effect of air content on salt scaling resistance of LWA concrete.

Entrainment of adequate air in concrete is a prerequiste for its good frost durability. This is seen from Figure 7.16 where concrete specimens with two levels of air entrainment were tested. Regardless of the replacement ratio of LWA, a lower air content yields more mass loss, accompanied with internal cracking indicated by a decrease in relative dynamic modulus (RDM). Close examination of the damaged surface profiles shows the removal of coarse aggregate (Figure 7.17), which partially contributes to the accelerated mass loss.

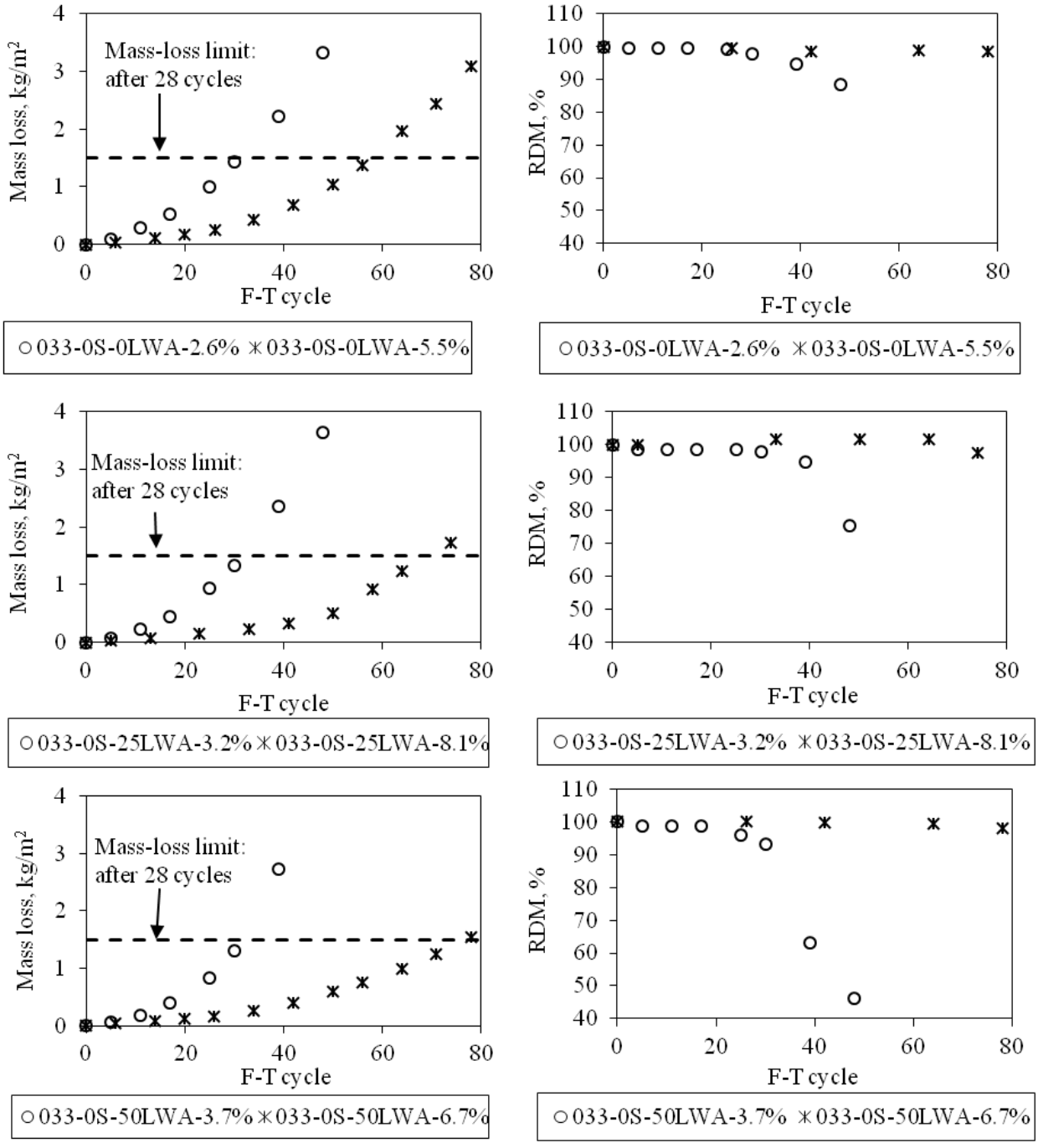

Figure 7.16 Effect of air content on salt frost scaling of LWA concrete

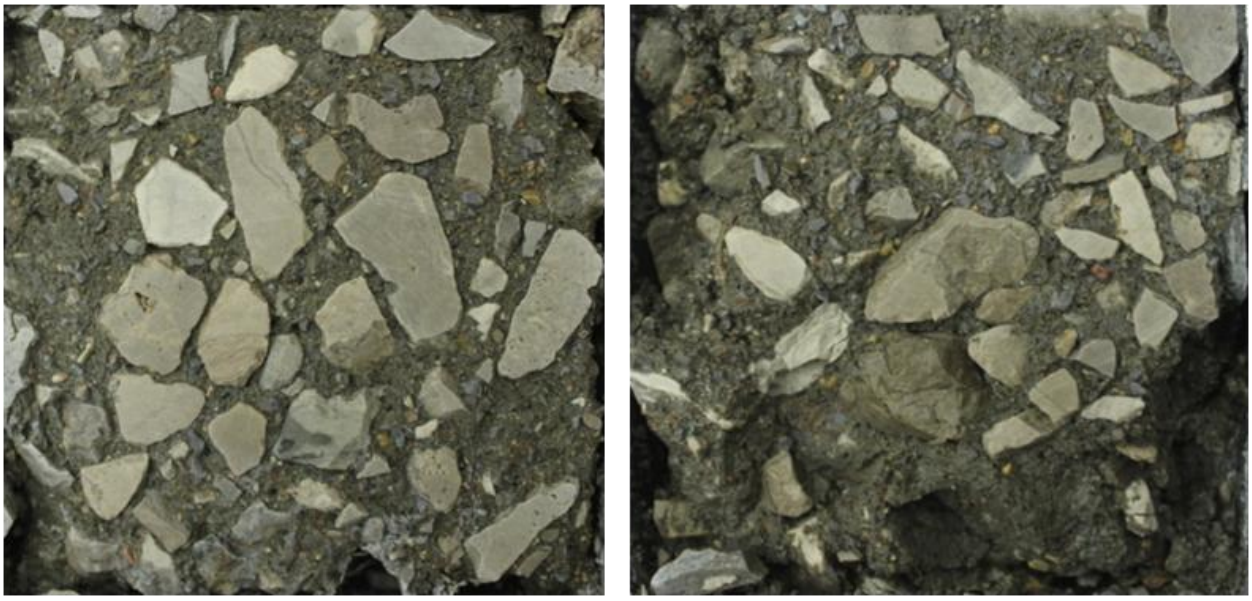

Figure 7.17 Surface profile of concretes with low air content after salt scaling test (48 cycles)

7.3.4 Effect of LWA and slag addition on salt scaling resistance of LWA concrete.

Concrete specimens with a medium to high air content was used to investigate the effect of LWA and slag cement, in order to elimiate the interference of internal cracking on the scaling results. It can be seen that no internal damage occurs in these specimens and the mass loss is limited (Figure 7.18 andFigure 7.19). In addition, partial replacement of sand with LWA, or portland cement with slag cement slightly improves the scaling resistance. This improvement may be a result of the reduced permeability of cement paste, which restricts the strength of cryogenic suction, a major mechanism for salt scaling (Liu and Hansen 2014).

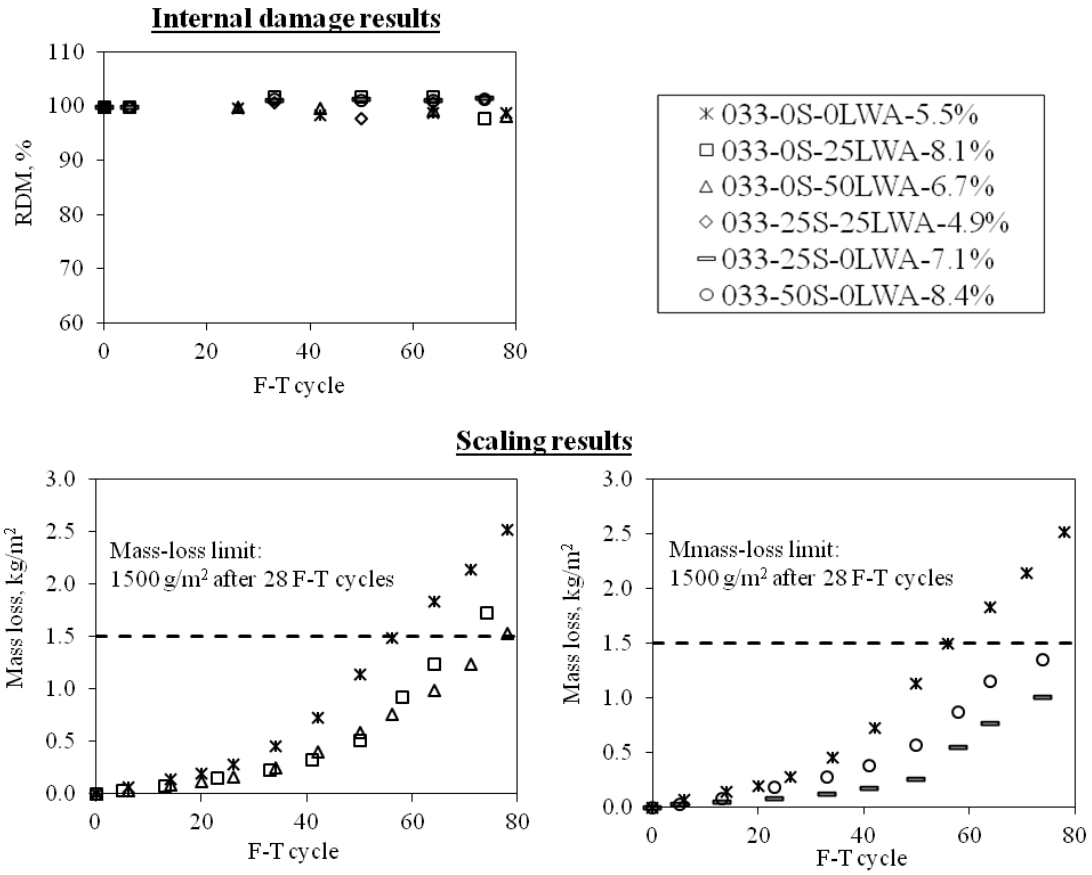

Figure 7.18 RDM and mass loss in concrete with LWA and with slag cement for different concretes

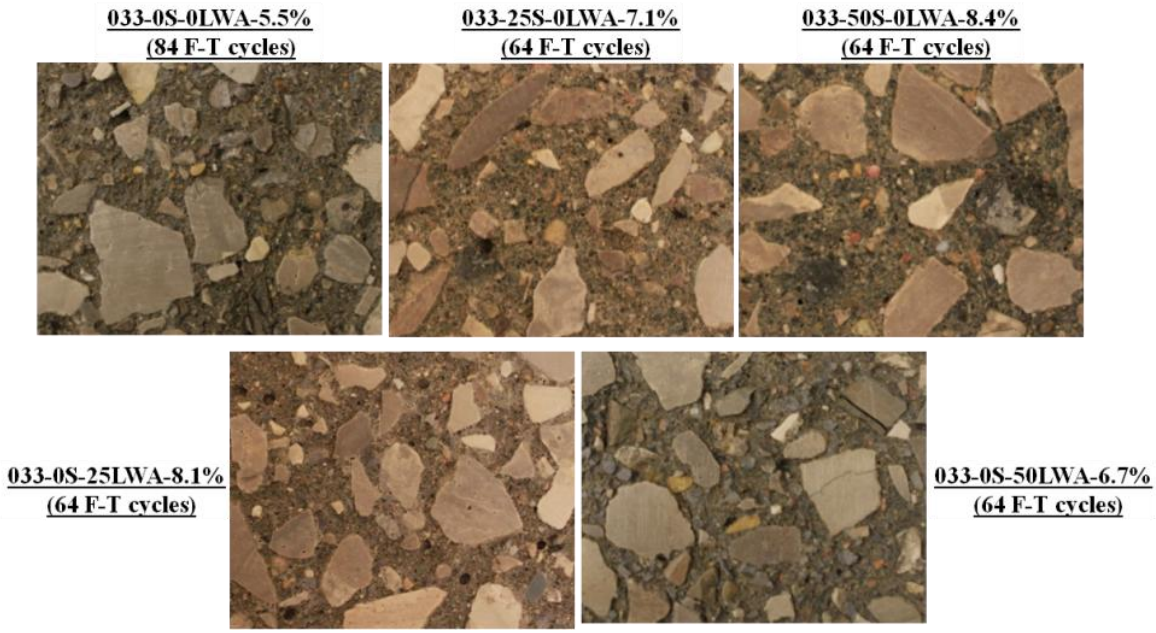

Figure 7.19 Scaled surface profiles of concretes at different F-T cycles

7.4 Surface treatment on salt frost scaling of field concrete

Surface treatment using silane has been proven to be very effective in reducing the moisture absorption through capillary suction in the previous chapter. In this section, an extended study was carried out on the effect of seven different sealants on salt frost scaling resistancer of field samples obtained from M-14 westbound. The sample cores were cut into specimens for scaling test and air void analysis (Figure 7.20).

Durability deterioration realted to salt frost scaling has been reported in this section of the pavement and air void analysis on the hardened concrete reveals that the Powers' spacing factor is above 200 μm (Table 7.3), even though the total air content is ~4%. Further microscopic examination of the polished specimen surface show signs of slight air void clustering and infilling (Figure 7.21), both of which tend to decrease the air void effectiveness.

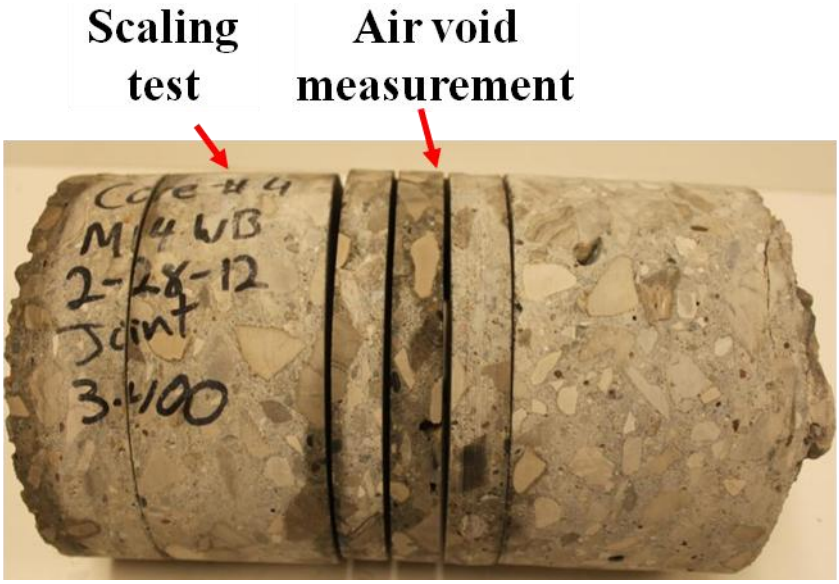

Figure 7.20 Concrete cores from M-14 Westbound

Table 7.3 Air void results of M-14 WB specimens

Spec.	air content, %		Powers' spacing factor (μm)	specific surface (mm^{-1})
	total air	entrained air (<0.5mm)		
#1	3.95	2.50	202	23.3
#2	4.15	2.28	267	19.1

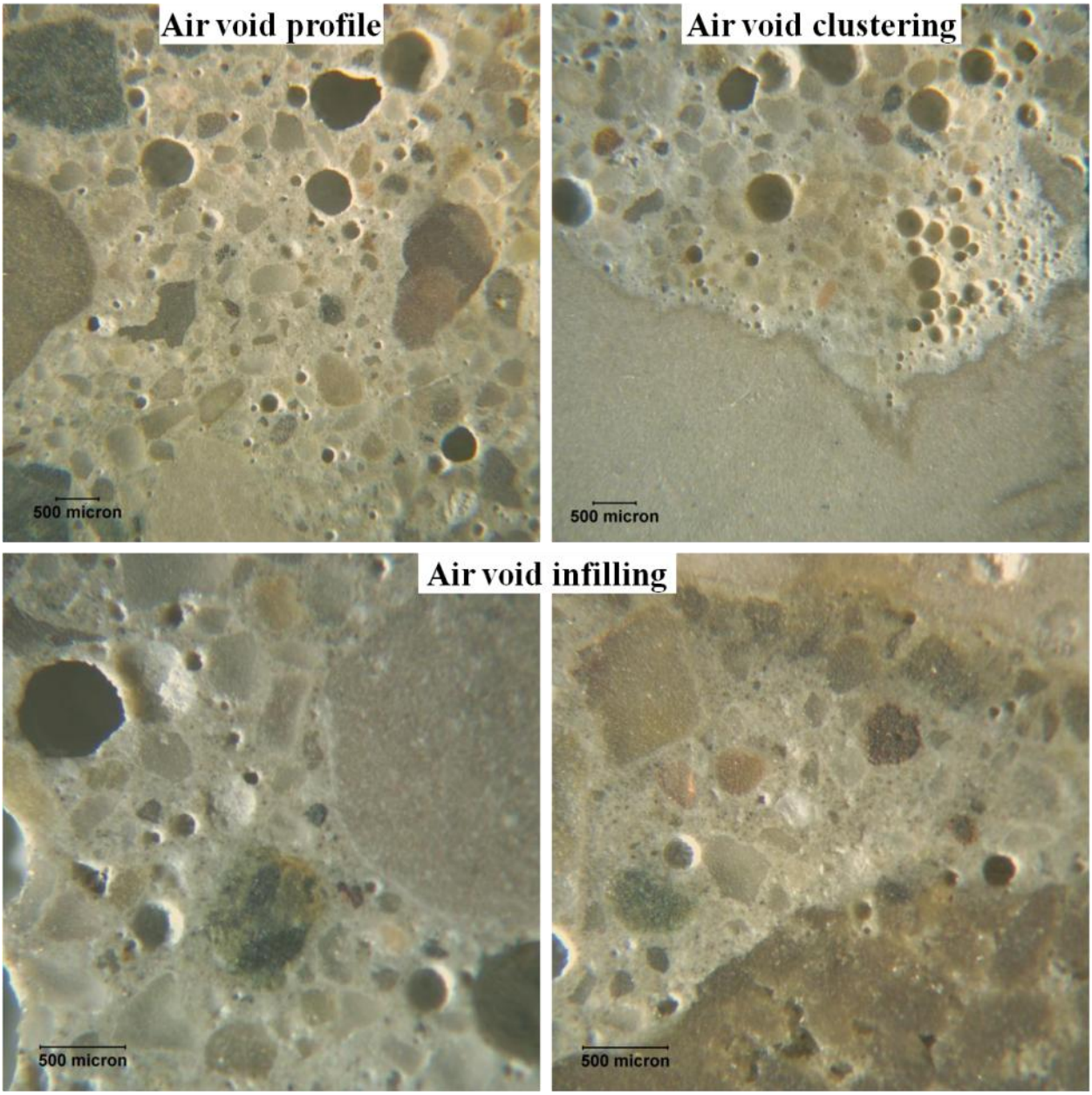

Figure 7.21 Microscopic pictures of air void system in M-14 WB specimens

The modified RILEM CIF method was used for salt frost scaling resistance evaluation. Two different preconditioning methods were used for sealant application. The only difference lies in the drying condition after sealant was applied to the specimen surface (Figure 7.22). Initially, method 2 was used where the treated specimens were dried in a sealed ziplock bag so as to prevent moisture loss from the presaturated body. Later, a modification was made and the treated specimens were dried in the open air (method 1).

Three categories of sealants were used: pore liners by forming a film on the pore walls and pore blocker by crystallization in pores and a combination of both. Their preconditioning procedure and dosage were listed in Table 7.4.

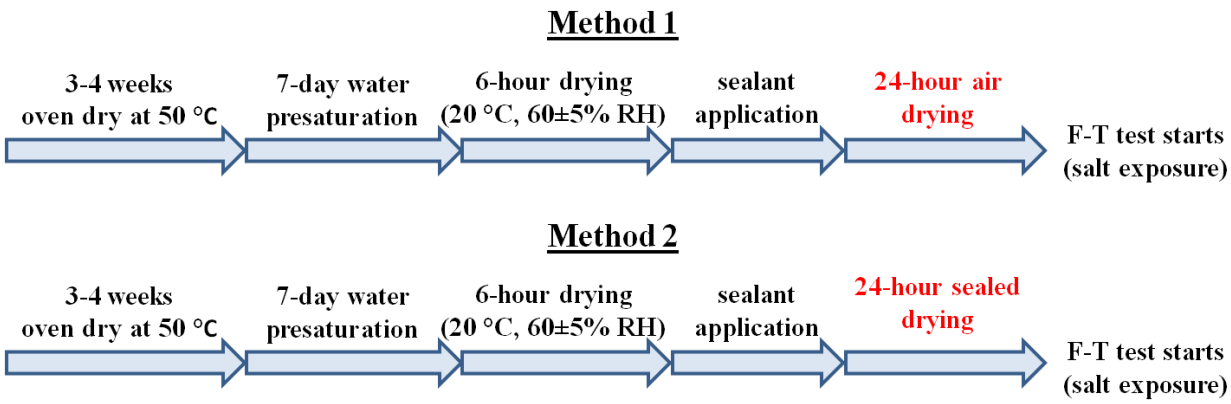

Figure 7.22 Sealant application procedures

Table 7.4 Sealant types and their application details

	Category	working mechanism	preconditioning procedure	dosage, m^2/L
sealant-1	100% silane-siloxane	film formation	1	5.4/6.2
sealant-2	--	crystallization	1	4.9/5.8
sealant-3	100% silane	film formation	1	6.8/6.6
			2	5.1/5.4
sealant-4	100% silane	film formation	1	4.5/7.8
sealant-5	Soy Methyl Ester-Polystyrene	film formation and crystallization	2	4.5/5.5
sealant-6	100% silane	film formation	2	5.5/5.9
sealant-7	40% silane	film formation	2	5.4/5.9

It can be seen from Figure 7.23 that the liquid sealants, either creamy or transparent, don't alter the normal appearance of the concrete. However, sealant 2-treated concrete surface shows a thin membrane, which may be a result of crystallization.

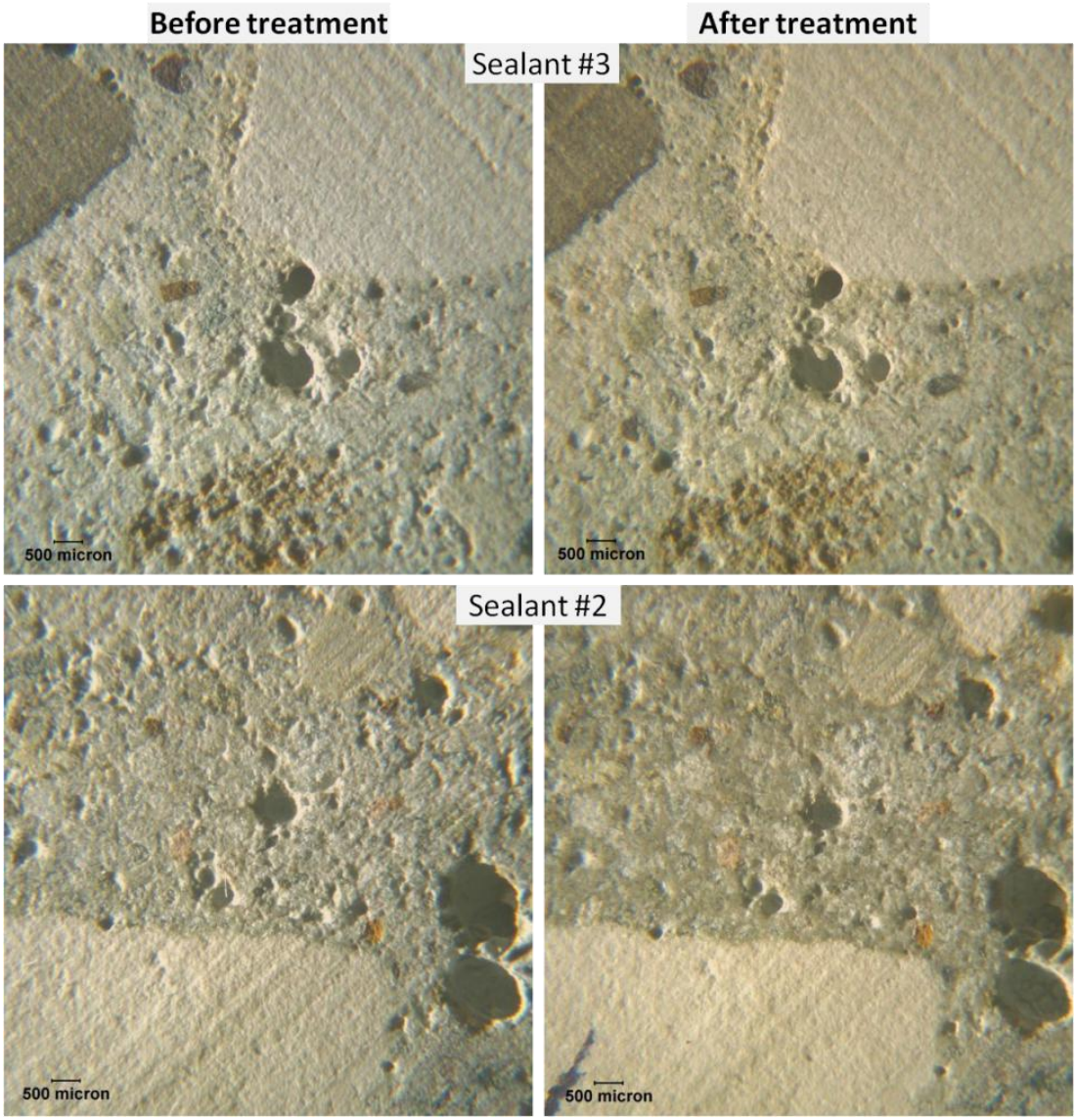

Figure 7.23 Surface profile before and after sealant application

The salt frost scaling results are presented as follows. The control specimens show severe surface scaling and internal damage within 30 F-T cycles, which is consistent with the poor air void system (Table 7.6 and Figure 7.25). Specimens treated using method 2 don't exhibit much improvement (Figure 7.27). This may be because the sealed drying condition creates a high humidity, which undermines the curing efficiency. As a result, a modified procedure was adopted by drying the treated specimens in the open air (20 ℃ and 60±5% RH). This substantially increases the scaling resistance and delays the generation of internal cracking (Figure 7.28, Figure 7.29 and Figure 7.30). The scaled surface is typically characterized by localized damage (Figure 7.29).

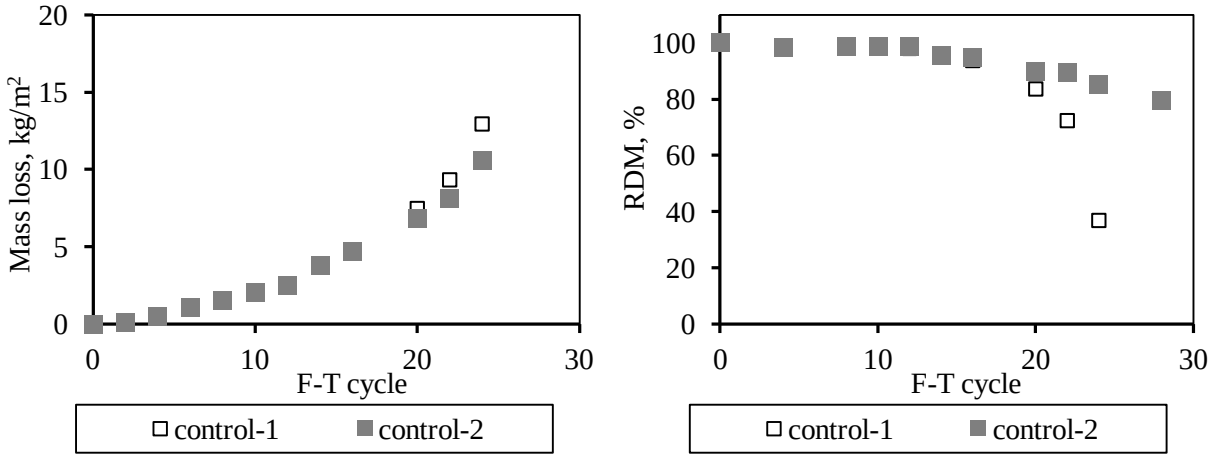

Figure 7.24 Mass loss and RMD change with F-T cycles in control specimens

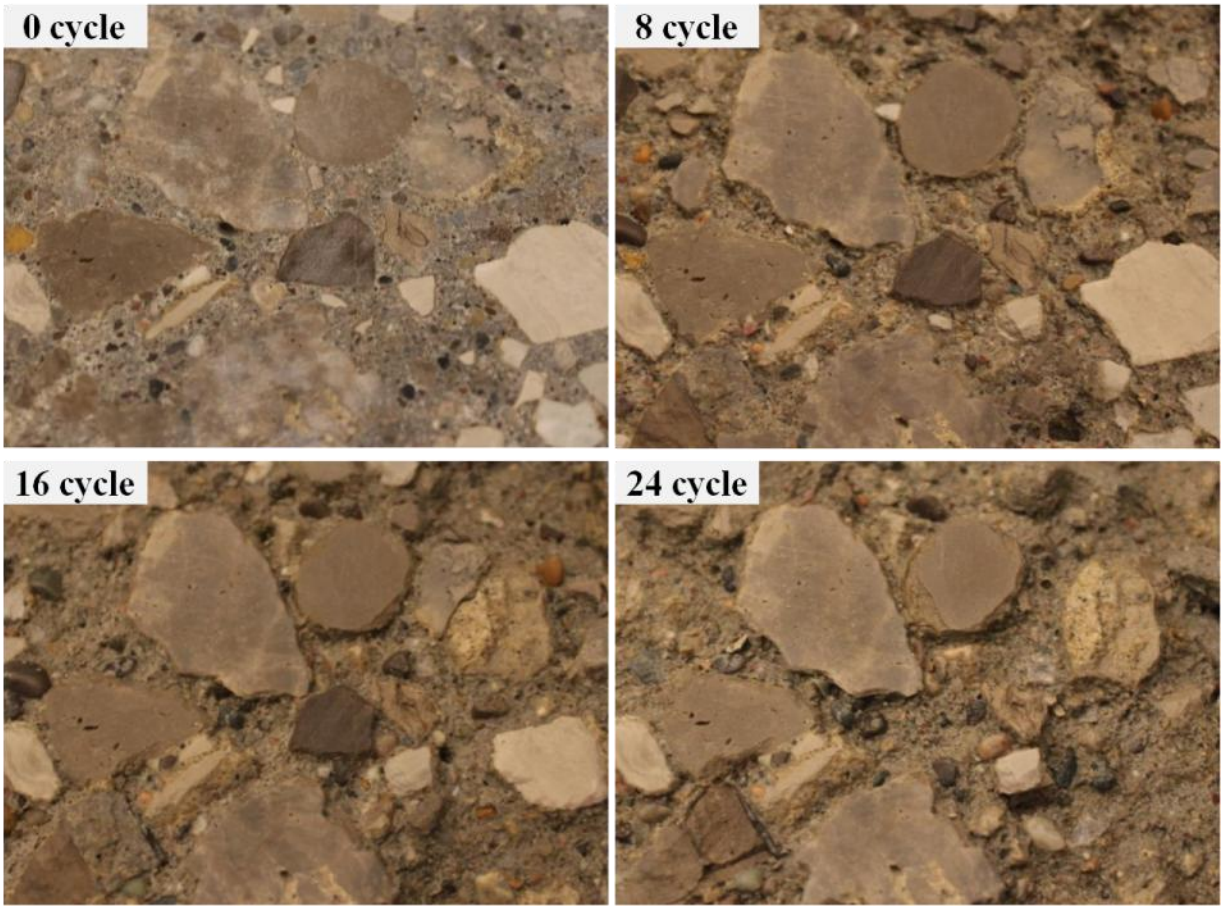

Figure 7.25 Surface profiles of control specimen #2 without surface treatment

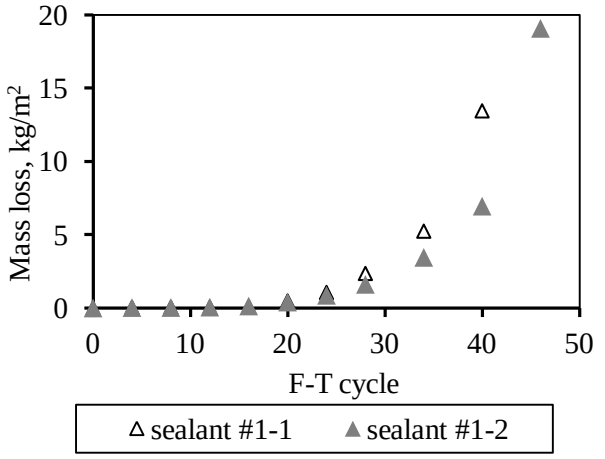
Mass loss, kg/m²
F-T cycle
sealant #1-1
sealant #1-2

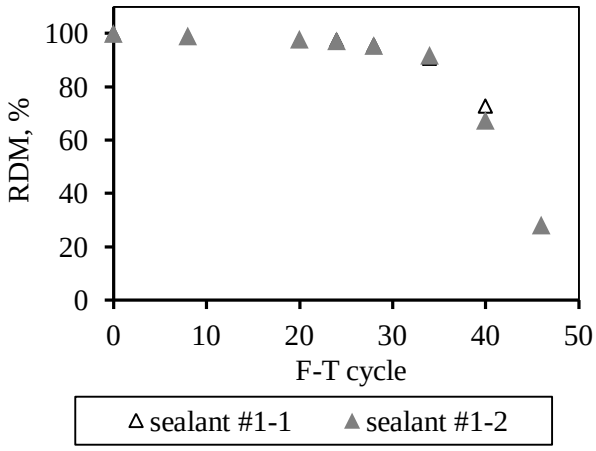
RDM, %
F-T cycle
sealant #1-1
sealant #1-2

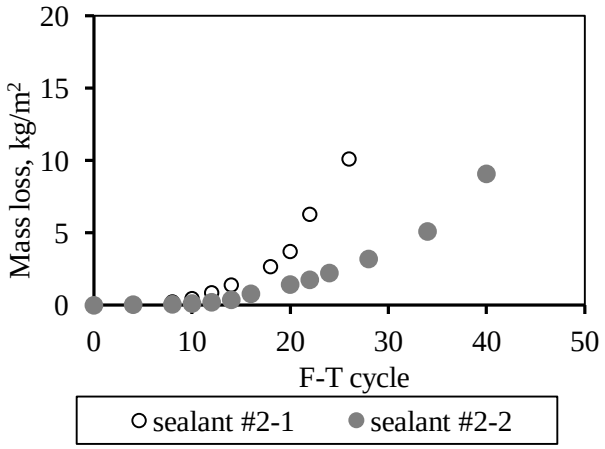
Mass loss, kg/m²
F-T cycle
sealant #2-1
sealant #2-2

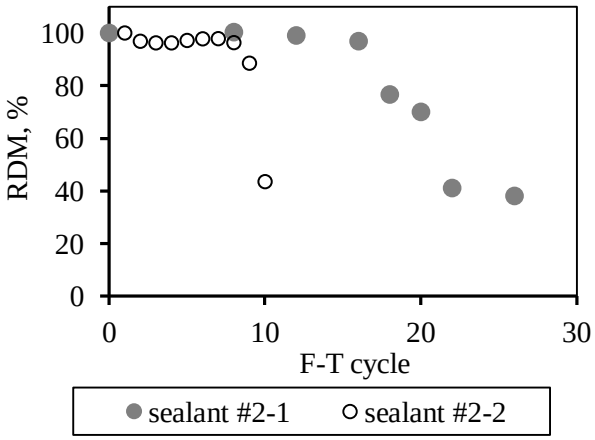
RDM, %
F-T cycle
sealant #2-1
sealant #2-2

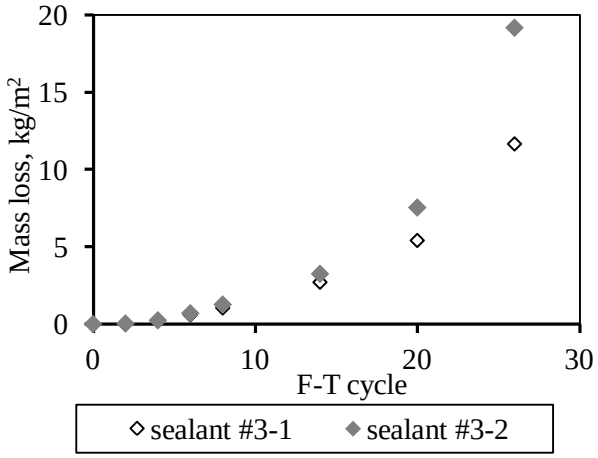
Mass loss, kg/m²
F-T cycle
sealant #3-1
sealant #3-2

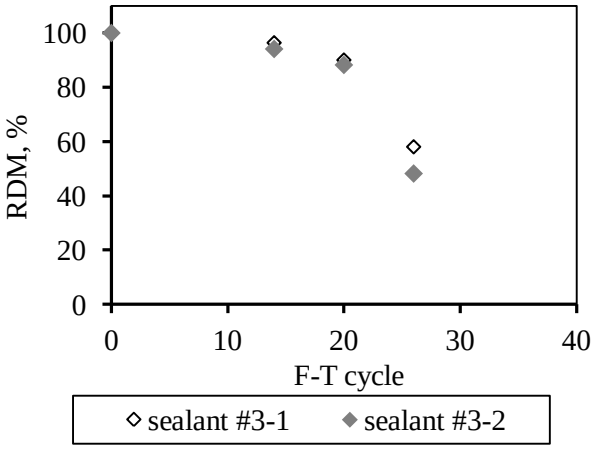
RDM, %
F-T cycle
sealant #3-1
sealant #3-2

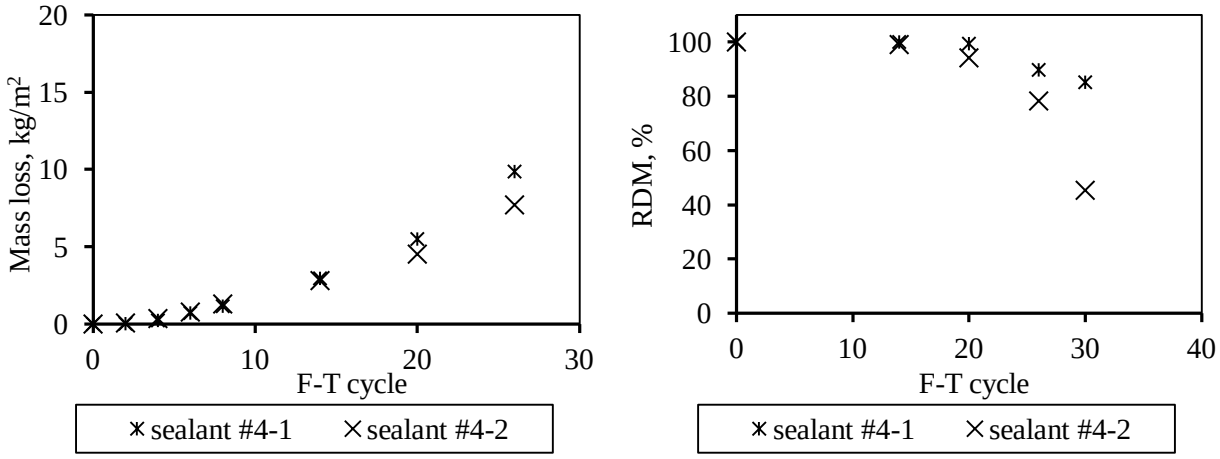

Figure 7.26 Mass loss and RMD change with F-T cycles in surface treated specimens using preconditioning procedure 2

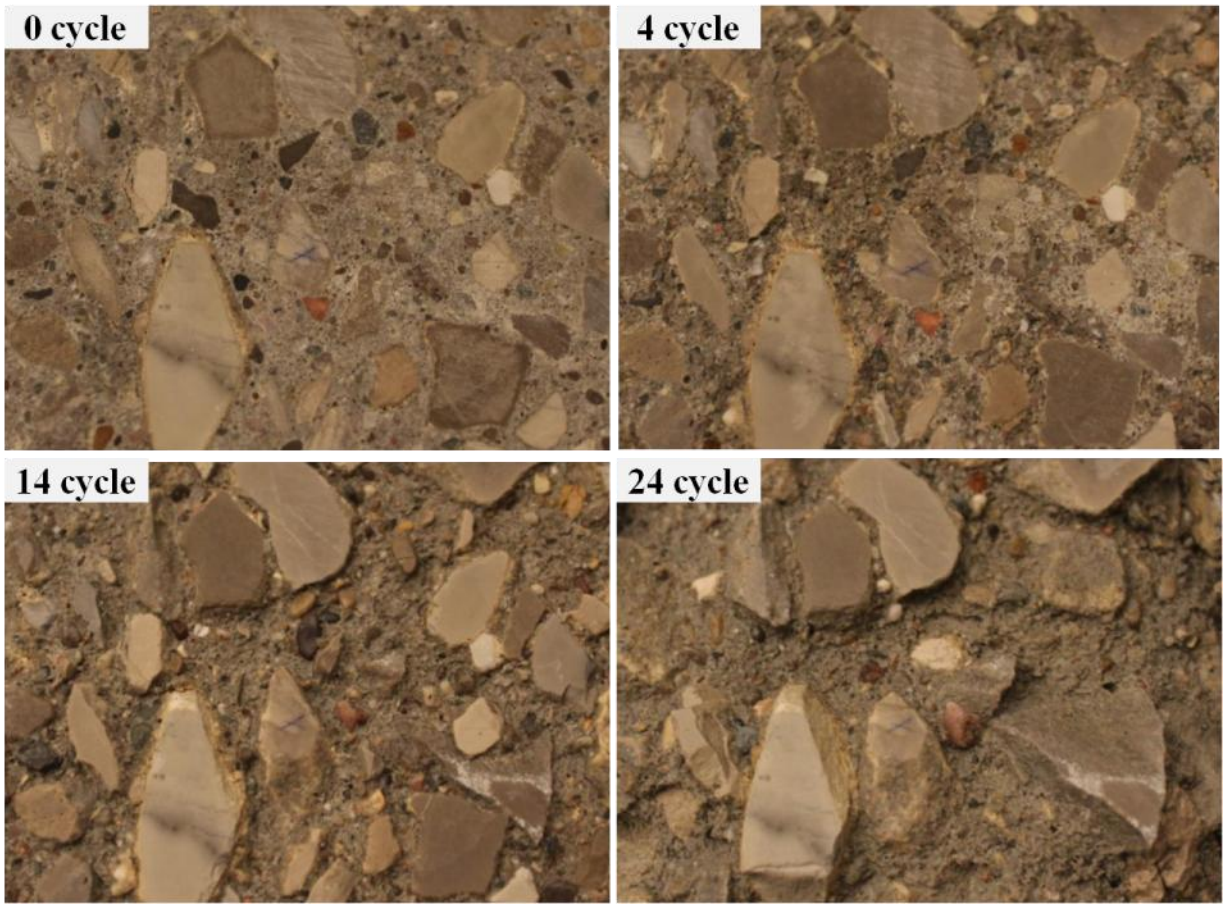

Figure 7.27 Surface profiles of specimen #1 with surface treatment using preconditioning procedure 2 (sealant #3)

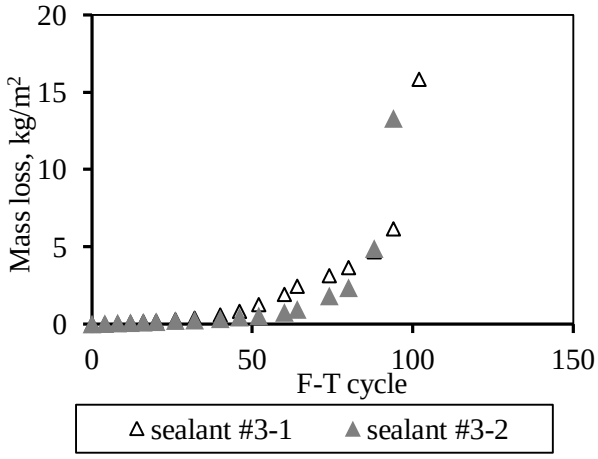
Mass loss, kg/m2
F-T cycle
sealant #3-1
sealant #3-2

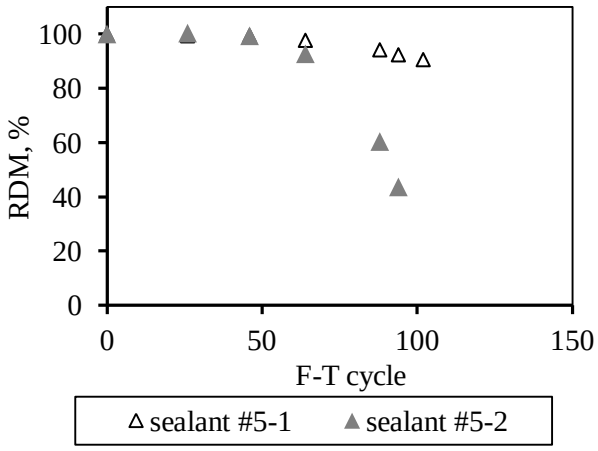
RDM, %
F-T cycle
sealant #5-1
sealant #5-2

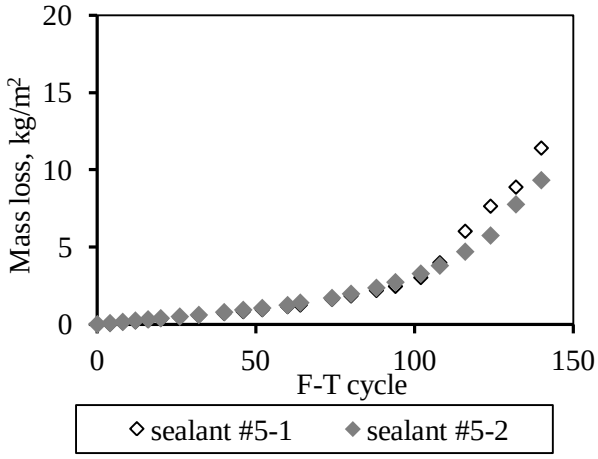
Mass loss, kg/m2
F-T cycle
sealant #5-1
sealant #5-2

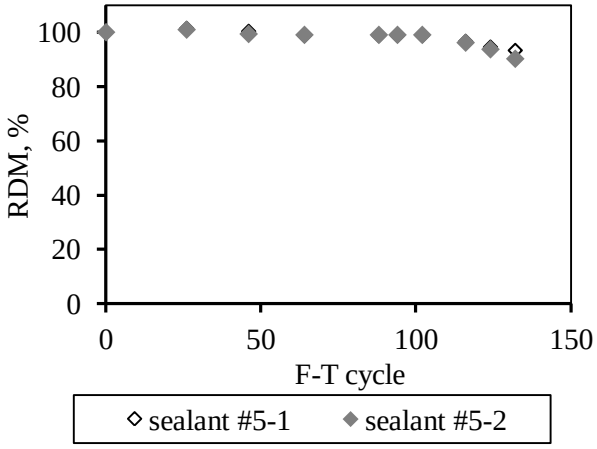
RDM, %
F-T cycle
sealant #5-1
sealant #5-2

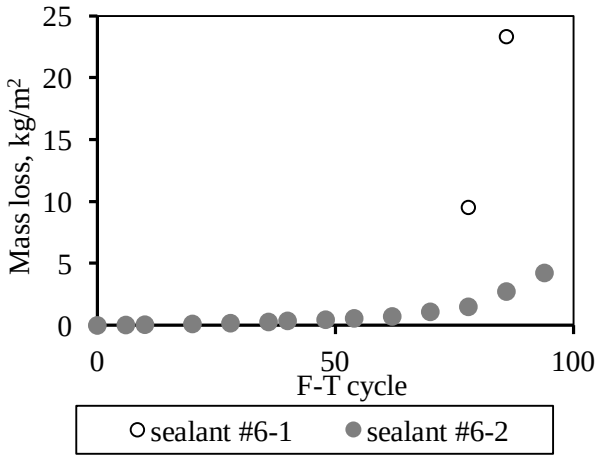
Mass loss, kg/m2
F-T cycle
sealant #6-1
sealant #6-2

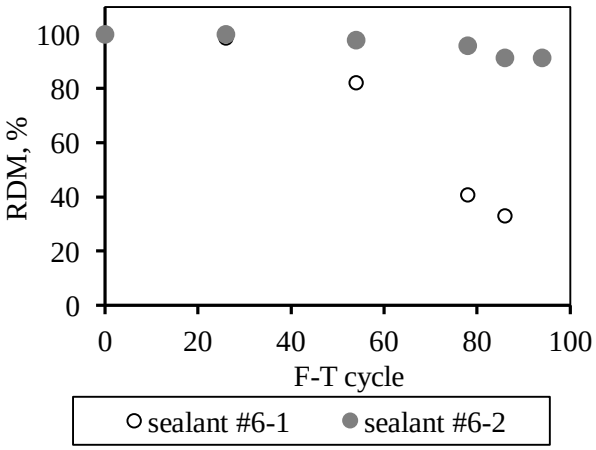
RDM, %
F-T cycle
sealant #6-1
sealant #6-2

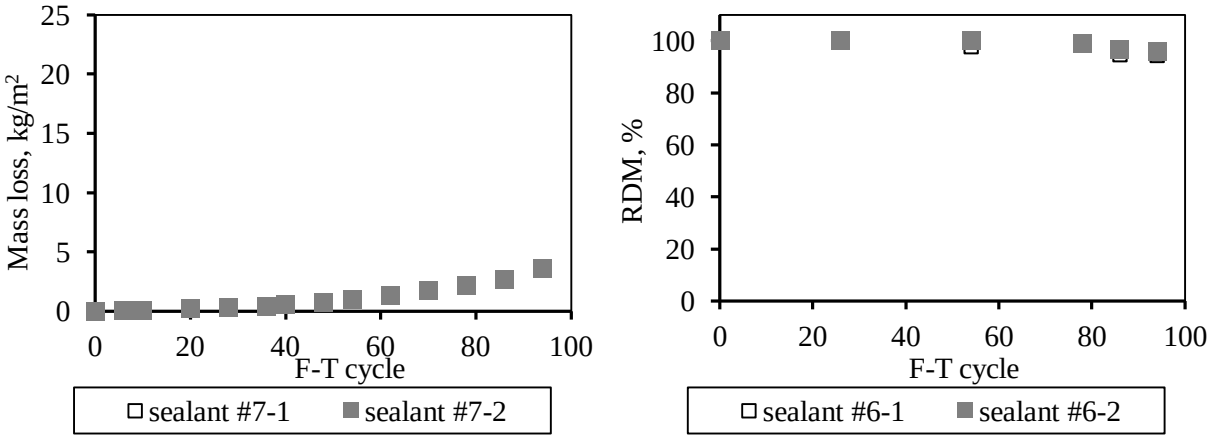

Figure 7.28 Mass loss and RMD change with F-T cycles in surface treated specimens using preconditioning procedure 1

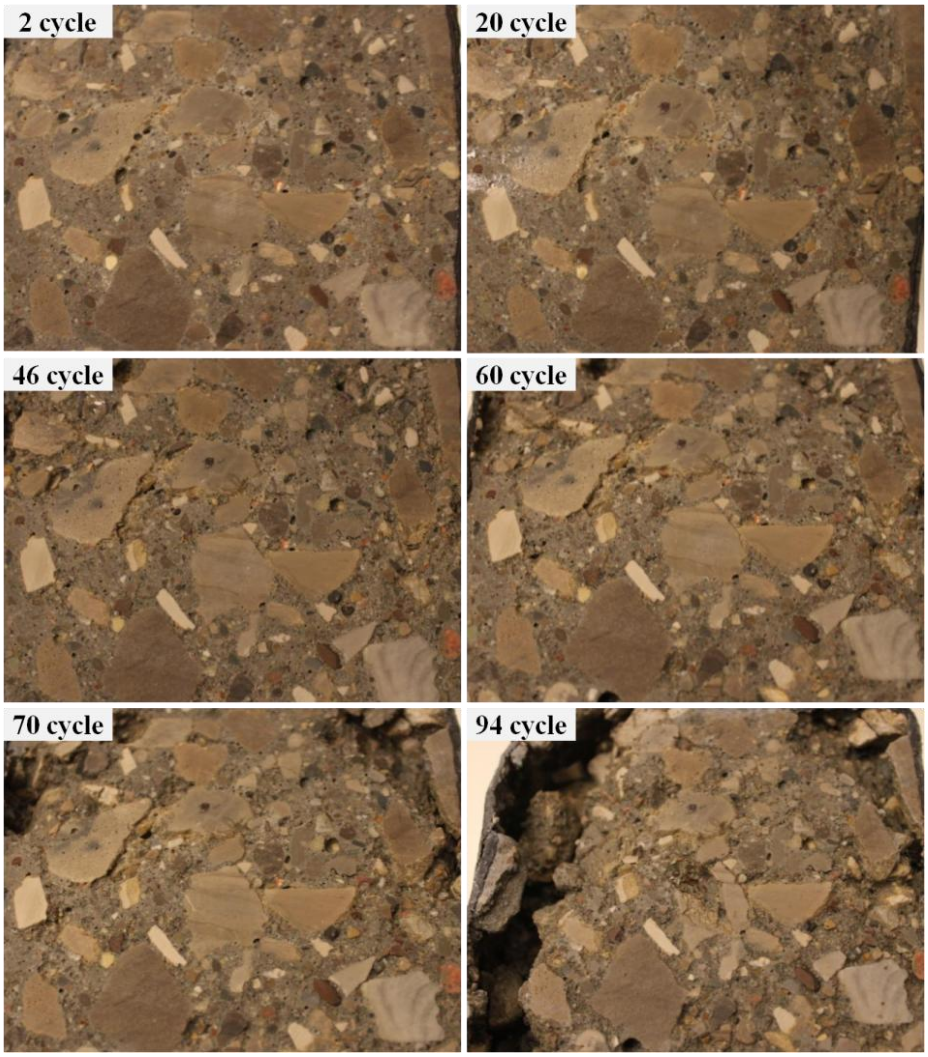

Figure 7.29 Surface profiles of specimen #2 with surface treatment using preconditioning procedure 1 (sealant #3)

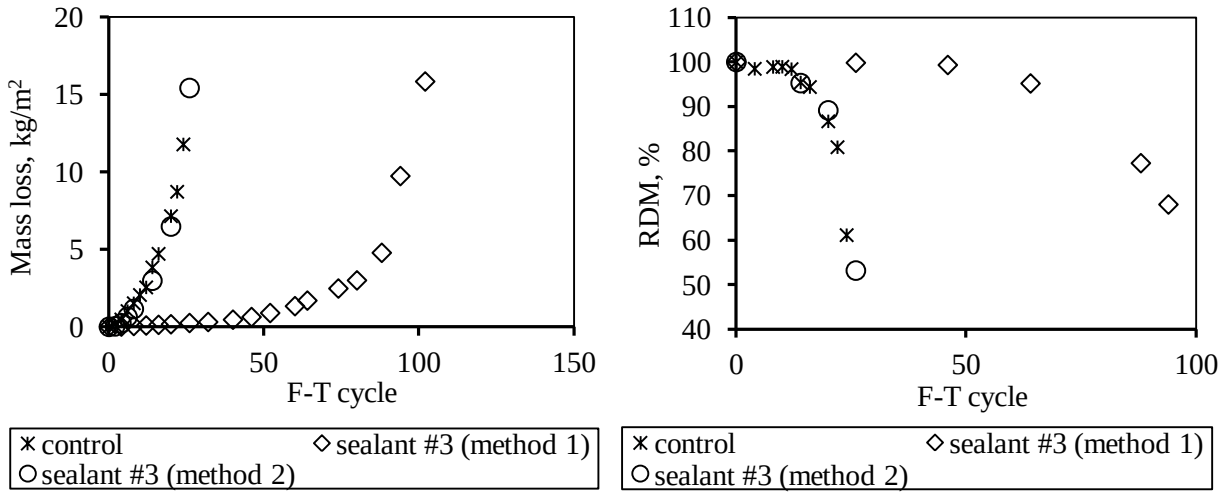

Figure 7.30 Effect of preconditioning method on surface treatment efficiency

7.5 Summary of findings

(1) High early-age strength concrete mixes for the rapid repair of pavement is characterized by a low w/b ratio and the addition of a combination of superplasticizer, accelerator and air entrainer. The dense paste structure and adequate air entrainment guarantees excellent salt scaling resistance in those concretes mixes.

(2) LWA is effective in reducing autogenous shrinkage, which is of major concern in HPC due to its low w/b ratio. Salt frost durability is not adversely affected by adding LWA as partial sand replacement when concrete is adequately air entrained.

(3) Different types of sealants tested show great potential in mitigating salt frost scaling and internal cracking if the appropriate preconditioning procedure is adopted.

Appendix

Table 7.5 Typical mix design for concrete placed in 2014

Mix	w/c ratio	Portland cement	Slag cement	Normal sand	LWA	Gravel	Water	water reducer	air entrainer	accelerator-1	accelerator-2	Slump	Fresh air
		lbs/cubic yard						oz/100 lb cementitious				inch	%
#1	0.315	658	0	1300	0	1767	207.4	8	8	25	25	4.75	3.8
#2	0.316	564	0	1487	0	1767	178.3	8	8	25	25	7.0	8.1
#3	0.315	493	165	1289	0	1767	207.4	8	8	25	25	7.5	7.2
#4	0.315	493	165	1289	0	1767	207.4	8	8	0	25	5.5	6.7
#5	0.315	658	0	847	295	1767	207.4	8	8	25	25	8.5	8.5
#6	0.315	493	165	855	278	1767	207.4	8	8	25	25	8.5	7.7

Table 7.6 Air void properties for all concrete mixes

Placement year	Mix	Linear traverse method					Point count method	
		Total air, %	Entrained air (<1.0mm)	Entrained air (<0.5mm)	Spacing factor, mm	Specific surface, mm^{-1}	Paste content, %	total air, %
2012	#1-1	5.70	3.64	3.53	0.117	33.82	22.5	5.80
	#1-2	5.66	5.10	3.39	0.113	37.31	23.9	5.80
	#2-1	8.25	7.30	6.40	0.071	38.96	22.7	8.70
	#2-2	9.28	8.15	7.06	0.073	38.31	25.9	8.50
	#3-1	5.10	3.57	3.44	0.137	32.86	24.3	5.70
	#3-2	4.52	4.09	3.16	0.131	36.60	24.5	5.90
	#4-1	9.32	6.55	6.19	0.086	24.88	20.3	9.90
	#4-2	8.37	6.68	5.52	0.094	29.98	23.6	8.80
2013	#1-1	4.33	3.25	2.75	145	32.25	22.1	4.80
	#1-2	4.13	3.11	2.68	140	35.01	23.3	4.00
	#2-1	6.47	5.19	3.77	111	31.91	23.0	5.80

	#2-2	7.23	5.76	4.07	117	27.82	24.0	8.40
	#3-1	7.78	6.3	4.56	119	26.79	24.7	6.60
	#3-2	6.87	5.85	4.48	105	31.85	22.9	6.30
	#4-1	5.90	4.85	4.21	101	39.54	25.4	4.50
	#4-2	4.68	4.02	3.31	91	44.03	24.3	4.90
	#5-1	8.43	6.23	3.73	137	20.82	24.0	9.3
	#5-2	8.62	7.18	4.84	164	19.79	23.8	9.3
	#6-1	2.56	1.84	0.39	503	13.72	27.4	2.2
	#6-2	2.53	1.65	0.99	479	13.00	27.4	2.6
	#7-1	7.00	5.72	4.63	93	36.77	23.8	7.5
	#7-2	6.59	5.17	4.16	109	33.04	23.8	6.7
	#8-1	10.13	7.75	6.52	61	34.36	21.3	9.7
	#8-2	8.25	7.30	5.92	86	31.17	23.6	8.7
	#9-1	6.88	6.83	6.36	81	43.60	24.8	7.1
	#9-2	5.36	5.25	4.78	94	45.00	24.3	6.8
	#10-1	5.09	4.55	4.00	126	36.86	25.7	4.9
	#10-2	5.83	4.50	3.76	143	31.00	26.4	6.3
	#11-1	6.25	5.30	4.67	88	43.92	24.3	6.6
	#11-2	7.23	5.38	4.60	105	36.13	27.4	7.3
	#12-1	6.07	5.32	4.80	88	46.52	24.8	5.6
	#12-2	5.22	4.53	4.07	95	48.35	24.4	5.3
	#1-1	4.33	3.25	2.75	145	32.25	22.1	4.80
	#1-2	4.13	3.11	2.68	140	35.01	23.3	4.00
	#2-1	6.47	5.19	3.77	111	31.91	23.0	5.80
	#2-2	7.23	5.76	4.07	117	27.82	24.0	8.40
	#3-1	7.78	6.3	4.56	119	26.79	24.7	6.60
	#3-2	6.87	5.85	4.48	105	31.85	22.9	6.30
	#4-1	5.90	4.85	4.21	101	39.54	25.4	4.50
	#4-2	4.68	4.02	3.31	91	44.03	24.3	4.90
	#5-1	8.43	6.23	3.73	137	20.82	24.0	9.3
	#5-2	8.62	7.18	4.84	164	19.79	23.8	9.3
	#6-1	2.56	1.84	0.39	503	13.72	27.4	2.2
	#6-2	2.53	1.65	0.99	479	13.00	27.4	2.6
	#7-1	7.00	5.72	4.63	93	36.77	23.8	7.5
	#7-2	6.59	5.17	4.16	109	33.04	23.8	6.7

	#8-1	10.13	7.75	6.52	61	34.36	21.3	9.7
	#8-2	8.25	7.30	5.92	86	31.17	23.6	8.7
	#9-1	6.88	6.83	6.36	81	43.60	24.8	7.1
	#9-2	5.36	5.25	4.78	94	45.00	24.3	6.8
	#10-1	5.09	4.55	4.00	126	36.86	25.7	4.9
	#10-2	5.83	4.50	3.76	143	31.00	26.4	6.3
	#11-1	6.25	5.30	4.67	88	43.92	24.3	6.6
	#11-2	7.23	5.38	4.60	105	36.13	27.4	7.3
	#12-1	6.07	5.32	4.80	88	46.52	24.8	5.6
	#12-2	5.22	4.53	4.07	95	48.35	24.4	5.3
2014	#1-1	3.78	2.44	2.18	127	40.32	23.6	4.4
	#1-2	3.20	2.48	1.84	154	37.57	26.0	4.0
	#2-1	8.36	6.63	5.55	64	38.71	21.5	8.0
	#2-2	9.09	7.44	6.47	62	37.88	23.0	8.6
	#3-1	8.42	7.34	5.95	73	39.44	24.3	8.4
	#3-2	9.64	7.10	6.12	71	36.06	24.8	9.1
	#4-1	4.92	4.32	3.68	125	38.97	27.4	4.4
	#4-2	5.27	4.52	4.12	83	55.56	26	4.9
	#5-1	6.82	6.24	5.79	66	48.30	21.6	7.4
	#5-2	6.81	5.34	4.76	73	45.35	22.5	7
	#6-1	8.45	7.26	6.12	77	42.95	27.9	8.3
	#6-2	5.74	4.72	3.87	111	41.57	28.1	5.6

CHAPTER 8 CONCLUSIONS

8.1 Major conclusions

Concrete degradation associated with salt frost scaling is a major concern in infrastructure, which can substantially shorten its service life. Many researchers have investigated the causes for this durability problem with no consensus reached so far. The research summarized in this thesis is aimed to consolidating a previously proposed mechanism based on an extensive experimental program involving an array of mix characteristics (two w/b ratio, two slag cement replacement levels and a wide distribution in air contents) and different test methods, in addition to various surface exposure conditions. This work links scaling resistance of concrete to the ability of the paste matrix to limit capillary suction. Key factors affecting this transport process are identified which lead to a performance-based evaluation methodology and ultimately provides guidance to the preparation of concrete mixes with improved durability and sustainability.

The major conclusions developed from this thesis work are listed below:

(1) Clarification of the relationship between freezing-thawing "pumping" effect and salt frost scaling

- The permanent bulk moisture uptake indicated by the weight gain of concrete specimens during the regular measurement in an F-T test shows no appreciable difference between water and salt exposures while the corresponding mass loss is quite different. This bulk absorption is not explicitly related to salt frost scaling due to its intrinsic property representing only the universal degree of saturation, thus its inability to account for the localized moisture condition in the surface region where scaling occurs, which is further complicated by the lack of experimental methods to accurately measure the actual moisture content in the scaled-off materials.

(2) Confirmation and extension of cryogenic suction as the major mechanism for salt frost scaling

- Cryogenic suction in the surface layer (~300 μm thick) is confirmed to be the major mode of liquid transport governing pore pressure buildup in concrete pores. This mechanism is thermodynamically characterized by the Gibbs free energy between ice and unfrozen water with the effect of temperature, pressure and salt concentration being accounted for.
- This work pioneered the measurement of pore volume by nitrogen sorption on both the scaled-off materials and control mortar samples. Results show significant increase in pore volume of the scaled-off materials collected during an F-T cycle. This is a direct result of ice growth that expands the original capillary pores. The expansive pressure causes compression on the interlayer pores. The net result is a large increase in apparent capillary porosity.
- Three components are identified which are essential in controlling the pore pressure buildup and thus the severity of surface scaling: (I) initial ice formation in concrete pores, (II) the presence of salt in the surface liquid and (III) the transport channel (viz. concrete pore system) connecting the external liquid and the concrete surface region. Each component is indispensible and their interaction leads to satisfactory interpretation of several experimental observations, such as the pessimum salt concentration effect, specimen thickness effect.
- A conceptual model for salt frost scaling is introduced which involves the interaction of the paste dilation due to pore expansion in the surface region and the overall contraction in the remaining bulk concrete. The resultant stress state in the surface region demonstrates compression in the two parallel directions and tension in the vertical direction, which causes paste swelling and scaling.

(3) Construction of performance-based criterion in evaluating scaling resistance

- The role of air-void system in scaling resistance is clarified. Air entrainment in the normal range has minor influence on sorptivity while the capillary pore system dominates the suction rate. Thus a lack of correlation is found between air void properties and scaling resistance. However, air entrainment is needed for protecting internal frost

damage due to instant ice formation, which causes disintegration between the mortar and coarse aggregate and results in accelerated mass loss increase.

- A clear empirical correlation between sorptivity and mass loss in air-entrained concretes at different numbers of F-T cycles is established, which indicates sorptivity is an effective parameter for salt frost scaling resistance.
- The theoretical nature of sorptivity is enhanced by a refined model to construct the moisture uptake curves based on the paste pore structure characteristics (pore volume and its size distribution). This model holds the potential to the development of a performance-based design of concrete mixes.

(4) Mitigation of salt frost scaling and its application to field samples

- The key technique in reducing surface scaling is to mitigate pore ice growth, the culprit for pore pressure buildup. Two approaches are proposed: (I) Modification of the paste pore structure towards a refined pore size and increased discontinuity and turtuosity by lowering the w/b ratio or the incorporation of supplementary cementitious materials (such as slag cement); (II) Introduction of hydrophobic liners on pore walls (such as silanes).
- An extensive experimental program is carried out to validate the two approaches on laboratory and field concrete mixes. Results show surface scaling is substantially reduced in concrete mixes with 0.33 w/b ratio or 045 w/b ratio with 50% slag cement replacement and is almost completely eliminated for an extended period in concrete mixes with silane-based surface treatment.

8.2 Recommendations for future work

Several experimental and modeling aspects based on this work can be further explored and they are presented as follows.

- Development of a unified service–life model on general frost damage in concrete
  Internal bulk cracking and superficial scaling are both related to the degree of saturation in concrete pores (including entrained air voids), the former being governed by the overall saturation level while the latter is a matter of localized saturation. Construction of a complete pore map (primarily capillary pores and air void system) can be realized by the combined nitrogen sorption and air void analysis measurement, based on which the

initial capillary suction rate (governing surface scaling) and the universal degree of saturation (governing bulk frost cracking) is able to be continuously monitored. The ultimate goal is to determine the critical limits for the two processes and develop a service-life model for their prediction.

- Further investigation on dynamics of ice growth under salt-frost exposure

  In this work, the ice growth has been characterized theoretically from the perspective of thermodynamics and experimentally from the continuous length-change measurement and its ultimate effect is reflected from the pore volume increase based on nitrogen sorption test of scaled-off materials. Nevertheless, one more dimension can be added to the dynamics of ice growth, that is the temperature change encompassing this exothermic process by utilizing low-temperature calorimeter. This will be an important compliment to the existing results.

- Modeling on the freezing deformation in concrete

  The cementitious matrix where freezing occurs is a typical viscoelastic material. Recent work by Prof. Will Hansen (Hansen et al. 2014) makes an important advancement towards the internal (shrinkage) stress calculation in concrete pore system using a constant viscoelastic hydration modulus. This work can be extended to frost damage which is another scenario of internal stress induced cracking problem.

REFERENCES

ACI Committee 301, (1999) “Specification for Structural Concrete (ACI 301-99)”, American Concrete Institute, Farmington Hills, MI, 49 pp.

ACI Committee 318, (2005) “Building Code Requirements for Structural Concrete (ACI 318-05) and Commentary (318R-05)”, American Concrete Institute, Farmington Hills, MI, 430 pp.

Aïtcin, P.-C., (1998) “High-Performance Concrete”, E & FN SPON, New York.

Alexander, M. G., Ballim, Y., Stanish, K., (2008) “A framework for use of durability indexes in performance based design and specifications for reinforced concrete structures”, *Materials and Structures*, Vol. 41, No. 5, pp. 921-936.

Arnfelt, H., (1943) “Damage on concrete pavements by wintertime salt treatment”, Meddelande 66, Statens Väginstitut, Stockholm (In Swedish).

ASTM C 231-00, (2000) “Standard test method for air content of freshly mixed concrete by the pressure method”, ASTM International, West Conshohocken, PA

ASTM C 457-00, (2000) “Standard test method for microscopical determination of parameters of the air-void system in hardened concrete”, ASTM International, West Conshohocken, PA, 14 pp.

ASTM C 672-00, (2000) “Standard test method for scaling resistance of concrete surfaces exposed to deicing chemicals”, ASTM International, West Conshohocken, PA.

ASTM C125-00, (2000) “Standard terminology relating to concrete and concrete aggregates”, ASTM International, West Conshohocken, PA, 6 pp.

ASTM C1585, (2013) “Standard test method for measurement of rate of absorption of water by hydraulic-cement concretes”, ASTM International, West Conshohocken, PA.

ASTM C192, (2013) “Standard practice for making and curing concrete test specimens in the laboratory”, ASTM International, West Conshohocken, PA.

Attiogbe, E. K., (1993) “Mean spacing of air voids in hardened concrete”, *ACI Materials Journal*, V. 90, No. 2, pp. 174-181.

Auberg, R., Setzer, M.J., (1997) “Influence of water uptake during freezing and thawing”, *Proceedings International RILEM Workshop on Resistance of Concrete to Freezing and Thawing with and without De-icing Chemicals*, Chapman & Hall, pp. 232-245.

Backstrom, J.E., Burrows, R.W., Mielenz, R.C., and Wolkodoff, V.E., (1958) “Origin, evolution, and effects of the air void system in concrete-Part 2: influence of type and amount of air-entraining agent”, *Journal of American Concrete Institute*, Vol. 55, pp. 261-272.

Bager, D.H., (2000) “Freeze-thaw damage and water-uptake in low water/cement ratio concrete”, *Structural Engineering and Materials–A Centenary Celebration*. Department of Structural Engineering and Materials Technical University of Denmark, 119-130.

Bager, D.H., Jacobsen, S., (1999) “A model for the destructive mechanism in concrete caused by freeze/thaw action”, *Rilem TC IDC Workshop on Frost Damage in Concrete*, Minneapolis, 1999, pp. 17-40.

Barrett, E.P., Joyner, L.G., Hallenda, P.H., (1951) “The determination of pore volume and area distributions in porous substances. I. Computations from nitrogen isotherms”, *Journal of American Chemistry Society*, Vol. 73, pp. 373–381.

Basheer, L., Cleland, D.J., (2006) “Freeze-thaw resistance of concretes treated with pore liners”, *Construction and Building Materials*, Vol. 20, No. 10, pp. 990-998.

Basheer, L., Cleland, D.J., (2011) “Durability and water absorption properties of surface treated concretes”, *Materials and Structures*, Vol. 44, No. 5, pp. 957-967.

Bauerecker, S., Ulbig, P., Buch, V., Vrbka, L., and Jungwirth, P., (2008) “Monitoring ice nucleation in pure and salty water via high-speed imaging and computer Simulations”, *The Journal of Physical Chemistry C*, Vol. 112, pp. 7631-7636.

Bentur, A., Igarashi, S-i., Kovler, K. (2001) “Prevention of autogenous shrinkage in high-strength concrete by internal curing using wet lightweight aggregates”, *Cement and Concrete Research*, Vol. 31, pp. 1587–1591.

Bentz, D.P., Ehlen, M.A., Ferraris, C.F., Garboczi, E.J., (2001) "Sorptivity-based service life predictions for concrete pavements", *Proceedings of 7th International Conference on Concrete Pavements*, Volume1, International Society for Concrete Pavements, Orlando, pp. 181-193.

Bentz, D.P., Koenders, E.A.B., Monnig, S., Reinhardt, H.-W., van Breugel, K., and Ye, G., (2007) "Materials science-based models in support of internal water curing", *RILEM state-of-the-art report on Internal Curing of Concrete*, RILEM Publications S.A.R.L, France, pp. 29-43.

Blanchard, D., Frémond, M., (1982) "Cryogenic suction in soils", *Proceedings of the Third International Symposium on Ground Freezing*, Hanover, New Hampshire, pp. 233-238.

Bollmann, K., and Stark, J., (1996) "Ettringitbildung im erhärteten Beton und Frost-Tausalz-Widerstand", Wiss. Zeitschrift Bauhaus-Universität Weimar, No.4/5, pp. 9-16.

Borgnakke, C., Hansen, W., Kang, Y., Liu, Z. and Koenders, E.A.B, (2012) "Cryogenic suction pump mechanism for combined salt- and frost exposure", *2nd International Conference on Microstructural-related Durability of Cementitious Composites (Microdurability 2012)*, Amsterdam, The Netherlands, pp. 777-785.

Chidiac, S.E., Panesar, D.K., (2006) "Sorptivity of concrete as an indicator of laboratory freeze-thaw scaling performance", *Proceedings International RILEM Workshop on Performance Based Evaluation and Indicators for Concrete Durability*, Madrid, Spain, pp. 59-66.

Christodoulou, C., Goodier, C.I., Austin, S.A., Webb, J., Glass, G.K., (2013) "Long-term performance of surface impregnation of reinforced concrete structures with silane", *Construction and Building Materials*, Vol. 48, pp. 708-716

Cordon, W. A., (1966) "Freezing and thawing of concrete-mechanisms and control", *ACI Monograph*, No. 3. Detroit, American Concrete Institute.

Coussy, O., (2005) "Poromechanics of freezing materials", *Journal of the Mechanics and Physics of Solids*, Vol. 53, pp. 1689–1718.

Dang, Y., Xie, N., Kessel, A., McVey, E., Pace, A., Shi, X., (2014) "A Accelerated laboratory evaluation of surface treatments for protecting concrete bridge decks from salt scaling", *Construction and Building Materials*, Vol. 55, pp. 128–135.

de Vries, J., Polder, R.B., (1997) "Hydrophobic treatment of concrete", *Construction and Building Materials*, Vol. 11, No. 4, pp. 259-265.

Everett, D. H., (1961) "The thermodynamics of frost damage to porous solids," *Transactions of Faraday Society*, No. 57, pp. 1541-1551.

Fagerlund, G., (1975) "Studies of the Destruction Mechanism at Freezing of Porous Materials", *6th International Congress on Problems Raised by Frost Action*, Le Havre, France, April 23-25, 28 pp.

Fagerlund, G., (1977) "Equations for calculating the mean free distance between aggregate particles or air-pores in concrete", CBI Forskning 8:77 Monograph, 28 pp.

Fagerlund, G., (1992) "Studies of the Scaling, the Water Uptake and the Dilation of Mortar Specimens Exposed to Freezing and Thawing in NaCl Solutions", *Freeze-Thaw and De-Icing Resistance of Concrete*, Lund Institute of Technology, Div. Building Materials, report TVBM-3048, pp 36-66.

Fagerlund, G., (1997) "Internal frost attack-state of the art", *Proceedings International RILEM Workshop on Resistance of Concrete to Freezing and Thawing with and without De-icing Chemicals*, Chapman & Hall, pp. 321-338.

Fagerlund, G., (2004) "A service life model for internal frost damage in concrete", Division of Building Materials, Lund Institute of Technology, Report TVBM-3119, Lund, Sweden, 48 pp.

Feldman, R. F. and Sereda, P. J., (1968) "A model for hydrated Portland cement paste as deduced from sorption-length change and mechanical properties", *Materials and Structures*, Vol. No. 6, pp. 509-520.

Feldman, R. F., (1983) "Significance of porosity measurements on blended cement performance", *Fly Ash Silica Fume, Slag and Other Mineral By-Products in Concrete*, SP-79, pp. 235-255.

Freitag, S.A., Bruce, S.M., (2010) "The influence of surface treatments on the service lives of concrete bridges", NZ Transport Agency research report 403, 91 pp.

Fridh, K., (2005) "Internal frost damage in concrete-experimental studies of destruction mechanisms," PhD thesis, Division of Building Materials, Lund Institute of Technology, Lund, Sweden, 378 pp.

Gagné, R., Houehanou, E., Jolin, M., Escaffit, P., (2011) "Study of the relationship between scaling resistance and sorptivity of concrete", *Canadian Journal of Civil Engineering*, Vol. 38, No. 11, pp. 1238-1248.

Garboczi, E.J., and Bentz, D.P., (1999) "Percolation aspects of cement paste and concrete-properties and durability", *ACI SP-189 (High-Performance Concrete: Research to Practice)*, pp 147-164.

Geiker, M., Thaulow, N., (1996) "Ingress of moisture due to freeze/thaw exposure", *Proceedings Nordic Research Seminar: Frost Resistance of Building Materials*, Lund University, pp. 159-162.

Hall, C. and Hoff, W. D., (2002) "Water transport in brick, stone and concrete", Spon Press, London, 318 pp.

Hall, C., (1989) "Water sorptivity of mortars and concretes: a review", *Magazine of Concrete Research*, Vol. 41, No. 147, pp. 51-61.

Hammer, T.A. and Sellevold, E.J., (1990) "Frost resistance of high-strength concrete", *ACI SP-121*, 457-487.

Hansen, W. and Kang, Y., (2010) "Durability study of the US-23 aggregate test road and recent JPCP projects with premature joint deterioration", Michigan Transportation Department Report RC-1534, 38 pp.

Hansen, W., Liu, Z., Koenders, E.A.B., (2014) "Viscoelastic stress modeling in cementitious materials using constant viscoelastic hydration modulus", *1st International Conference on Ageing of Materials and Structures (AMS 2014)*, Delft University of Technology, pp. 509-515.

Harnik, A.B., Meier, U. and Rösli A., (1980) "Combined influence of freezing and deicing salt on concrete-physical aspects", *Durability of Building Materials and Components, ASTM STP 691*, American Society for Testing and Materials, pp. 474-484.

Hazrati, Sk., Abesque, C., Pigeon, M., Sedran, T., (1997) "Efficiency of sealers on the scaling resistance of concrete in the presence of deicing salts", RILEM Proceedings 30, *Freeze-Thaw Durability of Concrete,* E & FN Spon, New York, pp. 165-196.

Helmuth, R.A., (1960) "Discussion on a paper by Nerenst", *4th International Symposium on the Chemistry of Cement*, Washington D.C., pp. 829-833.

Hooton, R.D., Mesic, T., Beal, D.L., (1993) "Sorptivity testing of concrete as an indicator of concrete durability and curing efficiency", *Proceedings The Third Canadian Symposium on Cement and Concrete,* Ottawa, pp. 264-275.

Jacobsen, S., (1995) "Scaling and cracking in unsealed freeze/thaw testing of portland cement and silica fume concretes", PhD Thesis, Norwegian Institute of Technology, Trondheim, 286 pp.

Jacobsen, S., (2002) "Liquid uptake mechanisms in wet freeze/thaw: review and modeling", *RILEM Proceedings PRO 25,* Cachan, France, pp. 41–51.

Jacobsen, S., Sellevold, E.J., (1994) "Frost/salt scaling testing of concrete-importance of absorption during test", *Nordic Concrete Research*, Vol. 14, pp. 26-44.

Jacobsen, S., Sœther, D.H., Sellevold, E.J., (1997) "Frost testing of high strength concrete: Frost/salt scaling at different cooling rates", *Materials and Structures*, Vol. 30, No. 1, pp 33-42.

Kang, Y., (2010) "Surface scaling mechanism and prediction for concrete", PhD Thesis, University of Michigan, 216 pp.

Kargol, M.A., Muller, U., Gardei, A., (2013) "Properties and performance of silane: blended cement systems", *Materials and Structures,* Vol. 46, No. 9, pp.1429–1439.

Karlsson, J. O. M., Cravalho, E. G. and Toner, M., (1994) "A model of diffusion limited ice growth inside biological cells during freezing", *Journal of Applied Physics*, Vol. 75, No. 9, pp. 4442-4455.

Kaufmann, J. P., (2000) "Experimental identification of damage mechanisms in cementitious porous materials on phase transition of pore solution under frost deicing salt attack", PhD thesis, Swiss Federal Institute of Technology Lausanne, 181 pp.

Kaufmann, J. P., (2004) "Experimental identification of ice formation in small concrete pores", *Cement and Concrete Research*, Vol. 34, No. 8, pp. 1421-1427.

Kozikowski, R. L. Jr., Vollmer, D. B., Taylor, P. C., and Gebler, S. H., (2005) "Factors affecting the origin of air-void clustering", SN2789, Portland Cement Association, Skokie, Illinois, 22 pp.

Kropp, J., (1995) "Relations between transport characteristics and durability", *Proceedings Performance Criteria for Concrete Durability*, London, Chapman & Hall.

Lindmark, S., (1998) "Mechanisms of salt frost scaling of Portland cement-bound materials: Studies and hypothesis," PhD thesis, Division of Building Materials, Lund Institute of Technology, Lund, Sweden, 286 pp.

Litvan, G.G., (1976) "Frost action in cement in the presence of De-Icers", *Cement and Concrete Research*, Vol. 06, No. 3, pp. 351-356

Liu, Z., Hansen, W., (2014) "Cryogenic suction as a major salt frost scaling mechanism in cementitious materials", Submitted to *Cement and Concrete Research*.

Liu, Z., Kang, Y., Hansen, W., and Borgnakke, C., (2012) "Cryogenic suction-a major salt scaling mechanism in highway concrete", 10th International Conference on Concrete Pavement, July 8-12, Quebec, Canada.

Lura, P., (2003) "Autogenous deformation and internal curing of concrete", PhD Dissertation, Delft University of Technology.

MacInnis, C. and Whiting, J.D., (1979) "The frost resistance of concrete subjected to a deicing agent", *Cement and Concrete Research*, Vol. 9, No. 3, pp. 325-335.

Manmohan, D., Mehta, P. K., (1981) "Influence of pozzolanic, slag, and chemical admixtures on pore size distribution and permeability of hardened cement pastes", *Cement, Concrete and Aggregates*, Vol. 3, No.1, pp. 63-67.

Marchand, J., Pigeon, M., Bager, D.H., Talbot, C., (1999) "Influence of chloride solution concentration on deicer salt scaling deterioration of concrete", *ACI Materials Journal*, Vol. 96, No. 4, pp. 429-435.

Marchand, J., Sellevold, E.J., Pigeon. M., (1994) "The deicer salt scaling deterioration of concrete-an overview", *ACI SP-145*, pp. 1-46.

Mindess, S., Young, J. F. and Darwin, D., (2003) "Concrete", 2nd Edition, Person Education Inc., 644 pp.

MTO LS-142, (2012) “Scaling Resistance of concrete surfaces exposed to deicing chemicals”, Ministry of Transportation, Ontario.

Naik, T.R., (2008) “Sustainability of concrete construction”, *Practice Periodical on Structural Design and Construction*, Vol. 13, No. 2, pp. 98-103.

Nguyen, H.T., Jacobsen, S., Melandsø, F., (2012) “Capillary suction model as pipes of different sizes: flow conditions and comparison with experiments”, *12th International Congress on Durability of Concrete*, Trondheim, pp. 1-15.

Nolan, É., Basheer, P.A.M., Long, A.E., (1995) “Effects of three durability enhancing products on some physical properties of near surface concrete”, *Construction and Building Materials*, Vol. 9, No. 5, pp. 267-272.

Note from E.J. Sellevold (Liquid permeability, capillary suction: PF-method), 1990.

Ollivier, J. P., Maso, J. C. and Bourdette, B., (1995) “Interfacial transition zone in concrete”, *Advanced Cement Based Materials*, Vol. 2, No. 1, pp. 30-38.

Ouyang C. and Lane O. J., (1999) “Effect of infilling of air voids by ettringite on resistance of concretes to freezing and thawing”, *ACI Special Publication*, Vol. 177, pp. 249-262.

Patek, J.; Hruby, J.; Klomfar, J., and Souckova, M., (2009) “Reference correlations for thermophysical properties of liquid water at 0.1 MPa”, *Journal of Physical and Chemical Reference Data*, V. 38, No. 1, pp. 21-29.

Penttala, V., and Al-Neshawy, F., (2002) “Stress and strain state of concrete during freezing and thawing cycles”, *Cement and Concrete Research*, Vol. 32, No. 9, pp. 1407-1420.

Petersson. P-E., (1991) “Scaling resistance of concrete. Testing according to SS 13 72 44. Freeze-Thaw and Deicing Resistance of Concrete”, Research Seminar Freeze-thaw and De-icing Resistance of Concrete, Lund, pp. 101-116.

Philleo, R. E., (1983) “A method for analyzing void distribution in air-entrained concrete”, *Cement, Concrete, and Aggregate*, Vol. 5, No. 2, pp. 128-130.

Pickett, G., (1953) “Flow of moisture in hardened Portland cement during freezing”, *Highway Research Board Proceedings*, Vol. 32, pp. 276-284.

Pigeon M., Marchand J. and Pleau R., (1996) “Frost resistant concrete”, *Construction and Building Materials*, Vol. 10, No. 5, pp. 339-348.

Pigeon, M., Pleau, R., (1995) “Durability of concrete in cold climates”, Modern Concrete Technology Series 4, E & FN SPON.

Pleau, R., and Pigeon, M., (1996) “The use of the flow length concept to assess the efficiency of air entrainment with regards to frost durability: Part I—description of the test method”, *Cement, Concrete, and Aggregate*, Vol. 18, No. 1, pp. 19-29.

Pleau, R., Plante, P., Gagné, R., and Pigeon, M., (1990) “Practical considerations pertaining to the microscopical determination of air void characteristics of hardened concrete (ASTM C 457 Standard)”, *Cement, Concrete, and Aggregates*, Vol. 12, No. 2, pp. 3-11.

Powers, T. C. and Brownyard, T. L., (1947) “Studies of the physical properties of hardened Portland cement paste”, *ACI Journal*, Vol. 18, No. 8, pp. 972-990

Powers, T. C., (1949) “The air requirement of frost-resistance concrete”, *Proceedings of Highway Research Board*, Bull. 39, Vol. 29, 28 pp.

Powers, T. C., (1965) “The mechanisms of frost action in concrete”, in Stanton Walker Lecture Series on the Materials Science, Lecture no 3, November.

Powers, T.C., (1945) “A working hypothesis for further studies of frost resistance of concrete”, *ACI Journal*. Vol. 16, No. 4, pp. 245-272.

Powers, T.C., and Helmuth, R.A., (1953) “Theory of volume changes in hardened Portland cement paste during freezing”, *Proceedings of Highway Research Board*, 32nd Annual Meeting, Bull. 46, pp. 285-297.

Punkki, J., Sellevold, E.J., (1994) “Capillary suction in concrete: Effects of drying procedure”, *Nordic Concrete Research*, Vol. 15, pp. 59-74.

Rachel J. D., Peter C. T. and Laura J. P., (2007) “Ettringite deposits in air voids,” *Journal of Transportation Research Board*, Vol. 1893, pp. 75-80.

Rilem Committee TC-117, (1995) “Draft recommendations for test methods for the freeze-thaw resistance of concrete, slab test and cube test”, *Materials and Structures*, vol. 28, pp 366-371.

Rønning, T.F., (1999) “Moisture absorption during freeze-thaw and relation to deterioration”, *Proceedings the 3rd Nordic Research Seminar: Frost Resistance of Building Materials*, Lund University, pp. 113-118.

Rønning, T.F., (2001) “Freeze-thaw resistance of concrete effect of: Curing conditions, moisture exchange and materials”, PhD Thesis, The Norwegian Institute of Technology, Trondheim, 416 pp.

Roy, D. M. and Idorn. G. M., (1982) “Hydration, structure and properties of blast furnace slag cements, mortars and concrete”. *ACI Journal*, pp. 444-457.

Sandström, T., Fridh, K., Emborg, M., Hassanzadeh, M., (2012) “The influence of temperature on water absorption in concrete during freezing”, *Nordic Concrete. Research,* Vol. 45, No. 1, pp. 45-58.

Schlorholtz, S., and Amenson, J., (1995) “Evaluation of microcracking and chemical deterioration in concrete pavements”, Final Report, Iowa DOT Project HR-358, Engineering Research Institute, Iowa State University, October, 1995, 205 pp.

Scrivener, K.L., Crumble, A. K. and Laugesen, P., (2004) “The interfacial transition zone (ITZ) between cement paste and aggregate in concrete”, *Interface Science*, Vol. 12, pp. 411-421.

Selander, A., (2010) “Hydrophobic impregnation of concrete structure-Effects on concrete properties”, PhD Thesis, Royal Institute of Technology, 45 pp.

Sellevold, E.J., Farstad, T. (1991) “Frost/salt-testing of concrete: effect of test parameters and concrete moisture history”, *Freeze-thaw and de-icing resistance of concrete*, edited by Fagerlund, G. and Setzer, M., Lund Institute of Technology, 1991, pp. 83-100.

Setzer, M. J., (1993) “On the abnormal freezing of pore water and testing on freeze-thaw and deicing salt resistance”, *International Workshop on the Resistance of Concrete to Scaling due to Freezing in the Presence of Deicing Salts*, Centre de Recherche Interuniversitaire sur le Beton, Universit éde Sherbrooke - Universit éLaval, Quebec, pp. 1-20.

Setzer, M. J., (2009) “Frost-attack on concrete—modeling by the micro-ice-lens model—evaluating by RILEM CIF test,” *Creep, Shrinkage and Durability Mechanics of Concrete and Concrete Structures*, Ise-Shima, Japan, Sept., pp. 971-977.

Setzer, M.J., Auberg, R., (1995) “Freeze-thaw and deicing salt resistance of concrete testing by the CDF method CDF resistance limit and evaluation of precision”, *Materials and Structures*, Vol. 28, NO. 1, pp. 16-31.

Setzer, M.J., Heine, P., Kasparek, S., Palecki, S., Auberg, R., Feldrappe, V., Siebel, E., (2004) “Test methods of frost resistance of concrete: CIF-Test: Capillary suction, Internal damage and Freeze thaw Test-Reference method and alternative methods A and B.”, *Materials and Structures*, Vol. 37, pp. 743-753.

Sha'at, A. A., Long, A. E., Montgomery, F. R., and Basheer, P. A. M., (1993) “Influence of controlled permeability formwork liner on the quality of the cover concrete”, *ACI-SP*, Vol. 139, pp. 91-106.

Snyder, K., Natesaiyer, K. and Hover, K., (2001) “The stereological and statistical properties of entrained air voids in concrete: a mathematical basis for air void system characterization”, *Materials Science of Concrete VI, The American Ceramic Society*, Westerville, OH, pp. 129–214.

Snyder, M. J., (1965) ”Protective coatings to prevent deterioration of concrete by deicing chemicals”, National Cooperative Highway research Program Report 16, Highway Research Board of the Division of Engineering and Industrial Research, National Academy of Sciences-National Research Council, pp. 1-21.

Sommer, H., (1979) “The precision of the microscopical determination of the air void system in hardened concrete”, *Cement, Concrete, and Aggregates*, Vol. 1, No. 1, pp. 49-55.

Stark, J., (1997) “Frost resistance with and without deicing salt-a purely physical problem?” Proceedings of the International RILEM Workshop, *Frost Resistance of Concrete*, London, UK, pp. 83-99.

Sun, Z., Scherer, G.W., (2010) “Effect of air voids on salt scaling and internal freezing”, *Cement and Concrete Research*, Vol. 40, No. 2, pp. 260-270.

Taber, S., (1930) “The mechanics of frost heaving”, *Journal of Geology*, Vol. 38, No. 4, pp. 303-317

Taus, V.L, Di Maio, A.A., Traversa, L.P., (2005) "Sorptivity: Parameter for the evaluation of cover concrete quality", *ACI SP*, Vol. 229, pp. 121-134.

Tittarelli, F., Moriconi, G., (2008) "The effect of silane-based hydrophobic admixture on corrosion of reinforcing steel in concrete", *Cement and Concrete Research*, Vol. 38, No. 11, pp. 1354–1357.

Tremblay, M.-H., Lory, F., Marchand, J., Scherer, G. W., Valenza, J.J., (2007) "Ability of the Glue Spall Model to Account for the De-Icer Salt Scaling Deterioration of Concrete", *Proc. 12th ICCC*, National Research Council of Canada, Montreal, Canada.

Valenza II, J. J., Scherer, G. W., (2006) "Mechanism of salt scaling", *Journal of American Ceramic Society*, Vol. 89, No. 4, pp. 1161–1179.

Verbeck, G. and Klieger, P., (1958) "Calorimeter-strain apparatus for study of freezing and thawing concrete", *Highway Research Board Bulletin*, No. 176, pp. 9-22.

Verbeck, G. J., Klieger, P., (1957) "Studies of salt scaling of concrete", *Highway Research Bulletin*, Bull. 150, Washington D.C., pp. 1-13.

Walker, H. N., (1980) "Formula for calculating spacing factor for entrained air voids", *Cement, Concrete, and aggregates*, Vol. 2, No. 2, pp. 63-66.

Wang F., Zhang Z., Li M., Huang D., Zhu Y., (2014) "Influence of chloride solution concentration difference on salt frost scaling of concrete", *Journal of Building Materials*, Vol. 17, No. 1, pp. 138-142.

Washburn, E.W., (1921) "The dynamics of capillary flow", *Physical Review*, Vol. 17, No. 3, pp. 273-283.

Wei, Y., (2008) "Modeling of autogenous deformation in cementitious materials, restraining effect from aggregate, and moisture warping in slabs on grade", PhD Dissertation, University of Michigan.

Weissenberger, J., Dieckmann, G., Gradinger, R. and Spindler, M., (1992) "Sea ice: a cast technique to examine and analyze brine pockets and channel structure", *Limnology and Oceanography*, Vol. 37, No. 1, pp. 179-183.

Wong, K.H., Weyers, E., Cady, P.D., (1983) “The retardation of reinforcing steel corrosion by alkyl-alkoxy silane”, *Cement and Concrete Research*, Vol. 13, No. 6, pp. 778–788.